

Faculty of Science and Engineering

Department of Spatial Sciences

Assessing climate change impacts on water
resources in the Ganges–Brahmaputra–Meghna
River Basin

Khandu

This thesis is presented for the Degree of

Doctor of Philosophy

of

Curtin University

September 2016

To the best of my knowledge and belief this thesis contains no material previously published by any other person except where due acknowledgement has been made. This thesis contains no material which has been accepted for the award of any other degree or diploma in any university.

KHANDU
01-09-2016

“It always seems impossible until it’s done”
- Nelson Mandela

Acknowledgment

I would like to express my deepest appreciation and gratitude to my lead supervisor Associate Professor Dr. -Ing Joseph L. Awange for his careful guidance, patience, and motivation. His knowledge, advice, and valuable comments and suggestions helped to gain a broad range of skills on geodetic applications to climate change and water resources. His deep understanding of climate change impacts on water resources made collaborations with several scientists across the world possible. Through this, I was able to improve my results and realise several joint publications. I would also like to thank my co-supervisors, Associate Professors Dr. -Ing. Michael Kuhn (Curtin University) and Dr. Richard Anyah (University of Connecticut, USA) for bringing in their valuable knowledge on climate and hydro-meteorological research. In particular, Dr. Richard Anyah brought the much needed experience of climate modelling to my study. Both co-supervisors have been very open to discussions and were very inspirational.

Apart from my supervisors, I would like to thank Dr. Ehsan Forootan (Cardiff University, UK), who was introduced to me by Professor Awange in 2013. His contribution to my research was undeniable. In particular, he gave me important suggestions on complex statistical techniques to analyze climate datasets. I also thank him for his support during my visit to the University of Bonn (Bonn, Germany). Additionally, I would like to thank all the co-authors of my papers for their contributions and for enlightening me on the multiple dimensions of climate and hydrology. I sincerely thank Dr. Rodrigo Mikosz Gonçalves of Federal University of Pernambuco (Brazil) for being a wonderful host during my research visit to the University. I experienced a completely different culture in Brazil and had a privilege of knowing a lot of wonderful research students.

I am grateful to Curtin Strategic International Research Scholarship (CSIRS) for granting me the PhD scholarship, without which I would not have had the opportunity to complete my studies. I would also like to acknowledge the financial supports of Prince Albert II Foundation of Monaco, the Intergovernmental Panel on Climate Change (IPCC), and Professor Bela Palancz of Budapest University of Technology and Economics (Hungary). These additional grants have allowed me to attend two regional climate modelling workshops and two research visits during the course of study. I would also like to thank the Landgate for providing me the opportunity to work with them. It helped me gain many important skills in geodetic data analysis, which were directly relevant to my study. In particular, I am grateful to Mr. Ken Leighton and Mrs. Linda Morgan for introducing me to Landgate, and other geodetic members to their support.

Finally, I would like to thank my mother for being such a wonderful mum to me and my brothers. She single-handedly raised us through all odds and helped us attain our goals. Her vision and hard work was immeasurable. Further, I would like to offer my deepest appreciation to my late grandfather, grandmother and aunt, whose supports were crucial during my early school days. Unfortunately, they couldn't live long enough to see me grow.

Abstract

1 The impact of climate change on water resources, and consequently on water availability,
2 is one of the major challenges faced by the society today. With over 650 million people,
3 the water resources in the Ganges–Brahmaputra–Meghna (GBM) River Basin are under
4 enormous pressure from both climate change and increasing demands from a rapidly
5 growing population. However, assessing climate change impacts on water resources in
6 the GBM River Basin is subject to large uncertainties both in climate model projections
7 and hydrological modelling approaches, mainly due to increasing demands of freshwater
8 resources and inadequate spatio-temporal representation of ground-based observation
9 systems. This thesis provides an improved understanding of climate change impacts
10 on water resources in the GBM River Basin through a combination of *in-situ* and
11 satellite remote sensing (SRS) observations, state-of-the-art regional climate modelling,
12 and hydrological modelling approaches. In particular, this thesis will assess (i) recent
13 changes and variations in rainfall and temperature, (ii) the role of climate change and
14 human water use on the basin’s water resources, (iii) high-resolution regional climate
15 models (RCMs) that are critical for understanding future changes in the regional water
16 cycle, (iv) potential changes in future drought and extreme wet occurrences, and (v) the
17 impacts of large-scale climate fluctuations on lower atmospheric temperature patterns,
18 which are addressed as follows.

19 Firstly, the potential benefits of readily available quasi-global satellite-based mea-
20 surements and global high-resolution retrospective analysis (reanalysis) products are
21 examined by comparing them with available *in-situ* gauge datasets from 1980–2013.
22 Observed temperature records show widespread warming across the basin, with a max-
23 imum increase of $0.6^{\circ}\text{C decade}^{-1}$ in the Himalayan region. Precipitation datasets show
24 pronounced monsoon rainfall decline, especially across the high rainfall regions of north-
25 east India, Bhutan, Nepal, and Bangladesh between 1998 and 2013. Additionally, both
26 global (e.g., El Niño Southern Oscillation Index, ENSO) and regional (e.g., Indian Ocean
27 Dipole, IOD) sea surface temperature (SST) variations significantly impact the basin’s
28 climate, contributing to about 10–20% (ENSO) and 8–10% (IOD) of the annual precipi-
29 tation. While precipitation products from Tropical Rainfall Measuring Mission (TRMM)
30 Multisatellite Precipitation Analysis (TMPA, since 1998) performs best among a suite
31 of other products, European Centre for Medium-Range Weather Forecasts (ECMWF)
32 retrospective analysis (ERA-Interim) and MERRA (Modern-Era Retrospective Anal-
33 ysis for Research and Applications) agrees well with the observed precipitation and
34 temperature, respectively.

35 Secondly, the observed impacts of precipitation variability and human water con-
36 sumption on the available freshwater storage (mainly groundwater, soil moisture, and
37 surface water) are investigated, particularly focussing on the last decade when large-
38 scale observations of total water storage (TWS) changes were made possible by the
39 state-of-the-art GRACE (Gravity Recovery and Climate Experiment) satellite mission.
40 The results indicate that both Ganges and Brahmaputra–Meghna River Basins have
41 lost significant amount of water mass since late 2002 at an average rate of 9.1 ± 4.5
42 $\text{km}^3 \text{ year}^{-1}$ and $10.5\pm 3.2 \text{ km}^3 \text{ year}^{-1}$ for the Ganges and Brahmaputra–Meghna River

43 Basin, respectively, albeit a general increase in soil moisture. By incorporating water
44 use models such as the WaterGAP (Water-Global Analysis and Prognosis version 2.2a)
45 Global Hydrological Model (WGHM), it is found that majority, if not all of the water
46 loss has resulted from excessive human water withdrawal, especially in the regions of
47 high agricultural activities (e.g., western Ganges River Basin and Bangladesh). Extreme
48 droughts, such as those of 2006 and 2009, had profound negative impacts on the basin's
49 water storage, which calls for a wider approach on transboundary water resources man-
50 agement.

51 Thirdly, the skills and limitations of two state-of-the-art high-resolution regional
52 climate models (RCMs) are assessed, focusing on the basic climate variables such as
53 precipitation and temperature. In general, the two RCMs: (i) Regional Climate Model
54 version 4.4 (RegCM4.4) and (ii) Providing REgional Climate Information for Impact
55 Studies (PRECIS), show reasonable skills in simulating Indian monsoon rainfall in the
56 GBM River Basin. However, the RCM simulations poorly reproduce the onset and with-
57 drawal of the Indian monsoon and its associated atmospheric circulations. The RCM
58 simulations forced by Global Climate Models (GCMs) fail to reproduce the observed
59 inter-annual variability of precipitation. However, they are able to reproduce the ob-
60 served temperature trends in the GBM River Basin. Climate change projections for the
61 next 80–90 years and drought and extreme wet occurrences are studied based on a range
62 of simulated RCM and GCM precipitation datasets. While the GBM River Basin is pro-
63 jected to warm by 2–4°C by 2100, with a likely increase in monsoon rainfall, severe and
64 extreme droughts are likely to be higher for the second half century (2050–2099). The
65 Ganges River Basin, Bangladesh, and parts of northeast India are more likely to be af-
66 fected by severe and extreme droughts than elsewhere, with a probability of 15–20% (~1
67 in 6 years) and 6–8% (~1 in 17 years), respectively. This will have major consequences
68 on the future water availability irrespective of a monsoon rainfall increase.

69 Finally, the benefits of using Global Navigation Satellite Systems (GNSS) radio oc-
70 cultation (RO) for monitoring temperature variations in UTLS (upper troposphere-
71 lower stratosphere) region are assessed by analysing monthly accumulated atmospheric
72 profiles from the ongoing COSMIC (Constellation Observing System for Meteorology,
73 Ionosphere, and Climate) RO mission for the period 2006–2013. The COSMIC mission
74 offers a unique opportunity in the GBM River Basin to potentially offset key limitations
75 in conventional observation systems (e.g., radiosondes). Many existing radiosondes, es-
76 pecially in the Indian territory are being upgraded with GPS (Global Position Systems)
77 sensors and comparisons with COSMIC RO data indicate that their observation qualities
78 have improved significantly. Further, COSMIC's superior spatial coverage enables finer
79 representation of UTLS, which will help to improve weather/climate predictions. Based
80 on eight years of COSMIC data, it is observed that ENSO accounted for ~73% of the
81 tropopause temperature and height variability. The tropopause temperature (height)
82 increased (decreased) by about 1.5°C (300 m) during 2009/2010 major El Niño event.
83 Additionally, the tropospheric temperature trends show a clear indication of warming,
84 although not significant over a short period of time.

Contents

| | | |
|-----|--|-----------|
| 85 | | |
| 86 | Abstract | x |
| 87 | 1 Introduction | 1 |
| 88 | 1.1 Climate change impacts on water resources | 1 |
| 89 | 1.2 Statement of the problem | 4 |
| 90 | 1.3 Objectives | 7 |
| 91 | 1.4 Thesis outline | 8 |
| 92 | 2 Precipitation and temperature variability | 10 |
| 93 | 2.1 Introductory remarks | 10 |
| 94 | 2.2 The Ganges-Brahmaputra-Meghna River Basin | 12 |
| 95 | 2.3 Data | 14 |
| 96 | 2.3.1 Available observational data | 14 |
| 97 | 2.3.2 Reanalysis products | 16 |
| 98 | 2.3.3 Sea surface temperature data | 17 |
| 99 | 2.4 Methods | 18 |
| 100 | 2.4.1 Trend analysis and significance testing | 18 |
| 101 | 2.4.2 Principal Component Analysis (PCA) | 21 |
| 102 | 2.5 Results and discussion | 22 |
| 103 | 2.5.1 Annual amplitudes and trends of rainfall and temperature | 22 |
| 104 | 2.5.2 Interannual variability of precipitation and temperature | 28 |
| 105 | 2.6 Concluding remarks | 34 |

| | | |
|-----|--|-----------|
| 106 | 3 Observed impacts of climate change and human water use on water | |
| 107 | resources | 36 |
| 108 | 3.1 Introductory remarks | 36 |
| 109 | 3.2 State of water use | 38 |
| 110 | 3.3 Data and methods | 39 |
| 111 | 3.3.1 Land surface models | 39 |
| 112 | 3.3.2 GRACE total water storage (TWS) changes | 41 |
| 113 | 3.3.3 WaterGAP Global Hydrology Model (WGHM) | 45 |
| 114 | 3.3.4 Extreme indices | 46 |
| 115 | 3.3.5 Error estimation | 47 |
| 116 | 3.4 Results and Discussion | 51 |
| 117 | 3.4.1 Uncertainties in hydro-meteorological datasets | 51 |
| 118 | 3.4.2 Observed changes in water storages | 53 |
| 119 | 3.4.3 Impact of hydro-meteorological extremes | 57 |
| 120 | 3.4.4 Impacts of human water abstraction | 64 |
| 121 | 3.5 Concluding remarks | 66 |
| 122 | 4 Assessing high-resolution regional climate model simulations | 68 |
| 123 | 4.1 Introductory remarks | 68 |
| 124 | 4.2 Key attributes of Regional Climate Models (RCMs) | 70 |
| 125 | 4.2.1 Model dynamics | 71 |
| 126 | 4.2.2 Boundary conditions | 72 |
| 127 | 4.2.3 Model parameterizations | 72 |
| 128 | 4.2.4 Model domain | 73 |
| 129 | 4.3 Regional climate model (RCM) data | 73 |
| 130 | 4.3.1 RegCM4.4 simulations and boundary conditions | 73 |
| 131 | 4.3.2 PRECIS model data | 76 |
| 132 | 4.4 Observational datasets and methods | 77 |
| 133 | 4.4.1 Observational datasets | 77 |

| | | | |
|-----|----------|--|-----------|
| 134 | 4.4.2 | Evaluation methods | 77 |
| 135 | 4.5 | Results | 78 |
| 136 | 4.5.1 | Seasonal precipitation and temperature mean climatology | 78 |
| 137 | 4.5.2 | Annual Cycles of precipitation and temperature | 85 |
| 138 | 4.5.3 | Onset and withdrawal of monsoon | 85 |
| 139 | 4.5.4 | Trends and interannual variations in precipitation and temperature | 89 |
| 140 | 4.6 | Concluding remarks | 94 |
| 141 | 5 | Future projection of droughts and wet events | 96 |
| 142 | 5.1 | Introductory remarks | 96 |
| 143 | 5.2 | Data and methods | 99 |
| 144 | 5.2.1 | Model and observational data used | 99 |
| 145 | 5.2.2 | Sea surface temperature data | 100 |
| 146 | 5.2.3 | Identification of extreme dry and wet events | 101 |
| 147 | 5.3 | Results | 102 |
| 148 | 5.3.1 | Model evaluation | 102 |
| 149 | 5.3.2 | Seasonal projections of precipitation and temperature | 106 |
| 150 | 5.3.3 | Future projection of drought and wet conditions | 109 |
| 151 | 5.3.3.1 | Frequency of drought and wet events | 109 |
| 152 | 5.3.3.2 | Drought and wet occurrences | 113 |
| 153 | 5.3.3.3 | Area affected by dry and wet spells | 117 |
| 154 | 5.4 | Discussion and summary | 119 |

| | | | |
|-----|----------|---|------------|
| 155 | 6 | Spatio-temporal variability of UTLS temperature based on COSMIC | |
| 156 | | GNSS RO | 122 |
| 157 | 6.1 | Introductory remarks | 122 |
| 158 | 6.2 | Data and methods | 124 |
| 159 | 6.2.1 | FORMOSAT/COSMIC RO data | 124 |
| 160 | 6.2.2 | Radiosonde data | 126 |
| 161 | 6.2.3 | Reanalysis products | 127 |
| 162 | 6.2.4 | Ocean–atmospheric indices | 129 |
| 163 | 6.2.5 | Comparison of radiosonde and COSMIC RO datasets | 129 |
| 164 | 6.2.6 | Tropopause temperatures and heights | 130 |
| 165 | 6.3 | Results and discussion | 130 |
| 166 | 6.3.1 | Evaluation of radiosonde observations | 130 |
| 167 | 6.3.1.1 | Temperature | 131 |
| 168 | 6.3.1.2 | Water vapour | 134 |
| 169 | 6.3.1.3 | Refractivity | 134 |
| 170 | 6.3.2 | Seasonal and interannual variability of UTLS temperature | 136 |
| 171 | 6.3.3 | Trends and variability of tropopause heights and temperatures | 141 |
| 172 | 6.4 | Concluding remarks | 146 |
| 173 | 7 | Conclusion and future outlook | 148 |
| 174 | 7.1 | Summary of the findings | 148 |
| 175 | 7.1.1 | Quality assessment of climate datasets | 148 |
| 176 | 7.1.2 | Key improvements in Regional Climate Models (RCMs) | 150 |
| 177 | 7.1.3 | Impacts of climate variability and change on water resources | 151 |
| 178 | 7.1.4 | Impacts of excessive water abstraction on various water storage | |
| 179 | | components | 152 |
| 180 | 7.2 | Future outlook | 154 |
| 181 | 7.2.1 | Simulating future hydrological droughts using RCM projected | |
| 182 | | temperature and precipitation | 154 |
| 183 | 7.2.2 | Improving spatial representation of climate datasets | 154 |
| 184 | 7.2.3 | Towards an integrated drought monitoring system | 155 |

| | | |
|-----|---------------------------|------------|
| 185 | References | 156 |
| 186 | Lists | 190 |
| 187 | List of Figures | 190 |
| 188 | List of Tables | 198 |
| 189 | Acronyms | 201 |
| 190 | Appendix | 203 |

191 1. Introduction

192 1.1 Climate change impacts on water resources

193 The Earth's climate has undergone significant changes throughout the course of its
194 history, much without any major anthropogenic interventions. In more recent years,
195 however, the global temperature has been rising at a much greater rate due to an in-
196 creasing concentrations of greenhouse gases (GHG) from human activities (IPCC, 2007,
197 2013). Based on the available instrumental records, the globally land and ocean tem-
198 perature has warmed on average by 0.85°C [0.65°C–1.06°C] over the period 1880 to
199 2012, 0.89°C [0.69°C–1.08°C] from 1901–2012, and 0.72°C [0.49°–0.89°C] between 1951
200 and 2012 (Hartmann et al., 2013). The past three decades has shown to be consider-
201 ably warmer than the previous decades with the last decade or so (from 2000s) being
202 the warmest (0.78°C from 2003–2012). Observational studies and climate model simu-
203 lations have shown that human activities, primarily due to burning of fossil fuels and
204 rapid changes in land cover, are contributing to climate change by warming the Earth's
205 atmosphere. Besides multi-decadal warming trends over the past century, observational
206 records of global/regional land surface temperatures also show considerable interannual
207 to decadal temporal and spatial variations due to periodic large-scale fluctuations in the
208 ocean and the atmosphere (e.g., Saji et al., 1999, Trenberth, 1997). These coupled ocean-
209 atmospheric fluctuations, for example El Niño Southern Oscillation (ENSO), influence
210 regional and local circulation patterns resulting in extreme weather/climatic conditions
211 (e.g., increasing frequency and intensity of droughts) over various parts of the world.

212 One of the most important aspects of climate change and variability is the evolution
213 of the hydrological cycle and its impact on freshwater resources. Changes in hydro-
214 logical cycle will lead to diverse impacts and risks on the society, mainly through its
215 impact on quantity, variability, timing, form, and intensity of precipitation. Although
216 water moves through the hydrological cycle, it is a locally variable resource, and vulner-
217 abilities to hydro-meteorological extremes such as floods and droughts can greatly vary
218 from region to region. With a population of over 650 million, the Ganges–Brahmaputra–
219 Meghna River Basin (GBM) in South Asia, has become highly vulnerable to climate
220 change, primarily threatening its various sources of freshwater system (Mirza et al.,
221 1998, Chowdhury and Ward, 2004, Immerzeel, 2008, Immerzeel et al., 2010, 2014, Papa
222 et al., 2015, Khandu et al., 2016a). The water resources in the GBM River Basin are
223 heavily reliant on the Indian monsoon rainfall and perennial river systems from glacier-
224 ized Himalayas and its enormous groundwater reserves beneath the great fluvial plains
225 of Ganges, Brahmaputra, and Meghna rivers that are in fact very much governed by
226 changing global/regional climate.

227 The Indian summer monsoon accounts for 60–90% of the annual precipitation over
228 a four month period (June to September) and is the single largest source of freshwater
229 in the region. However, most studies indicate that the Indian monsoon circulation has
230 been weakening over the past few decades (e.g., Ramanathan et al., 2005, Chung and

231 Ramanathan, 2006, Sinha et al., 2011, Turner and Annamalai, 2012) leading to an overall
232 decline in monsoon precipitation since the 1950s, although it is likely to increase in the
233 future (e.g., Kumar et al., 2006, Caesar et al., 2015, Whitehead et al., 2015). While the
234 current decline is being attributed to the weakening meridional thermal gradient across
235 Asia in response to the warming Indian Ocean (Chung and Ramanathan, 2006, Roxy
236 et al., 2014) and radiative cooling effects from increasing aerosol concentrations over
237 Asia (Ramanathan et al., 2005, Lau et al., 2009), future increases may likely result from
238 enhanced moisture transport over the monsoon region. Any changes in the quantity and
239 variability of monsoon rainfall will have profound impact on the basin's water resources,
240 particularly through its effect on runoffs, soil moisture, and groundwater, as well as
241 through changing frequency and magnitude of floods and meteorological droughts. The
242 Intergovernmental Panel on Climate Change (IPCC) predicts an increased risk of flood
243 hazards and short-term droughts across Asia (Jiménez-Cisneros et al., 2014).

244 The Himalayan mountains in the northern GBM River Basin have the largest concen-
245 tration of glaciers outside the polar region with an approximate area of 22,800 km² based
246 on the most recent estimates of Bolch et al. (2012). Most glaciers in the eastern and
247 central Himalayas are accumulated during the Indian summer monsoon (Bolch et al.,
248 2012), whereas the western areas accumulate snow fall mainly during the winter when
249 westerlies or extratropical storms dominate the weather pattern (Dimri et al., 2015).
250 These glaciers store large reserves of freshwater providing continuous flows to thousands
251 of tributaries that eventually form the Ganges, Brahmaputra, and Meghna river sys-
252 tems, which combine to form the third largest freshwater outlet in the world (Steckler
253 et al., 2010). Most Himalayan glaciers are found to be melting at a faster rate in recent
254 decades since the mid-19th century (ICIMOD, 2007, Eriksson et al., 2009, Immerzeel
255 et al., 2010, Inman, 2010, Sherler et al., 2011, Bolch et al., 2012, Jacob et al., 2012),
256 except for few areas in the Karakoram where indications of stability or mass gain were
257 reported (Bolch et al., 2012). Although glacier responses vary in time and space, recent
258 modelling studies have suggested a moderate loss of glacier mass over the remaining
259 21st century (Radić and Hock, 2010). Using a high-resolution cryospheric hydrological
260 model, Immerzeel et al. (2012) estimated a higher mass loss along the southern slopes of
261 central and eastern Himalayas (covering Nepal and Bhutan) predicting a 75% reduction
262 in glacier area by 2088 under a projected warming rate of 0.6°C decade⁻¹. This will
263 have a dramatic impact on the regional hydrological regime both in terms of future
264 water availability and water-related disasters. The gradual loss of glaciers in the com-
265 ing decades will reduce river flows, especially during winter and spring affecting water
266 supplies across all sectors (e.g., domestic, industrial and agriculture). More accelerated
267 glacier melts will be even more catastrophic to humanity and the hydropower sector for
268 the downstream valleys and plains due to increased risks of glacial lake outburst floods
269 (GLOF, ICIMOD, 2007).

270 Groundwater resources are an essential component of the hydrological cycle and
271 are a primary source of freshwater for human consumption, agriculture, and industrial
272 uses, across many parts of the world. Globally, groundwater contributes to 36%, 42%,
273 and 27% of the water used for domestic, agriculture, industrial purposes, respectively,
274 amounting to one third of all freshwater withdrawals (Döll et al., 2012, Richey et al.,
275 2015). Groundwater is resilient to short-term meteorological droughts and associated

276 increased demands during droughts and supplement surface water resources. But it can
277 be highly vulnerable to frequent and prolonged periods of dry spells. The GBM River
278 Basin holds one of the largest reserves of groundwater, particularly along the great
279 Gangetic Plains of India and Nepal, and across Bangladesh and Assam (India), with a
280 potential yield of 108.5 km³/year, 21 km³/year, and 10.7 km³/year, respectively (FAO,
281 2011, Mukherjee et al., 2015). Currently, groundwater accounts for about 60–80% of the
282 domestic water supplies across these areas and contributes to more than 85% of water
283 for agriculture, which is about 35% of the global groundwater withdrawal (Shamsud-
284 duha, 2013, Mukherjee et al., 2015). Climate change effects groundwater resources (both
285 quality and quantity) through its impact from precipitation variability (e.g., floods and
286 droughts), increased atmospheric water demands, reduced (sub-) surface water, ground-
287 water recharge/discharge, saltwater intrusion, and other bio-geochemical activities (Tay-
288 lor et al., 2013, Famiglietti, 2014).

289 With rapidly increasing population and its associated increase in demands for fresh-
290 water, the combined impacts of climate change and human water abstraction represents
291 a serious threat to the sustainability of freshwater resources in the GBM River Basin.
292 Recent satellite-based observations have already shown a significant loss of groundwater
293 over the past decade with significant portion of them resulting from human water ab-
294 straction (Rodell et al., 2009, Tiwari et al., 2009, Shamsudduha et al., 2009b, Khandu
295 et al., 2016a). While the projections of the direct impacts of climate change on ground-
296 water resources remains unclear due to large uncertainties in climate model projec-
297 tions (particularly, precipitation), groundwater changes are expected to occur primarily
298 through increasing water demands to meet the growing population and its associated
299 socio-economic activities (e.g., irrigation, land use change) (Taylor et al., 2013). Never-
300 theless, groundwater recharge projections are found to be closely related to projected
301 changes in precipitation and extreme events (Taylor et al., 2013), suggesting a potential
302 increase in recharge rates considering a probable increase in monsoon rainfall (Kumar
303 et al., 2006, Kripalani et al., 2007, Caesar et al., 2015, Whitehead et al., 2015). Similarly,
304 soil moisture and surface water storage (e.g., runoffs) is predicted to increase during the
305 crop-growing season (see, Mishra et al., 2014, Whitehead et al., 2015). Other climate
306 change impacts on groundwater resources include degradation of groundwater quality
307 and salt water intrusion as users dig deeper into the ground, which are beyond the scope
308 of this thesis.

309 The overall movement of water through the hydrological cycle can be characterised by
310 a simple water balance equation: $\Delta S = P - E - Q$, where ΔS is the total water storage or
311 TWS (representing the sum of groundwater, soil moisture, vegetation, surface water), P
312 is the precipitation, E is the evapotranspiration, and Q is the runoff, at various spatial
313 and temporal scales. To supplement ground-based observations and water resources
314 management over large and poorly gauged areas of the GBM River Basin, satellite
315 remote sensing (SRS) plays a crucial role in monitoring the various components of
316 the hydrological cycle. SRS can now effectively monitor almost all components of the
317 water balance equation. Precipitation is being remotely sensed using both infra-red
318 (IR) and microwave (MW) sensors on board geostationary satellites and low-Earth
319 orbiting satellites (e.g., Tropical Rainfall Measuring Mission, TRMM, Kummerow et al.,

1998). IR-based rainfall estimates have a longer historical record and have higher spatio-temporal resolution than the more accurate (and shorter temporal record) MW-based estimates but suffer from higher uncertainty due to various problems (Ebert et al., 2007). E is being monitored using MODerate Resolution Imaging Spectroradiometer (MODIS) onboard NASA's Terra and Aqua satellites (Justice et al., 2002). Satellite altimetry missions such as Topex/Poseidon, Jason I and II, and the European Space Agency (ESA) observe variations of the Earth's surface water volumes including oceans, seas, lakes, reservoirs, and rivers (Shum et al., 1995, Berry et al., 2005).

TWS can be further broken down into groundwater storage (GWS), (sub-) surface water storage (SWS), canopy water storage or water stored in vegetation (CWS). While the individual components of TWS are still difficult to monitor (especially GWS) using SRS techniques, the launch of the Gravity Recovery And Climate Experiment (GRACE, Tapley et al., 2004) mission in 2002 enabled the closure of the terrestrial water budget by providing large-scale quantitative estimates of changes in TWS fields (ΔS) on an approximately monthly basis. SRS-based observations are regularly assimilated in retrospective analysis (or reanalysis) and land surface and hydrological models that are widely used to quantify climate change impacts on various hydrological components (e.g., Döll et al., 2003, Mishra et al., 2014). The performance of reanalyses have significantly improved with the assimilation of additional data from SRS-based observations (e.g., Rodell et al., 2004, Saha et al., 2010, Dee et al., 2011, Rienecker et al., 2011, Döll et al., 2014). Real-time SRS observations such as hourly or sub-hourly rainfall estimates (e.g., Janowiak et al., 2001, Huffman et al., 2007, Funk et al., 2015) are increasingly used in operational weather forecasts to monitor extreme weather events such as storms, flooding, and landslides. Climate models and hydrological models add knowledge to the key climate and hydrologic process and has been rigorously applied to understand the contributions of climate change (both natural and man-made) and other drivers (e.g., land use change, water use) on water resources (Meehl et al., 2007, Taylor et al., 2012, 2013, Döll et al., 2014).

1.2 Statement of the problem

Considering the complex interplay between natural climate variability, anthropogenic contribution (e.g., increasing emission of GHGs and landuse change), and growing societal demands for freshwater, assessing the impacts of climate change on water resources, and consequently water availability is a monumental process that requires enormous interdisciplinary research and cross-sector collaboration. The general approach to quantifying climate change impacts on water resources includes: (i) assessing historical changes in climate characteristics (e.g., rainfall, temperature, runoff, soil moisture) based on existing ground-based observations, (ii) evaluating the skills of climate (both regional and global) and hydrological model simulations of the past and present by comparing its output variables with available observational datasets, (iii) simulating future climate characteristics using multiple GCMs, (iv) downscaling projections from coarse grid GCM outputs to a finer resolution using downscaling methods such as dynamical or statistical approaches, as required by hydrological models, (v) applying the projected future

362 changes in e.g., rainfall, temperature, evapotranspiration, as inputs to a hydrological
363 model (e.g., soil moisture, groundwater). More advanced approaches incorporate global
364 water use models to simulate the combined impacts of human water consumption (for
365 domestic, agriculture, and industrial purposes) and climate change and variability on
366 water availability (e.g., Döll et al., 2003, Döll et al., 2012).

367 However, each step outlined above entails representing the most up-to-date knowl-
368 edge of global change and identifying uncertainties from a large number of sources,
369 including, observations (e.g., Andermann et al., 2011, Prakash et al., 2014, Khandu
370 et al., 2015), reanalysis systems (e.g., Kishore et al., 2016, Khandu et al., 2016c), cli-
371 mate models (e.g., Knutti et al., 2010, Knutti and Sedláček, 2013), internal climate
372 variability (e.g., Turner et al., 2007, Deser et al., 2012, Thompson et al., 2015), regional
373 downscaling methods (e.g., Rockel, 2015), hydrological models (Mendoza et al., 2015),
374 and non-climatic drivers (e.g., Taylor et al., 2013, Clark et al., 2016). While above
375 sources of uncertainties are common to most parts of the world and are continuously
376 being addressed (Clark et al., 2016), they are often heightened or amplified over certain
377 areas of the globe such as the GBM River Basin due to its varied climatic and hydro-
378 logic regime. These can be characterised by rugged mountains of the Himalayas (Barros
379 et al., 2004), high interannual variations of the Indian monsoon (Krishnamurthy and
380 Kinter III, 2003, Krishnamurthy and Krishnamurthy, 2014), high population density
381 and inefficient water use (Central Ground Water Board, 2014, Famiglietti, 2014), lack
382 of adequate observational data, and complexities involved in mapping hydrologic com-
383 ponents on a large-scale (Shamsudduha et al., 2009b, Central Ground Water Board,
384 2014, Mukherjee et al., 2015), which are briefly summarized below.

385 Firstly, the GBM River Basin is a transboundary basin shared by five developing
386 countries: Bangladesh, Bhutan, India, Nepal and Tibet (southern China), where public
387 access to hydrometeorological data among the riparian countries are limited or restricted
388 (Chowdhury and Ward, 2004, Prasai and Surie, 2015). More recently, Prasai and Surie
389 (2015) found little progress on transboundary data sharing despite the enactments of
390 Right To Information (RTI) laws and insistence for openness between the governments
391 in the region. The study also exposed many intergovernmental problems related to
392 issues such as poor record keeping, lack of data and/or maintenance, among others.
393 Further, basic climate monitoring networks (e.g., rain gauges) are spatially sparse, par-
394 ticularly along the Himalayan mountains (Duncan and Biggs, 2012, Khandu et al., 2015)
395 and sometimes insufficient (e.g., groundwater data). For instance, proper monitoring of
396 rainfall and temperature in Bhutan began only in the mid-1990s and are mostly located
397 in towns (NEC, 2011). There are economic challenges and other difficulties in operating
398 weather stations in the uninhabited regions of the Himalayas, thus, long-term *in-situ*
399 records of snow/ice and other important variables such as rainfall and temperature are
400 very few and often discontinuous. Most readily available quasi-global high-resolution
401 SRS-based observations have short temporal records and have been found to exhibit
402 limited skills in representing the key metrics of variability and change (e.g., precipita-
403 tion) (Andermann et al., 2011, Duncan and Biggs, 2012, Prakash et al., 2014, Khandu
404 et al., 2015). Nevertheless, their free access has enabled important contribution to the
405 development of physical and statistical algorithms to address these issues.

406 Secondly, due to lack of ground-based data and data sharing problems, previous stud-
407 ies on climate change impacts on water resources have been primarily restricted within
408 the geographical domain of the riparian nations, especially within India (e.g., Roy and
409 Balling, 2004, Goswami et al., 2010, Jain et al., 2012, Devineni et al., 2013, Chowdary
410 et al., 2014, Mishra and Liu, 2014, Mishra et al., 2014, Mukherjee et al., 2015) and
411 Bangladesh (e.g., Mirza et al., 2003, Chowdhury, 2003, Hoque et al., 2007, Immerzeel,
412 2008, Islam et al., 2008, Gain et al., 2011, Biemans et al., 2013, Shahid et al., 2015). Al-
413 though Bhutan, Nepal and other parts of the GBM River Basin received enormous focus
414 in recent years with help from several regional initiatives and international finances such
415 as Water and Global Change (WATCH, <http://www.eu-watch.org/>), Twinning Euro-
416 pean and South Asian River Basins (BRAHMATWINN, [http://www.brahmatwinn.
417 uni-jena.de/](http://www.brahmatwinn.uni-jena.de/)), Himalayan Glacier Retreat and Changing Monsoon Pattern (High-
418 Noon, <http://www.eu-highnoon.org/>), and Assessment of the Causes of Sea-level Rise
419 Hazards and Integrated Development of Predictive Modeling Towards Mitigation and
420 Adaptation (BanD-AID, <http://igfagcr.org/funded-projects/>), there are still big
421 knowledge gaps and limited awareness within the region.

422 Thirdly, assessing and quantifying climate change impacts on water resources, has
423 become an interdisciplinary task that requires more integrated approaches through com-
424 bination of climate change/variability, human contributions, and water use, all of which
425 are subject to substantial uncertainties (Treidel et al., 2012, Taylor et al., 2013, Clark
426 et al., 2016). New satellite data retrieval algorithms provide enormous opportunity to
427 improve spatio-temporal variations in individual water components and bridge impor-
428 tant resource and knowledge gaps for the region (Duncan and Biggs, 2012). The ongoing
429 SRS missions have contributed immensely to address the recent groundwater problems
430 in the GBM River Basin (Rodell et al., 2009, Tiwari et al., 2009), which will inform to
431 structure better water resources management. However, measurements from satellites
432 only cannot attribute changes in various water anomalies to different sources. Climate
433 and hydrological models, in particular, play an integral role in identifying these sources
434 and its uncertainties (Knutti and Sedláček, 2013). Climate modelling studies in the re-
435 gion have primarily been focussed on the Indian monsoon using coarse resolution GCMs
436 (Annamalai et al., 2007, Kripalani et al., 2007, Sengupta and Rajeevan, 2013, Sperber
437 et al., 2013, Su et al., 2013, Chaturvedi et al., 2014, Sarthi et al., 2015) or RCMs of
438 approximately 50×50 km grid (e.g., Dash et al., 2006, Kumar et al., 2006, Ramesh and
439 Goswami, 2014, Salvi et al., 2014). Only few studies have applied high resolution (25×25
440 km or finer) RCMs to study future climate changes and their associated impacts in the
441 GBM River Basin (Srinivas et al., 2012, Mathison et al., 2013, Caesar et al., 2015, White-
442 head et al., 2015). More studies are needed to characterize and minimise uncertainties
443 throughout the modelling process, and as well as to improve climate and hydrological
444 modelling capabilities, particularly along the Himalayan Mountains and coastal regions
445 (Asian Development Bank, 2012).

1.3 Objectives

In order to address some of the issues highlighted in Section 1.2, as well as to improve our understanding of the basin hydrology, this thesis examines the observed and future impacts of climate variability/change on water resources in the GBM River Basin. In particular, it aims to highlight the important contributions and limitations of existing observational datasets (especially those obtained from SRS-based measurements) and global high-resolution reanalyses, and climate/hydrological models for the most recent period of 1980–2015, which will be addressed in the following specific objectives:

- (i) assess the most recent changes (1980–2013) in precipitation and temperature using the most up-to-date records of multiple global and regional spatially interpolated high-resolution ground-based observations, quasi-global SRS-based precipitation estimates, and global high-resolution reanalysis products. This study aims to quantify the recent observed changes in precipitation and temperature, identify the sources of seasonal changes and extreme variations, and examine the role of large-scale ocean-atmospheric fluctuations on basin's climate. This study also sets out the potentials and limitations of SRS-based observations and high global-resolution reanalysis products in representing the key climate characteristics of the GBM River Basin.
- (ii) quantify the observed impacts of climate change/variations and human water abstraction on basin's water storage potential, including the effects of precipitation extremes on surface water storage, soil moisture, and TWS. This includes estimating relative uncertainties in soil moisture data simulated by existing reanalysis systems and land and/or hydrological models, determining most suitable approach for applying low-resolution GRACE time-variable gravity field solutions to obtain reliable estimates of TWS changes for the GBM River Basin, and applying hydrological model data to quantify the impacts of human water use.
- (iii) examine the skills of two high-resolution state-of-the-art RCMs: (a) Regional Climate Model version 4.4 (RegCM4.4) and (b) Providing REgional Climate Information of Impact Studies (PRECIS), and explore the impacts of 21st climate change projections on water resources in the GBM River Basin, focusing on the future meteorological droughts and extreme wet events. As a principal driver to the future water availability, increase in drought frequencies will exert additional pressure on the basin hydrological system and its water supplies. The study also examines the future occurrences of drought and wet frequencies using multiple RCM and GCM simulations.
- (iv) examine potential benefits of applying Global Navigation Satellite Systems (GNSS) radio occultation (RO) for monitoring temperature variations in upper-troposphere lower-stratosphere (UTLS) region based on approximately 8 years (2006–2013) of high quality atmospheric profiles retrieved from the ongoing COSMIC (Constellation Observing System for Meteorology, Ionosphere, and Climate) RO mission. The COSMIC RO mission delivers more than 400 well-distributed RO profiles

487 across the GBM River Basin enabling a major breakthrough in a region that has
488 a very poor upper air monitoring network.

489 1.4 Thesis outline

490 Some of the chapters presented in this thesis are originally written as research articles
491 and most of them have already been published. My other contributions to the field of
492 climate change studies that are indirectly related to the present study are an inform of
493 collaborative research (see, [Awange et al., 2015](#), [Forootan et al., 2015](#), [Awange et al.,](#)
494 [2016a](#)). Table 1.1 presents the list of papers, references, and their relationship to re-
495 spective chapters. Those accrued from collaborative researches are marked as asterisk
496 (*). A chart illustrating the overall summary of this thesis highlighting the studies con-
497 ducted and their relevancy to the overall objective is shown in Fig. 1.1, which are briefly
498 summarized as follows.

499 Following this introductory chapter, the subsequent chapters are presented in their
500 original format of the respective journals with minor changes to align with the above
501 mentioned objectives. In Chapter 2, the basic climatic characteristics of the GBM River
502 Basin are characterized by analysing the precipitation and temperature changes and
503 seasonal variations for the past three decades. Several climate datasets are assessed for
504 their strengths and weakness through literature review and by comparing with obser-
505 vations, particularly focusing on high-resolution precipitation datasets from SRS and
506 global reanalyses. The chapter also discusses the role of large-scale ocean-atmospheric
507 circulation patterns on the regional rainfall and temperature variability by quantifying
508 their contribution. In Chapter 3, the observed impacts of climate variability (particularly
509 precipitation) and uncontrolled abstraction of groundwater use is examined, by making
510 use of reanalysis-based soil moisture and TWS changes simulated by WaterGAP (Water
511 - Global Analysis and Prognosis version 2.2a) Global Hydrological Model (WGHM) and
512 those derived from time-variable gravity fields observed by the twin-satellite GRACE.

513 In Chapter 4, the skills of two high-resolution RCMs are evaluated in terms of their
514 seasonal and interannual variations and long-term trends. Rainfall and temperature data
515 simulated by Regional Climate Model version 4.4 (RegCM4.4) and Providing REgional
516 Climate Information of Impact Studies (PRECIS) for the period 1982-2012 are com-
517 pared with observed datasets described in Chapter 2. RegCM4.4 is run at a 25×25
518 km grid resolution over a spatial domain of $[65^\circ\text{E}-110^\circ\text{E}, 5^\circ\text{N}-40^\circ\text{N}]$, forced by lateral
519 boundary conditions from reanalysis products, GCMs, and proxy sea surface tempera-
520 ture (SST) data. Six sets of PRECIS model simulations are obtained from the UK Met
521 Office. Chapter 5 presents the range of climate change projections for temperature and
522 precipitation for the remaining 20st century. Potential impacts of projected changes from
523 precipitation and temperature on water storage potentials are discussed by analysing
524 the future drought and wet frequencies for two periods, 2001–2050 and 2050–2099. In
525 Chapter 6, a detailed assessment of the UTLS temperature over the GBM River Basin
526 and their relevance to the basin climate is presented using monthly accumulated atmo-
527 spheric profiles retrieved from the GNSS COSMIC RO mission over the past 8 years.

528 Finally, Chapter 7 summarizes the contribution of this study and outlines some impor-
 529 tant issues for future research in the region.

Table 1.1: Lists of papers published/submitted under respective chapters. The published ver-
 sion of the papers are provided in the Appendix.

| Title | Journal | Chapter | References |
|---|-----------------------|-----------|--|
| 1. An evaluation of high-resolution gridded precipitation products over Bhutan (1998-2012) | Int. J. Climatol. | Chapter 2 | Khandu et al. (2015) |
| 2. Changes and variability of precipitation and temperature in the Ganges–Brahmaputra–Meghna River Basin based on global high-resolution reanalyses | Int. J. Climatol. | Chapter 2 | (Khandu et al., 2016c) |
| 3. Exploring the influence of precipitation extremes and human water use on total water storage (TWS) changes in the Ganges-Brahmaputra–Meghna River Basin | Water Resour. Res. | Chapter 3 | Khandu et al. (2016a) |
| 4. Assessing regional climate simulations of the last 30 years (1982-2012) over Ganges–Brahmaputra–Meghna River Basin | Clim. Dyn. | Chapter 4 | in Press |
| 5. Interannual variability of upper tropospheric and lower stratospheric (UTLS) temperature over Ganges–Brahmaputra–Meghna basin based on COSMIC GNSS RO data | Atmos. Meas. Tech. | Chapter 6 | Khandu et al. (2016b) |
| 6. Exploring hydro-meteorological drought patterns over the Greater Horn of Africa (1979-2014) using remote sensing and reanalysis products | Adv. Water. Resour. | * | Awange et al. (2016a) |
| 8. Quantifying the impacts of ENSO and IOD on rain gauge and remotely sensed precipitation products over Australia | Remote Sens. Environ. | * | Forootan et al. (2015) |
| 9. Uncertainties in remotely-sensed precipitation data over Africa | Int. J. Climatol. | * | Awange et al. (2015) |

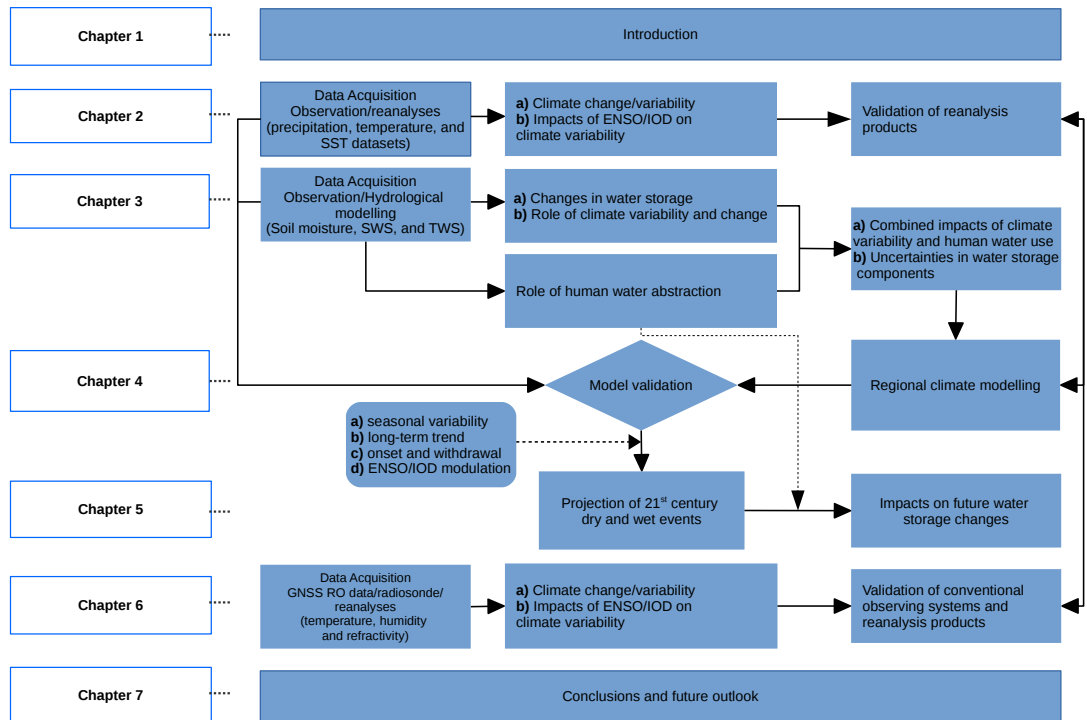


Figure 1.1: Outline of this thesis illustrating the studies conducted in each chapter.

530 2. Precipitation and temperature 531 variability

532 2.1 Introductory remarks

533 Estimating long-term trends in surface air-temperature (hereinafter called “tempera-
534 ture”) and precipitation are crucial for identifying climate change. Precipitation and
535 temperature are two critical components of the water and energy cycles, and precipita-
536 tion in particular, due to its high spatio-temporal variability, is one of the most difficult
537 fluxes to simulate in dynamical models (Flato et al., 2013). So, as critical as it is in
538 the water and energy cycles, precipitation is a critical metric in the quality of many
539 existing and emerging retrospective analyses (reanalyses). Evaluating climate models
540 require consistent long-term observational records. Hydrological or land surface models,
541 in particular, require high quality of climate forcing data (e.g., precipitation) to simu-
542 late other components of the water balance (e.g., soil moisture, (sub-) surface runoff)
543 terms. Satellite remote-sensing (SRS)-based estimates and reanalyses offer an alterna-
544 tive approach to *in-situ* observations where gauge-based networks are sparse and their
545 analyses are often delayed or not shared across a common hydrological basin (Duncan
546 and Biggs, 2012, Peña-Arancibia et al., 2013).

547 Reanalysis outputs are generated by forecast models with fluxes constrained by
548 available gauge- and SRS-based observations, and thus are sensitive to both the ob-
549 serving systems and model physics. The release of several global reanalyses over the
550 past two decades (e.g., Kalnay et al., 1996, Onogi et al., 2005, Uppala et al., 2005,
551 Onogi et al., 2007, Saha et al., 2010, Dee et al., 2011, Rienecker et al., 2011) pro-
552 vided several decades of various hydro-climatic data that are highly valuable for under-
553 standing the global/regional climate change process. The most widely used reanalysis
554 products include those developed at the National Centers for Environmental Predic-
555 tion (NCEP)/National Center for Atmospheric Research (NCAR) (see, Kalnay et al.,
556 1996, Kanamitsu et al., 2002), and at the European Center for Medium-Range Weather
557 Forecasts (ECMWF) (see, Uppala et al., 2005, Dee et al., 2011). Japan Meteorological
558 Agency (JMA) and the Central Research Institute of Electric Power Industry (CRIEPI)
559 have released two versions of reanalyses (JRA-25 and JRA-55) with the goal of provid-
560 ing consistent and high-quality reanalysis specifically over Asia (Onogi et al., 2005,
561 2007, Kobayashi et al., 2015). More recently, the National Aeronautic and Space Ad-
562 ministration (NASA) produced a global high-resolution reanalysis called the Modern-
563 Era Retrospective Analysis for Research and Applications (MERRA, Rienecker et al.,
564 2011) covering the satellite-era, while NCEP produced another high-resolution reanal-
565 ysis called the Climate Forecast System Reanalysis (CFSR, Saha et al., 2010).

566 While reanalysis products are considered to be near-perfect representations of the
567 atmospheric state, they suffer from many deficiencies at various time- and spatial-scales.
568 Considering that many global high-resolution reanalyses have become available during

569 the past few years (e.g., [Saha et al., 2010](#), [Dee et al., 2011](#), [Rienecker et al., 2011](#)), it
570 is vital to evaluate their skills in terms of how they represent key climate features over
571 different parts of the world. The spatio-temporal heterogeneity of orography and climate
572 (particularly, precipitation) of the Ganges–Brahmaputra–Meghna (GBM) River Basin
573 in South Asia presents one of the most challenging tests to any observing and modelling
574 systems. The Indian summer monsoon, which dominates the annual rainfall contribution
575 (by about 60–90%) is a result of complex interplay between the atmosphere, land, and
576 the Indian ocean processes that takes place at various spatial- and temporal-scales. The
577 pressure gradients that is formed between the south and north Indian ocean leads to a
578 cross-equatorial flow in the lower troposphere, which carries enormous moisture towards
579 the Indian sub-continent. These monsoon rainfall pattern is further modulated by steep
580 mountains of the Himalayas ([Barros et al., 2004](#)) along various stages of its flow in the
581 GBM River Basin, resulting in numerous high rainfall spots and dry regions.

582 Only few studies have assessed the quality of rainfall and temperature variability of
583 reanalysis products over the GBM River Basin, with all of them focusing over India and
584 during the monsoon season ([Misra et al., 2012](#), [Kishore et al., 2016](#)). [Kishore et al. \(2016\)](#)
585 indicated that ECMWF reanalysis (ERA-Interim, [Dee et al., 2011](#)) was more closer to
586 observed values than MERRA, CFSR, and JRA-25 during the monsoon season between
587 1989 and 2007. In another comparison study, [Misra et al. \(2012\)](#) indicated that there are
588 significant differences in the climatology of evaporation in the three reanalyses: CFSR,
589 MERRA, and NCEP II, which will have huge implications on precipitation and tem-
590 perature across South Asia. Particularly, the study found significantly less continental
591 evaporation in CFSR compared to MERRA and NCEP II, which may be attributed to
592 how each reanalyses treat the atmospheric-land interactions. These results suggest that
593 reanalysis products are still evolving and requires continuous validation over the Indian
594 monsoon region.

595 This chapter examines the long-term trends and interannual variability of rainfall
596 and temperature over the GBM River Basin using various existing gridded gauge-based
597 datasets and global high-resolution reanalyses over the period 1980–2013. The second
598 objective is to evaluate the quality of three global high-resolution reanalyses: (i) ERA-
599 Interim ($0.79^\circ \times 0.79^\circ$), (ii) MERRA ($0.50^\circ \times 0.67^\circ$), (iii) CFSR ($0.50^\circ \times 0.50^\circ$), in
600 estimating the long-term trends and the interannual variability of rainfall and temper-
601 ature, which are important metrics for identifying climate change. The study is com-
602 plemented by two SRS-based precipitation estimates: (i) Tropical Rainfall Measuring
603 Mission (TRMM) Multisatellite Precipitation Analysis (TMPA, 1998–2014) ([Huffman
604 et al., 2007](#)) and (ii) Climate Hazards Group InfraRed Precipitation (CHIRP, 1982–
605 2014) ([Funk et al., 2012](#)), both of which have a relatively long period of precipitation
606 records. Many studies have already examined the seasonal skills of various existing
607 SRS-based precipitation estimates across different parts of the GBM River Basin (e.g.,
608 [Andermann et al., 2011](#), [Duncan and Biggs, 2012](#), [Prakash et al., 2014](#), [Khandu et al.,
609 2015](#)), but have not addressed their long-term skills. Gauge-based datasets used here
610 include: Asian Precipitation Highly Resolved Observational Data Integration Towards
611 Evaluation of Water Resources (APHRODITE V1101, [Yatagai et al., 2012](#)), Climate
612 Research Unit (CRU TS3.22, [Harris et al., 2013](#)), and Global Precipitation Climatology

613 Centre (GPCC version 6, [Schneider et al., 2014](#)). The findings of this study has been re-
614 cently published in the *International Journal of Climatology* (see, [Khandu et al., 2016c](#))
615 and contains no major changes from the published version.

616 Section 2.2 describes the climatological characteristics of the GBM River Basin. In
617 Section 2.3, a brief review of the available rainfall and temperature datasets is presented
618 as well as the statistical methods used to analyze and compare the various datasets. The
619 section further discusses the accuracy of several near-global high-resolution SRS-based
620 precipitation products in the region and their contribution to the understanding of basin
621 rainfall hydrology. The results are presented and discussed in Section 2.5 and the chapter
622 is summarized in Section 2.6.

623 2.2 The Ganges-Brahmaputra-Meghna River Basin

624 The GBM River Basin in South Asia is a combination of three large river basins with
625 a drainage area of about 1.7 million km² ([FAO, 2011](#)). Although the three river basins
626 have distinct physiological and climatological characteristics, they are considered to be
627 a single river basin that is shared by India (64%), China (18%), Nepal (9%), Bangladesh
628 (7%) and Bhutan (3%) (Fig. 2.1). The three river systems join upstream of the GBM
629 delta in Bangladesh to form the third largest freshwater outlet (with an annual discharge
630 of $\sim 1,350 \text{ km}^3$) to the world's oceans, being exceeded only by the Amazon and the Congo
631 river systems ([Chowdhury and Ward, 2004](#), [Steckler et al., 2010](#)). The headwaters of
632 Ganges (Brahmaputra) rivers originate from the Himalayan mountains of Gangotri
633 glaciers (northern slope of the Himalayas in Tibet) while the Meghna river, originates
634 in the mountains of north-eastern India. The Ganges is joined by several smaller rivers
635 (or tributaries) from across India and Nepal forming one of the largest alluvial plains
636 in northern India. A portion of Ganges river ($\sim 50\%$) is diverted into the Hooghly river
637 at Farakka Barrage before reaching Bangladesh as a part of a treaty (called Farakka
638 Treaty) signed between India and Bangladesh in 1996 to share the precious Ganges river
639 (see, http://www.thewaterpage.com/farakka_water_treaty.htm).

640 The Brahmaputra river, also known as Yarlung Tsangpo (in Tibet), flows eastwards
641 before turning southwards into Arunachal Pradesh (India). It then turns westwards,
642 which is joined by many tributaries from northeast India and Bhutan, before entering
643 Bangladesh (also called Jamuna). The Meghna river originates from the hilly mountains
644 of Manipur (India), flowing southwest to join the Ganges and Brahmaputra rivers that
645 together flow into the Bay of Bengal and a small part of West Bengal (India) forming
646 the greatest deltaic plain in the world at the confluence.

647 The GBM River Basin features distinct climatic characteristics due to the Indian
648 monsoon variability and unique topographic regime that includes the Himalayan moun-
649 tains and great plains of Ganges, Terai, parts of northeast India, and Bangladesh. These
650 irregular topographic variations significantly impact on the spatial precipitation distri-
651 bution through alteration of monsoonal flow, resulting in pronounced orographic rainfall
652 along the Southern Foothills of Nepal, Bhutan and northeast India and considerably

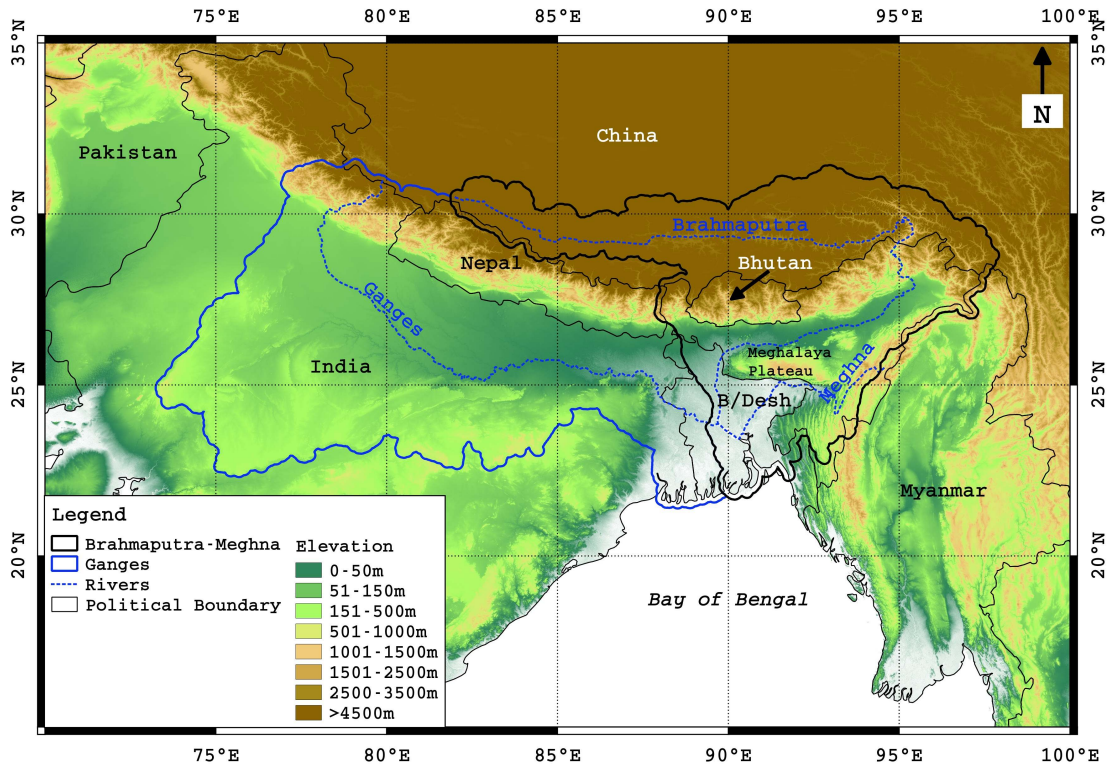


Figure 2.1: Overview of the Ganges–Brahmaputra–Meghna River Basin in South Asia. Brahmaputra and Meghna River Basins are merged together, which is represented by the thick black polygon, while the Ganges River Basin is shown in thick blue polygons. This representation will be used for the remainder of this thesis. Source: [Khandu et al. \(2016a\)](#).

653 lower rainfall on the lee sides of the mountains and the western Ganges River Basin.
 654 The Ganges River Basin is characterized by significant snowfall and precipitation in
 655 the northwest of its upper region and very high precipitation in the downstream regions
 656 (such as the delta regions of Bangladesh). The downstreams areas of Brahmaputra River
 657 Basin are directly located on the monsoon flow and hence, some of the areas receive
 658 significantly higher rainfall than the Ganges, while the world’s highest precipitation is
 659 received at Cherapunji (Meghalaya, India) located in the Meghna River Basin.

660 The winter precipitation over the western Himalayas is mainly driven by the mid-
 661 latitude sub-tropical jets known as the Western Disturbances, which is critical to the
 662 formation of snow/glaciers ([Dimri et al., 2015](#)). While the winter precipitation is mostly
 663 well below 50 mm, the Indian monsoon accounts for 60–90% of the annual rainfall total
 664 in the GBM River Basin recording over 1200 mm/month from June to September over
 665 Meghalaya (India) and southwest of Bhutan. The spatial temperature distribution is
 666 a function of altitude that decreases from as high as 40s (°C) during summer in the
 667 plains (e.g., Bangladesh) to as low as -30s (°C) in the Himalayas during winter. In this
 668 thesis, the Brahmaputra and Meghna River Basins are treated as one river basin because
 669 of their similar climatological characteristics, particularly during the Indian monsoon

670 season. Accordingly, the basin-averages are reported by spatially averaging over the two
 671 basins.

672 2.3 Data

673 2.3.1 Available observational data

674 Precipitation and temperature are the two key climate variables, which can be mea-
 675 sured directly to infer climate variability and change as well as to evaluate prediction
 676 skills of climate models. In particular, precipitation is highly variable both in time and
 677 space, and are poorly predicted by climate models. Accurate and reliable estimation of
 678 precipitation requires dense gauge or radar networks that are not easily achievable in
 679 rugged Himalayan mountainous regions (e.g., Bhutan and Nepal). Thus, gridded pre-
 680 cipitation products spatially interpolated from *in-situ* observational records may not
 681 present accurate rainfall estimates over regions with sparse rain gauge stations (e.g.,
 682 Duncan and Biggs, 2012, Khandu et al., 2015). Figure 2.2 shows the spatial distribution
 683 of rain gauges over GBM River Basin that were used to derive (a) APHRODITE V1101
 684 (hereinafter as APHRODITE), (b) CRU version TS3.22 (hereinafter as CRU_TS3.22),
 685 and (c) GPCC Full Analysis version 6 (hereinafter as GPCCv6) based on a 10 year
 686 period 1995–2005, where maximum number of gauges were reported. It is evident from
 687 Fig. 2.2 that gauge density is sparse across the GBM River Basin, especially in the high
 688 altitudes of southern Tibet, western Ganges, Bhutan, Bangladesh, and northeast India.
 689 Of the three datasets, CRU_TS3.22 has the least number of stations (Fig. 2.2b), much
 690 of which has been made available via the World Meteorological Organization’s (WMO)
 691 Global Telecommunications System (GTS). The German Weather Service (DWD) has
 692 released the updated version (version 7) of GPCC data towards the end of 2015 (see,
 693 ftp://ftp.dwd.de/pub/data/gpcc/html/fulldata_v7_doi_download.html) but was
 694 not available during the time of this write up.

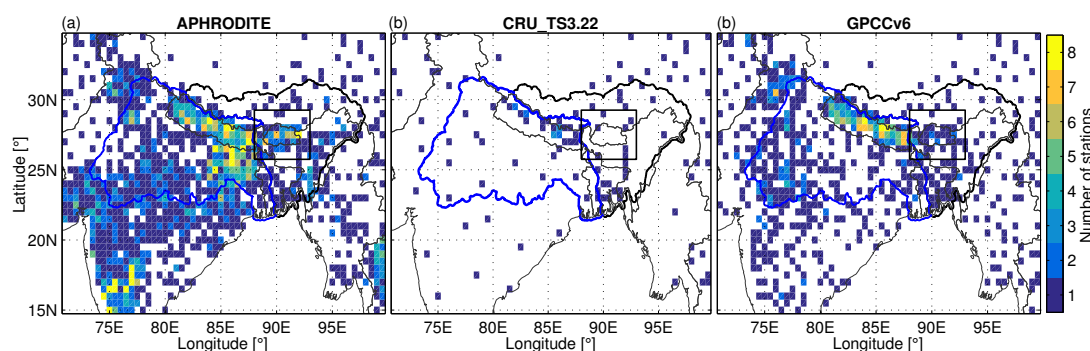


Figure 2.2: Spatial distribution of rain gauge stations across the GBM River Basin and its neighbouring regions that were used in (a) APHRODITE, (b) CRU_TS3.22, and (c) GPCCv6. Modified from Khandu et al. (2015).

695 APHRODITE precipitation data has been evaluated across various parts of the GBM
 696 River Basin including Bhutan, Nepal, and India by various studies (e.g., Rajeevan et al.,

697 2008, Andermann et al., 2011, Xue et al., 2013, Prakash et al., 2015, Khandu et al., 2015).
698 Andermann et al. (2011) reported that APHRODITE exhibits the least bias and high
699 r-square values at both daily and monthly scales when compared to other daily grid-
700 ded precipitation products over Nepal. Over India Rajeevan et al. (2008) and Prakash
701 et al. (2015) indicated that APHRODITE is well correlated (>0.6) with high-quality
702 Indian Meteorological Department (IMD) gridded daily precipitation data on a $1.0^\circ \times$
703 1.0° grid. Over Bhutan, Khandu et al. (2015) found that APHRODITE was compara-
704 ble to independently gridded precipitation estimates. All of these studies demonstrate
705 that APHRODITE is a reliable product at least for the validation period. Prakash
706 et al. (2015) evaluated several land-based precipitation data including APHRODITE,
707 CRU_TS3.22, and GPCCv6 over India using high-density IMD rainfall data and in-
708 dicated that APHRODITE and GPCCv6 were highly correlated with IMD data. The
709 study also reported that GPCCv6 estimates were found to be quantitatively closer to
710 IMD data during the monsoon, while APHRODITE precipitation estimates are found
711 to be lower than GPCCv6 and IMD datasets (see also, Yatagai et al., 2012).

712 Many global/near-global high-resolution SRS-based precipitation products have been
713 released over the past decade with daily or finer temporal resolutions. Table 2.1 shows
714 the details of various SRS-based precipitation products that have been applied across the
715 GBM River Basin. The quality of these products have been investigated in a number of
716 studies (e.g., Yin et al., 2008, Andermann et al., 2011, Duncan and Biggs, 2012, Shrestha
717 et al., 2012, Xue et al., 2013, Prakash et al., 2014, Khandu et al., 2015). These stud-
718 ies suggest that SRS-based estimates generally underestimate monsoon rainfall. Their
719 limited skills in detecting rainfall over rain-shadow regions and generally overestimating
720 daily rainfall amounts over high-altitude regions is also reported in e.g., Andermann
721 et al. (2011), Duncan and Biggs (2012), Prakash et al. (2014). Based on these findings,
722 APHRODITE (1979–2007), GPCC (1979–2010) and TMPAv7 (1998–2013) precipita-
723 tion estimates (both daily and monthly) are used to examine the long-term trends and
724 variability of precipitation and for evaluating various reanalysis products in the GBM
725 River Basin. To compromise on the varying spatial resolution among the different pre-
726 cipitation products, both APHRODITE and TMPAv7 products are linearly interpolated
727 (using inverse distance weighting function) to a $0.5^\circ \times 0.5^\circ$ grid.

728 Currently, there exists several gridded temperature datasets derived from surface
729 observations across the globe. A list of high-resolution gridded temperature datasets
730 derived from *in-situ* observations are shown in Table 2.2. The daily mean (T_{ave}) gridded
731 temperature data made available by APHRODITE is the only high-resolution ($0.25^\circ \times$
732 0.25°) gauge-based product over Asia and covers the period from 1961–2007. A monthly
733 time-series of gridded temperature data compiled from a recent version of the Global
734 Historical Climatology Network (GHCN2) and several other sources has been released
735 by the University of Delaware (UDEL, Legates and Willmott, 1990, Willmott and Robe-
736 son, 1995). The dataset (currently version 3.01, UDELv3.01) has been recently used by
737 Chowdary et al. (2014) to study the impacts of large-scale atmospheric-ocean interac-
738 tions on surface temperature over India. CRU regularly updates its global-land surface
739 temperature data (see, Harris et al., 2013) and is the most widely used temperature
740 dataset globally.

Table 2.1: Details of rain gauge products and near-global high-resolution SRS-based precipitation products that have been regularly applied over various parts of the GBM River Basin.

| Product | Period | Spatial Resl. | Temporal Resl. | Coverage | References |
|--|--------------|--------------------------------|----------------|-------------|---------------------------|
| Rain gauge products | | | | | |
| APHRODITE | 1951–2007 | $0.25^\circ \times 0.25^\circ$ | Daily | Asia | Yatagai et al. (2012) |
| IMD | 1971–2005 | $1.0^\circ \times 1.0^\circ$ | Daily | India | Rajeevan and Bhate (2009) |
| GPCCv6 | 1901–2010 | $0.50^\circ \times 0.50^\circ$ | Monthly | Global-land | Schneider et al. (2014) |
| CRU_TS3.23 | 1901–2014 | $0.50^\circ \times 0.50^\circ$ | Monthly | Global-land | Harris et al. (2013) |
| CPC | 1948–present | $0.25^\circ \times 0.25^\circ$ | Daily | Global-land | Xie et al. (2007) |
| Satellite-based precipitation estimates | | | | | |
| CHIRP | 1981–present | $0.05^\circ \times 0.05^\circ$ | Weekly | 50°S–50°N | Funk et al. (2014) |
| CMORPH | 2003–present | $0.25^\circ \times 0.25^\circ$ | 3-hourly | 50°S–50°N | Joyce et al. (2004) |
| CPC-RFE | 2001–present | $0.10^\circ \times 0.10^\circ$ | Daily | South Asia | Xie et al. (2002) |
| GSMaP_MVK | 2002–present | $0.10^\circ \times 0.10^\circ$ | 1-hourly | 60°S–60°N | Ushio et al. (2009) |
| NRL-Blend | 2002–present | $0.10^\circ \times 0.10^\circ$ | 3-hourly | 60°S–60°N | Turk and Miller (2005) |
| PERSIANN | 2000–present | $0.25^\circ \times 0.25^\circ$ | 6-hourly | 50°S–50°N | Sorooshian et al. (2000) |
| TRMM 3B42v6 | 1998–2010 | $0.25^\circ \times 0.25^\circ$ | 3-hourly | 50°S–50°N | Huffman et al. (2007) |
| TRMM 3B42v7 | 1998–2014 | $0.25^\circ \times 0.25^\circ$ | 3-hourly | 50°S–50°N | Huffman and Bolvin (2013) |

Table 2.2: List of gridded temperature datasets used in this study. All datasets consist of land surface air temperatures derived from ground-based stations across the region.

| Product | Period | Spatial Resl. | Temporal Resol. | Coverage | References |
|-----------|-----------|--------------------------------|-----------------|-------------|-----------------------------|
| APHRODITE | 1951–2007 | $0.25^\circ \times 0.25^\circ$ | Daily | Asia | Yasutomi et al. (2011) |
| CRU | 1901–2013 | $0.50^\circ \times 0.50^\circ$ | Monthly | Global-land | Harris et al. (2013) |
| UDel | 1900–2012 | $0.50^\circ \times 0.50^\circ$ | Monthly | Global-land | Willmott and Robeson (1995) |

741 2.3.2 Reanalysis products

742 Reanalyses have made significant contributions to many global/regional hydrological
743 and climatic studies. With the release of many new high-resolution reanalyses in the
744 past decade (e.g., Kalnay et al., 1996, Onogi et al., 2007, Saha et al., 2010, Dee et al.,
745 2011), their application into regional- and basin-scale studies have become increasingly
746 valuable. Yet certain elements of the analyzed fields (e.g, precipitation) remain highly
747 uncertain at global and regional scale both in terms of trends and interannual variabil-
748 ities. The reliability of reanalysis fields can considerably vary in space and time due
749 to lack of adequate observational data, instrumental changes, changing mix of observa-
750 tions, biases in observations, etc., which can introduce spurious variability and trends
751 into reanalysis fields. Since reanalysis products are increasingly used as regional climate
752 forcing data and hydrological model inputs, it is vital to estimate their skills in the
753 region. A reanalysis system consists of (i) a “data assimilation system” that combines
754 available observations from various data sources and (ii) a “forecast model” consisting of
755 a atmospheric model at its core, which is often coupled to a land surface model and/or
756 ocean model (e.g., Kalnay et al., 1996, Dee et al., 2011, Onogi et al., 2007).

757 Many reanalysis products have been assessed using gauge-based observations over
758 various parts of the GBM River Basin (e.g., Peña-Arancibia et al., 2013, Shah and
759 Mishra, 2014, Forsythe et al., 2014, Kishore et al., 2016). Shah and Mishra (2014) eval-
760 uated MERRA, ERA-Interim, and CFSR with observed data from IMD, APHRODITE

761 and TMPA and found median biases in seasonal monsoon precipitation (temperature)
 762 of 10% (-0.39°C), 34% (-0.21°C), and 11% (-0.44°C), respectively, over the Indian sub-
 763 continent. The products also failed to accurately reproduce the observed trends in the
 764 monsoon season precipitation and temperature over India. [Kishore et al. \(2016\)](#) re-
 765 ported that precipitation fields of ERA-Interim, MERRA, CFSR, and JRA-25 generally
 766 showed very good correlation with IMD data and captured the annual cycle reasonably
 767 well. However, these studies are carried out at continental scales and there is a urgent
 768 need to address their potential applications in hydro-climatic studies at regional level
 769 such as the GBM River Basin. Three global atmospheric reanalyses namely, (a) ERA-
 770 Interim/Land ([Balsamo et al., 2015](#)), hereinafter referred to as ERA-Interim only, (b)
 771 MERRA Land ([Rienecker et al., 2011](#)), hereinafter referred to as MERRA only, and (c)
 772 CFSR ([Saha et al., 2010](#)) were considered here mainly because of their improvement in
 773 simulating the land-surface state (see [Table 2.3](#) for details). These land-based reanalyses
 774 has been particularly designed to accurately simulate the land-surface state (moisture
 775 content/temperature) of soil, vegetation, and snow/ice to understand the impacts of
 776 climate change in recent years ([Rienecker et al., 2011](#), [Balsamo et al., 2015](#)).

Table 2.3: Details of the three reanalyses used in this study. All datasets consist of terrestrial surface air temperatures.

| Product | Period | Spatial Resl. | Temporal Resl. | Coverage | References |
|------------------|--------------|---------------|----------------|----------|---|
| ERA-Interim Land | 1979–2010 | 0.79° × 0.79° | 6-hourly | Global | Dee et al. (2011) |
| MERRA Land | 1980–2010 | 0.67° × 0.50° | 6-hourly | Global | Rienecker et al. (2011) |
| CFSR | 1979–present | 0.50° × 0.50° | 6-hourly | Global | Saha et al. (2010) |

777 2.3.3 Sea surface temperature data

778 In order to determine the mechanisms for seasonal and interannual variations of pre-
 779 cipitation and temperature, their time-series were correlated with the observed sea
 780 surface temperatures (SSTs) obtained from the Met Office Hadley Centre, UK (see,
 781 <http://www.metoffice.gov.uk/hadobs/hadisst/>). The Hadley Centre Global Sea Ice
 782 and Sea Surface Temperature (HadISST, [Rayner et al., 2003](#)) is a combination of
 783 monthly global fields of SST and sea ice concentration covering the period 1871–present.
 784 The 1.0° × 1.0° globally-complete monthly gridded HadISST data was developed based
 785 on a complex process involving a reduced space optimal interpolation technique applied
 786 to SST data from the Marine Data Bank (mainly obtained through ship tracks) and
 787 International Comprehensive Ocean-Atmospheric Data Set (ICOADS) through to 1981.
 788 From 1982 onwards, the dataset was complemented by a blend of *in-situ* and adjusted
 789 SRS-derived SSTs. Where the SSTs are covered with ice, a different analysis is per-
 790 formed by combining sea ice data from historical charts from shipping, expeditions and
 791 other activities, passive microwave SRS retrievals, and NCEP operational ice analyses.
 792 For this study, HadISST data from 1980–2013 covering 50°N–50°S is used.

793 In addition, two ocean-atmospheric indices covering the same period, namely: (a)
 794 Niño3.4 (or Ocean Niño Index, ONI) index ([Trenberth, 1990](#)) and (b) Dipole Mode

795 Index (DMI, Saji et al., 1999) are used to examine the impacts of natural climate vari-
 796 abilities such as El Niño Southern Oscillation (ENSO) and Indian Ocean Dipole (IOD),
 797 respectively. It should be noted that ENSO and IOD variability may also be influenced
 798 by long-term changes due to e.g., climate change but may not be necessarily detected
 799 on a shorter time-scale. ENSO is commonly measured by sea surface temperature (SST)
 800 anomalies in the equatorial Pacific ocean, typically over (5°N–5°S, 120°–170°W), which
 801 is also known as Niño3.4 region (see, Trenberth, 1990). ENSO events are said to occur
 802 if SST anomalies exceed $\pm 0.5^\circ\text{C}$ for three consecutive months or more. Warm and cold
 803 ENSO phases are referred to as El Niño and La Niña events, respectively, which are rep-
 804 resented by anomalous warming of the central and eastern tropical Pacific (warm phase),
 805 and vice versa. ENSO events are marked by significant variations in surface and upper-
 806 air conditions such as prolonged droughts and heavy rainfall events at the surface and
 807 anomalous warming or cooling of the upper-tropospheric lower-stratospheric (UTLS) re-
 808 gion. Niño3.4 index was obtained from the National Oceanic and Atmospheric Adminis-
 809 tration (NOAA, see, <http://www.esrl.noaa.gov/psd/data/climateindices/list/>).

810 On the other hand, IOD is commonly measured by the difference of SST anomalies
 811 between the western (50°E–70°E and 10°S–10°N) and eastern (90°E–110°E and 10°S–
 812 0°S) equatorial Indian ocean, which is also referred to as DMI. Positive IOD events are
 813 identified by a cooler than normal water in the tropical eastern Indian Ocean and warmer
 814 than normal water in the tropical western Indian Ocean. These positive IOD events are
 815 associated with a shift of active convection from eastern Indian Ocean to the west leading
 816 to potentially higher than normal rainfall over parts of the Indian subcontinent. DMI was
 817 obtained from the Japan Agency for Marine–Earth Science and Technology (see, <http://www.jamstec.go.jp/frsgc/research/d1/iod/>). Monthly ENSO and IOD indices are
 818 shown in Fig. 2.3.
 819

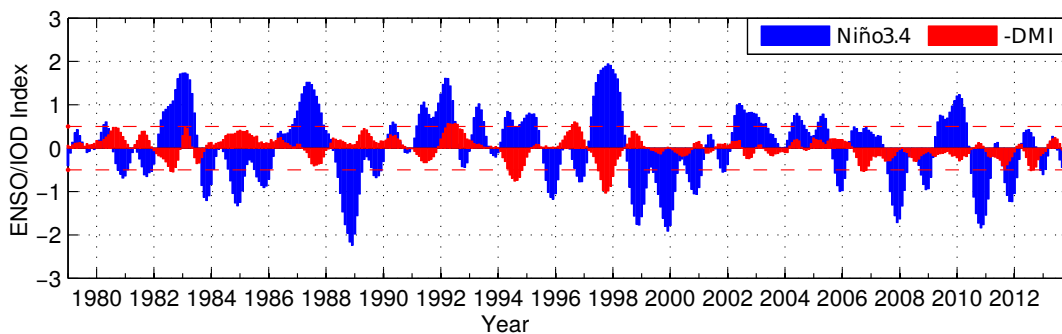


Figure 2.3: Monthly ENSO (Niño3.4 and IOD (-DMI) indices between 1980 and 2014.

820 2.4 Methods

821 2.4.1 Trend analysis and significance testing

822 Monthly rainfall and temperature anomalies are calculated relative to the data period
 823 from e.g., 1980–2010 and long-term trends are estimated and tested using both *paramet-*
 824 *ric* (e.g., Helsel and Hirsch, 2002, pp 221–264) and *non-parametric* (e.g. Mann, 1945,

825 Kendall, 1962, Sen, 1968, Hirsch and Slack, 1984) methods. Parametric tests are consid-
 826 ered to be more powerful but require data to be independent and normally distributed,
 827 which is rarely the case for climate datasets. Non-parametric methods on the other hand,
 828 do not require the assumption of normality and therefore, are considered to be more
 829 robust. In order to account for the differences between the two widely used methods,
 830 both parametric and non-parametric tests are applied to robustly determine the trends
 831 in precipitation and temperature. The two statistical methods are described next.

832 (a) Trend estimation

833 For illustration purposes, let us consider a data matrix $\mathbf{X}_{n \times m}$, containing the time-
 834 series of monthly rainfall (or temperature) data over the GBM River Basin, after re-
 835 moving their long-term temporal mean, where n describes the time (in months) and m
 836 represents the spatial locations (as stations or grids).

837 (i) **Multiple linear regression (MLR):** The MLR model can be formulated to
 838 determine trends and seasonality in a time-series as:

$$\begin{aligned} \mathbf{X} = x(j) = & \beta_1(j).t + \beta_2(j).\cos(2\pi t) + \beta_3(j).\sin(2\pi t) \\ & + \beta_4(j).\cos(4\pi t) + \beta_5(j).\sin(4\pi t) + \epsilon(t), \end{aligned} \quad (2.1)$$

839 where β_1 – β_5 are the coefficients of MLR for $j = 1, \dots, m$, and ϵ are the random error
 840 terms. The coefficients $\beta_{1..5}(j)$ are determined from the least squares adjustment
 841 technique. The adjusted coefficients $\hat{\beta}_{1..5}(j)$ can be interpreted as linear trends
 842 (β_1), mean annual variability (β_2, β_3), and semi-annual variability (β_4, β_5) in terms
 843 of the amplitude and phase. The dominant terms representing the linear trend,
 844 annual and semi-annual terms can be removed from the time-series to represent
 845 the interannual variability that describe the anomalies associated with large-scale
 846 ocean-atmospheric variations such as ENSO and IOD modes, among others. These
 847 temporal anomalies ($\hat{\mathbf{X}}$) can be mathematically formulated as:

$$\begin{aligned} \hat{\mathbf{X}} = \hat{x}(j) - & [\beta_1(j).t + \beta_2(j).\cos(2\pi t) + \beta_3(j).\sin(2\pi t) \\ & + \beta_4(j).\cos(4\pi t) + \beta_5(j).\sin(4\pi t)], \end{aligned} \quad (2.2)$$

848 (ii) **Sen’s slope estimation:** The least squares estimation of regression coefficient β_1
 849 may be vulnerable to gross errors and sensitive to skewed datasets such as precip-
 850 itation. Sen (1968)’s slope estimator is the most common approach for estimating
 851 trends for such datasets as the method is less insensitive to outliers. Sen (1968)’s
 852 slope estimation begins by calculating the slopes (T_i) of all data pairs by:

$$T_i = \frac{x_k - x_l}{k - l} \quad \text{for } i = 1, 2, \dots, n, \quad (2.3)$$

853 where x_k and x_l are data values at time k and l ($k > l$), respectively. The median
 854 values of these n values of T_i is the Sen’s slope (β), which is calculated as:

$$\beta = \begin{cases} T_{\frac{n+1}{2}} & n \text{ is odd} \\ \frac{1}{2} \left(T_{\frac{n}{2}} + T_{\frac{n+2}{2}} \right) & n \text{ is even} \end{cases} \quad (2.4)$$

855 where β can be both positive (increasing trend) or negative (decreasing trend).

856 **(b) Significance testing**

857 In order to determine whether the trend values calculated above are statistically
 858 significant or not, a hypothesis testing is carried out. Typically, in hypothesis testing,
 859 the null hypothesis is denoted by $H_0: \beta_1 = 0$ (indicating no trend) and the alternative
 860 hypothesis by $H_1: \beta_1 \neq 0$ (reject H_0). Two commonly used approaches are described
 861 below:

862 (i) **Mann-Kendall Test:** The Mann-Kendall test (Mann, 1945, Kendall, 1962) fol-
 863 lows a non-parametric approach, which searches for a monotonic change in time
 864 without necessarily assuming their statistical distribution. The test statistics (S)
 865 is defined as:

$$S = \sum_{i=1}^{n-1} \sum_{j=i+1}^n \text{sgn}(x_j - x_i), \quad (2.5)$$

866 where n is the number of data points. Assuming $(x_j - x_i) = \theta$, the value of $\text{sgn}(\theta)$
 867 is calculated as:

$$\text{sgn}(\theta) = \begin{cases} 1 & \text{if } \theta > 0 \\ 0 & \text{if } \theta = 0 \\ -1 & \text{if } \theta < 0 \end{cases} \quad (2.6)$$

868 S represents the sum of positive and negative changes for all the data pairs and
 869 for samples ($n > 10$), the test is conducted using a normal distribution with mean,
 870 variance, and test value of:

$$E[S] = 0$$

$$\text{Var}[S] = \frac{n(n-1)(2n+5) - \sum_{k=1}^n t_k(t_k-1)(2t_k+5)}{18}, \quad (2.7)$$

871

$$Z = \begin{cases} \frac{S-1}{\sqrt{\text{Var}(S)}} & \text{if } S > 0 \\ 0 & \text{if } S = 0 \\ \frac{S+1}{\sqrt{\text{Var}(S)}} & \text{if } S < 0 \end{cases} \quad (2.8)$$

872 If $|Z| > z_{\alpha/2}$ (where $\alpha/2$ indicates the quantile of the normal distribution), the
 873 null hypothesis (no trend, denoted by H_0) is rejected at α significance level (at 5%)
 874 in a two sided test. For seasonal and annual time-series, it is also important to
 875 take into account the autocorrelation structure (or serial correlation) in the data.
 876 Autocorrelation increases the probability of detecting significant trends. Hamed
 877 and Rao (1998) suggested a modified Mann-Kendall approach by considering the
 878 autocorrelation between the ranks of the data. This is done by modifying the
 879 variance, Here, the modified Mann-Kendall test was used and the null hypothesis
 880 was tested at 95% confidence level.

881 (ii) **Student t -test:** Students t -test is one of the widely used method for determining
 882 whether the trend is statistically significant. For example, consider a time-series
 883 of rainfall anomalies ($x(t)$) with an estimated linear trend of $\hat{\beta}_1$, it's residuals
 884 ($\epsilon(t)$) can be derived as difference of observed rainfall anomalies ($x(t)$) and those
 885 estimated from e.g., MLR model ($\hat{x}(t)$) over $t = 1, 2, \dots, n$ months:

$$\epsilon(t) = x(t) - \hat{x}(t), \quad (2.9)$$

886 and the standard error (S_β) of $\hat{\beta}_1$ is defined as

$$S_\beta = \frac{S_\epsilon}{\sqrt{\sum_{t=1}^n (t - \bar{t})^2}}, \quad (2.10)$$

887 where S_ϵ^2 , variance of the residuals (ϵ) is given by

$$S_\epsilon^2 = \frac{1}{n-2} \sum_{t=1}^n \epsilon(t)^2, \quad (2.11)$$

888 In order to examine whether the trend in $x(t)$ is significantly different from 0, a
 889 test value is computed as a ratio between the estimated trend ($\hat{\beta}_1$) and its standard
 890 error (S_β):

$$t_\beta = \frac{\hat{\beta}_1}{S_\beta} \quad (2.12)$$

891 assuming that t_β follows a t -distribution. The null hypothesis (of no trend) is
 892 rejected if $|t| < t_{\text{crit}}$, where t_{crit} is the point on the student's t -distribution with
 893 $n-2$ degrees of freedom. It should be noted here that while the t -test is simple and
 894 powerful to normally distributed data (such as temperature), it is less powerful
 895 against non-normal datasets (such as precipitation).

896 2.4.2 Principal Component Analysis (PCA)

897 Both weather and climate are a result of complex non-linear interaction between various
 898 components of the Earth system and contain significant temporal and spatial correla-
 899 tions, which makes the physical interpretation difficult based on simple data analysis
 900 alone. To circumvent this challenge, many statistical approaches have been explored to
 901 reduce three-dimensional (3D) geophysical data such as precipitation, surface air tem-
 902 perature, and SST data into few components (see, Preisendorfer, 1988). This process
 903 helps to interpret data and possibly help explain the possible physical mechanisms that
 904 cannot be inferred from simple statistical methods. Among the many advanced statisti-
 905 cal methods used in ocean/atmospheric science, principal component analysis (PCA,
 906 Preisendorfer, 1988) is considered on of the simplest and a widely used data exploratory
 907 approach. PCA is based on a second order statistics that allows for a space-time display
 908 of spatio-temporal data such as precipitation and temperature in a very few modes. In
 909 general, PCA has gained multiple applications and have been used in various geophys-
 910 ical and climatic applications for dimension reduction (or removing white noise), pattern

911 extraction, and comparison of different datasets (see, [Hannachi et al., 2007](#), [Forootan,](#)
912 [2014](#), for a detailed review of its mathematical derivation and applications).

913 The central idea of the PCA is to find a set of orthogonal spatial patterns (Empirical
914 Orthogonal Functions or EOFs) along with a set of associated uncorrelated time-series
915 or principal components (PCs) that captures most of the observed variance (expressed
916 in %) from the available spatio-temporal data such as precipitation and temperature. In
917 summary, the EOF decomposition can be written as $\mathbf{X}_{(n,m)} \cong \mathbf{P}_{(n,k)} \mathbf{E}_{(m,k)}^T$ where $\mathbf{X}_{(n,m)}$
918 is the space (m)-time (n) data (e.g., precipitation) with its temporal mean removed,
919 $\mathbf{E}_{(m,k)}$ contains the EOFs with k number of retained modes, and $\mathbf{P}_{(n,k)}$ are the PCs
920 derived by projecting the original data ($\mathbf{X}_{(n,m)}$) on the orthogonal base-functions or
921 EOFs $\mathbf{E}_{(m,k)}$, i.e., $\mathbf{P}_{(n,k)} = \mathbf{X}_{(n,m)} \mathbf{E}_{(m,k)}$. This method can be applied at various stages
922 of the data in order to improve signal-to-noise ratio as well as to help interpret spatio-
923 temporal variations in geophysical data. PCA is applied in this study to isolate the
924 likely effects of ENSO and IOD on the precipitation and temperature changes in the
925 GBM River Basin.

926 2.5 Results and discussion

927 2.5.1 Annual amplitudes and trends of rainfall and temperature

928 The mean annual amplitudes of monthly rainfall from gauge-based GPCCv6, SRS-based
929 TMPAv7 and CHIRP, and three reanalysis products (i.e., ERA-Interim, MERRA, and
930 CFSR) are shown in Fig. 2.4. Precipitation over the GBM River Basin shows signifi-
931 cant spatial variability for all the months as a result of the Indian monsoon and the
932 orographically induced precipitation along the Himalayan mountains. The highest pre-
933 cipitation amplitudes are observed over the Brahmaputra–Meghna River Basin, while
934 the Ganges River Basin show relatively low rainfall amplitudes except over few regions
935 such as central Nepal (Fig. 2.4a–c). These annual amplitude maps closely relate to the
936 average monsoon rainfall from June–September (JJAS) as indicated in Fig. 2.5. Note
937 that the spatial patterns of JJAS rainfall is more localised, especially in the GPCCv7
938 data (Fig. 2.5a) indicating that SRS-based precipitation estimates exhibit a larger foot-
939 print (Fig. 2.5b–c) rendering a larger area of maximum rainfall in its high resolution
940 versions. There are three regions: (a) Meghalaya, (b) southwest Bhutan, and (c) north-
941 ern Arunachal Pradesh that receive the highest monthly rainfall amount (~ 1200 mm
942 during the JJAS) and hence shows the largest amplitudes in all the observed datasets
943 (Fig. 2.4a–c). Both TMPAv7 and CHIRP (1998–2013) show similar magnitudes of an-
944 nual maps as GPCCv6 (Fig. 2.4b–c) but substantially underestimate monsoon rainfall
945 in the high rainfall regions (Fig. 2.5b–c), albeit for different periods.

946 However, reanalysis products (specifically ERA-Interim and MERRA) significantly
947 underestimate the annual amplitudes (Fig. 2.4d–e) and the JJAS rainfall amount (Fig.
948 2.5d–e) with respect to APHRODITE and GPCCv6. MERRA, in particular failed to
949 generate rainfall structures over Nepal and along the coastal areas of the Bay of Ben-
950 gal (Fig. 2.4e and 2.5e), while both ERA-Interim and MERRA can barely capture the

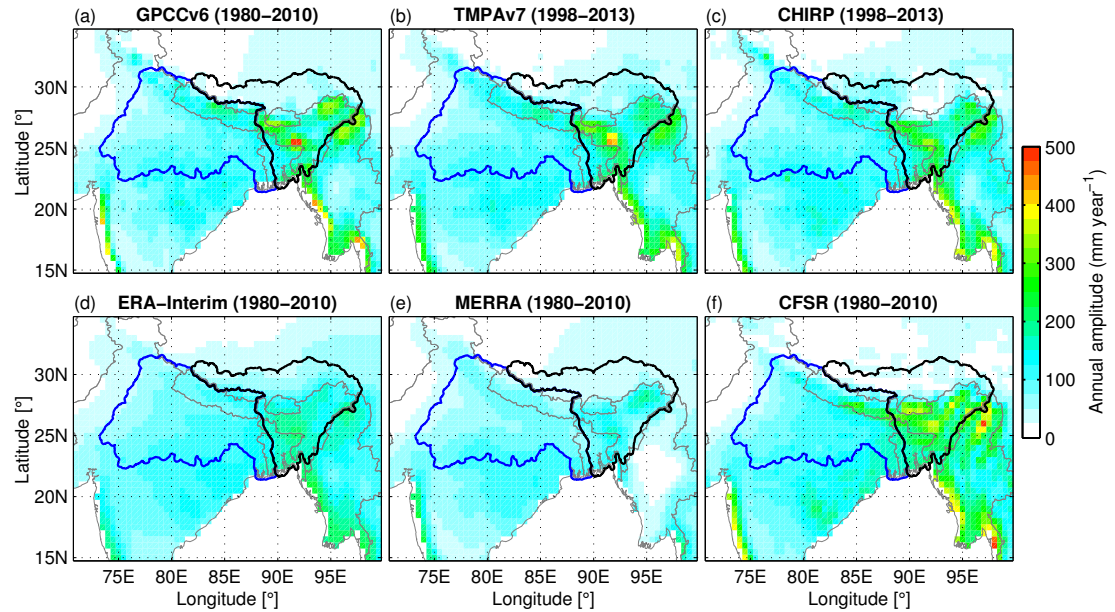


Figure 2.4: Spatial variations of mean annual amplitudes of monthly rainfall over the GBM River Basin based on (a) GPCCv6 (1980–2010), (b) TMPAv7 (1998–2013), (c) CHIRP (1998–2013), (d) ERA-Interim (1980–2010), (e) MERRA (1980–2010), (f) CFSR (1980–2010).

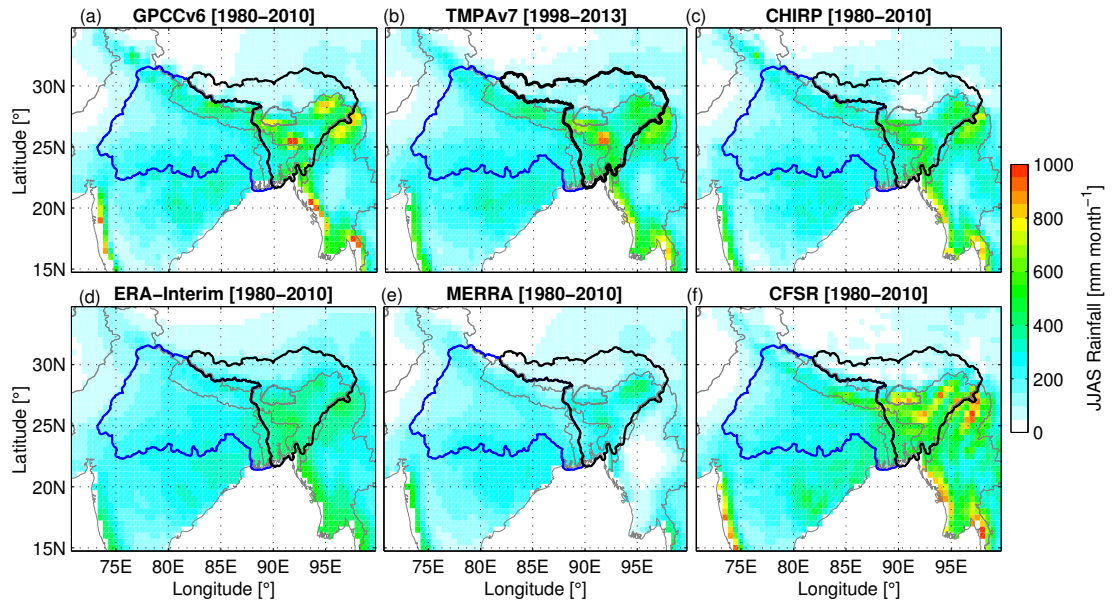


Figure 2.5: Spatial distribution of monsoon (JJAS) rainfall over the GBM River Basin (a) GPCCv6 (1980–2010), (b) TMPAv7 (1998–2013), (c) CHIRP (1998–2013), (d) ERA-Interim (1980–2010), (e) MERRA (1980–2010), (f) CFSR (1980–2010).

951 monsoon rainfall pattern (Fig. 2.5d–e). CFSR, on the other hand, highly overestimates
 952 the annual amplitude and also misplaces the high rainfall region of southwest of Bhutan
 953 towards the east (Fig. 2.4f and 2.5f). While a strong agreement between TMPAv7 and

954 GPCCv6 is expected, the differences between GPCCv6 and reanalysis products (es-
 955 pecially, ERA-Interim and MERRA) is striking, given that both products are adjusted
 956 with observed rainfall datasets. For example, MERRA underestimates annual amplitude
 957 by 21–37% over the GBM River Basin (Table 2.4). CHIRP and APHRODITE estimates
 958 are also considerably lower than the other observed products over the basin (Table 2.4),
 959 an observation that has also been noted, e.g., by Prakash et al. (2015).

Table 2.4: Annual amplitudes of various precipitation and temperature products over the Ganges and Brahmaputra-Meghna-River Basins over the period 1980–2013.

| Data | Precipitation [mm year ⁻¹] | | Temperature [°C] | |
|-------------------------|--|--------------------|------------------|--------------------|
| | Ganges | Brahmaputra-Meghna | Ganges | Brahmaputra-Meghna |
| APHRODITE [1980–2007] | 260.3 | 263.9 | - | - |
| GPCCv6 [1980–2010] | 310.0 | 346.3 | - | - |
| CRU_TS3.22 [1980–2007] | 284.1 (280.4) | 334.5 (330.0) | 6.9 | 7.0 |
| TMPAv7 [1998–2013] | 320.7 | 330 | - | - |
| CHIRP [1998–2013] | 342.4 | 308.8 | - | - |
| ERA-Interim [1980–2010] | 308.8 | 329.2 | 5.6 | 5.3 |
| MERRA [1980–2010] | 244.2 | 219.4 | 9.0 | 8.7 |
| CFSR [1980–2010] | 345.4 | 379.5 | 8.2 | 8.4 |

960 Figure 2.6 shows the spatial variability of annual amplitude of surface tempera-
 961 ture over the GBM River Basin (over the period 1980–2010) based on observed data
 962 (CRU_TS3.22 and UDEL) and three reanalysis products (ERA-Interim, MERRA,
 963 and CFSR). The annual amplitudes of temperature increases with altitude with both
 964 CRU_TS3.22 and UDEL gauge datasets (Fig. 2.6a–b) showing considerably high
 965 (>8°C) variations in the Tibetan region (located entirely in the Brahmaputra River
 966 Basin) and parts of the western Ganges River Basin (Indian region). The tempera-
 967 ture varies by 5–8°C over western Nepal, northern Bhutan, and Arunachal Pradesh (in
 968 India), while the lowest annual variations (~5°C) are observed over Bangladesh and
 969 eastern India. The annual amplitude of temperatures shown by the reanalysis products
 970 exhibit very similar spatial structures but their magnitudes vary considerably across
 971 the basin. While ERA-Interim tend to underestimate annual amplitudes (Fig. 2.6c),
 972 MERRA and CFSR products (Fig. 2.6d–e) overestimate annual amplitudes (by around
 973 3–4°C) with respect to CRU_TS3.22 dataset, especially in the Ganges River Basin and
 974 in the Tibetan region. The basin-averaged annual amplitudes (of temperature) are given
 975 in Table 2.4, which shows that MERRA depicts the largest annual variation followed
 976 by CFSR in the GBM River Basin. The maximum surface temperature over Ganges
 977 and Brahmaputra–Meghna River Basins occur during May and July, respectively, while
 978 their minimum temperatures occur in January.

979 Changes in temperature and precipitation are estimated both in observations and re-
 980 analysis products for the period 1980–2010 using both parametric and non-parametric
 981 methods described in Section 2.4. Precipitation trends are also calculated for vari-
 982 ous time periods between 1980 and 2013 to shows the precipitation changes based on
 983 APHRODITE (1980–2007) and SRS-based (TMPAv7 and CHIRP) precipitation prod-
 984 ucts. Precipitation trends estimated between 1980 and 2007 indicates a negative trend
 985 (up to 10–15 mm decade⁻¹) mainly over the Ganges River Basin, and are consistently
 986 shown by all the observed products (i.e., APHRODITE, CRU_TS3.22, GPCCv6). Fig-

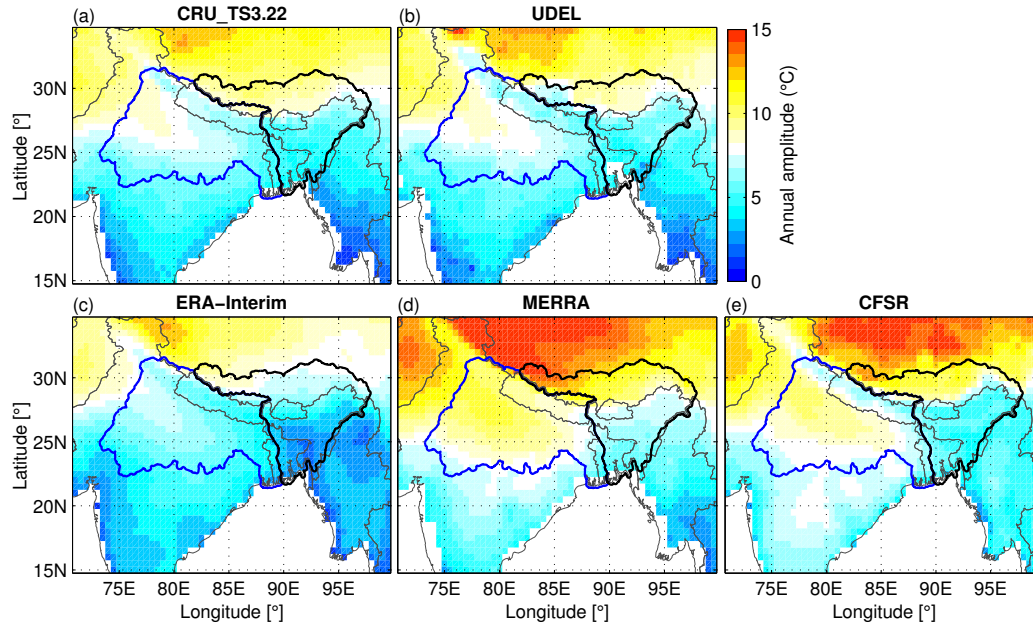


Figure 2.6: Spatial patterns of annual amplitudes of temperature over the GBM River Basin based on (a) CRU_TS3.22, (b) UDEL, (c) ERA-Interim, (d) MERRA, and (e) CFSR for the period 1980–2010.

987 ure 2.7 shows the precipitation changes over the GBM River Basin based on GPCCv6
 988 (1980–2010), TMPAv7 and CHIRP (1998–2013), and the three reanalyses (1980–2010).
 989 The long-term (1980–2010) trend based on GPCCv6 data shows mostly negative trends
 990 across both the river basins with a declining rate of 10–20 mm decade⁻¹ (Fig. 2.7a).
 991 However, TRMMv7 indicated a relatively large decline in precipitation over the last
 992 decade, especially along the main monsoonal flow (covering Bangladesh, Bhutan, north-
 993 east India, and Nepal), with a decline of 20–35 mm decade⁻¹ (Fig. 2.7b) between 1998
 994 and 2013. Both TMPAv7 and CHIRP (Fig. 2.7b–c) indicate strong decline in precipi-
 995 tation over the last decade in the Brahmaputra–Meghna River Basin (39 mm/dec in
 996 TMPAv7 during June–August). During the same period, however, the western Ganges
 997 River Basin recorded an increase in precipitation, with an estimated rate of 12 mm
 998 decade⁻¹ in TMPAv7 (see, Fig. 2.7b and Table 2.5), although it is not replicated by
 999 the CHIRP product due to a larger area of precipitation decrease in the eastern Ganges
 1000 River Basin (Fig. 2.7c).

1001 Among the reanalyses, ERA-Interim tends to capture the observed trends but its
 1002 trend values are significantly larger than the observed GPCCv6 data over western Nepal
 1003 and eastern India (Fig. 2.7d), while MERRA and CFSR show completely opposite signs
 1004 of change over the Brahmaputra–Meghna River Basin (Fig. 2.7e–f). The basin-averaged
 1005 seasonal precipitation trends given in Table 2.5 show precipitation decline for all the
 1006 seasons in both the river basins, especially in winter in most of the datasets including
 1007 reanalysis products. Consistent with the spatial trend patterns shown in Fig. 2.7, the
 1008 basin-averaged trends values of MERRA and CFSR indicate anomalously large increas-
 1009 ing trends in summer in the Brahmaputra–Meghna River Basin between 1980 and 2010

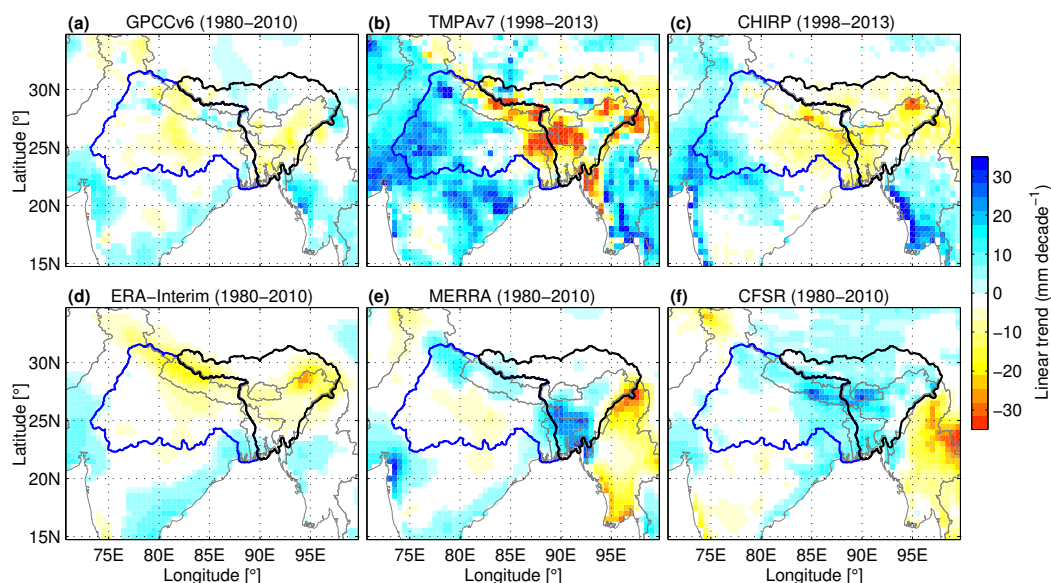


Figure 2.7: Precipitation changes over the GBM River Basin based on (a) GPCCv6 (1980–2010), (b) TMPAv7 (1998–2013), (c) CHIRP (1998–2013), (d) ERA-Interim (1980–2010), (e) MERRA (1980–2010), (f) CFSR (1980–2010). Trend values that are not significant at 95% confidence level are masked out.

1010 (Table 2.5). Precipitation changes in reanalyses depend on model parameterizations
 1011 (e.g., convection scheme, moisture transport), quality of assimilated observations, as-
 1012 simulation of new observations. Instrumental changes and changing mix of observations
 1013 will affect the quality of precipitation fields in time as well as introduce spurious jumps
 1014 that might impact on the long-term trends. As such, most physical models have limited
 1015 skills in simulating the weakening Indian monsoon circulation (Ramanathan et al., 2005,
 1016 Chung and Ramanathan, 2006) and the effects of ENSO and IOD on the precipitation
 1017 trends, and thus, the reliability of reanalyses to some extent, are seasonally dependent
 1018 as shown in Table 2.5.

Table 2.5: Precipitation trends (mm decade^{-1}) estimated from observed and reanalysis products for various periods between 1980 and 2013. Values that are significant at 95% confidence level are highlighted in bold.

| Rainfall Products | Ganges [mm decade^{-1}] | | | | Brahmaputra-Meghna [mm decade^{-1}] | | | |
|-------------------------|------------------------------------|--------|--------|-------------|--|-------------|--------------|-------------|
| | Winter | Spring | Summer | Autumn | Winter | Spring | Summer | Autumn |
| GPCCv6 [1980–2010] | -0.7 | -12 | 0.2 | -2.9 | -0.8 | 0.2 | -4.5 | -1.9 |
| TRMMv7 [1998–2013] | 2.1 | -6.1 | 12.4 | -6.6 | -0.1 | -4.6 | -39.0 | -3.3 |
| CHIRP [1998–2013] | 1.1 | -2.0 | -7.0 | -10.3 | 0.0 | -3.9 | -20.2 | -9.2 |
| ERA-Interim [1980–2010] | -1.5 | -9.5 | -5.8 | -3.6 | -6.8 | -12.6 | -6.9 | -2.8 |
| MERRA [1980–2010] | 1.1 | 9.0 | 3.0 | -2.0 | 5.9 | 17.4 | 3.0 | -1.1 |
| CFSR [1980–2010] | -0.8 | 18.1 | 1.9 | -2.1 | 0.9 | 19.8 | 5.0 | -3.2 |

1019 Observed changes in temperature based on CRU_TS3.22 and UDEL (Fig. 2.8a–b)
 1020 show significant warming over majority of the GBM River Basin with intense warming
 1021 trends (up to $0.6^\circ\text{C decade}^{-1}$) over northern Brahmaputra River Basin (southern Ti-
 1022 bet). The warming patterns are very similar between CRU_TS3.22 and UDEL but the

1023 latter did not show any significant warming over Bangladesh. The warming trends in the
 1024 northern parts of GBM River Basin are well reproduced by the reanalysis products, even
 1025 though their magnitudes differ considerably between the three products and across the
 1026 region (Fig. 2.8c–e). In reanalysis systems, surface temperature outputs are still closely
 1027 related to the model parameterizations and hence, model uncertainties may play a sig-
 1028 nificant role in representing the spatial variability in very heterogeneous topographic
 1029 regions such as the GBM River Basins. However, the temperature trends shown by the
 1030 reanalysis products generally agree more than precipitation, because unlike precipita-
 1031 tion, temperature variations are more consistent and most reanalysis systems directly
 1032 assimilate near-surface temperature data from both radiosonde and satellite sources.
 1033 However, ERA-Interim barely shows any significant warming trends in the Ganges River
 1034 Basin (Fig. 2.8c) despite their use of near-surface atmospheric temperature datasets
 1035 (Dee et al., 2011), which might be related to how it constrains the land surface effects
 1036 on evaporation.

1037 There are few grids in MERRA and CFSR (Fig. 2.8d–e) that show negative spurious
 1038 trends in the northern Brahmaputra and western Ganges River Basin, respectively,
 1039 which cannot be understood at this time. CFSR also uses precipitation observations
 1040 over land to better constrain their soil moisture (Saha et al., 2010). The excessive
 1041 warming seen in CFSR over the Himalayan region (Fig. 2.8e) correlates with the large
 1042 precipitation increases indicating that warming in this region may be caused by other
 1043 changes such as decrease in snow/ice cover. The basin-averaged trends are estimated
 1044 for all the four seasons and are given in Table 2.6. Consistent with the spatial patterns
 1045 observed in Fig. 2.8, the basin-averaged seasonal trends based on CRU_TS3.22 and
 1046 UDEL also indicates significant warming in both the river basins during the spring,
 1047 autumn, and winter. CRU_TS3.22 also showed significant warming trends (0.21°C/dec)
 1048 in the Brahmaputra-Meghna River Basin during summer. ERA-Interim was not able to
 1049 reproduce these seasonal temperature trends, but MERRA and CFSR agreed well with
 1050 observed data in the Brahmaputra-Meghna River Basin (Table 2.6). Note that all the
 1051 reanalysis products indicate negative (although not significant) temperature trends in
 1052 summer over the Ganges River Basin.

Table 2.6: Linear trends in temperature ($^{\circ}\text{C decade}^{-1}$) derived from observations and reanalysis products for the period 1980–2010. The values that are significant at 95% confidence level are shown in bold.

| | CRU_TS3.22 | UDEL | ERA-Interim | MERRA | CFSR |
|---------------------------|-------------|-------------|-------------|-------------|-------------|
| Ganges | | | | | |
| Spring | 0.38 | 0.36 | 0.08 | 0.16 | 0.52 |
| Summer | 0.1 | 0.03 | -0.22 | -0.4 | -0.17 |
| Autumn | 0.41 | 0.27 | 0.08 | 0.21 | 0.31 |
| Winter | 0.41 | 0.26 | 0.32 | 0.31 | 0.42 |
| Brahmaputra-Meghna | | | | | |
| Spring | 0.42 | 0.39 | 0.15 | 0.26 | 0.43 |
| Summer | 0.21 | 0.09 | -0.06 | 0.1 | 0.02 |
| Autumn | 0.46 | 0.28 | 0.06 | 0.28 | 0.33 |
| Winter | 0.64 | 0.48 | 0.35 | 0.43 | 0.8 |

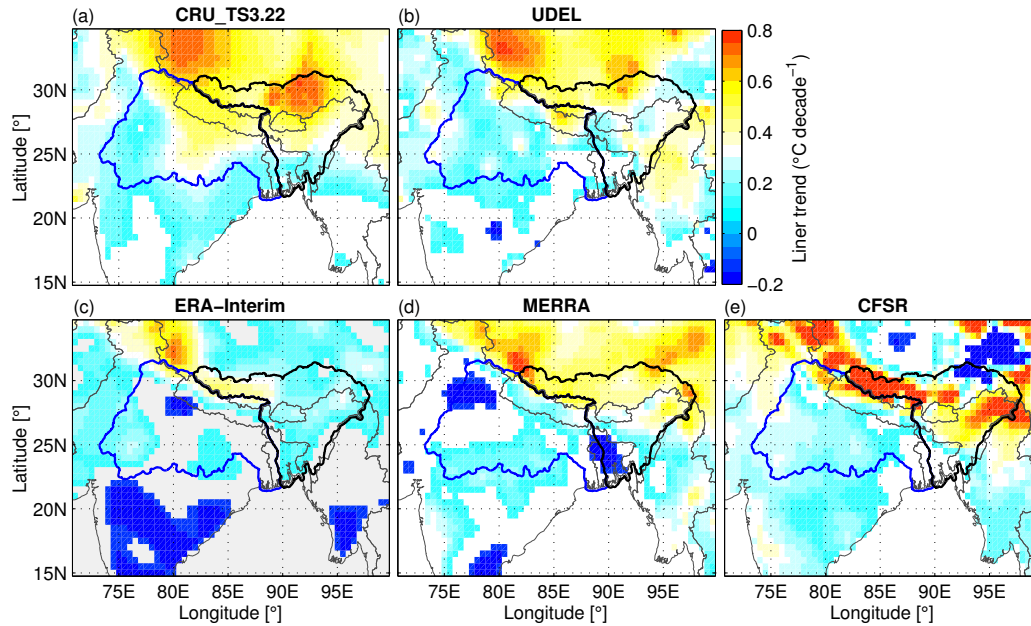


Figure 2.8: Spatial variation of temperature trends based on (a) CRU_TS3.22, (b) UDEL, (c) ERA-Interim, (d) MERRA, and (e) CFSR for the period 1980–2013 in the GBM River Basin. Trend values that are not significant at 95% confidence level are not shown.

1053 2.5.2 Interannual variability of precipitation and temperature

1054 PCA is applied to the deseasonalized (annual cycle removed) and detrended (linear trend
 1055 removed) time-series anomalies of temperature and precipitation focusing on the period
 1056 1980–2010 to understand the most recent climate variations of the GBM River Basin.
 1057 First, PCA is applied to monthly temperature anomalies (annual signals removed) of
 1058 CRU_TS3.22 to derive the leading modes of variability and its associated EOFs (i.e.,
 1059 spatial patterns) as well as the PCs (i.e., temporal patterns). Temperature anomalies of
 1060 other products are projected onto the EOFs (of CRU_TS3.22) to generate the respective
 1061 temporal patterns. Although previous studies have used various statistical methods to
 1062 determine the number of modes to be retained (see details in, Forootan, 2014), only the
 1063 first two leading modes are retained here based on the well-distinguished variance con-
 1064 tribution. Figure 2.9 shows the PCA modes of CRU_TS3.22 temperature data together
 1065 with the projected temporal components of UDEL and the three reanalysis temperature
 1066 fields. The first leading mode explains about 43% of the variance, which shows strong
 1067 positive anomalies over the western GBM River Basin and northern Brahmaputra basin
 1068 (Fig. 2.9a). The second EOF exhibits two homogeneous regions with positive (negative)
 1069 anomalies over Ganges (Brahmaputra–Meghna) River Basin, accounting for 13% of the
 1070 variability (Fig. 2.9b).

1071 The corresponding PCs (Fig. 2.9c–d) show substantial interannual variability be-
 1072 tween 1980 and 2010. PC 1 shows the extreme warm (e.g., 1988, 1999) and cold (e.g.,
 1073 1997–1998, 2008–2009) episodes (Fig. 2.9c) with dominant affects in the western Ganges
 1074 River Basin (Fig. 2.9a). The patterns are quite similar in the second PC (Fig. 2.9d) but

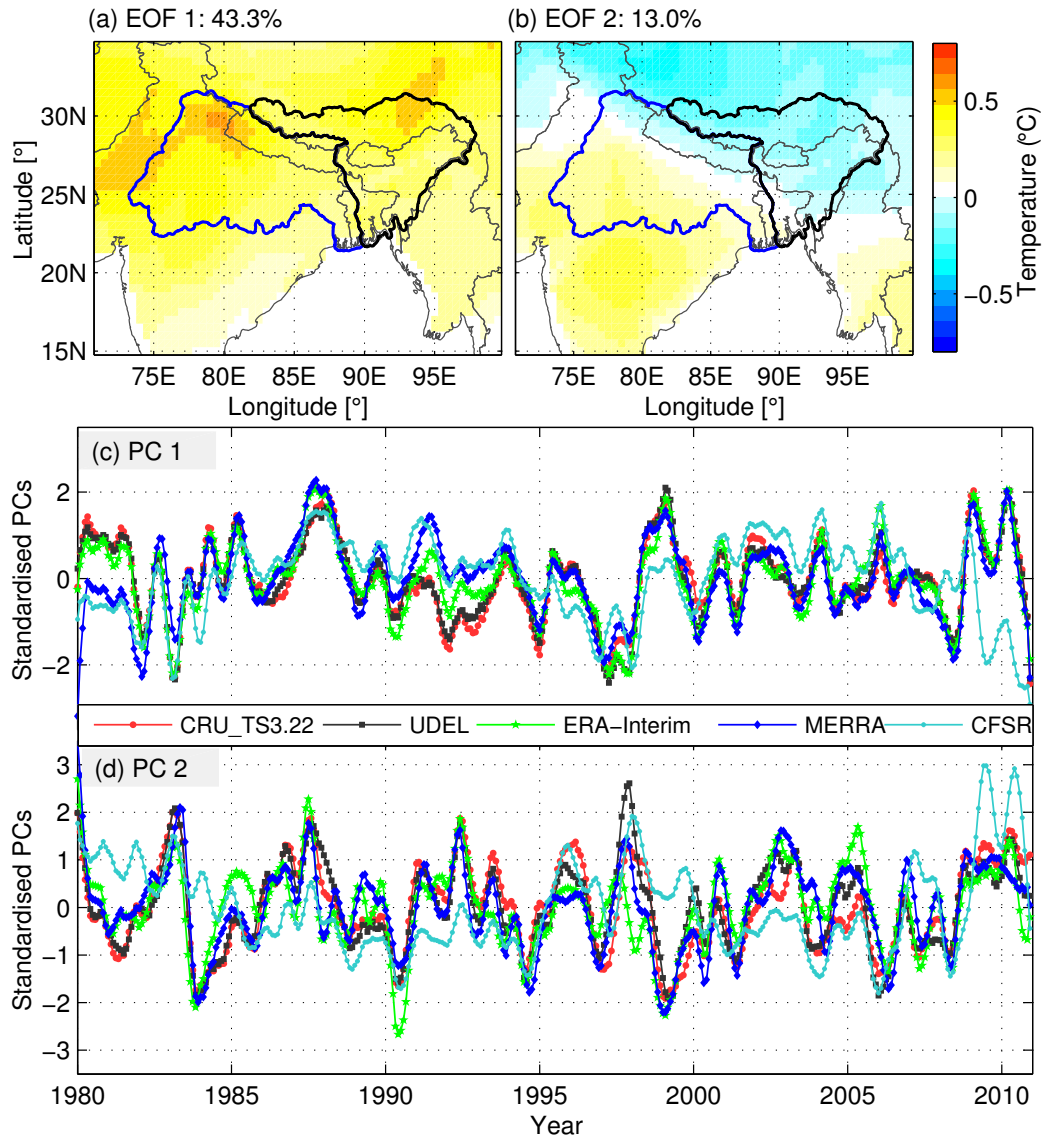


Figure 2.9: Spatial patterns of EOFs (a & b) and temporal components or PCs (c & d) based on first two leading modes of PCA analysis on monthly temperature anomaly of CRU_TS3.22 over the period 1980–2013. PCs of UDEL, ERA-Interim, MERRA, and CFSR indicated in (c & d) are derived by projecting their respective anomalies onto the EOFs of CRU_TS3.22.

1075 tend to differ during the periods 1982–1984 and 1996–2000. UDEL agrees very well
 1076 with CRU_TS3.22 with a correlation of 0.95 and 0.90 for PC 1 and PC 2, respectively
 1077 (Table 2.7). The temporal patterns are captured very well by the reanalysis products
 1078 (Fig. 2.9c–d), especially with ERA-Interim and MERRA showing high correlations with
 1079 CRU_TS3.22 (Table 2.7). The correlations between CRU_TS3.22 and MERRA for PC
 1080 2 is found to be higher (0.79) than those with ERA-Interim (0.68) whereas CFSR agrees
 1081 only moderately for both the PCs.

Table 2.7: Correlation between CRU_TS3.22 and other temperature products over the GBM River Basin for the period 1980–2010. Correlations were computed between the PCs of first two leading modes of CRU_TS3.22 and other products.

| Temperature products | PC 1 | PC 2 |
|----------------------|------|------|
| UDEL | 0.95 | 0.90 |
| ERA-Interim | 0.89 | 0.68 |
| MERRA | 0.79 | 0.77 |
| CFSR | 0.41 | 0.48 |

1082 In order to identify the possible physical mechanisms for these interannual variations,
 1083 the two PCs (Fig. 2.9c–d) are correlated with the SST anomalies (50°N–50°S) for the
 1084 period 1980 to 2010. Although several studies have followed the same procedure to
 1085 quantify the role of global SST variations on land surface temperature, but most of
 1086 them have focused on the Indian sub-continent (Hingane et al., 1985, Kothawale et al.,
 1087 2010, Chowdary et al., 2014). The analysis presents an updated understanding of the
 1088 SST impacts on land surface temperatures in the GBM River Basin, using a PCA-
 1089 based approach. Figure 2.10 shows the correlation between the two PCs (Fig. 2.9c-d)
 1090 and the SST anomalies covering the region 50°N–50°S. PC 1 appears to be highly
 1091 correlated with SST anomalies over the Arabian Sea, moderately correlated with SST
 1092 anomalies over Bay of Bengal and the western tropical Pacific Ocean, and negatively
 1093 correlated with SST over the western Pacific Ocean (Fig. 2.10a and c). This suggests
 1094 that warm temperatures in the western Ganges River Basin are likely driven by positive
 1095 temperature anomalies in the Arabian Sea, and remote forcings such as weak La Niña-
 1096 type events arising from warmer SSTs in the western tropical Pacific Ocean. PC 2, on
 1097 the other hand, is found to be highly correlated with SST anomalies in the western
 1098 tropical Indian Ocean and the western tropical Pacific Ocean. The correlation patterns
 1099 over the tropical Indian Ocean are similar to that of the IOD (Saji et al., 1999) and those
 1100 over western tropical Pacific Ocean resemble the El Niño patterns indicating that both
 1101 ENSO and IOD play a significant role in surface temperature variability across the GBM
 1102 River Basin. Their effects are positive (negative) in the Ganges (Brahmaputra-Meghna)
 1103 River Basin.

1104 These correlation coefficient values are found to be very weak in the reanalysis prod-
 1105 ucts, with only MERRA (and to some degree ERA-Interim) being able to reasonably
 1106 capture the spatial patterns (Fig. 2.10e–h). ERA-Interim and MERRA show consis-
 1107 tent positive correlations in the Arabian Sea, the Indian Ocean, western tropical Pacific
 1108 Ocean, and the Atlantic Ocean that are exhibited by CRU_TS3.22 data (Fig. 2.10e &
 1109 g), although MERRA shows a completely opposite pattern in eastern Pacific Ocean.
 1110 CFSR, on the other hand, do not show any significant correlations with SST anomalies
 1111 (Fig. 2.10i). For PC 2, SST correlation with MERRA exhibits the closest agreement with
 1112 those shown by CRU_TS3.22 (Fig. 2.10h), which is closely followed by ERA-Interim
 1113 (Fig. 2.10f). To quantify the impacts of remote SST on the surface temperature anom-
 1114 alies, PC 2 (Fig. 2.9c) is correlated with Niño3.4 and DMI indices and are shown in Table
 1115 2.8. The correlation coefficient between PC 2 (of CRU_TS3.22) and Niño3.4 (DMI) are
 1116 found to be 0.55 (0.23), both of which are statistically significant at 95% confidence
 1117 level. Correlation with Niño3.4 index is higher for MERRA, followed by ERA-Interim

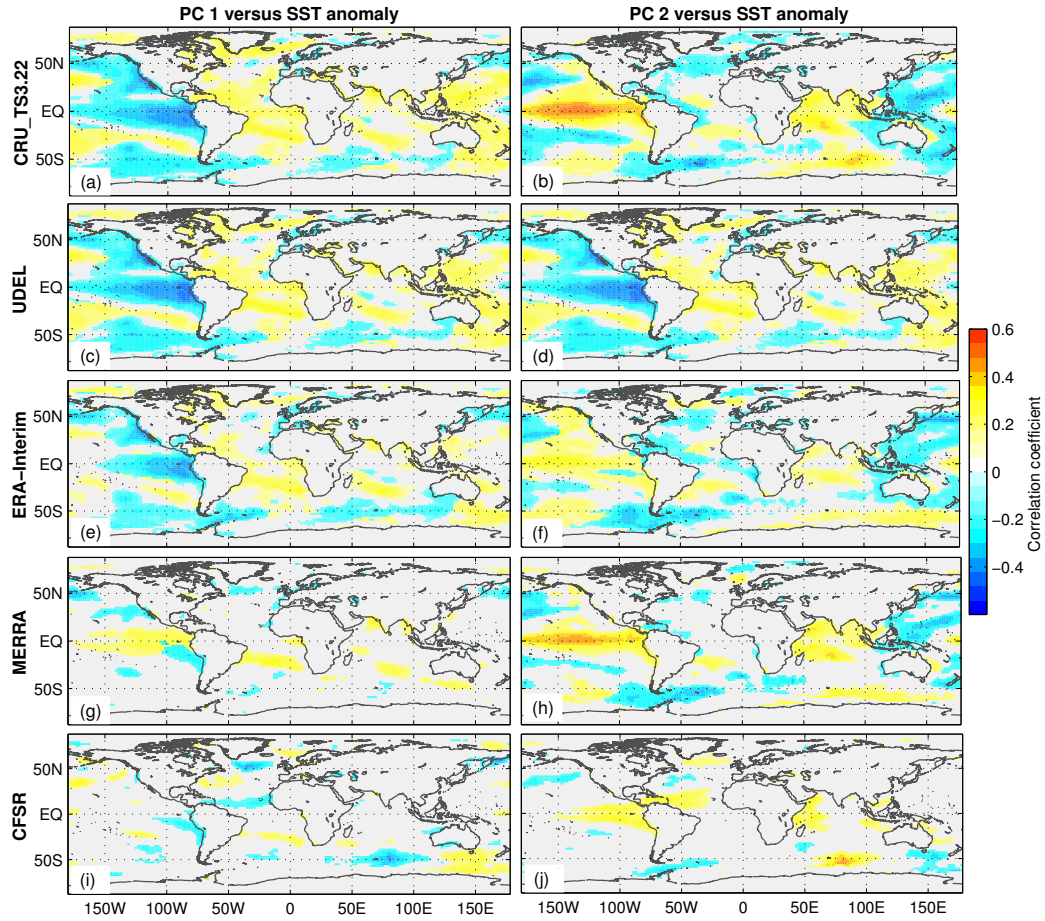


Figure 2.10: Correlation coefficients between monthly SST anomalies and surface temperature anomalies (represented by PC 1 and PC 2) derived from various observed and reanalysis temperature products for the period 1980–2013. Only those values that are significant at 95% confidence level are retained.

1118 and CFSR, which are consistent with the spatial correlation patterns shown in Fig. 2.10.
 1119 However, it is observed that CFSR temperature product is better correlated with DMI
 1120 than those of MERRA and ERA-Interim, which is also evident in Fig. 2.10j. The results
 1121 shown here are quite interesting because ERA-Interim, albeit having consistent temporal
 1122 anomalies with respect to CRU_TS3.22 indicates lower correlations with SSTs.

Table 2.8: Correlation between SST anomalies and the first two PCs of various temperature products for the period 1980 to 2010. The correlation values that are significant at 95% confidence level are highlighted bold.

| Temperature Products | Nino3.4 vs PC 2 | DMI vs PC 2 |
|----------------------|------------------------------|------------------------------|
| CRU_TS3.22 | 0.53 (at 3 month lag) | 0.24 (at 3 month lag) |
| UDEL | 0.56 (at 3 month lag) | 0.22 (at 3 month lag) |
| ERA-Interim | 0.35 (at 3 month lag) | 0.05 (at 3 month lag) |
| MERRA | 0.46 (at 3 month lag) | 0.13 (at 3 month lag) |
| CFSR | 0.27 (at 3 month lag) | 0.30 (at 3 month lag) |

1123 Similarly, the impacts of ENSO and IOD on the basin precipitation are studied. A
1124 multilinear regression approach is used here by fitting the deseasonalised precipitation
1125 anomalies with normalized ENSO and IOD indices (represented by Niño3.4 and DMI),
1126 each with respect to their data period, e.g., APHRODITE (1998–2007), TMPAv7 (1998–
1127 2013), GPCCv6 (1980–2010), and the reanalysis products (1980–2010). The statistical
1128 significance of the regressed values are tested using a student’s t -test at 95% confidence
1129 level based on the correlation coefficients between Niño3.4/DMI indices and precipita-
1130 tion anomalies at each grid. The estimated spatial correlation patterns between Niño3.4
1131 (and DMI) and observed precipitation anomalies (e.g., APHRODITE, GPCCv6) sug-
1132 gest that both ENSO and IOD substantially influence the basin precipitation regime,
1133 particularly affecting the core monsoon region (Bangladesh, northeast India, Bhutan,
1134 and Nepal) and parts of central India. Figure 2.11 shows the precipitation anomalies
1135 associated with ENSO and IOD. In general, the positive ENSO mode (or El Niño) is
1136 associated with significant reduction of rainfall ($\sim 15 \text{ mm year}^{-1}$) mainly over the west-
1137 ern Ganges River Basin (including southern Nepal, Uttar Pradesh, Bihar, Meghalaya in
1138 India and southwest of Bhutan).

1139 While the ENSO impacts are mainly concentrated over western Nepal and its sur-
1140 roundings from 1980 to 2007 (Fig. 2.11a), the period of 1998–2013 saw widespread re-
1141 duction of rainfall in the Ganges and northern Brahmaputra River Basins (Fig. 2.11b).
1142 However, a slight increase ($\sim 5\text{--}10 \text{ mm year}^{-1}$) in rainfall can be seen over Bangladesh
1143 during the same period. The IOD mode (Fig. 2.11c–d), on the other hand is associated
1144 with increase (decrease) in rainfall in the southeastern parts of Ganges River Basin
1145 (Bangladesh and Meghalaya in India). During the same period, widespread decreases
1146 in rainfall are observed over Bangladesh, which are likely linked to frequent positive
1147 IOD events during the period (Fig. 2.11d). Overall, ENSO dominates the basin pre-
1148 cipitation variability (contributing to $\sim 10\text{--}20\%$ of total rainfall), while IOD presents a
1149 modest contribution of $\sim 8\text{--}10\%$ of the total annual rainfall variability. These estimates
1150 can be derived by dividing the ENSO and IOD amplitudes by root-mean-squares of the
1151 monthly rainfall amount (see e.g., Forootan et al., 2015).

1152 The influence of ENSO and IOD on precipitation between 1980 and 2010 shown
1153 by GPCCv6 (Fig. 2.12a and e) are found to be consistent with those indicated by
1154 APHRODITE from 1980–2007 (Fig. 2.11a and c), but with slightly higher precipitation
1155 contribution in GPCCv6. This could be due to the more frequent events of La Niña (e.g.,
1156 in 2007–2008) and El Niño (e.g., in 2006 and 2009–2010) events towards the end of 2010
1157 (see, Khandu et al., 2016a). Among the reanalysis products, ERA-Interim shows the
1158 closest agreement with gauge-based precipitation product, GPCCv6 (Fig. 2.12b and f)
1159 whereas MERRA (Fig. 2.12c and g) and CFSR (Fig. 2.12d and h) either underestimate
1160 or overestimate rainfall contribution due to ENSO and IOD events. However, it should be
1161 noted that the spatial patterns of ENSO and IOD contributions are captured reasonably
1162 well by all the products.

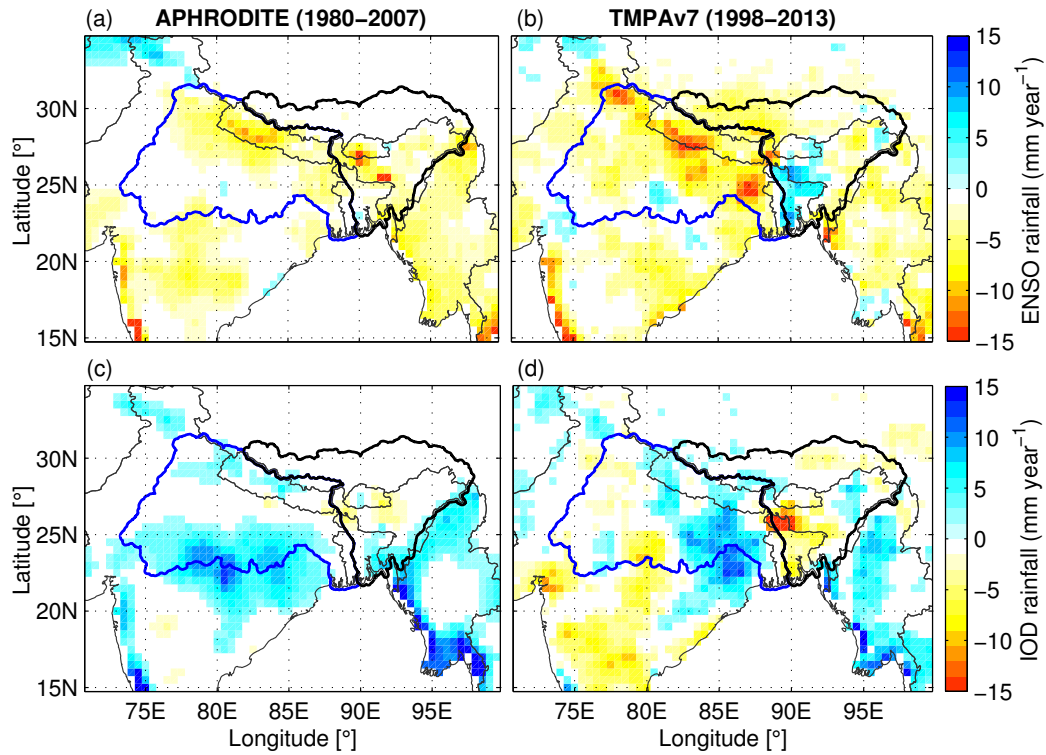


Figure 2.11: Regression of Niño3.4 index and DMI on precipitation anomalies of APHRODITE (1980-2007) and TMPAv7 (1998-2013). Values that are not significant at 95% confidence level based on student's *t*-test are not shown.

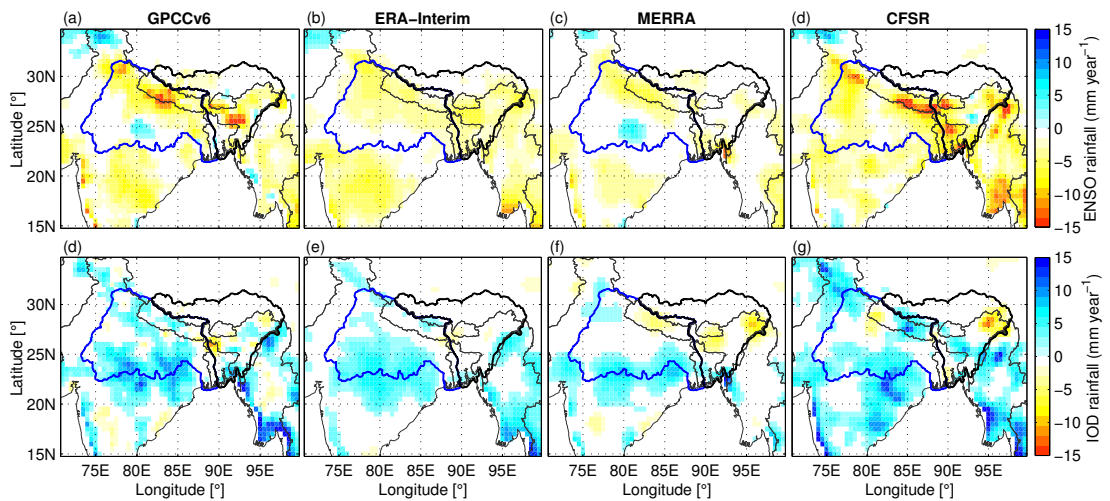


Figure 2.12: Regression Niño3.4 index and DMI on the precipitation anomalies of GPCCv6 and reanalysis products for the period 1980-2010. Precipitation contributions that are not significant at 95% confidence level based on student's *t*-test are not shown.

1163 2.6 Concluding remarks

1164 This chapter provides an updated understanding on the climate change and variability
1165 of the GBM River Basin by analyzing monthly precipitation and temperature datasets
1166 from different sources for the most recent period 1980–2013. Although the primary ob-
1167 jective here is to present the recent updates in basin’s climate and the likely impacts
1168 of large-scale ocean-atmospheric variations such as ENSO and IOD, it also presents an
1169 assessment of current global high-resolution satellite-based precipitation estimates and
1170 reanalysis products describing their potentials and limitations for hydro-meteorological
1171 applications in the region. The reanalysis systems in particular, provide long time-series
1172 of climate datasets that are required for understanding various aspects of global/regional
1173 climate variability and change. They also provide important climate forcing data for re-
1174 gional climate models and land surface/hydrological models. The temperature records
1175 exhibit widespread warming across the GBM River Basin during the last three decades.
1176 Warming appears to be more intense in the Himalayas (across western Nepal and Ti-
1177 betan region) of the Brahmaputra–Meghna River Basin, showing an increasing rate of
1178 $0.6^{\circ}\text{C decade}^{-1}$. Precipitation changes are found to be more scattered across the GBM
1179 River Basin, with an overall decline between 1980 and 2010. The declining rate has
1180 accelerated since the late 1990s in the core monsoon areas of the Brahmaputra–Meghna
1181 River Basin, which is clearly depicted by the recent SRS-based precipitation products
1182 such as TMPAv7 and CHIRP. However, the monsoon precipitation appears to be in-
1183 creasing in the western Ganges River Basin between 1998 and 2013 at a rate of 12 mm
1184 decade^{-1} .

1185 Surface temperature variations can be widely explained by the first two leading modes
1186 of PCA, which togetherly account for $\sim 56\%$ of the total variability. The first mode
1187 exhibits basin-wide positive anomalies with increasing magnitudes towards the west
1188 and north, which are found to be associated with warming SSTs in the Arabian Sea
1189 and the La Niña phase. The second mode depicts a dipole-type pattern with positive
1190 (negative) anomalies over Ganges (Brahmaputra–Meghna) River Basins and are found
1191 to be significantly correlated with SST anomalies over western tropical Indian Ocean
1192 and eastern tropical Pacific Ocean, closely depicting the ENSO/IOD patterns. Similarly,
1193 ENSO and IOD events significantly influence the seasonal rainfall variability across the
1194 GBM River Basin, contributing to about 10–20% and 8–10% to the total annual rainfall,
1195 respectively, mainly over the core monsoon region (Bangladesh, northeast India, Bhutan,
1196 and Nepal) and central India (southern Ganges River Basin).

1197 Reanalysis products tend to have generally poor skills in reproducing the observed
1198 seasonality and long-term trends in precipitation, although, they appear to perform
1199 reasonably well for temperature. The skills of three reanalysis products analyzed in
1200 this study appears to vary across the region and on the type of metrics being assessed.
1201 Hence, it may be summarized that no single reanalysis is superior for both rainfall and
1202 temperature in reproducing the observed patterns. For instance, MERRA temperature
1203 data compares well with CRU_TS3.22, while ERA-Interim agrees well with GPCCv6
1204 precipitation data in terms of long-term trend and interannual variability. However,
1205 both MERRA and ERA-Interim products are barely able to capture the spatial pre-
1206 cipitation variability, while CFSR products shows a shift in high rainfall regions along

1207 the Himalayan Foothills towards the east. MERRA significantly underestimated annual
1208 precipitation amplitude by about 21–37%), whereas CFSR overestimated it by about
1209 9% with respect to GPCPv6. Despite substantial seasonal biases, these products rea-
1210 sonably represent the effects of global and regional (or local) SST variations. Due to
1211 substantial disagreements between observed datasets and recently generated reanaly-
1212 sis products, there are still important limitations on their regional use, particularly for
1213 trend analysis. The next chapter uses soil moisture outputs to determine climate change
1214 effects on water resources in the GBM River Basin, which will further justify the use of
1215 reanalysis products.

1216 3. Observed impacts of climate 1217 change and human water use on 1218 water resources

1219 3.1 Introductory remarks

1220 With a population of over 650 million, the GBM River Basin is also one of the most
1221 populous river basins on Earth and its agriculture and food security is heavily reliant on
1222 its available surface water and groundwater resources. Although graced with abundant
1223 freshwater resources, the GBM's water resources are becoming increasingly vulnerable
1224 to climate variability (such as prolonged droughts) due to rapid rise in population and
1225 its demand for more freshwater (Rodell et al., 2009, Tiwari et al., 2009, Shamsudduha
1226 et al., 2009b, Central Ground Water Board, 2014, Papa et al., 2015). Observational
1227 (e.g., Rodell et al., 2009, Tiwari et al., 2009, Shamsudduha et al., 2009b, Chen et al.,
1228 2014a, Central Ground Water Board, 2014, Shahid et al., 2015, Khandu et al., 2016a)
1229 and hydrological modelling studies (e.g., Döll et al., 2014, Khandu et al., 2016a) re-
1230 vealed alarming depletion of groundwater and surface water storage across many parts
1231 of the river basin, particularly along the vast fluvial plains of Ganges, Brahmaputra,
1232 and Bangladesh as they are being withdrawn at a far greater rate than it can be re-
1233 plenished. The situation is being worsened during the prolonged meteorological drought
1234 events. The state-of-the-art GRACE (Gravity Recovery and Climate Experiment, Ta-
1235 pley et al., 2004) time-variable gravity field measurements first reported the appalling
1236 pictures of large-scale deterioration of available water storage in the GBM River Basin.
1237 This mainly includes groundwater and surface water stored along the Gangetic Plains,
1238 northeast India, and Bangladesh (e.g., Rodell et al., 2009, Tiwari et al., 2009, Chen
1239 et al., 2014a, Khandu et al., 2016a, Long et al., 2016) and glaciers and snow water
1240 equivalent in the Himalayas (e.g., Matsuo and Heki, 2010, Jacob et al., 2012).

1241 Changes in global/regional climate (e.g., temperature changes and associated changes
1242 in spatio-temporal distribution and intensity of precipitation) has been shown to influ-
1243 ence the basin's hydrological budget. While the Indian monsoon precipitation is pro-
1244 jected to largely increase in the future based on climate model projections (see, Anna-
1245 malai et al., 2007, Turner and Annamalai, 2012), current assessments have indicated
1246 significant decline in rainfall in the GBM River Basin during the past few decades (see,
1247 Chapter 2). Studies have attributed this rainfall decline to the overall weakening of
1248 the Indian monsoon circulation and possible radiative cooling affects from increasing
1249 aerosol concentration across South Asia (e.g., Ramanathan et al., 2005, Chung and
1250 Ramanathan, 2006, Lau et al., 2009). Climate model experiments have shown that in-
1251 creasing aerosol concentrations may significantly reduce monsoon rainfall through sur-
1252 face cooling (and consequent reduction of the meridional thermal contrast between the
1253 northern and southern Indian Ocean) and atmospheric heating due to absorption of
1254 solar radiation (Lau and Kim, 2006, Bollasina et al., 2011). The rainfall decline has

1255 been shown to be substantially higher in the Brahmaputra-Meghna River Basin from
1256 1998 to 2014 (Khandu et al., 2016c), further adding to the growing water scarcity in the
1257 region. Changes in monsoon onset and withdrawal as well as length of rainy days may
1258 also have a major impact on the available water resources as it directly affects surface
1259 water availability and groundwater discharge.

1260 Further, natural variability, especially the ENSO (e.g., Chowdhury and Ward, 2004),
1261 IOD (e.g., Saji et al., 1999, Ashok et al., 2001), and Eurasian snow depth levels (Im-
1262 merzeel, 2008) have been shown to influence the basin's climate, which are imitated
1263 as year-to-year variations in precipitation as well as in other components of the water
1264 storage changes. Extreme rainfall events and droughts have become more frequent over
1265 central India, Bangladesh, and Nepal (e.g., Baidya et al., 2008, Rajeevan et al., 2008,
1266 Shahid, 2011, Menon et al., 2013), whereas heavy monsoon rains have largely declined
1267 in the Brahmaputra–Meghna River Basin (e.g., Roy and Balling, 2004, Goswami et al.,
1268 2010). Precipitation variability caused by ENSO and IOD events are translated into
1269 various components of the water storage including soil moisture, (sub-) surface runoff,
1270 glaciers and snow water equivalent, and groundwater across different spatial and tem-
1271 poral scales. However, despite numerous studies on climate change impacts on water
1272 resources, detection and attribution of water storage changes in the GBM River Basin
1273 remains largely unexplored.

1274 The twin-satellite GRACE mission, through its time-variable gravity field obser-
1275 vations, has provided continuous images of large-scale changes in total water storage
1276 (TWS) on an approximately monthly scale since 2002 (Tapley et al., 2004). Over the
1277 oceans TWS reflects the ocean bottom pressure and on land it is interpreted as the
1278 sum of groundwater, soil moisture, surface water, snow and ice (Rodell and Famiglietti,
1279 2001, Tapley et al., 2004). Thus, TWS changes estimated from GRACE time-variable
1280 gravity field solutions over large river basins such as the GBM allows us to monitor
1281 water storage changes on both spatial and temporal scales. With more than 13 years
1282 of continuous data, the GRACE mission has emerged as one of the most valuable tools
1283 for monitoring global (and regional) water resources (see, Chen et al., 2014b, Wouters
1284 et al., 2014, for a review), especially in the GBM River Basin, where groundwater and
1285 surface water resources are being rapidly withdrawn to meet the increasing needs of
1286 its growing population (e.g., Shamsudduha et al., 2009a, Shum et al., 2011, Central
1287 Ground Water Board, 2014). In particular, Khandu et al. (2016a) studied the impacts
1288 of climate variability/change and human water use on the basin's water resources using
1289 a suite of hydro-climatic data including GRACE-derived TWS changes, soil moisture
1290 from reanalysis products and land surface models, and hydrological simulations of water
1291 storage changes. The study found that both meteorological droughts and human water
1292 abstraction have played a role in the recent decline in available water resources in the
1293 GBM River Basin.

1294 To further explore and understand the combined impacts of climate variability and
1295 human water abstraction, this chapter presents an updated information and description
1296 of results of Khandu et al. (2016a) by extending the study period to 2015. Some of
1297 the results presented here are largely adopted from Khandu et al. (2016a) as no data
1298 updates have occurred following this publication. Section 3.2 presents a brief summary

1299 of the state of water use in the GBM River Basin. Section 3.3 describes the various
 1300 datasets used and methods applied to understand the role of climate variability and
 1301 human water use. The results are presented and discussed in Section 3.4, and finally,
 1302 this study is summarized and concluded in Section 3.5.

1303 3.2 State of water use

1304 The GBM River Basin synthesizes a complex interplay of Indian monsoon, glacierized
 1305 Himalayan mountains, and its high groundwater potentials of the vast fluvial plains
 1306 of Ganges and Assam. The Indian monsoon system largely defines the climate and
 1307 hydrology of the GBM River Basin, contributing to a significant portion (60–90%) of its
 1308 annual precipitation. The Himalayan glaciers and snowmelts provide much of the surface
 1309 water storage ensuring a perennial flow of thousands of tributaries of the GBM river
 1310 system. The Himalayan mountains in the northern GBM River Basin have the largest
 1311 concentration of glaciers outside the polar region covering an approximate area of 22,800
 1312 km² (Bolch et al., 2012). Although, their overall contribution to the annual runoff in
 1313 the Ganges and Brahmaputra rivers is relatively small (~2%) during the summer, the
 1314 surface water storage (SWS), consisting of the rivers, floodplains, lakes and wetlands
 1315 contributes up to ~ 40–50% of the GRACE-derived TWS variations in the GBM River
 1316 Basin (Papa et al., 2015).

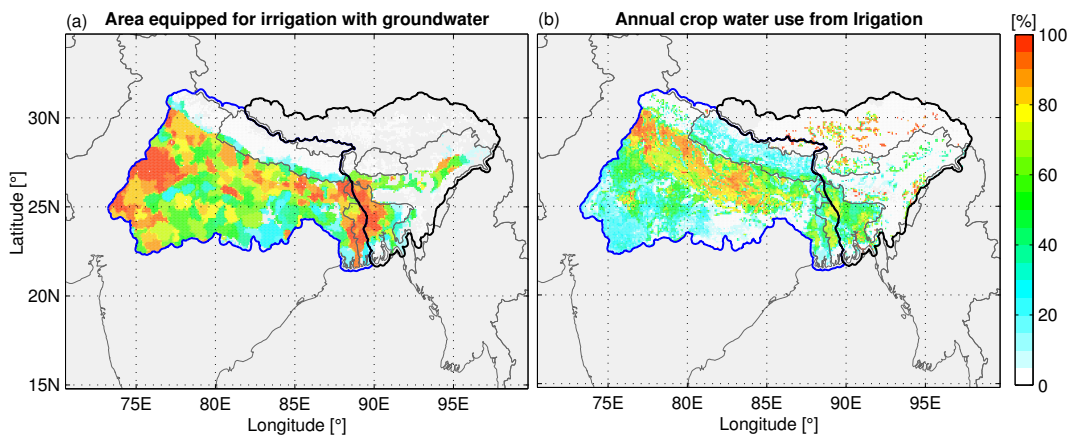


Figure 3.1: The Ganges (thick black polygon) and Brahmaputra–Meghna (thick blue polygon) and its (a) area equipped for irrigation (%) from AQUASTAT data of the Food and Agricultural Organization (FAO) of the United Nations and (b) annual water use in irrigated agriculture (%) from Global Crop Water Model for the period 1998–2002.

1317 However, with rapid rise in population and its associated demands for freshwater,
 1318 the GBM River Basin has one of the highest consumptive water use in the world.
 1319 Groundwater accounts for about 60–80% of the domestic water use and more than
 1320 85% of it being used for irrigation (Mukherjee et al., 2015, Long et al., 2016). This
 1321 represents approximately 35% of the groundwater withdrawal in the world (Mukherjee
 1322 et al., 2015). Thus, to understand the effect of climate variability/change on water
 1323 resources, it is necessary to understand the state of the water resources and their usage

1324 in the GBM River Basin. Figure 3.1a shows that more than 80% of grid cells in the
1325 western Ganges River Basin, Ganges Plains and major part of Bangladesh is equipped
1326 for agricultural irrigation by either surface water or groundwater (see, <http://www.fao.org/nr/water/aquastat/irrigationdrainage/treemap/index.stm>). An approximate
1327 percentage use of groundwater for irrigation is shown in Figure 3.1b, which indicates
1328 highest groundwater use (up to 90%) along the Ganges Plain covering the Indian states
1329 of Haryana, Uttar Pradesh and Bihar. Bangladesh uses about 40–80% of groundwater
1330 for irrigation mostly concentrating in the northwestern region (Shahid et al., 2015),
1331 while few areas in northeast India and southern Tibet also relies on groundwater for
1332 irrigation.
1333

1334 3.3 Data and methods

1335 TWS changes (ΔS) are directly related to changes in fluxes over time (t), i.e., precip-
1336 itation (P), evapotranspiration (E), and runoff (R), through the simple water balance
1337 equation: $\Delta S(t) = P(t) - E(t) - R(t)$. In this study, precipitation is used as the primary
1338 meteorological forcing variable to assess the impacts of climate variability on TWS (and
1339 soil moisture) in the GBM River Basin. Soil moisture represents a portion of water held
1340 in the uppermost part of the Earth’s surface and is a major component of TWS for sus-
1341 taining agriculture. Groundwater (Shamsudduha et al., 2009b, Mukherjee et al., 2015,
1342 Long et al., 2016) and SWS (Papa et al., 2015) forms the major component of TWS
1343 in the GBM River Basin and are often disaggregated using GRACE and land surface
1344 model data (e.g., Rodell et al., 2009, Tiwari et al., 2009, Long et al., 2016). This is
1345 not being done here as this study aims to understand the overall water storage changes
1346 determined from GRACE measurements only and soil moisture datasets serve as proxy
1347 for TWS for the long-term investigation.

1348 The datasets used here include: (i) monthly gridded gauge-based precipitation prod-
1349 ucts: GPCP version 7 (1980–2013, Becker et al., 2013, hereinafter as GPCPv7) (), and
1350 CRU_TS3.22 (1980–2014, Harris et al., 2013) and merged SRS-based estimates from
1351 TMPA (1998–2015 Huffman et al., 2007), (ii) TWS changes derived from GRACE (Ta-
1352 pley et al., 2004) time-variable gravity field solutions (August 2002–September 2015),
1353 (iii) soil moisture products from three different reanalyses (1980–2015) and Global Land
1354 Data Assimilation System (GLDAS, from 2002–2015, Rodell et al., 2004), and (iv) simu-
1355 lated TWS (and surface water) from the Water-Global Assessment and Prognosis (Wa-
1356 terGAP version 2.2a) Global Hydrology Model (WGHM, Döll et al., 2003, 2014) for
1357 the period 1980–2009. While the precipitation products have been already described in
1358 Chapter 2, the remaining datasets used in this chapter are described below.

1359 3.3.1 Land surface models

1360 Land surface and hydrological models have long played an important role in under-
1361 standing the global land hydrology processes. Global hydrological models ingest millions
1362 of satellite- and ground-based observations to generate optimal fields of land surface

1363 states (e.g., soil moisture and surface temperature) and fluxes (e.g., evaporation and
1364 sensible heat flux). The land surface states such as soil moisture, canopy water storage
1365 (CWS), and snow water equivalent can be combined to generate water storage changes
1366 relating to about 2–3 meters below the land surface. Since the contribution of CWS
1367 and snow water equivalent is relatively small in most regions, most studies rely on soil
1368 moisture to assess the global/regional water balances and climate change impacts on
1369 water resources and agriculture (see, [Seneviratne et al., 2010](#), for a review). However,
1370 soil moisture generated by land surface/hydrological can vary considerably among dif-
1371 ferent models and forcing data. To determine the spatio-temporal consistencies among
1372 various available soil moisture products, this study includes data generated by reanal-
1373 ysis systems and land surface models. These include the NASA’s Global Land Data
1374 Assimilation System (GLDAS, [Rodell et al., 2004](#)), namely, Noah, and soil moisture
1375 produced by three global reanalyses, namely (i) Climate Prediction Center (CPC, [van
1376 den Dool et al., 2003](#)), (ii) Modern Era Retrospective Analysis for Research Application
1377 (MERRA, [Rienecker et al., 2011](#)), and (iii) ERA-Interim ([Dee et al., 2011](#)). The key
1378 attributes of these products are given in Table 3.1 and their basic features are described
1379 below:

1380 i **GLDAS Noah:** GLDAS is a unique uncoupled land surface model with advanced
1381 land surface modeling and data assimilation techniques, designed to generate opti-
1382 mal fields of land surface states and fluxes through assimilation of huge quantity of
1383 ground-based and SRS-based observational products ([Rodell et al., 2004](#)). GLDAS
1384 drives several models including Noah, Mosaic, VIC, and Community Land Model
1385 (CLM) (for details, see, [Rodell et al., 2004](#)), with variable soil layers and depth
1386 columns, and are run at a $0.25^\circ \times 0.25^\circ$ horizontal resolution. The GLDAS outputs
1387 are produced in near real-time (typically within 48 h of the present), which is im-
1388 portant for many hydrological applications. Previous studies have used these models
1389 to decompose GRACE-derived TWS fields to derive groundwater storages over vari-
1390 ous parts of the GBM River Basin (e.g., [Rodell et al., 2009](#), [Tiwari et al., 2009](#),
1391 [Shamsudduha et al., 2009b](#)). However, ([Khandu et al., 2016a](#)) found that long-term
1392 GLDAS soil moisture datasets produced at $1.0^\circ \times 1.0^\circ$ grid revealed large spurious
1393 jumps between 1995 and 1997, which are not consistent with other soil moisture
1394 products. Hence, in this study, the high-resolution ($0.25^\circ \times 0.25^\circ$) version of Noah
1395 is analysed for the period 2002–2015.

1396 ii **CPC:** The Climate Prediction Center (CPC) at National Oceanic and Atmospheric
1397 Administration (NOAA) generates global monthly soil moisture estimates at 0.5°
1398 $\times 0.5^\circ$ resolution from 1948–present by forcing a one-layer hydrological model with
1399 observed precipitation and temperature ([van den Dool et al., 2003](#)). The soil mois-
1400 ture datasets are updated monthly for near-real-time applications such as drought
1401 monitoring and large-scale hazard assessments (see, [http://www.esrl.noaa.gov/
1402 psd/data/gridded/data.cpcsoil.html](http://www.esrl.noaa.gov/psd/data/gridded/data.cpcsoil.html)). The CPC soil moisture has been widely
1403 used and has been found to agree well with those from different sources (e.g., [Guo
1404 et al., 2007](#)).

1405 iii **MERRA:** The Modern Era Retrospective Analysis for Research Application
1406 (MERRA, [Rienecker et al., 2011](#)) reanalysis, is a state-of-the-art global reanaly-

1407 sis based on an updated modelling and data assimilation system for the satellite-
 1408 era (1979 onwards) produced by the National Aeronautic and Space Administra-
 1409 tion (NASA, US) using the Goddard Earth Observing Data Assimilation Version 5
 1410 (GEOS-5). MERRA reanalysis integrates various observational datasets from mod-
 1411 ern observing systems such as satellite-based estimates (Rienecker et al., 2011) to
 1412 describe various conditions of the meteorological and hydrological process including,
 1413 among others, soil moisture, snow/ice and canopy water. The retrospective-analyses
 1414 is run globally at a relatively high spatial resolution ($0.67^\circ \times 0.50^\circ$) and data are
 1415 available at 6-hourly, daily, and monthly scales. MERRA also generates TWS that
 1416 roughly represents the soil moisture in the root zone layer, and is considered as soil
 1417 moisture in this study (see, <http://gmao.gsfc.nasa.gov/merra/>).

1418 iv **ERA-Interim**: ERA-Interim is a global atmospheric reanalysis produced by the
 1419 European Center for Medium Range Weather forecast (ECMWF) with an improved
 1420 atmospheric model and data assimilation system from its previous versions (Dee
 1421 et al., 2011). The reanalysis produces several key land surface parameters such
 1422 as soil moisture, vegetation, and snow water equivalent, among others, by com-
 1423 bining various global observational datasets using an integrated forecast model.
 1424 These outputs are produced at various time-scales and at a spatial resolution of
 1425 $0.79^\circ \times 0.79^\circ$. In this study, monthly soil moisture data from four volumetric layers
 1426 are obtained from ECMWF data portal (<http://apps.ecmwf.int/datasets/data/interim-full-daily/>).

Table 3.1: Summary of the soil moisture products used in the study.

| Products | Spatial resolution | No. of layers | Total depth (m) | References |
|--------------------------|--------------------------------|---------------|-----------------|--|
| CPC (reanalysis) | $0.50^\circ \times 0.50^\circ$ | 1 | 1.60 | van den Dool et al. (2003) |
| MERRA (reanalysis) | $0.50^\circ \times 0.67^\circ$ | 1 | ~1.00 | Rienecker et al. (2011) |
| ERA-Interim (reanalysis) | $0.79^\circ \times 0.79^\circ$ | 4 | 2.55 | Dee et al. (2011) |
| Noah (GLDAS) | $0.25^\circ \times 0.25^\circ$ | 4 | 2.00 | Chen et al. (1996), Rodell et al. (2004) |
| WGHM | $0.50^\circ \times 0.50^\circ$ | 1 | ~1.00 | Alcamo et al. (2003), Döll et al. (2003), Müller Schmied et al. (2014) |

1428 It is also important to note that advances in SRS has enabled estimation of soil
 1429 moisture fields at a high global resolution (e.g., $0.25^\circ \times 0.25^\circ$). Data sets include
 1430 measurements from e.g., Advanced Microwave Scanning Radiometer series (AMSR-E
 1431 Njoku et al., 2003), the Soil Moisture Ocean Salinity (SMOS, Kerr et al., 2001), and
 1432 Soil Moisture Active Passive (SMAP, Entekhabi et al., 2010). The most comprehensive
 1433 set of SRS-based soil moisture is provided by the European Space Agency (ESA, see,
 1434 <http://www.esa-soilmoisture-cci.org/node/202>) with a spatial resolution of 0.25°
 1435 $\times 0.25^\circ$ covering a period of 37 years until 2015.

1436 3.3.2 GRACE total water storage (TWS) changes

1437 Gravity Recovery and Climate Experiment (GRACE) is a joint satellite mission of
 1438 National Aeronautics and Space Administration (NASA) and the German Aerospace

1439 Center (Deutsches Zentrum für Luft- und Raumfahrt, DLR) that has been continuously
 1440 monitoring the spatial and temporal variations of the Earth’s gravity field since March
 1441 2002 (Tapley et al., 2004). The GRACE mission consists of two satellites that are placed
 1442 ~ 220 km apart in a near circular polar orbit at an elevation of about 500 km (Fig. 3.2).
 1443 By tracking the distance between the satellites accurately with the help of a K-band
 1444 microwave ranging system, a precise spatio-temporal variation of the Earth’s gravity
 1445 field can be obtained (Tapley et al., 2004). The variation in the inter-satellite range is
 1446 attributed to the change in the Earth’s mass distribution within, at, and above its surface
 1447 (Wahr et al., 1998, 2004, Tapley et al., 2004). Contributions from other sources such as
 1448 Ocean and Earth tides, atmospheric disturbances associated with synoptic storms and
 1449 seasonal climatic variations, and Earth’s rotation are removed prior to estimating the
 1450 surface mass distribution (Wahr et al., 1998). Assuming negligible effects from glacial
 1451 isostatic adjustment (or crustal rebound) in the GBM River Basin, mass changes derived
 1452 from GRACE can be attributed entirely to variations of water storage changes.

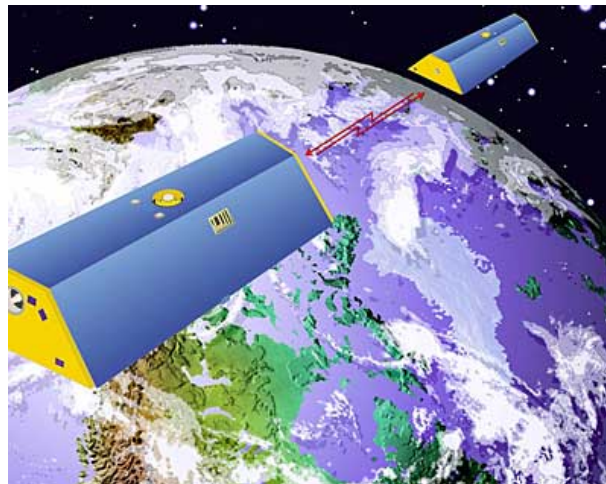


Figure 3.2: The concept of the GRACE satellite mission. The two satellites move in tandem to detect changes in Earth’s gravity field. Separations as small as 10 microns are detected. Source: www.spaceflightnow.com/rockot/grace.

1453 Since its launch in 2002, GRACE satellites have provided unprecedented records of
 1454 large-scale variations in total water storage (TWS) across various parts of the globe (see,
 1455 Chen et al., 2014b, Wouters et al., 2014, for a review). GRACE datasets are provided
 1456 as approximately monthly gravity field solutions in the form of dimensionless Stoke’s
 1457 coefficients (C_{lm}, S_{lm}) to a maximum degree (l) and order (m), $L_{max} = 120$ by the
 1458 three official GRACE processing centers, (i) Center for Space Research (CSR), (ii) Geo-
 1459 Forschungszentrum (GFZ), and (iii) Jet Propulsion Laboratory (JPL). This is termed
 1460 as GRACE Level 2 data. The current release (RL05) is made available through their of-
 1461 ficial portal (e.g., <ftp://podaac.jpl.nasa.gov/allData/grace/L2>). Several other in-
 1462 stitutions (e.g., University of Graz, Austria, Centre National d’Etudes Spatiales, CNES,
 1463 France) also independently process GRACE time-variable field solutions and are even
 1464 available as gridded TWS anomalies. These spherical harmonic coefficients (C_{lm}, S_{lm})
 1465 can be used to estimate equivalent water heights (EWH) or TWS changes ($\Delta S(\theta, \lambda)$ in
 1466 mm) following Wahr et al. (1998),

$$\Delta S(\theta, \lambda) = \frac{M}{4\pi a^2 \rho_w} \sum_{l=2}^{L_{max}} \sum_{m=0}^l \frac{2l+1}{1+k_l} \tilde{P}_{lm}(\cos\theta) [\Delta C_{lm} \cos(m\lambda) + \Delta S_{lm} \sin(m\lambda)], \quad (3.1)$$

1467 where θ and λ are geocentric co-latitude and longitude, respectively, a is Earth's
 1468 mean radius (6.371×10^6 m), ρ_w is the average density of water (i.e., $1,000$ kg/m³), and
 1469 M is the mass of the Earth (5.97219×10^{24} kg); \tilde{P}_{lm} are the fully normalized associated
 1470 Legendre functions of degree l and order m , and ΔC_{lm} and ΔS_{lm} are the changes of
 1471 the spherical harmonic coefficients, which is generally calculated by subtracting the
 1472 temporal mean from the monthly coefficients (C_{lm}, S_{lm}); and k_l is the Love number
 1473 associated with the degree l .

1474 Although GRACE solutions are processed over time with improved model back-
 1475 grounds and algorithms, spherical harmonic coefficients at higher degrees still feature
 1476 strong stripping patterns in the spatial domain. In order to suppress these (“noise”)
 1477 effects, GRACE coefficients need to be filtered either in the spectral or spatial domain.
 1478 GRACE filters are broadly classified into (i) isotropic (e.g., [Jekeli, 1981](#), [Wahr et al.,](#)
 1479 [1998](#)) and (ii) anisotropic (e.g., [Han et al., 2005](#), [Swenson and Wahr, 2006a](#), [Kusche,](#)
 1480 [2007](#)) filters. After applying the smoothing kernel (W_l) in the spectral domain, Eq. 3.1
 1481 can be written as

$$\frac{\Delta S}{\Delta t}(\theta, \lambda) = \frac{M}{4\pi a^2 \rho_w} \sum_{l=2}^{L_{max}} \sum_{m=0}^l \frac{2l+1}{1+k_l} W_l \tilde{P}_{lm}(\cos\theta) [\Delta C_{lm} \cos(m\lambda) + \Delta S_{lm} \sin(m\lambda)]. \quad (3.2)$$

1482 For this study, the GRACE solutions (RL05) are filtered using the non-isotropic
 1483 decorrelation filter proposed by [Kusche et al. \(DDK2, 2009\)](#) to reduce the north-south
 1484 striping patterns as well as the correlated noises since it eliminates the two-stage filtering
 1485 process of, (i) de-stripping, for example, based on [Swenson and Wahr \(2006a\)](#) and
 1486 (ii) spatial smoothing with a certain radius based on [Jekeli \(1981\)](#). GRACE filters
 1487 (see, Eq. 3.2), however, causes significant damping of signal amplitudes and spatial
 1488 leakages that leads to substantial biases of storage changes over the land ([Awange et al.,](#)
 1489 [2009](#), [Longuevergne et al., 2010](#)). In addition, truncation at L_{max} (typically to degree
 1490 and order 60) due to limited range of spherical harmonic coefficients limits the spatial
 1491 resolution GRACE-derived TWS fields to few hundreds kms, e.g., $l_{max}=60$ represents a
 1492 half-wavelength of ~ 330 km ([Awange et al., 2009](#), [Landerer and Swenson, 2012](#)). This
 1493 effect is known as the “spectral leakage”. Leakage happens over any area of mass change,
 1494 though to a greater extend over areas with strong spatial variations of mass changes,
 1495 e.g., coastal regions and small river basins ([Chen et al., 2006](#), [Awange et al., 2009](#)).

1496 Biases in GRACE TWS changes caused by filtering and signal leakages can be re-
 1497 stored either (i) by a scaling factor approach (e.g., [Longuevergne et al., 2010](#), [Landerer](#)
 1498 [and Swenson, 2012](#)) or (ii) by a forward modelling approach (e.g., [Chen et al., 2014a](#)).
 1499 The scaling factor, derived from water storage changes from land surface or hydrological

1500 models, have been widely applied to restore GRACE signals (e.g., Longuevergne et al.,
 1501 2010, Landerer and Swenson, 2012). The forward modelling approach has been shown
 1502 to be effective in reducing leakage biases in GRACE estimates over North India (Chen
 1503 et al., 2014a, Long et al., 2016). The forward modelling approach is more challeng-
 1504 ing and requires more computation resources due to the iteration involved (see, Chen
 1505 et al., 2014a, Long et al., 2016). Hence, a gridded multiplicative scale factor is estimated
 1506 based on Landerer and Swenson (2012) from the water storage changes derived from the
 1507 GLDAS Noah land surface model at $0.5^\circ \times 0.5^\circ$ grid resolution. Figure 3.3 shows the
 1508 derived scale factor and correlation coefficient between filtered and unfiltered data. The
 1509 scale factors are generally larger than one, except in the core Himalayan region, indicat-
 1510 ing that signal dampening is strong in the GBM River Basin, (Fig. 3.3a). Correlation
 1511 coefficients closer to one in Fig. 3.3b suggests that signal shape is not strongly affected
 1512 by the filter in most of the region. Lower correlation values typically occur along the
 1513 strong gradients such as along the Himalayan Range, where spatial decorrelation length
 1514 is very short.

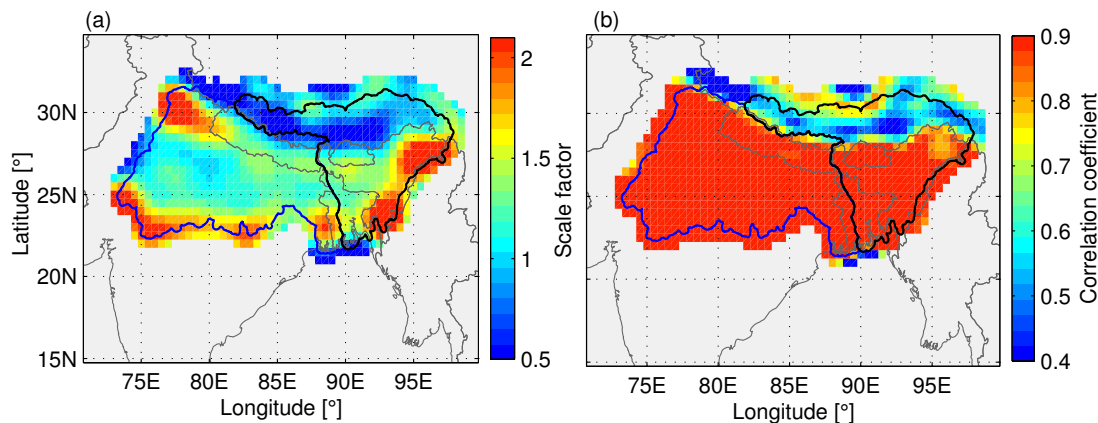


Figure 3.3: (a) Gridded scale factor derived by fitting a least squares approach of Landerer and Swenson (2012), (b) correlation between filtered and unfiltered GLDAS soil moisture.

1515 Further, GRACE coefficients of degree 1 (C_{10} ; C_{11} ; S_{10}) and 2 (C_{20}) terms describ-
 1516 ing the movement of the Earth's center-of-mass (or the geocenter), and the Earth's
 1517 dynamic oblateness, respectively, are not well-determined by GRACE satellites, and
 1518 must be corrected with more accurate values estimated from e.g., Satellite Laser Rang-
 1519 ing (SLR, Cheng et al., 2013). The omission of degree 1 can have considerable impact on
 1520 the recovery of e.g., high-latitude mass variability and large-scale oceanic mass change
 1521 (Chambers, 2004, Chen et al., 2005, Chambers et al., 2007, Swenson et al., 2008). For
 1522 instance, Chambers (2004) noted that inclusion of degree 1 terms in GRACE datasets
 1523 reduced annual amplitude biases from 15% to 1%. Similarly, Chambers et al. (2007)
 1524 reported that ignoring degree 1 trends in TWS analysis can highly underestimate the
 1525 rate of ocean mass change (by up to 30%). Although recent release (RL05) of GRACE
 1526 solutions showed significant improvement compared to previous releases, especially for
 1527 C_{21} and S_{21} (see e.g., Chen et al., 2004, Chambers, 2006, Chen and Wilson, 2008),
 1528 GRACE C_{20} time-series are reported to be still highly uncertain compared to SLR-
 1529 values (Chambers, 2006, Chen and Wilson, 2008). To take into account both these terms,

1530 the time-series of degree one ($C_{10}; C_{11}; S_{10}$) and two (C_{20}) coefficients of GRACE data
1531 are replaced by those derived by Swenson et al. (2008) and Cheng and Tapley (2004),
1532 respectively.

1533 The GRACE TWS changes are analyzed for a common grid resolution of $0.5^\circ \times 0.5^\circ$.
1534 The soil moisture datasets are processed in the same way as GRACE-derived TWS
1535 changes by applying the DDK2 filter in the spectral domain, truncating at the maximum
1536 degree and order of 60 when converting to grid and finally by multiplying with the
1537 gridded scale factor applied to GRACE datasets.

1538 3.3.3 WaterGAP Global Hydrology Model (WGHM)

1539 The Water-Global Analysis and Prognosis (WaterGAP) Global Hydrological Model
1540 (WGHM), developed by the Universities of Kassel and Frankfurt in Germany, is de-
1541 signed to assess current global/regional water resources as well as estimate impacts of
1542 global change on the freshwater systems (Döll et al., 2003, 2014). It specifically focuses
1543 on the interactions between humans and the terrestrial hydrology by integrating cli-
1544 mate variability/change, human water use, and increasing demographics of the world.
1545 Thus, WGHM simulates the impact of demographic, socio-economic, and technological
1546 changes on water use as well as the impact of climate change and variability on wa-
1547 ter availability and irrigation water use (Alcamo et al., 2003, Döll et al., 2014, Müller
1548 Schmied et al., 2014). WGHM consists of a hydrological model that computes water
1549 storages and fluxes (surface runoff, groundwater recharge, river discharge, water storage
1550 in soil, groundwater and surface water bodies) over land except Antarctica, and a global
1551 water use model that simulates human water use (for irrigation, livestock, households,
1552 thermal power plant and manufacturing) on a daily basis on a horizontal grid on 0.5°
1553 $\times 0.5^\circ$ resolution.

1554 Through these integration and simulation, WGHM produces water storage changes
1555 including TWS, groundwater, soil moisture, (sub-) surface water resulting from several
1556 model variants, with each model variant differing in terms of the amount of irrigation
1557 water use and the quantity of groundwater recharge from surface water bodies (Döll
1558 et al., 2014). Table 3.2 shows the various model variants of the current WaterGAP
1559 model version 2.2a (or WaterGAP2.2a). Detailed description of these variants can be
1560 found in Döll et al. (2014) and Müller Schmied et al. (2014). For instance, the “NOUSE”
1561 run considers an idealised case based on the natural variability only, without any water
1562 use, whereas “IRR70_S” experiment assumes 70% of water being used for irrigation with
1563 “_S” indicating the contribution of groundwater recharge from surface water bodies (10
1564 mm day⁻¹ in IRR70_S). WaterGAP2.2a is forced by monthly precipitation data from
1565 GPCCv6 (Schneider et al., 2014) and temperature, cloud cover, and number of wet days
1566 (all monthly grids) from the CRU_TS3.10 data (Harris et al., 2013).

1567 The individual outputs of these model variants have been already examined by
1568 Döll et al. (2014) to estimate the global groundwater depletion. By comparing TWS
1569 changes simulated by WGHM with various model variants with independent esti-
1570 mates of GRACE-derived TWS changes and available literature (including ground-
1571 water well observations and regional modeling), the study indicated that “IRR70_S”

Table 3.2: Model variants of WaterGAP 2.2a. The model variants used in this study are indicated by an asterisk (*). Source: Döll et al. (2014)

| Abbreviation of model variants | Groundwater recharge per unit area of surface water body (mm/day) | Consumptive water use for irrigation as a fraction of optimal water use (%) |
|--------------------------------|---|---|
| IRR100 | 0 | 100 |
| IRR100_S | 10 | 100 |
| IRR70_S* | 10 | 70 |
| NOUSE_S* | 10 | 0, and no other water use |
| IRR70_S3 | 3 | 70 |
| IRR70_S1 | 1 | 70 |

1572 provides the best estimate of human water use across many parts of the world includ-
 1573 ing the GBM River Basin. In this study, therefore, monthly TWS outputs (as well
 1574 as surface water storage) of (i) “NOUSE”, and (ii) “IRR70_S” of WaterGAP2.2a are
 1575 used to estimate the TWS variations relating to both natural variability and grow-
 1576 ing human water use. The outputs of the WaterGAP2.2a can be found at [http:](http://www.uni-frankfurt.de/49903932/7_GWdepletion?)
 1577 [//www.uni-frankfurt.de/49903932/7_GWdepletion?](http://www.uni-frankfurt.de/49903932/7_GWdepletion?).

1578 3.3.4 Extreme indices

1579 Climate extremes can be defined as occurrences of a value of a climate variable (e.g.,
 1580 temperature, precipitation) above (or below) a certain threshold value near the upper
 1581 (or lower) ends of the range of observed values of the variable (IPCC, 2012). Climate
 1582 extremes such as droughts are usually characterized using statistical indices derived
 1583 from daily or monthly climate variables such as precipitation, over a period of 30 years
 1584 (see, Klein Tank et al., 2009). Among others, the standardised precipitation index (SPI)
 1585 developed by McKee et al. (1993) and Palmer Drought Severity Index (PDSI) developed
 1586 by (Palmer, 1965) are the two widely used hydro-meteorological indices to quantify
 1587 droughts and monitor its development. The two methods have been extended over the
 1588 years to include more variables (see, e.g., Dai et al., 2004, Dai, 2013, Mishra et al., 2014).
 1589 While PDSI is more complicated, SPI can easily adapted to describe meteorological
 1590 drought conditions (e.g., precipitation). SPI can be also used to hydrological droughts
 1591 using soil moisture, runoffs, among others. It should be mentioned here that hydro-
 1592 climatic extremes such as droughts can also occur at sub-seasonal to seasonal scales
 1593 such as flash floods and heat waves (IPCC, 2012). Two types of indices are estimated
 1594 in this study, which are described below:

- 1595 (i) **Standardised Precipitation Index (SPI):** The SPI developed by McKee et al.
 1596 (1993) from monthly precipitation data provides an effective statistical measure
 1597 of both dry (and wet) events on various time scales (typically for 3, 6, 9, 12, 24,
 1598 48 months). SPI can be estimated by calculating the cumulative probability, most
 1599 commonly by fitting a Gamma distribution on the monthly and seasonal (the past
 1600 2, 3, ... up to 48 months) precipitation data, which is then normalized by an inverse
 1601 normal (Gaussian) function (see, McKee et al., 1993). SPI is a dimensionless in-
 1602 dex where negative values indicate below normal precipitation and positive values

1603 imply above-normal precipitation. The SPI time-scales reflect the impact of pre-
 1604 cipitation extremes on the availability of water resources (e.g., soil moisture and
 1605 groundwater) at varying time-scales. For instance, soil moisture conditions respond
 1606 to precipitation anomalies on a relatively short time-scale (e.g., 3 month), whereas
 1607 groundwater and stream flows reflect the long-term (e.g., 6 months or more) pre-
 1608 cipitation anomalies. In this study, SPI is computed for both precipitation and
 1609 soil moisture based on 12 month and 6 month time-scales, respectively, to assess
 1610 the impact of precipitation extremes on water resources in the GBM River Basin.
 1611 Table 3.3 summarizes the possible interpretations of drought and wet conditions
 1612 based on the derived SPI values (see also, [McKee et al., 1993](#), [Hirschi et al., 2011](#)).

1613 (ii) **Standardised Indices (SI)**: It is found that SPI computed from GRACE TWS
 1614 changes fail to realistically describe drought conditions in the GBM River Basin.
 1615 For this reason, a standardised index (SI) is developed for GRACE TWS changes.
 1616 The dominant signals such as linear trends and annual signals are removed prior
 1617 to computing the SI by using the multilinear regression approach described in
 1618 Section 2.4. The estimated SI indices are further standardized by multiplying with
 1619 the standard deviations of SPI (from soil moisture) so that the resulting values
 1620 can be interpreted in a similar manner as shown in Table 3.3.

Table 3.3: Various categories of extreme rainfall events and drought based on SPI and SIs of soil moisture and TWS (see e.g., [McKee et al., 1993](#)).

| SPI/SI | Category |
|----------------|------------------|
| +2.0 and above | Extreme wet |
| +1.0 to +1.99 | Very wet |
| +0.99 to -0.99 | Normal |
| -1.0 to -1.99 | Moderate drought |
| -2.0 and below | Extreme drought |

1621 3.3.5 Error estimation

1622 Both weather and climate extremes such as heat waves, droughts, and heavy rainfall
 1623 events have wide consequences on the society and the ecosystem. The reliability of cli-
 1624 mate impact studies, especially resulting from precipitation extremes and its associated
 1625 impacts on water resources can be partly determined by our ability to quantify uncer-
 1626 tainties in various datasets used to represent the extremes. Modelled and SRS-based
 1627 products are often characterized by large uncertainties both spatially and temporally
 1628 as demonstrated in Chapter 2 using multi-source precipitation products. Uncertain-
 1629 ties can be quantified in a number of different ways: (i) comparing with more accurate
 1630 ground-based *in-situ* observations (see, Chapter 2), (ii) comparing output variables from
 1631 land-surface or hydrological models (e.g., evapotranspiration, runoffs) by using multi-
 1632 source precipitation and soil moisture data (see, e.g., [Xue et al., 2013](#), [Siddique-E-Akbor
 1633 et al., 2014](#)), and (iii) by estimating relative uncertainties based on multiple datasets of
 1634 the same variable (see, e.g., [Koot et al., 2006](#), [Awange et al., 2015](#)). The first approach

1635 is generally complicated by the lack of well-distributed ground-based observational net-
 1636 works. Observational networks of soil moisture stations are very scarce in the GBM
 1637 River Basin (see, [Robock et al., 2000](#)) while groundwater data from India (e.g., [Central Ground Water Board, 2014](#)), Bangladesh (e.g., [Shamsudduha et al., 2009a](#), [Shahid](#)
 1638 [et al., 2015](#)) and Nepal (e.g., [Gautam and Prajapati, 2014](#)) are not publicly available.
 1639

1640 In this study, a generalized three-cornered-hat (TCH) method ([Koot et al., 2006](#)) is
 1641 adopted to estimate relative uncertainties in each of the hydrological products of rainfall,
 1642 soil moisture, and TWS over the GBM River Basin. These uncertainty estimates are
 1643 then used as a basis for computing the ensemble mean of each of the variables over a
 1644 common time period for further analysis in this study. The motivation to use TCH for
 1645 error estimation stems from the fact that unlike conventional approaches, TCH does not
 1646 require true reference fields and can be estimated from at least three products of the
 1647 same variable (see, [Koot et al., 2006](#), [Awange et al., 2015](#)). This is particularly relevant
 1648 here because ground-based observations of soil moisture and TWS are almost negligible
 1649 to none existence over majority of the GBM River Basin. Even the gridded gauge-based
 1650 precipitation products also exhibit high levels of uncertainties (see, Chapter 2). The
 1651 generalized TCH method can be formulated as follows [Koot et al. \(2006\)](#) and [Awange](#)
 1652 [et al. \(2015\)](#):

1653 Consider a monthly time-series of three or more available products of the same vari-
 1654 able (e.g., soil moisture) stored as X_i where $i = 1, \dots, L$ available products (say $L=3$ for
 1655 the three GLDAS products). Each time-series can be expressed as a sum of true signal
 1656 (s) and the noise (ϵ_i) associated with the product:

$$X_i = S + \epsilon_i, \forall i = 1, \dots, L \quad (3.3)$$

1657 With the above definition, the TCH method relies on an important hypothesis that each
 1658 time-series contains a noise (ϵ) that precludes them from attaining the true estimate.
 1659 The information about the noises can be obtained by taking the differences between the
 1660 time-series of all the products (i.e., $L - 1$):

$$Y_{iR} \equiv X_i - X_r = \epsilon_i - \epsilon_N, \quad i = 1, \dots, L - 1 \quad (3.4)$$

1661 where X_r is the reference time-series. It is important to note that the results are inde-
 1662 pendent of the choice of one series or another (see e.g., [Koot et al., 2006](#), [Awange et al.,](#)
 1663 [2015](#)). The samples of the $L - 1$ differences derived from Eqn. 3.4 can be stored as a
 1664 matrix Y_L^N , where N is the length of the time-series (or number of months):

$M \times (N - 1)$ matrix as:

$$\mathbf{Y} = [\mathbf{y}_1 \quad \mathbf{y}_2 \quad \cdots \quad \mathbf{y}_{(N-1)}], \quad (3.5)$$

$$\mathbf{Y}_L^N = \begin{bmatrix} \mathbf{y}_1^1 & \mathbf{y}_2^1 & \cdots & \mathbf{y}_{L-1}^1 \\ \vdots & \vdots & \vdots & \vdots \\ \mathbf{y}_1^N & \mathbf{y}_2^N & \cdots & \mathbf{y}_{L-1}^N \end{bmatrix} \quad (3.6)$$

1665 The covariance of the above matrix of differences is then computed:

$$\mathbf{S} = \text{cov}(\mathbf{Y}), \quad (3.7)$$

1666 where $\text{cov}(\circ)$ is the covariance operator, and elements of \mathbf{S} ($s_{i,j}$) are either variance
1667 estimates for $i = j$ or covariance estimates for $i \neq j$. By introducing a $L \times N$ covariance
1668 matrix of the individual noises $\mathbf{R}_{ij} = \text{cov}(\epsilon_i, \epsilon_j)$, Eqn. 3.7 can be expressed as

$$\mathbf{S} = \mathbf{J} \cdot \mathbf{R} \cdot \mathbf{J}^T, \quad (3.8)$$

1669 where matrix \mathbf{J} is given by

$$\mathbf{J}_{(N-1)N} = \begin{bmatrix} 1 & 0 & \cdots & 0 & -1 \\ 0 & 1 & \cdots & 0 & -1 \\ \vdots & \vdots & \ddots & \vdots & \vdots \\ 0 & 0 & 0 & 1 & -1 \end{bmatrix}. \quad (3.9)$$

1670 Since there are only $N(N-1)/2$ equations for \mathbf{S} , Eqn.3.8 is undetermined. To get a
1671 unique solution an additional condition needs to be imposed, which is supplied partially
1672 by the condition of positive definiteness that holds for any normal covariance matrix.
1673 This condition of positive definiteness, which can be met if and only if $|\mathbf{R}| > 0$, reduces
1674 the number of unknowns to L (Galindo and Palacio, 2013, Koot et al., 2006). This condi-
1675 tion restricts the solution domain for the free parameters (r_{iL}, \dots, r_{LL} , $i = 1, \dots, L-1$),
1676 but is not sufficient to determine the solution. The free parameters should be chosen
1677 in such a way that the sum of the estimated correlations between all the time-series
1678 is minimal considering the constraint $|\mathbf{R}| > 0$. This generalized method allows for a
1679 good estimation of the variances of weakly correlated time-series but not their covari-
1680 ances. Using this method here to determine uncertainties in various datasets makes the
1681 assumption that correlations between the noises of different datasets are low.

1682 In the following, an example is shown to demonstrate that generalized TCH method
1683 is independent of the reference datasets. Even though the generalized TCH method
1684 was adapted for more than three datasets, the example below is shown for only three
1685 time-series (x_1, x_2, x_3) taken from three different soil moisture products (Fig. 3.4). Table
1686 3.4 shows the covariance matrices and the individual noise estimates for the three time-
1687 series. By considering x_1 as the reference (column 1 in Table 3.4), the diagonal of \mathbf{R} gives

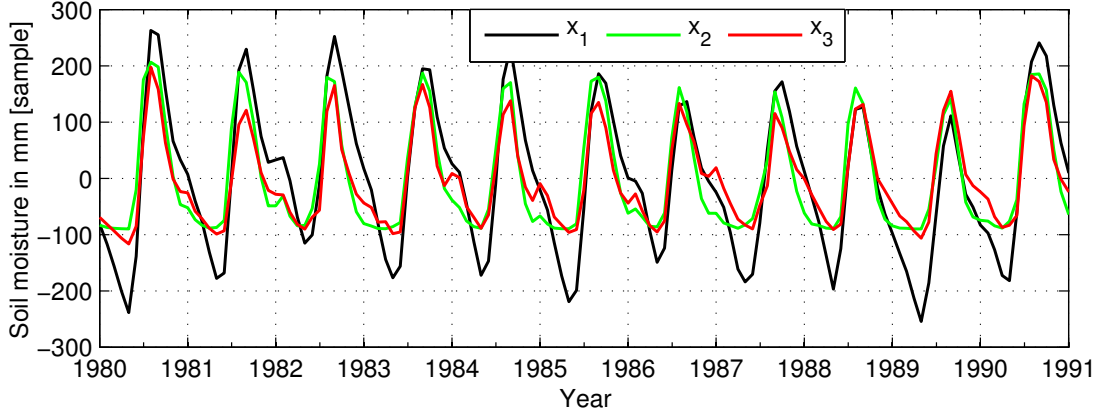


Figure 3.4: A sample time-series of 3 datasets x_1 , x_2 , and x_3 that are used to demonstrate the generalized TCH approach.

Table 3.4: Example of TCH algorithm.

| X_1 (“reference”) | x_2 (“reference”) | x_3 (“reference”) |
|--|--|--|
| $S = cov(x_2 - x_1, x_3 - x_1)$ | $S = cov(x_1 - x_2, x_3 - x_2)$ | $S = cov(x_1 - x_3, x_2 - x_3)$ |
| $S = \begin{bmatrix} 4854.1 & 3973.6 \\ 3973.6 & 4243.3 \end{bmatrix}$ | $S = \begin{bmatrix} 4854.1 & 880.5 \\ 880.5 & 1150.2 \end{bmatrix}$ | $S = \begin{bmatrix} 4243.3 & 269.7 \\ 269.7 & 1150.2 \end{bmatrix}$ |
| $R = \begin{bmatrix} 63.0 & 0 & 0 \\ 0 & 29.7 & 0 \\ 0 & 0 & 16.4 \end{bmatrix}$ | $R = \begin{bmatrix} 29.7 & 0 & 0 \\ 0 & 16.4 & 0 \\ 0 & 0 & 63.0 \end{bmatrix}$ | $R = \begin{bmatrix} 16.4 & 0 & 0 \\ 0 & 63.0 & 0 \\ 0 & 0 & 29.7 \end{bmatrix}$ |

1688 the variances of x_2 , x_3 , and x_1 along the diagonal. With x_2 as reference, the variances
 1689 given as x_1, x_3 , and x_2 , and similarly for x_3 as the reference, indicating that the choice
 1690 of the reference does not affect the final solution.

1691 However, the estimated uncertainties from Eqn. 3.8 are not adequate and can be rela-
 1692 tive to the total signal contained in the individual datasets. This leads to the estimation
 1693 of signal-to-noise ratio (SNR) to determine the overall magnitude of uncertainty. SNR
 1694 can be expressed as a ratio of total signal derived from the individual root-mean-squares
 1695 (RMS) to the estimated noise (σ) for the time period considered (t) (see, e.g., Awange
 1696 et al., 2015):

$$\text{SNR} = \frac{\text{RMS}(t)}{\sigma} \quad (3.10)$$

1697 Using several precipitation products from different sources, Awange et al. (2015)
 1698 showed that uncertainty estimates from generalized TCH method were found to be
 1699 generally consistent with those of the conventional methods. Finally, these SNR values
 1700 are used to create a single time-series ($X(t)$) for, especially soil moisture and GRACE-
 1701 derived TWS changes based on a inverse distance weighting approach, where SNR values
 1702 act as weights (w):

$$\bar{x}(t) = \frac{\sum_{i=1}^N w_i x_i}{\sum_{i=1}^N w_i}, \quad (3.11)$$

$$\text{where } \frac{w_i}{\sum w_i} = 1 \text{ and,}$$

$$i = 1, 2, 3, \dots, N.$$

1703 No error estimations are done for WGHM model as it is a stand alone product and
1704 it's soil moisture variations are found to be too small compared to other datasets.

1705 3.4 Results and Discussion

1706 3.4.1 Uncertainties in hydro-meteorological datasets

1707 In this section, the uncertainties of various datasets used in this study are investigated.
1708 The uncertainties in precipitation, soil moisture, and GRACE-derived TWS changes are
1709 estimated using the generalized TCH algorithm described in Section 3.3.5. For the pre-
1710 cipitation, the relative uncertainties between GPCCv7, CRU_TS3.22, and TMPAv7 are
1711 estimated for the common data period of 1998–2013. Figure 3.5 shows the relative error
1712 estimates and the resulting signal-to-noise ratio of the three precipitation products. It is
1713 seen that the magnitude of uncertainties are generally greater in the high rainfall areas
1714 such as the Himalayan Foothills and northeast India, whereas most of the Ganges River
1715 Basin exhibit substantially lower uncertainties (Fig. 3.5a–c). Among the three datasets
1716 evaluated here, CRU_TS3.22 appears to be highly uncertain over Nepal, Bhutan, east-
1717 ern Bangladesh, and the entire northeast India, indicating error magnitudes of up to
1718 60 mm year⁻¹ (Fig. 3.5c). The uncertainty estimates derived from spatially averaged
1719 precipitation in the two river basins are given in Table 3.5. The results are consistent
1720 with the spatial patterns shown in Fig. 3.5a–b, indicating that CRU_TS, which is devel-
1721 oped from far lesser gauges amounts to a higher uncertainty. This is further confirmed
1722 by the SNR plots in Fig. 3.5d–e. It is observed that GPCCv7 is better than TMPAv7,
1723 while CRU_TS3.22 exhibits the lowest SNR values. The similarity between GPCCv7
1724 and TMPAv7 reflects the dependency between the two products as GPCCv6 is being
1725 used to correct systematic biases in TRMMv7 precipitation estimates (Huffman et al.,
1726 2007, Huffman and Bolvin, 2013).

1727 The assessment of soil moisture datasets is more challenging given that soil moisture
1728 products strongly differ among the models used e.g., number of soil layers and the depth
1729 of the soil column. For instance, the CPC datasets are based on a single layer Leaky
1730 Bucket model with a depth of about 1 m, whereas ERA-Interim has 4 layers with a
1731 total depth of 2.55 m (see, Table 3.1). The GLDAS soil moisture datasets are generated
1732 over a soil depth of 2 m (e.g., Noah) and hence are likely to differ at various spatial
1733 and temporal scales. Among the four datasets, Noah exhibits the lowest uncertainties
1734 in the two river basins with a magnitude of 11.2 mm and 13.9 mm in the Ganges and

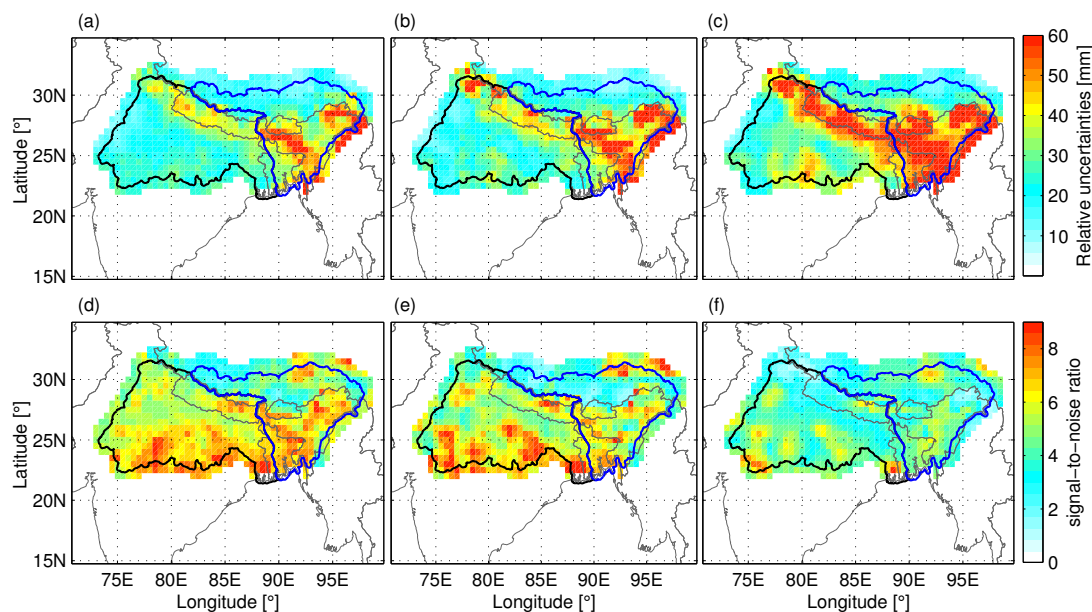


Figure 3.5: Relative uncertainties of (a) GPCCv7, (b) TMPAv7, and (c) CRU_TS3.22, and SNR values for (d) GPCCv7, (e) TMPAv7, and (f) CRU_TS3.22 estimated for the period 1998–2015.

Table 3.5: Uncertainties in precipitation (1998–2013), soil moisture (2002–2015), and GRACE TWS changes (2002–2015) in the two sub-basins of GBM River Basin estimated based on the generalized TCH method.

| | Precipitation [1998–2013] | | | |
|--------------------|---------------------------|-----------------|------------------|-----------|
| | GPCCv7 [mm] | CRU_TS3.22 [mm] | TMPAv7 [mm] | |
| Ganges | 9.7 | 16.4 | 10.7 | |
| Brahmaptura–Meghna | 8.6 | 13.3 | 8.6 | |
| | Soil Moisture [2002–2015] | | | |
| | CPC [mm] | MERRA [mm] | ERA-Interim [mm] | Noah [mm] |
| Ganges | 20.3 | 13.3 | 17.1 | 11.2 |
| Brahmaptura–Meghna | 13.0 | 20.7 | 24.3 | 13.9 |
| | GRACE TWS [2002–2015] | | | |
| | CSR [mm] | GFZ [mm] | JPL [mm] | |
| Ganges | 9.7 | 11.2 | 11.2 | |
| Brahmaptura–Meghna | 9.1 | 12.4 | 11.9 | |

1735 Brahmaputra–Meghna River Basin, respectively (Table 3.5). ERA-Interim shows higher
 1736 uncertainty than CPC and MERRA in both the river basins, while CPC and MERRA
 1737 tends to have a regional effect. Figure 3.6 shows the spatial distribution of SNR values
 1738 in the GBM River Basin. It is apparent that CPC has high SNR values over Bangladesh
 1739 and northeast India (to some extent) (Fig. 3.6a), whereas MERRA, ERA-Interim, and
 1740 Noah exhibits high SNR values in the Ganges River Basin (Fig. 3.6b–d). The SNR
 1741 values indicate that GLDAS is more robust in estimating soil moisture in the region.
 1742 Since there are substantial uncertainties in all the soil moisture products, all of them

1743 are used to analyze water storage changes in this study. As mentioned GLDAS is only
 1744 shown between 2002–2015.

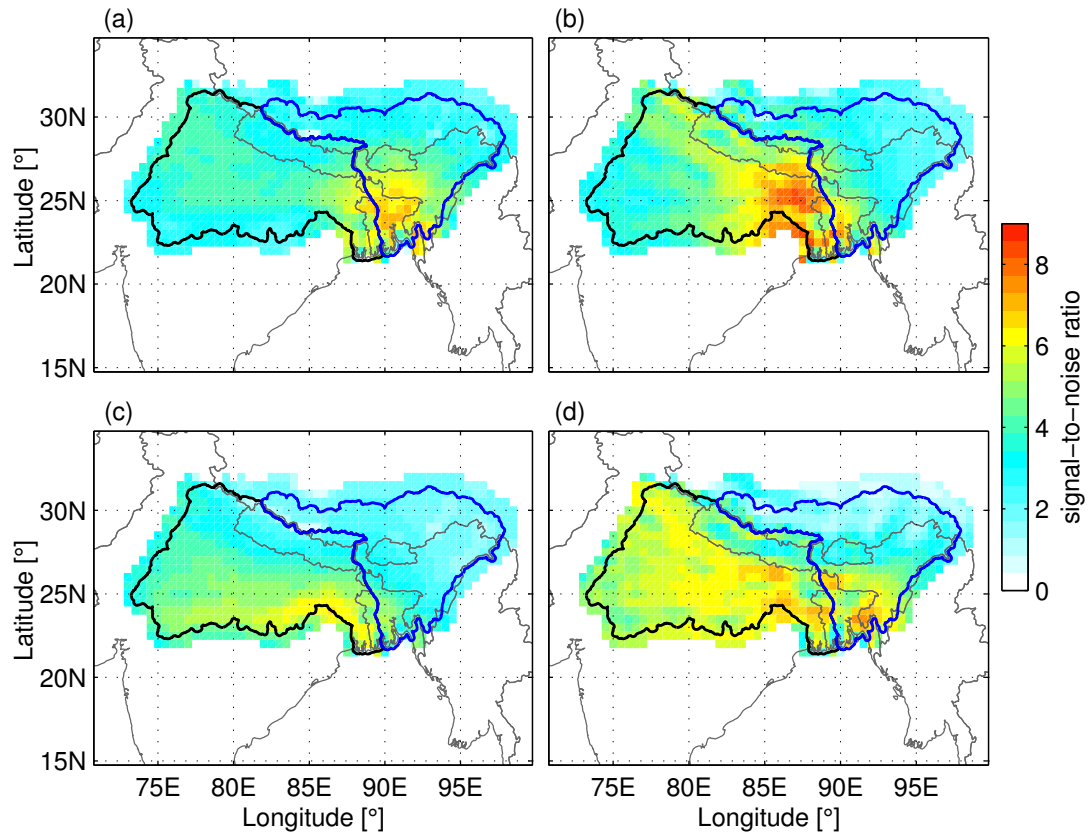


Figure 3.6: Spatial distribution of SNR values for (a) CPC, (b) MERRA, (c) ERA-Interim, and (d) Noah soil moisture datasets estimated for the period 2002–2015.

1745 Similarly, the GRACE TWS changes derived from three official centers are compared.
 1746 Overall, the CSR product shows the lowest uncertainties in the GBM River Basin with
 1747 an error magnitude of ~ 9.5 mm compared to GFZ and JPL products (Table 3.5). The
 1748 higher performance of CSR product is reflected in Fig. 3.6. While all three GRACE
 1749 products show high SNR values for the entire northeast India and Bangladesh, CSR ex-
 1750 hibits the largest SNR value in the region (Fig. 3.7a) suggesting that CSR may be better
 1751 suited for investigating water storage changes in the GBM River Basin. The GRACE
 1752 uncertainties of ~ 1 cm estimated in this study are consistent with those reported by
 1753 Chambers and Bonin (2012) over low- and mid-latitude oceans based on Release 05.
 1754 Based on these results, only GRACE TWS changes from CSR is considered for further
 1755 analysis.

1756 3.4.2 Observed changes in water storages

1757 The long-term (and decadal) changes in various components of the water storage in the
 1758 GBM River Basin are analyzed. In particular, the water storage components studied

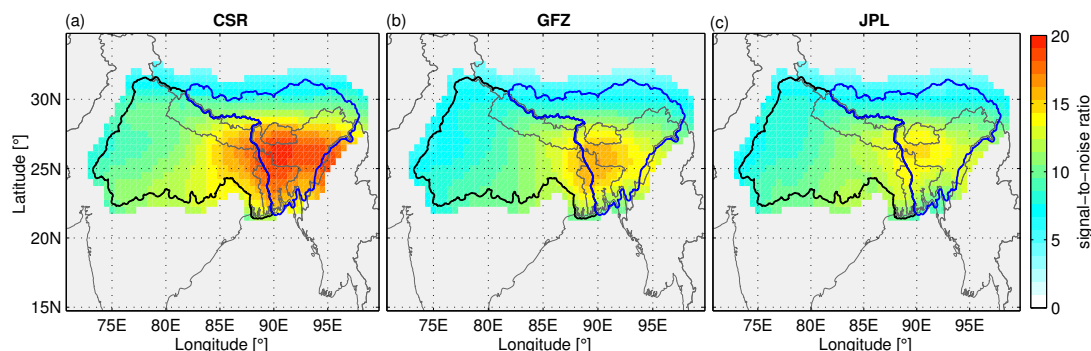


Figure 3.7: Spatial distribution of SNR values of TWS changes derived from (a) CSR, (b) GFZ, and (c) JPL for the period 2002–2015..

1759 here include soil moisture, surface water storage, and TWS. While no significant changes
 1760 in monsoon precipitation are observed between 1980 and 2013 (see, Chapter 2), there
 1761 have been pronounced decline in rainfall over high rainfall regions of northeast India,
 1762 Bhutan, Nepal, and Bangladesh in the Brahmaputra–Meghna River Basin. Figure 4.9
 1763 shows the spatially averaged monsoon (June–September, JJAS) precipitation anomaly
 1764 in the Ganges and Brahmaputra–Meghna River Basin between 1980–2013 based on
 1765 GPCCv7 and CRU_TS3.22. It is observed that even though there is a general decrease
 1766 in monsoon rainfall in both the river basins, the Ganges River Basin has recorded
 1767 substantially higher rainfall since 2010 (Fig. 4.9a), whereas the Brahmaputra–Megha
 1768 River Basin has remained relatively dry since 1988 (Fig. 4.9b). The precipitation decline
 1769 in the Brahmaputra–Meghna River Basin has however, become quite significant after
 1770 1998, indicating an average decline of about $15 \text{ mm decade}^{-1}$ based on GPCCv7. Note
 1771 that TMPAv7 has recorded an even higher rate of decline during the same period.

1772 Figure 3.9 shows the mean annual amplitudes and linear trends in three reanalysis-
 1773 based soil moisture datasets for the period 1980–2015. The spatial distribution of mean
 1774 annual amplitudes of three soil moisture datasets reveal maximum variation in the low
 1775 altitude areas, especially in the southern Ganges River Basin and its variation decreases
 1776 rapidly towards the north with less than 60 mm year^{-1} (Fig. 3.9a–c). Although the spa-
 1777 tial patterns are very similar across all three datasets, ERA-Interim exhibits the largest
 1778 mean annual amplitude and CPC shows the smallest variation. All three soil moisture
 1779 products show a positive trend between 1980 and 2015, suggesting that there may be an
 1780 overall increase in soil moisture in the GBM River Basin (Fig. 3.9d–f). CPC exhibits the
 1781 highest rate of increase ($35 \text{ mm decade}^{-1}$), especially in Bangladesh, northeast India,
 1782 and along the Himalayan Foothills (Fig. 3.9d), whereas the trend magnitudes are much
 1783 smaller in MERRA and ERA-Interim (Fig. 3.9e–f). However, given the level of uncer-
 1784 tainty involved in land surface modelling in the reanalysis systems, the trend results
 1785 may be spurious, as they are not consistent with overall decrease in precipitation, as
 1786 well as the recent increase in soil moisture droughts in the Ganges River Basin (Mishra
 1787 et al., 2014). It should be mentioned here that trend estimates in the Ganges River
 1788 Basin could be affected by a recent anomalous increase in rainfall (see, Fig. 4.9a).

1789 The changes in precipitation and soil moisture are further investigated for the period
 1790 2002–2015 coinciding with the GRACE mission. Figure 3.10 shows the linear trends

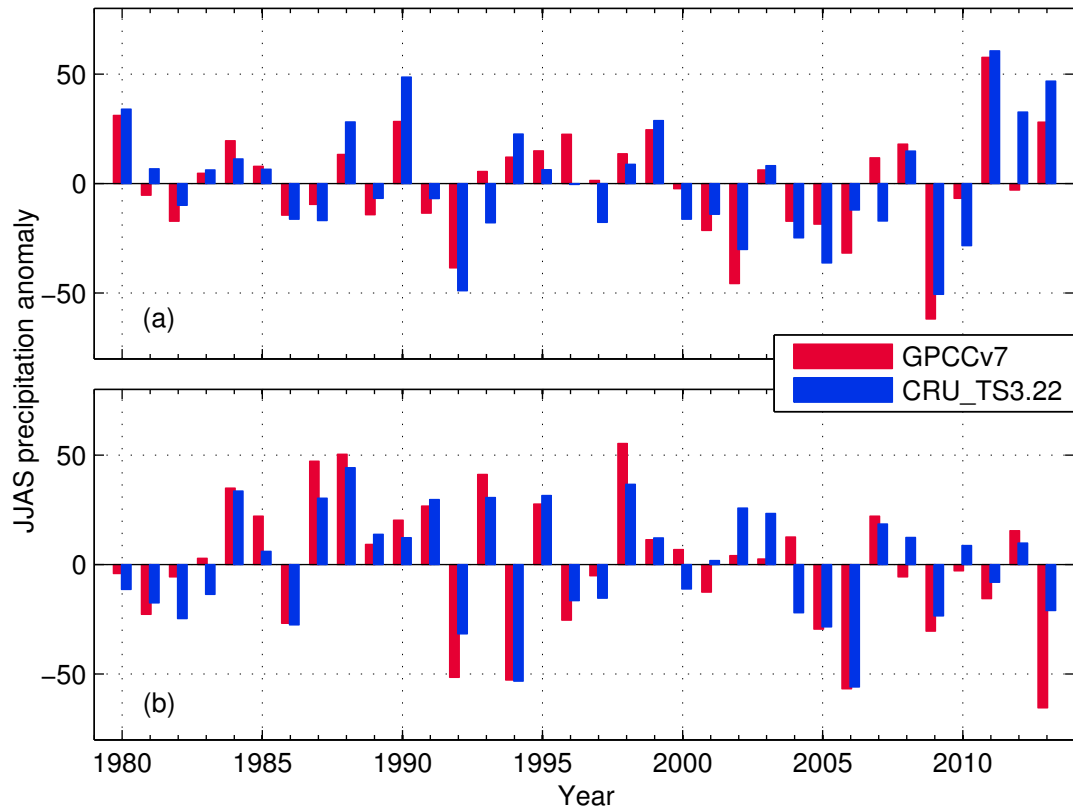


Figure 3.8: JJAS precipitation variations in the (a) Ganges and (b) Brahmaputra–Meghna River Basin between 1980 and 2013 based on GPCCv7 and CRU_TS3.22 datasets.

1791 in TMPAv7 precipitation estimates, reanalysis- and Noah-based soil moisture datasets,
 1792 and GRACE-derived TWS changes. As mentioned before and in Chapter 2, precipi-
 1793 tation changes have largely been opposite in the two river basins with increasing (de-
 1794 creasing) trend in the Ganges (Brahmaputra–Meghna) River Basins (Fig. 3.10a). It
 1795 is seen from Fig. 3.11a–b that precipitation is increasing and decreasing at a rate of
 1796 $8.0 \text{ km}^3 \text{ decade}^{-1}$ (2002–2014) and $8.3 \text{ km}^3 \text{ decade}^{-1}$ (2002–2015) in the Ganges and
 1797 Brahmaputra–Meghna River Basin, respectively. Additionally, there appears to be an
 1798 increase in precipitation variability in the Ganges River Basin, especially in the last 5
 1799 years (Fig. 3.11a). For the same period, the soil moisture has increased substantially
 1800 based on the average of three reanalysis products (Fig. 3.10b) in the Ganges River Basin,
 1801 which are consistent with the increasing precipitation rates. The trends are much smaller
 1802 for Noah but still indicates a wetting trend in the Ganges River Basin (Fig. 3.10c). Thus,
 1803 the increase in soil moisture may be attributed to an increase in rainfall, although other
 1804 factors may play a crucial role for the increase (e.g., decrease in evapotranspiration).
 1805 The overall increasing trends are estimated at $\sim 23 \text{ km year}^{-1}$ and $\sim 8.0 \text{ km year}^{-1}$ in
 1806 the Ganges and Brahmaputra–Meghna River Basin, respectively (Fig. 3.11c–d).

1807 On the other hand, the GRACE-derived TWS exhibits a drastic decline in water
 1808 storage over majority of the GBM River Basin, indicating decreasing rates of up to
 1809 $30\text{--}40 \text{ mm year}^{-1}$ in the Indian states of Haryana, Uttar Pradesh and Assam (Fig.

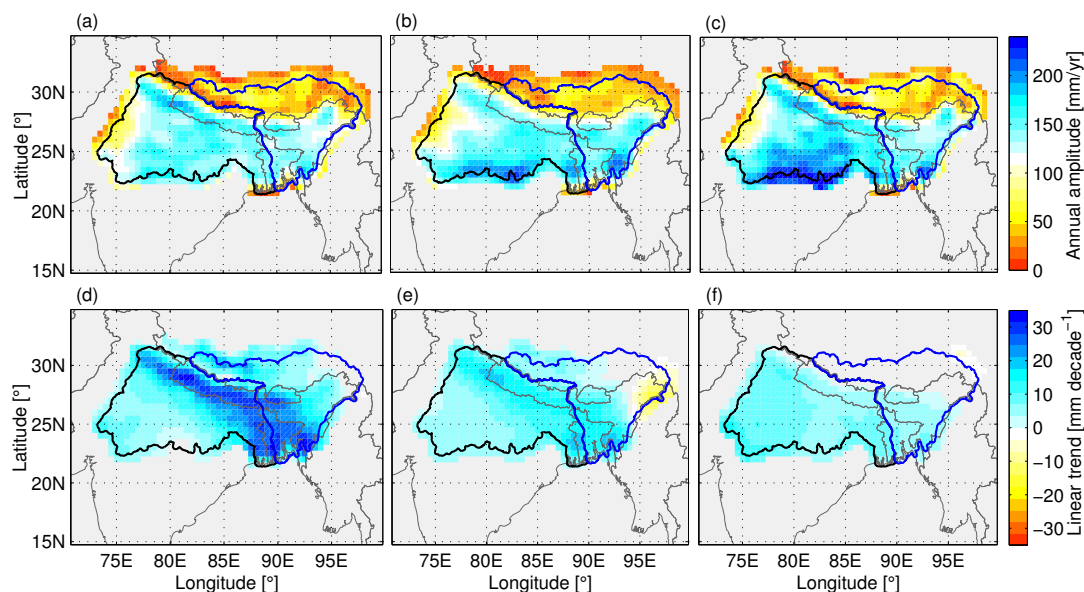


Figure 3.9: Mean annual amplitudes and linear trends in soil moisture obtained from (a & d) CPC, (b & e) MERRA, and (c & f) ERA-Interim estimated for the period 1980–2015. Only values that are significant at 95% confidence level are shown. Updated from [Khandu et al. \(2016a\)](#).

1810 3.10d). This alarming decline in water storage has been reported in a number of studies
 1811 ([Rodell et al., 2009](#), [Tiwari et al., 2009](#), [Chen et al., 2014a](#), [Khandu et al., 2016a](#), [Long](#)
 1812 [et al., 2016](#)) and has been largely attributed to excessive groundwater withdrawals,
 1813 particularly in those northern states of Haryana and Uttar Pradesh (see, [Fig. 3.1](#)). The
 1814 rapid deterioration of TWS in the Indian state of Assam do not relate to the percentage
 1815 of water use nor area equipped for irrigation. This trend has been barely reported (e.g.,
 1816 [Khandu et al., 2016a](#)). Based on the GRACE datasets for the period August 2002 to
 1817 September 2015 ([Fig. 3.11e–f](#)), Ganges and Brahmaputra–Meghna River Basins exhibit
 1818 a declining trend of $9.1 \text{ km}^3 \text{ year}^{-1}$ and $10.5 \text{ km}^3 \text{ year}^{-1}$, respectively. The Ganges
 1819 River Basin has gained a significant amount of water mass since the last major drought
 1820 event in 2009/2010, showing a gain of $\sim 8.0 \text{ km}^3 \text{ year}^{-1}$ from its initial declining rate of
 1821 almost $\sim 20 \text{ km}^3 \text{ year}^{-1}$ from 2003–2009 ([Fig. 3.11e](#)). The gain in TWS in the Ganges
 1822 River Basin can be attributed to the recent jump in precipitation, potentially as a result
 1823 of two or three moderate to major La Niña events. The increasing trend in TWS in the
 1824 southern GBM River Basin ([Fig. 3.10d](#)) clearly reflects the higher rate of increase in
 1825 precipitation in the same region ([Fig. 3.10a](#)).

1826 The trend results also indicate a rapid decline in TWS in the Brahmaputra–Meghna
 1827 River Basin, with a decreasing rate of $10\text{--}30 \text{ mm year}^{-1}$, especially over Bangladesh and
 1828 northeastern India. Unlike the Ganges River Basin, the TWS continued to decline after a
 1829 brief jump in 2011 ([Fig. 3.11f](#)), with an overall declining rate of $10.5 \text{ km}^3 \text{ year}^{-1}$ between
 1830 2002 and 2015 (145 months). Although there are some spatial inconsistencies between
 1831 precipitation and TWS decline in the region, it is evident that the driving precipitation
 1832 played a crucial role in the TWS decline. Considering that groundwater is the single

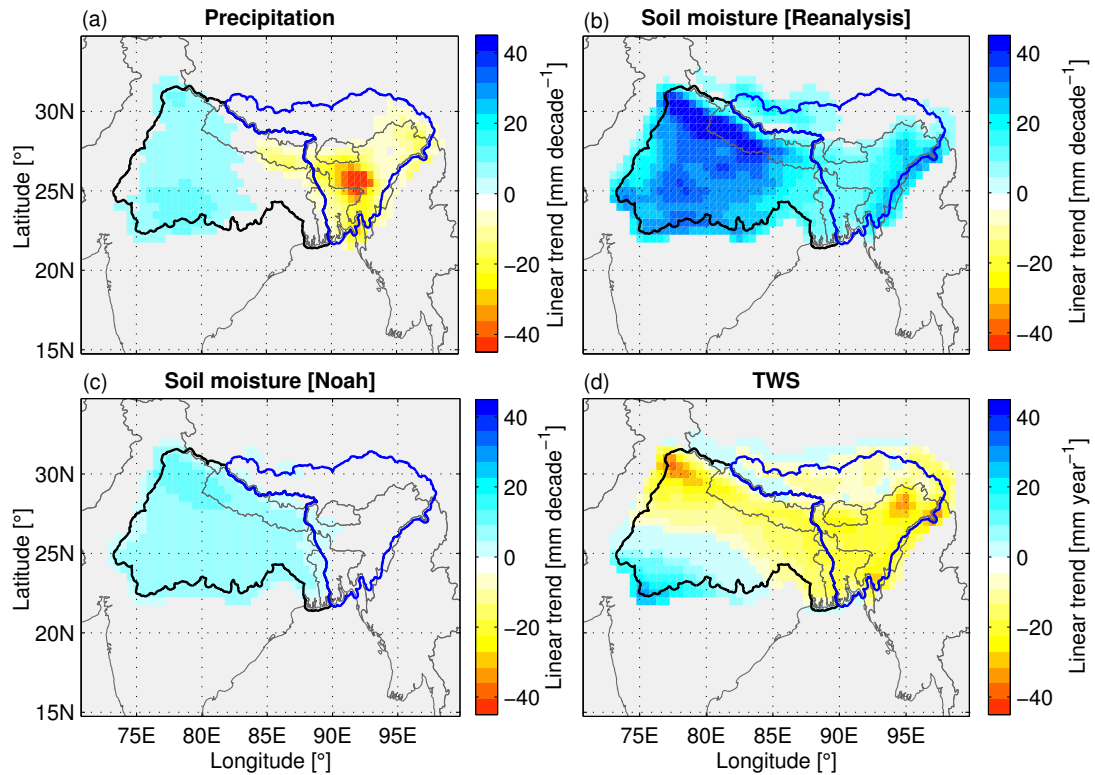


Figure 3.10: Linear trends in: (a) precipitation [TMPAv7], (b) soil moisture [reanalysis], (c) soil moisture [Noah], and (d) TWS [GRACE] estimated for the period 2002–2015. Values that are not significant at 95% confidence interval are not shown. Modified from [Khandu et al. \(2016a\)](#).

1833 largest component of the TWS, excessive groundwater abstraction further diminishes
 1834 water resources in the region. Groundwater depletion has been reported across most
 1835 parts of Bangladesh by [Döll et al. \(2014\)](#) using simulated groundwater changes from
 1836 WGHM. Observational-based studies based on data compiled from *in-situ* bore holes
 1837 confirm that groundwater exploitation has reached critical levels across several districts
 1838 of northwestern Bangladesh (e.g., [Shamsudduha et al., 2009b](#), [Shahid et al., 2015](#)). Apart
 1839 from groundwater and soil moisture, [Papa et al. \(2015\)](#) reported that SWS contributes
 1840 up to 45% to TWS and thus, plays an important role the basin's freshwater resources.
 1841 Previous studies have indicated that SWS appears to be declining at a significant rate
 1842 in the Brahmaputra–Meghna River Basin, whereas it has been found to be increasing
 1843 in the Ganges River Basin, especially between 2002 and 2009 (e.g., [Papa et al., 2015](#),
 1844 [Khandu et al., 2016a](#)).

1845 3.4.3 Impact of hydro-meteorological extremes

1846 Although water resources in the GBM River Basin are under enormous pressure from
 1847 increasing population and associated growing socio-economic needs, assessment of hy-
 1848 drological shifts over short time-scales could be subject to natural variability resulting

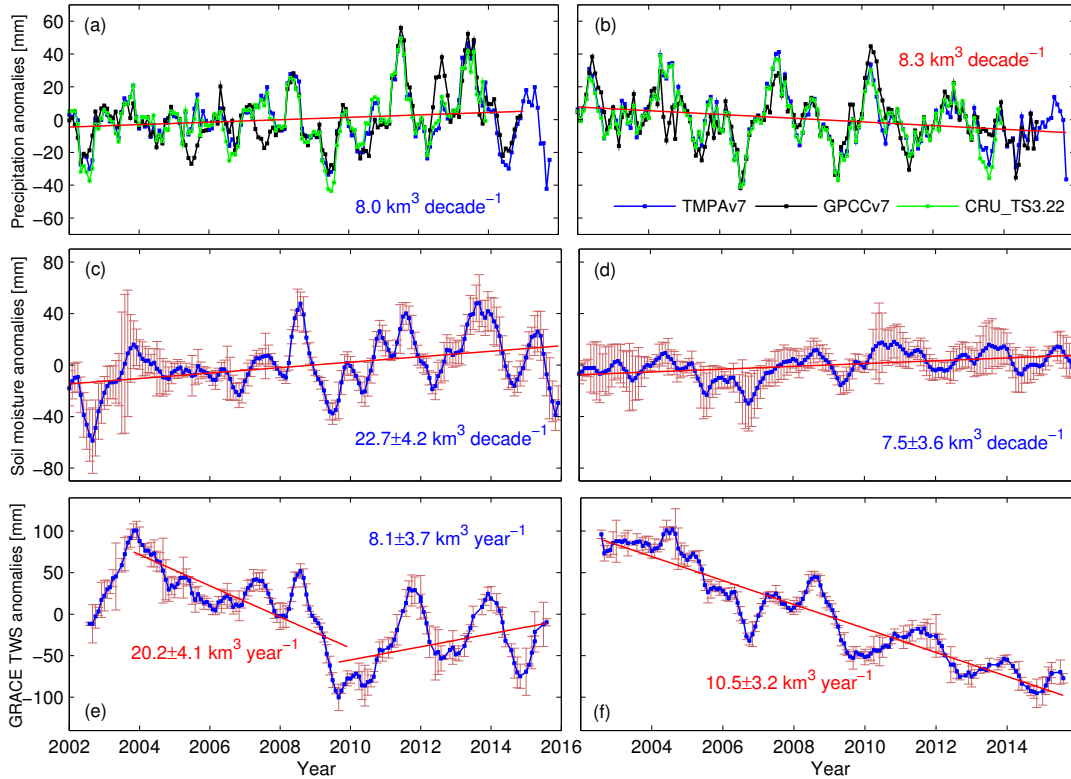


Figure 3.11: (a–b) Precipitation anomalies derived from GPCCv7, CRU_TS3.22, and TMPAv7, (c–d) soil moisture anomalies plotted as a weighted average of four datasets, and (e–f) GRACE TWS anomalies plotted as a weighted average of data from three sources (CSR, GFZ, and JPL) for the Ganges and Brahmaputra–Meghna River Basins, respectively. The trend lines are indicated by red lines and their values are shown.

1849 from large-scale climate variations such as ENSO and IOD on interannual time-scales
 1850 and Pacific Decadal Oscillation (PDO) on decadal time-scales. Individual components
 1851 of TWS, e.g., soil moisture and SWS, can be significantly impacted by changing rain-
 1852 fall pattern in association with the changing phase of, for example, ENSO. Similarly,
 1853 prolonged droughts may pose additional pressure on the groundwater availability.

1854 This section examines the possible influences of climate variability (especially meteo-
 1855 rological droughts) on TWS (as well as soil moisture) in the GBM River Basin. To get an
 1856 understanding how precipitation effects TWS, the cumulative sums of precipitation, soil
 1857 moisture, and TWS anomalies (linear trend and annual signal removed) are shown for
 1858 the two river basins between 2002 and 2015 in Fig. 3.12. It is observed that precipitation
 1859 and soil moisture increased slightly from 2004 to 2008 but has drastically declined (by
 1860 about 400 mm) from 2009 to 2010 in the Ganges River Basin (Fig. 3.12a). It has then
 1861 increased substantially until 2014. The close association between precipitation and soil
 1862 moisture variability suggests that soil moisture is primarily driven by precipitation. Al-
 1863 though the two are closely related, there are substantial differences in the Brahmaputra–
 1864 Meghna River Basin (Fig. 3.12b). The largest decline in the Brahmaputra–Meghna River
 1865 Basin has occurred between 2005 and 2006.

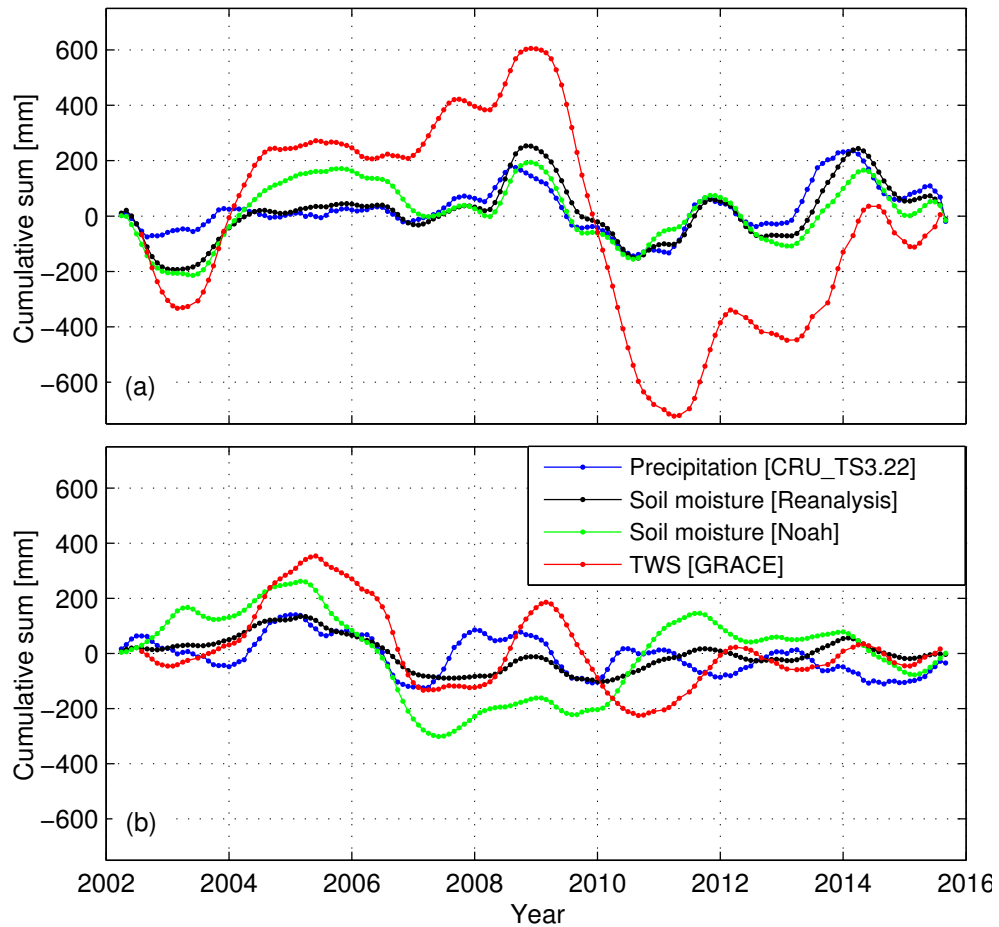


Figure 3.12: Cumulative sums of precipitation, soil moisture, and GRACE-derived TWS changes in (a) Ganges, and (b) Brahmaputra River Basins. Updated from [Khandu et al. \(2016a\)](#).

1866 The effect of precipitation can be clearly observed in the GRACE-derived TWS
 1867 changes in both river basins, but more so in the Ganges River Basin. The temporal
 1868 patterns of TWS closely resembles the driving precipitation but are amplified during
 1869 anomalous changes in precipitation. For example, TWS declined by about 1200 mm
 1870 from 2009 to 2011 (in ~ 29 months) and increased by almost 650 mm from 2011 to
 1871 2014 in the Ganges River Basin (Fig. 3.12a). Similarly, TWS declined by about 600 mm
 1872 from 2005 to 2006 in the Brahmaputra–Meghna River Basin following a drastic decline
 1873 in rainfall (Fig. 3.12b). Thus, Fig. 3.12 demonstrates the dependency between driving
 1874 precipitation and TWS (and soil moisture) indicating that Ganges River Basin may be
 1875 more vulnerable to abrupt changes in precipitation due to an overall larger effect from
 1876 human water abstraction. Both the major declines have occurred during the positive
 1877 ENSO phase (i.e., El Niño) but had a varying effect on the two river basins. For example,
 1878 the moderate El Niño of 2005/2006 has mainly affected the Brahmaputra–Meghna River
 1879 Basin, whereas the major El Niño of 2009/2010 had lasting effects on the Ganges River
 1880 Basin. It should be mentioned here that the 2005/2006 El Niño was accompanied by a

1881 strong positive IOD event, which is found to have a negative effect on precipitation in
 1882 the high rainfall regions of Brahmaputra–Meghna River Basin (see, Fig. 2.12).

1883 To further examine the effects of precipitation variability on TWS, the respective
 1884 indices are computed. It is observed that the 12 month SPI derived from monthly
 1885 precipitation closely relates to 6 month SPI estimated from soil moisture products.
 1886 Figure 3.13 shows the SPI derived from precipitation and soil moisture, and SI esti-
 1887 mated from GRACE-derived TWS changes for the two river basins. Both river basins
 1888 experienced several meteorological droughts between 1980 and 2015. For instance, the
 1889 Ganges River Basin has experienced four severe to extreme (SPI < -1.5) meteorologi-
 1890 cal droughts (1991–1994, 2001–2003, 2005–2007, and 2009–2010, Fig. 3.13a), while the
 1891 Brahmaputra–Meghna River Basin experienced six major droughts (1981–1983, 1986,
 1892 1992–1994, 1999, 2005–2006, and 2009–2010, Fig. 3.13a) for the same period. Soil mois-
 1893 ture droughts have mainly occurred as a result of meteorological droughts. Similarly,
 1894 the observed variations in GRACE-derived TWS changes clearly reflect the precipita-
 1895 tion changes. The last two major precipitation increases from 2011 to 2014 has lead
 1896 to a significant recovery of TWS in the Ganges River Basin but the relation between
 1897 precipitation and TWS seem to have declined in the Brahmaputra–Meghna River Basin
 1898 during the same period.

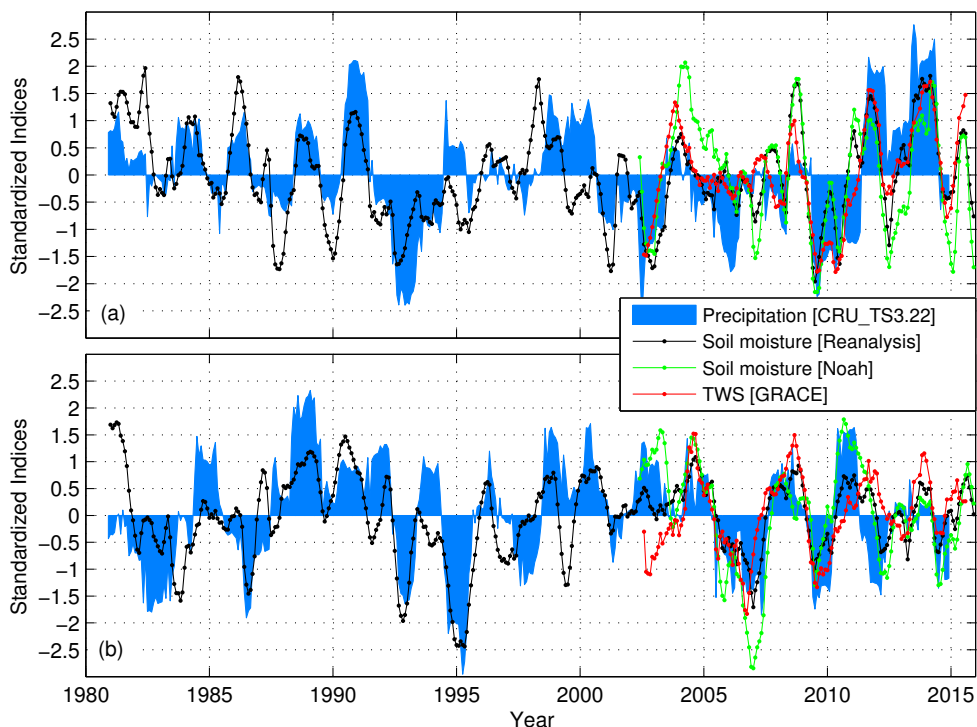


Figure 3.13: SPI of precipitation (at 12 month time-scale) and soil moisture (at 6 month time-scale), and SI of TWS for the (a) Ganges and (b) Brahmaputra River Basins. These indices are derived for the respective data periods. Updated from [Khandu et al. \(2016a\)](#).

1899 Fig. 3.14 shows the spatial patterns of correlation coefficients between the various
 1900 hydrological datasets calculated from their respective indices (linear trend removed) for

1901 the common data period of 2002 to 2015. The correlation values computed for the two
 1902 river basins are provided in Table 3.6. It is observed that both soil moisture and TWS
 1903 responds strongly to precipitation across majority of the Ganges River Basin, indicating
 1904 correlation values of more than 0.6 (Fig. 3.14a–c). Parts of northeast India and northern
 1905 Brahmaputra River Basin also show significant correlation with precipitation. However,
 1906 major parts of the Brahmaputra–Meghna River Basin (Bangladesh, Bhutan, northeast
 1907 India) exhibit a rather weak response to precipitation variability. In particular, GRACE-
 1908 derived TWS changes show very low correlation values (of less than 0.4) indicating that
 1909 there may be other factors affecting TWS variations in these areas. As indicated in
 1910 Table 3.6, the reanalysis-based soil moisture datasets are more (~ 0.74) related to
 1911 precipitation than those generated by the Noah land surface model (~ 0.70), whereas
 1912 GRACE-derived TWS changes indicate a correlation coefficient of 0.77 and 0.50 in the
 1913 Ganges and Brahmaputra–Meghna River Basin, respectively.

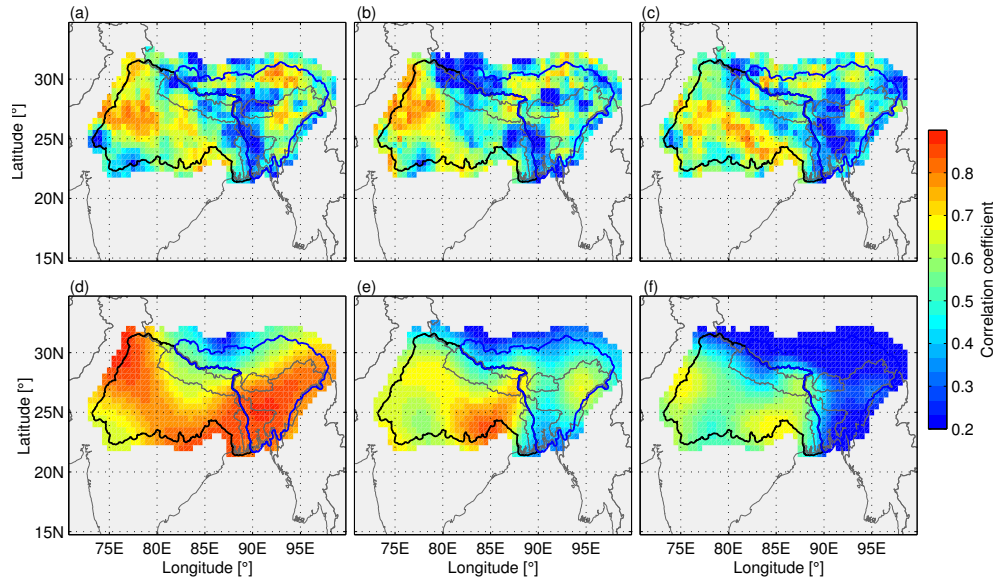


Figure 3.14: Spatial distribution of correlation coefficients between (a) precipitation and reanalysis-based soil moisture, (b) precipitation and Noah-based soil moisture, (c) precipitation and GRACE-derived TWS, (d) soil moisture datasets of reanalysis and Noah, (e) reanalysis-based soil moisture and GRACE-derived TWS, and (f) Noah-based soil moisture and GRACE-derived TWS, estimated for the common data period of 2002 to 2015.

1914 Both reanalysis- and Noah-based soil moisture products are highly correlated over
 1915 majority of the GBM River Basin with correlation coefficients of 0.8 (Table 3.6), except
 1916 for a few grid cells in the northern Brahmaputra–Meghna River Basin (Fig. 3.14d).
 1917 It is also observed that reanalysis-based soil moisture datasets are more correlated to
 1918 GRACE-derived TWS changes than Noah-based soil moisture data (Fig. 3.14e–f). The
 1919 correlations coefficients are significantly higher in the Ganges River Basin compared to
 1920 those estimated in the Brahmaputra–Meghna River Basin, indicating a correlation of
 1921 0.41 between Noah-based soil moisture and GRACE-derived TWS changes (Table 3.6).

1922 Figure 3.15 compares the frequency of meteorological and hydrological (i.e., soil mois-
 1923 ture from the average of three reanalysis products) droughts that lasted for at least three

Table 3.6: Correlation coefficients and time lags between SPI (6-month) and SI of soil moisture and TWS in the GBM River Basin for the period 2002–2015.

| | Ganges | Brahmputura–Meghna |
|---|--------|--------------------|
| Precipitation/Soil moisture [Reanalysis] | 0.75 | 0.73 |
| Precipitation/Soil moisture [Noah] | 0.68 | 0.69 |
| Soil moisture [Reanalysis]/Soil moisture [Noah] | 0.80 | 0.83 |
| Precipitation/TWS [GRACE] | 0.77 | 0.50 |
| Soil moisture [Reanalysis]/TWS [GRACE] | 0.80 | 0.70 |
| Soil moisture [Noah]/TWS [GRACE] | 0.66 | 0.41 |

1924 months (with SPI/SI below -0.9) between 1980 and 2014. According to [McKee et al.](#)
 1925 (1993), drought begins when the SPI falls below zero and ends with positive value follow-
 1926 ing a value of -1.0 or less but a threshold on -0.9 (corresponding a cumulative probability
 1927 of 0.18) is chosen here to avoid false alarm of droughts. It is seen in Fig. 3.15a that max-
 1928 imum droughts (up to 10 or 11) have occurred in the northern Ganges River Basin and
 1929 majority of the Ganges and Brahmaputra–Meghna River Basins (especially northeast
 1930 India) have also experienced more than six droughts during the past three decades. The
 1931 number of soil moisture droughts clearly reflect meteorological droughts in the Ganges
 1932 River Basin and the far northeast India (Fig. 3.15b). However, Bangladesh is found to
 1933 be quite resilient to soil moisture droughts, which has recorded at the most six droughts
 1934 for the entire period.

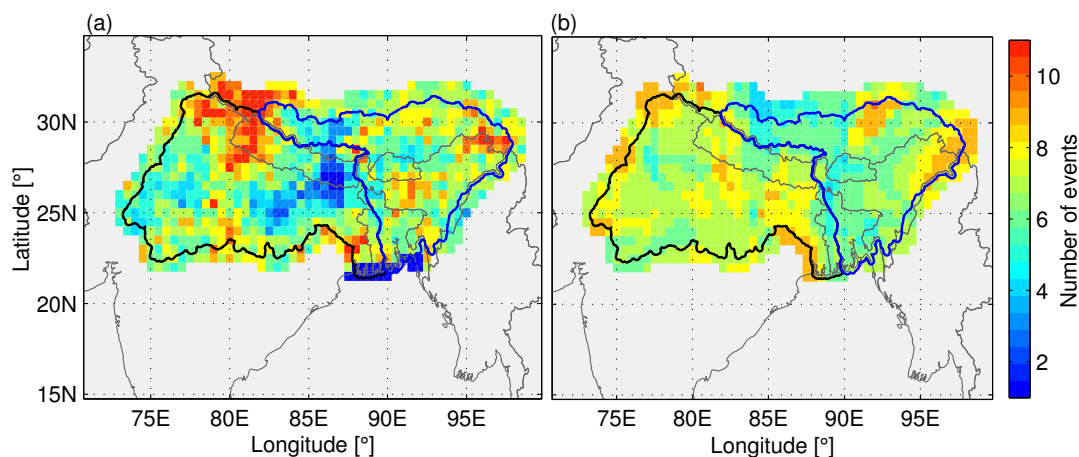


Figure 3.15: Number of drought events calculated from (a) precipitation (12 month time-scale SPI) and (b) soil reanalysis-based soil moisture (6 month time-scale SPI) between 1980–2014.

1935 The duration and intensity of the 2009/2010 major drought is shown in Fig. 3.16
 1936 and 3.17, respectively. This major drought mainly affected the Ganges River Basin and
 1937 in particular, the meteorological droughts in the southern parts of the basin lasted
 1938 for nearly 20 months between 2009 and 2011 (Fig. 3.16a). Other parts of the Ganges
 1939 River Basin and northeast India exhibit at least 10 to 15 months of drought. The soil
 1940 moisture products resemble the driving precipitation but their magnitudes are much
 1941 lower except for the southern Ganges River Basin (Fig. 3.16b–c). Both reanalysis and
 1942 Noah products show less than 4 months of drought in the Brahmaputra–Meghna River

1943 Basin, whereas the GRACE-derived TWS resembles the precipitation affects in both the
 1944 river basins (Fig. 3.16d). This can be clearly observed from their maximum intensity
 1945 (Fig. 3.17), in which TWS responds strongly to the driving precipitation (Fig. 3.17a
 1946 and d). Noah-based soil moisture appears to relate better to precipitation (Fig. 3.17)
 1947 than the reanalysis-based products (Fig. 3.17b).

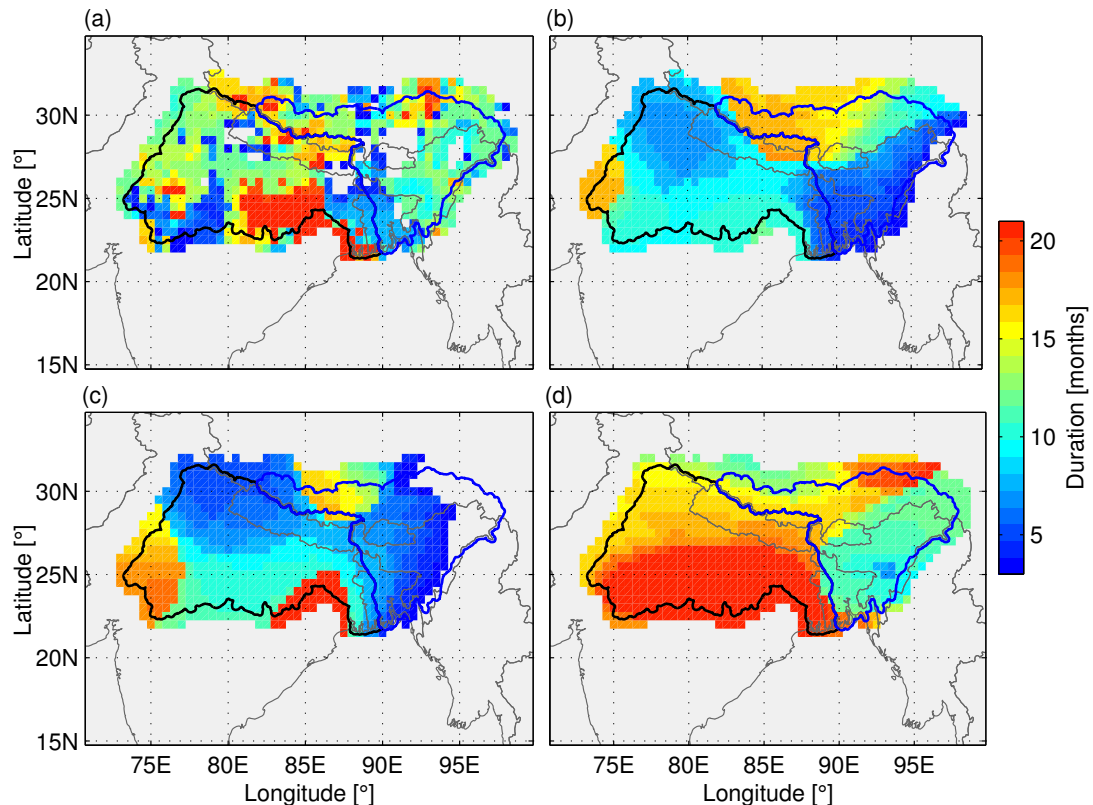


Figure 3.16: Duration of the 2009/2010 drought event calculated from (a) precipitation, (b) reanalysis-based soil moisture, (c) Noah-based soil moisture, and (d) GRACE-derived TWS changes. The duration of drought is calculated by counting the number of months when SPI continuously remain below -0.9 between January 2009 and December 2010.

1948 The year-to-year variations in precipitation are often influenced by large-scale climate
 1949 variations such as ENSO and IOD. The impact of ENSO/IOD on rainfall variability has
 1950 already been discussed in detail in Chapter 2. For example, El Niño or the warm phase
 1951 of ENSO events are generally associated with dry periods over most the GBM River
 1952 Basin, while La Niña or the cold phase of ENSO generally bring more rain, and has
 1953 specifically lead to a rapid jump in precipitation in the Ganges River Basin in the past
 1954 4–5 years, leading to a swift recovery in TWS. On the other hand, positive IOD events
 1955 have been found to decrease rainfall over Bangladesh and northeast India, which has
 1956 been the case in the recent years due to increase in sea surface temperatures (SST) in
 1957 the western equatorial Indian Ocean. The ENSO and IOD effects on precipitation is
 1958 shown to clearly translate to soil moisture and TWS variations in the two river basins.
 1959 The recent droughts of 2005/2006 and 2009/2009 reflect their effects on TWS, although
 1960 it must be mentioned that ENSO/IOD may not necessarily lead to drastic changes in

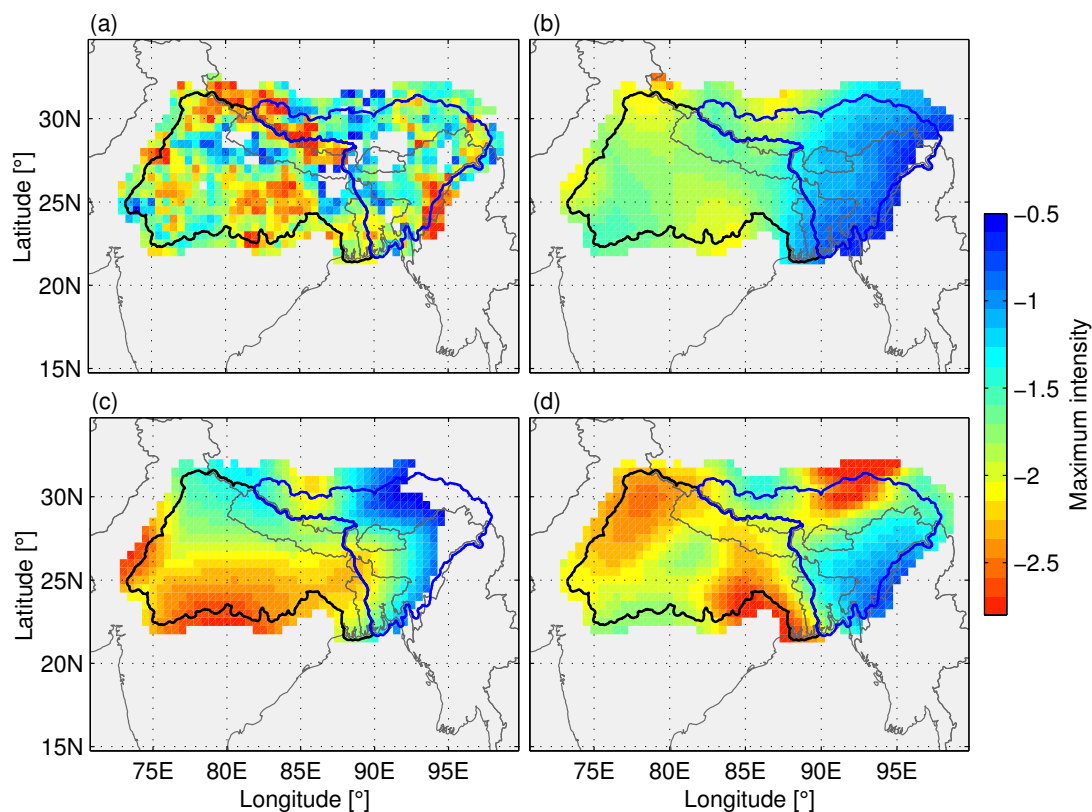


Figure 3.17: Maximum drought intensity of the 2009/2010 drought event calculated from (a) precipitation, (b) reanalysis-based soil moisture, (c) Noah-based soil moisture, and (d) GRACE-derived TWS changes.

1961 precipitation or TWS (e.g., 1998). ENSO/IOD variations are by themselves affected
 1962 by decadal ocean-atmospheric oscillations such PDO (e.g. Meehl et al., 2006, Krishna-
 1963 murthy and Krishnamurthy, 2014) and tend to produce varying affects depending on
 1964 the phase of decadal oscillations.

1965 3.4.4 Impacts of human water abstraction

1966 The results presented in Sections 3.4.2 and 3.4.3 represents the overall water storage
 1967 changes based on existing observations or modelling approaches that include both nat-
 1968 ural variability and anthropogenic influences (including human water use). Although it
 1969 may be difficult to objectively disaggregate the influences of climate variability/change
 1970 and human water abstraction, WGHM provides a reasonable approach to separate their
 1971 influences on global/regional water storage changes (Döll et al., 2003, 2014, Müller
 1972 Schmied et al., 2014). Therefore, to assess the effects of human water abstraction (or
 1973 withdrawal) on TWS in the GBM River Basin, TWS data from two WGHM model
 1974 variants are analysed here. By subtracting IRR70_S TWS (representing both natural
 1975 and human water use) from NOUSE TWS (representing the natural variability), the

1976 resulting variations include only those influenced by the human water abstraction. The
 1977 remaining section is directly adapted from [Khandu et al. \(2016a\)](#).

1978 Figure 3.18 shows the root-mean-square (RMS) of (IRR70_S - NOUSE) TWS
 1979 changes, representing the average magnitude of total water withdrawals during the
 1980 simulation period of 1979–2009. Based on the simulation, it is clear that human wa-
 1981 ter withdrawal is highly significant across the western Ganges River Basin including
 1982 the upstream of Ganges River and across northwestern Bangladesh. The RMS values
 1983 exceed more than 0.3 m in these regions and are found to be very high (more than 1 m)
 1984 where GRACE-derived TWS changes indicated widespread decline in TWS (see, Fig
 1985 3.10d). Groundwater depletion is the single largest factor determining water availability
 1986 in these regions ([Rodell et al., 2009](#), [Tiwari et al., 2009](#), [Shamsudduha et al., 2009a](#),
 1987 [Central Ground Water Board, 2014](#), [Shahid et al., 2015](#)), and its contribution to TWS
 1988 and rapid declining rates mainly reflect the TWS abstraction. The simulation results
 1989 are consistent with those released by the Indian government on the use of groundwater
 1990 resources (e.g., [Central Ground Water Board, 2014](#)) and the TWS trends shown in Fig.
 1991 3.10d and 3.11e–f.

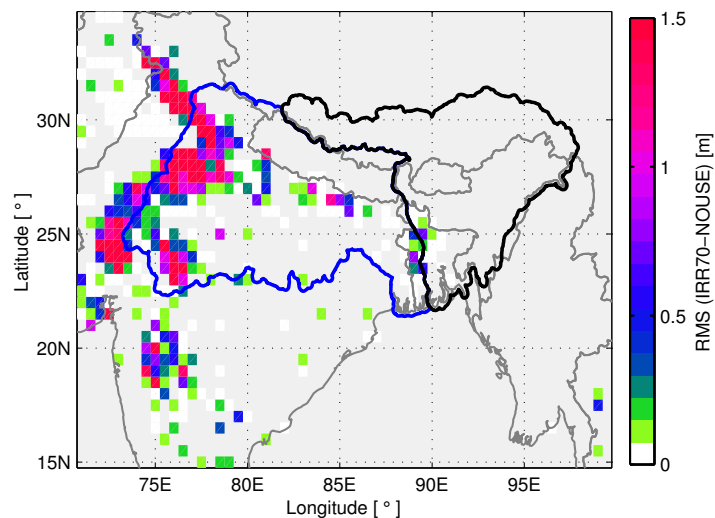


Figure 3.18: RMS of difference between natural TWS (“NOUSE” and those under the influence of human water abstraction (IRR70_S) indicating the level of human water abstraction. Modified from [Khandu et al. \(2016a\)](#).

1992 Since human water abstraction appears to be very high in the Ganges River Basin
 1993 (Fig. 3.18), the basin-averaged time-series of NOUSE and IRR70_S are further ana-
 1994 lyzed. Figure 3.19 compares time-series of “NOUSE” and “IRR70_S” TWS changes
 1995 between 1979 and 2009 in the Ganges River Basin. The differences between the two
 1996 time-series are also plotted in Fig. 3.19 in order to show the temporal variations of
 1997 TWS resulting from human water use only. The TWS value of the first month (January
 1998 1979) is removed from both time-series to help interpret the trend results. The difference
 1999 between IRR70_S and NOUSE increases with time (shown by the thick black line in
 2000 Fig. 3.19), indicating a clear trend of human water usage and its impacts on TWS in

the Ganges River Basin. The linear trend of the difference plotted in Fig. 3.19 shows a declining trend of 14 mm year^{-1} (or $15 \text{ km}^3 \text{ year}^{-1}$) between 1979 and 2009.

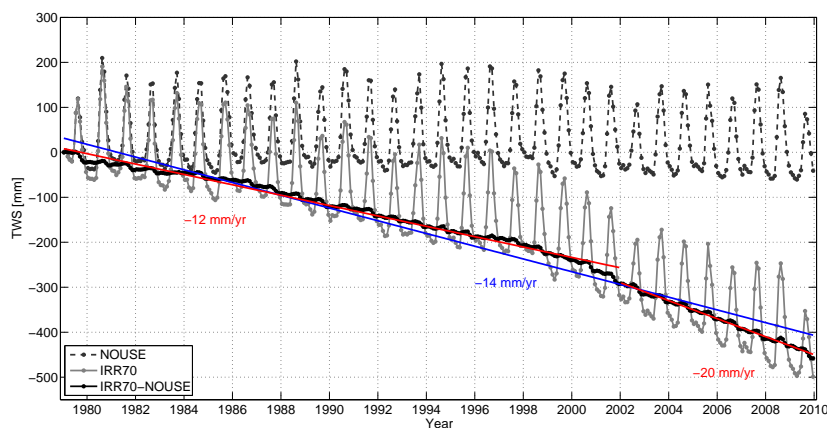


Figure 3.19: time-series of natural TWS (“NOUSE”, black dashed line), TWS under the influence of human water use (“IRR70_S”, gray line), and their difference (black line). Linear trends are shown for 1979–2009, 1979–2001 and 2002–2009. Adapted from [Khandu et al. \(2016a\)](#).

The intensity of human water use and TWS abstraction has increased by two-folds between 2002 and 2009 indicating a decreasing rate of 20 mm year^{-1} (or $22 \text{ km}^3 \text{ year}^{-1}$) compared to the period of 1979–2001 (12 mm year^{-1} (or $13 \text{ km}^3 \text{ year}^{-1}$)). The trend estimates between 2002 and 2009 is consistent with GRACE-derived TWS changes for the same period (see, Fig. 3.11e–f) and those reported in [Tiwari et al. \(2009\)](#) and [Richey et al. \(2015\)](#). The increasing level of groundwater abstraction in the Ganges River Basin was also reported in a global basin study in [Richey et al. \(2015\)](#). Besides the impact of human water abstraction, several studies indicate that Himalayan glaciers are retreating due to climate change ([Scherler et al., 2011](#), [Bajracharya et al., 2015](#)), which could also contribute to the overall decline of TWS in both the sub-basins through increased runoffs during the spring season (March–May).

3.5 Concluding remarks

The Ganges–Brahmaputra–Meghna (GBM) River Basin is highly vulnerable to climate variability such as droughts and extreme wet events (e.g., [Mirza et al., 1998](#), [Bates et al., 2008](#), [Jiménez-Cisneros et al., 2014](#), [Pervez and Henebry, 2015](#)). Intensification of droughts or extreme wet events will likely exacerbate growing water scarcity in the region, which has already reached critical levels over the years due to over exploitation of ground/surface water resources. In this study, a suite of observed rainfall, reanalysis-based soil moisture, and GRACE total water storage (TWS) changes, along with hydrological model outputs are used to examine the impacts of climate variability (focusing mainly on meteorological droughts) and human influences on the GBM’s water storage for the period 1980 to 2014. In the absence of long-term observations of TWS, soil moisture datasets generated by three reanalysis systems are used as TWS proxies for the period 1980–2015.

2027 Based on the GRACE-derived TWS changes, two key regions: (i) north-western
2028 Ganges (includes Haryana, Uttarakhand, and Uttar Pradesh) and (ii) central
2029 Brahmaputra-Meghna (includes northern Bangladesh, northeast India, and Bhutan)
2030 have indicated the highest loss of water mass, which indicated a declining trend of about
2031 30–40 mm year⁻¹ between 2002 to 2015. On average, TWS is found to be declining at a
2032 rate of 9.1 ± 4.5 km³ year⁻¹ and 10.5 ± 3.2 km³ year⁻¹ in the Ganges and Brahmaputra-
2033 Meghna River Basin, respectively. While the alarming rate of TWS decline (~ 20 km³
2034 year⁻¹) in the Ganges River Basin has subsided since 2010, with an increase (~ 8 km³
2035 year⁻¹) in the last five years due to an anomalous jump in precipitation, TWS in the
2036 Brahmaputra–Meghna River Basin tend to decline further. Extreme climate variations
2037 such as prolonged meteorological droughts have an lasting effect on the TWS, which is
2038 being exemplified by the recent droughts of 2005/2006 and 2009/2010, both of which
2039 have been associated with major ENSO/IOD events. TWS and soil moisture variations
2040 strongly respond to precipitation changes, and in particular, they are highly correlated
2041 in the Ganges River Basin, with a correlation coefficient of 0.6 or more.

2042 Although short-term TWS changes are strongly influenced by climate variability
2043 such as prolonged meteorological droughts and extreme wet events, the water storage
2044 changes across many parts of the GBM River Basin are under enormous pressure from
2045 ever increasing population and its associated socio-economic changes. Apart from daily
2046 consumptive water use, irrigated agriculture uses about 60–90% of the groundwater and
2047 SWS continues to be extracted even at higher rate through diversion of the GBM river
2048 system (Papa et al., 2015). Ground-based observations and hydrological model simula-
2049 tions have consistently shown that groundwater declines have been caused by excessive
2050 withdrawals of surface/groundwater across the GBM River Basin (Shamsudduha et al.,
2051 2009b, Central Ground Water Board, 2014, Shahid et al., 2015). The linear trends of
2052 WGHM simulated TWS changes analyzed in this study are consistent with the TWS
2053 changes derived from GRACE datasets, which indicated that human water abstraction
2054 has intensified between 2002 and 2009 compared to 1979-2001.

2055 Water storage components (e.g., soil moisture, SWS) simulated by reanalysis systems
2056 and land surface/hydrological models strongly vary in the GBM River Basin. Besides
2057 large differences in mean annual amplitudes, long-term linear trends estimated from
2058 reanalysis datasets showed varying increasing trends between 1980 and 2015 and are
2059 markedly higher than Noah-based soil moisture for the period 2002–2015, albeit both
2060 indicating positive trends. Based on the generalised TCH algorithm, ERA-Interim ex-
2061 hibited the largest uncertainties with a magnitude of about 20 mm year⁻¹, whereas
2062 Noah-based soil moisture data appears to more accurate than those produced by the
2063 reanalysis systems. Among the three GRACE products, the CSR datasets showed the
2064 lowest uncertainties (of less than 1 cm), which agrees with the most recent studies.

2065 4. Assessing high-resolution regional 2066 climate model simulations

2067 4.1 Introductory remarks

2068 The global climate system is influenced by a number of physical and dynamical pro-
2069 cesses across a broad range of spatio-temporal scales. Global climate models (GCMs)
2070 are mathematical tools based on well-established physical laws that are applied to repre-
2071 sent physical and dynamical processes and simulate the climate system (Randall et al.,
2072 2007, Flato, 2011, Flato et al., 2013). With a long history of development, GCMs are
2073 able to adequately represent large-scale climate features such as general circulation of
2074 the atmosphere and the ocean, and large-scale patterns of, for example, precipitation
2075 and temperature. However, their spatial resolution is still too coarse (about 100–200
2076 km) to represent many fundamental regional or local climate aspects such as position,
2077 intensity, and the frequency of rainfall along the Himalayan Foothills (Kripalani et al.,
2078 2007, Ramesh and Goswami, 2014, Saha et al., 2014). While coupled Ocean-Atmospheric
2079 GCMs (AOGCMs) can also be run at high horizontal resolutions to better simulate the
2080 aspects of regional or local climate information (e.g., Kitoh and Endo, 2016), they are
2081 currently limited to very short time-scales (e.g., 10 years) due to high computational
2082 cost. For instance, Rajendran and Kitoh (2008) performed a very high global resolution
2083 (20 km) GCM simulation for two 10-year time-slices and found that spatial distribution
2084 of precipitation over steep mountains could be improved. However, few studies have
2085 used global variable-resolution models to improve the spatial resolution of the region of
2086 interest (e.g., Lal et al., 2008).

2087 One of the methods currently employed to remedy the coarse global model resolution
2088 is by applying regional climate models (RCMs) to dynamically downscale GCM outputs
2089 or global reanalyses over a region of interest (see e.g., Jones et al., 2004, Giorgi et al.,
2090 2012). Regional models improve on GCMs to provide high-resolution key inputs suitable
2091 for assessing climate change impacts on water resources at regional to local scales.
2092 By selecting a spatial domain covering a region of interest, RCMs can generate high-
2093 resolution (e.g., 10 km or higher) climate information within that domain by improving
2094 the spatial representation of regional forcings such as topography, land cover, land-
2095 sea thermal contrasts, air pollution, and other small-scale features (e.g., lakes) (Wang
2096 et al., 2004, Rummukainen, 2009, Rummukainen et al., 2015). As a result, RCMs are
2097 better suited for providing inputs to climate impact studies relevant for adaptation
2098 planning and developing mitigation strategies at various levels of the society. The most
2099 recent reviews on RCM studies (e.g., Rummukainen et al., 2015) explores the possibility
2100 of running very high (spatial) resolution RCMs in an effort to eliminate the use of
2101 convective parametrizations schemes. Such advances can be particularly beneficial for
2102 the complex topographic region of the Himalayas, which is highly sensitive to the use
2103 of different cumulus convective schemes (see e.g., Dash et al., 2006, Sinha et al., 2013).

2104 Early studies on RCM simulations of the Indian monsoon in the mid-1990s mainly
2105 focused on the suitability of model domains (e.g., location and size) and their ability
2106 to generate regional circulation feedbacks in response to e.g., topography based on few
2107 months to a couple of years of simulations (e.g., [Bhaskaran et al., 1996](#), [Ji and D, 1997](#)).
2108 Since then, many RCM studies have been carried out to (i) verify their ability to simulate
2109 the Indian monsoon (e.g., [Lucas-Picher et al., 2011](#), [Srinivas et al., 2012](#), [Dash et al.,](#)
2110 [2015](#)), (ii) examine the model sensitivity to various cumulative parameterization schemes
2111 (e.g., [Raju et al., 2015](#), [Dash et al., 2006](#)), and (iii) provide long-term climate projections
2112 over various parts of the Indian monsoon region ([Kumar et al., 2006](#), [Yadav et al., 2008](#),
2113 [NEC, 2011](#), [Rahman et al., 2012](#), [Mathison et al., 2013](#), [Caesar et al., 2015](#)). Given
2114 the importance of regional climate variability/change, existing RCMs (e.g., [Skamarock](#)
2115 [et al., 2008](#), [Giorgetta et al., 2013](#)) are refined to include more physical and chemical
2116 processes representing the land surface and vegetation, biogeochemistry, and aerosols,
2117 thereby, edging towards developing a full Regional Earth System Model ([Rummukainen](#)
2118 [et al., 2015](#)).

2119 The aforementioned studies have made significant contributions to the understand-
2120 ing of the regional climate process and on the model's ability to simulate the Indian
2121 monsoon. However, most of the model assessment studies mentioned above are limited
2122 to the Indian monsoon and were based on 50 km grid resolution or less, whereas higher
2123 resolution models are mostly run for sensitivity purposes. While model sensitivity stud-
2124 ies are important for identifying correct model parameterizations and isolating regional
2125 feedbacks, they may not adequately provide meaningful climate statistics as well as
2126 identify key model errors relating to the internal climate variability. More importantly,
2127 since the reliability of future regional climate projections are very much dependent on
2128 how well dynamically downscaled GCMs represent the historical and present climate,
2129 it is equally important to assess the accuracy of RCMs driven by various global mod-
2130 els. This will help understand how well RCMs are able to rectify or amplify spatial
2131 misrepresentations (e.g., precipitation) in the parent GCMs and identify model errors
2132 resulting from the use of different physics and parameterizations schemes, among oth-
2133 ers. This chapter seeks to explore the potential strengths and limitations of two current
2134 state-of-the-art RCMs: (i) Regional Climate Model (RegCM) version 4.4 (RegCM4.4,
2135 [Giorgi et al., 2012](#)) and (ii) Hadley Centre's Providing REgional Climate Information of
2136 Impact Studies (PRECIS, [Jones et al., 2004](#)) performed on a 25 km horizontal resolution
2137 forced by various coupled ocean-atmospheric GCMs and Earth System Models (ESMs),
2138 by assessing the key climate features over the GBM River Basin.

2139 The GBM River Basin exhibits a broad range of extremes that are particularly chal-
2140 lenging from a climate modelling perspective, such as (i) in topography, ranging from
2141 the world's highest mountains to the largest deltas, (ii) in precipitation, from arid to
2142 semi-arid areas of western Ganges River Basin to the vast plains subject to flooding as
2143 well as a long range of Himalayan Foothills that are subject to intense orographic rains,
2144 and (iii) large snow/glacial areas that are highly vulnerable to warming. The model
2145 evaluations are carried out with respect to the available observational-based gridded
2146 datasets and reanalysis-based fields (as discussed in Chapter 2 on a wide range of met-
2147 rics, including (i) the seasonal precipitation and temperature means (ii) the onset and
2148 withdrawal of the monsoon, and (iii) the long-term trends and interannual variability

2149 and their response to global and local sea surface temperatures (SSTs). The findings
2150 presented in chapter has been submitted to *Climate Dynamics* with minor revisions
2151 based on the suggestions provided by the Reviewers.

2152 Section 4.2 describes a general concept of downscaling coarse resolution GCMs using
2153 RCMs and their developments based on most up-to-date reviews. The key attributes
2154 of RegCM4.4 and PRECIS models and their simulations and respective input datasets
2155 or boundary conditions used are discussed in Section 4.3. Observational datasets and
2156 methods used to evaluate the model outputs are presented in Section 4.4. Section 4.5
2157 evaluates the precipitation and temperature fields simulated by the two RCMs, while
2158 Section 4.6 provides a general findings of this study.

2159 4.2 Key attributes of Regional Climate Models (RCMs)

2160 The development of RCMs is motivated by the need for regional- to local-scale climate
2161 information in order to circumvent the limitations of low-resolution GCMs that cur-
2162 rently do not represent many key aspects of regional climate processes. The principle
2163 behind RCMs is the concept of “downscaling” (Giorgi and Mearns, 1991). The down-
2164 scaling technique attempts to translate large-scale atmospheric fields from GCMs into
2165 high-resolution climate information using additional information over a region of in-
2166 terest. Downscaling techniques can be classified into two main categories: (i) *statistical*
2167 *downscaling* (see, Maraun et al., 2010, for a review) and (ii) *dynamical downscaling* (see,
2168 Giorgi and Mearns, 1991, Wang et al., 2004, Rummukainen, 2009, Rummukainen et al.,
2169 2015, for a review). The former is based on finding robust statistical relationship be-
2170 tween large-scale climate variables (as predictors) and local variables (as predictands),
2171 while the latter relies on the same physical-dynamical description of global/regional cli-
2172 mate process that forms the core of GCMs, which can be achieved through, for example,
2173 using RCMs (Christensen et al., 2007).

2174 Even though computationally efficient, empirical (or statistical) downscaling meth-
2175 ods are limited by the assumptions of stationarity, where statistical relationship between
2176 present day climate also holds true for the possible future climate under various forcing
2177 conditions. Nevertheless, statistical downscaling methods are important tools for pro-
2178 viding high-resolution climate information (Maraun et al., 2010). On the other hand,
2179 RCMs relies on the assumption that given detailed representations of physical process
2180 and adequate regional information (e.g., high-resolution topography, land-use), they
2181 can generate realistic regional climate information consistent with the large-scale atmo-
2182 spheric (and/or land surface/ocean) fields provided by the parent GCMs or reanalyses
2183 (Giorgi and Mearns, 1991, Wang et al., 2004, Rummukainen, 2009). Figure 4.1 shows
2184 the overall process of dynamic downscaling using RCMs. A regional model consists of
2185 its dynamical core but use boundary conditions (e.g., air temperature, wind, humidity)
2186 from either GCMs or observation-based reanalysis systems to produce high-resolution
2187 climate information (e.g., temperature or precipitation) over a region of interest.

2188 Following numerous reviews on RCMs (e.g., Giorgi and Mearns, 1991, Wang et al.,
2189 2004, Rummukainen, 2009, Rummukainen et al., 2015), some caveats of regional climate
2190 modelling are given below:

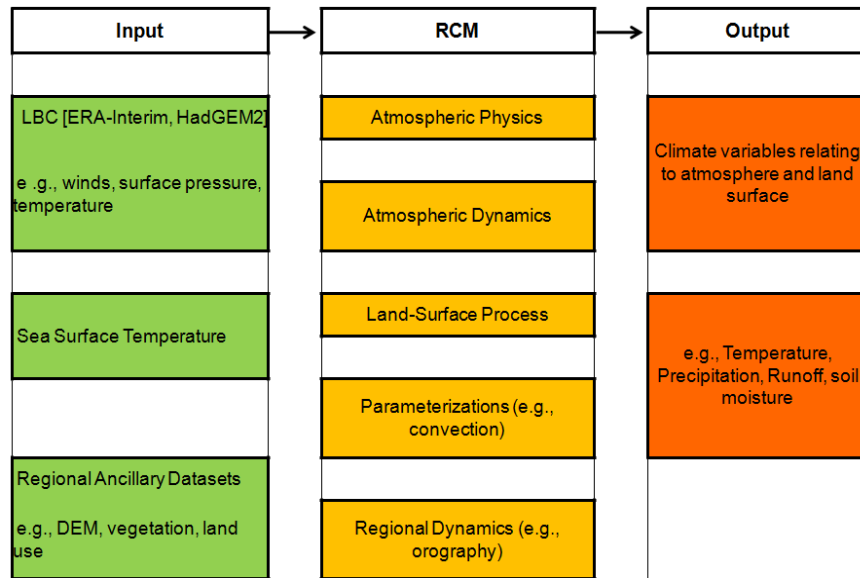


Figure 4.1: Process involved in regional climate modelling using RCMs. Modified from Mathison et al. (2013)

2191 4.2.1 Model dynamics

2192 On a broad scale, RCMs can be classified into *hydro-static* and *non-hydrostatic* models
 2193 that are run on variety of horizontal and vertical grid coordinate systems, except for
 2194 those developed as regional spectral model (RSM, Juang et al., 2014). A large number
 2195 of RCMs are formulated based on the hydro-static assumption, e.g, REgional MOdel
 2196 (REMO, Jacob and Podzun, 1997), Providing REgional Climates for Impacts Studies
 2197 (PRECIS, Jones et al., 2004), and Regional Climate Model (RegCM, Giorgi et al., 2012),
 2198 while few RCMs such as COnsortium for SMall scale MOdeling Climate Limited-area
 2199 Modelling (COSMO-CLM, Doms et al., 2015), Regional Atmospheric Modelling System
 2200 (RAMS, Snook et al., 1995), and Weather Research and Forecasting (WRF, Skamarock
 2201 et al., 2008) provide options to include non-hydrostatic terms, which allows for providing
 2202 very high-resolution (less than 5 km) simulations. Very high-resolution models also to
 2203 some degree eliminate the need for convective parameterizations, thus, allowing for
 2204 improved simulations of diurnal cycles of convection and precipitation, including onset,
 2205 duration, and intensity, as well as of tropical cyclone (TC) intensity and fine structure
 2206 of the TC eyewall (Rummukainen et al., 2015).

2207 High-resolution modelling can also be achieved through multiple nesting approaches,
 2208 which is currently available in many existing RCMs (e.g., RegCM, COSMO-CLM,
 2209 WRF). Most RCMs use either a terrain-following pressure coordinate system, or a
 2210 terrain-following height coordinate system (e.g., RAMS) with 17 levels or more with
 2211 the model top being in the lower stratosphere (typically between 50 hPa and 5 hPa).
 2212 Most RCMs were originally developed as atmosphere-only models, which are later cou-
 2213 pled with land surface models to incorporate feedbacks from the land surface process
 2214 (e.g., Pal, 2007). Today, most RCMs are coupled with global oceanic models for spe-

2215 cific applications. With increasing computing power and model advancement, RCMs are
2216 evolving towards a comprehensive regional climate model system through inclusion of
2217 bio-geochemistry and aerosol processes (see, [Rummukainen et al., 2015](#)).

2218 4.2.2 Boundary conditions

2219 RCMs are limited area models (LAM) that require lateral boundary conditions (LBCs),
2220 and lower and upper boundaries, which can be collectively referred to as “driving data”
2221 or just “boundary conditions”. These datasets are usually supplied by GCMs or global
2222 reanalyses. The basic boundary conditions include air temperature, humidity, and cir-
2223 culation (wind fields) typically at 6-hour time intervals, as well as SSTs and sea ice
2224 (usually at 6 hourly, weekly, or at monthly scales). Since these datasets come in dif-
2225 ferent time-scales, they require interpolation in time between two successive boundary
2226 conditions to match the temporal resolution of the RCMs. The boundary conditions are
2227 incorporated by building a “relaxation zone” just inside their lateral boundaries that are
2228 typically 4-10 grid wide from all four sides. Most RCMs use an exponential boundary
2229 relaxation scheme in order to provide LBCs to the RCM. [Giorgi et al. \(1993b\)](#) showed
2230 that a large buffer zone with exponentially decreasing weights provides a smoother tran-
2231 sition between the prescribed LBCs and the regional climate simulations. The size of the
2232 relaxation zone may also depend on the model resolution, which increases as a function
2233 of model resolution.

2234 4.2.3 Model parameterizations

2235 RCMs share problems that are inherent to the parent GCMs or reanalyses, in which
2236 RCMs tend to enhance the spatial resolution compared to parent GCMs but pushes
2237 those processes that take place on a smaller scale towards the finer scales. Physical
2238 processes that take place on much smaller spatial scales than the RCM resolution are
2239 described using “parameterization” (or approximation) techniques. Among the many pa-
2240 rameterization schemes employed in RCMs, the most widely discussed is the “convective”
2241 parameterization scheme since it plays a critical role in representing the cloud process
2242 and the resulting precipitation field ([Emanuel and Rothman, 1999](#)). Various cumulative
2243 convective schemes have been applied over the Indian monsoon using several RCMs and
2244 have shown that Indian summer monsoon is very sensitive to convective parameteriza-
2245 tion schemes (e.g., [Dash et al., 2006](#), [Srinivas et al., 2012](#)).

2246 For example, [Dash et al. \(2006\)](#) found close agreement between model simulated
2247 precipitation and observed rainfall over India using the Grell parameterization scheme
2248 ([Grell, 1993](#)) in RegCM3 ([Pal, 2007](#)). Similar results were obtained by [Nayak et al. \(2015\)](#)
2249 using the updated version of RegCM (RegCM4, [Giorgi et al., 2012](#)). [Srinivas et al. \(2012\)](#)
2250 used WRF version 3 model to simulate the Indian summer monsoon from 2000-2009 and
2251 indicated that Betts-Millor-Janjic convection scheme produced the best simulation of
2252 rainfall over west coast, central, and northeast India. More recently, [Sinha et al. \(2013\)](#)
2253 used various cumulative convection schemes available in RegCM3 and found that the

2254 Massachusetts Institute of Technology (MIT)-Emanuel convective scheme (Emanuel,
2255 1991, Emanuel and Rothman, 1999) features better simulation of rainfall for a 30 km
2256 resolution over the Indian monsoon region, which includes the Himalayan Foothills and
2257 the northeast India.

2258 4.2.4 Model domain

2259 The sensitivity of regional climate modelling to the size of the chosen domain has a long
2260 history of debate (see e.g., Leduc and Laprise, 2009, and references therein). There is no
2261 permanent solution for choosing a domain. An important condition is that RCM domain
2262 has to be large enough to allow the full development of small-scale features, but still suf-
2263 ficiently small enough to not let flow solutions deviate too much away from the driving
2264 model. Boundary lines must not cut across mountain ranges or sharp precipitation fea-
2265 tures, which is a challenging concept, especially over the Indian monsoon region, where
2266 the northern limit usually falls along the Tibetan Plateau. Previous studies have shown
2267 that Indian summer monsoon is sensitive to domain size (e.g., Bhaskaran et al., 1996,
2268 2012, Dash et al., 2015) and indicated that one domain may not sufficiently reproduce
2269 the observed climate of all subregions within the domain. Thus, sensitivity studies must
2270 be conducted before selecting a RCM domain in order to carry out long-term climate
2271 simulation.

2272 4.3 Regional climate model (RCM) data

2273 4.3.1 RegCM4.4 simulations and boundary conditions

2274 Regional Climate Model version 4.4 (RegCM4.4, Giorgi et al., 2012) is the fourth gener-
2275 ation of the regional climate modelling framework originally developed by Giorgi et al.
2276 (1993a,b) and Pal (2007). RegCM4.4 is a hydrostatic model with a terrain following
2277 vertical coordinate run on an Arakawa B-grid scheme. It is based on the hydrostatic
2278 version of the National Center for Atmospheric Research (NCAR)/Pennsylvania State
2279 University (PSU) Mesoscale Model version 5 (MM5, Grell et al., 1994). RegCM4.4 in-
2280 cludes substantial improvements both in terms of model physics and softwares compared
2281 to its previous version, RegCM3 (Pal, 2007). The most notable improvement is the flex-
2282 ibility to use mixed cumulus convective schemes over land and ocean (see, Giorgi et al.,
2283 2012). For this chapter, the RegCM4.4 model domain is centered over the Indian mon-
2284 soon region covering South Asia and parts of the Tibetan Plateau and Southeast Asia
2285 (2°N – 37°N , 61°E – 108°E) on a 25 km grid resolution ($\sim 0.22^{\circ} \times 0.22^{\circ}$) for the period
2286 1981–2012. Table 4.1 describes the main settings of this simulation. Figure 4.2 shows
2287 the model domain illustrating the topography at four different spatial scales as well
2288 as the Ganges and Brahmaputra–Meghna River Basin. The topographic details of the
2289 Himalayan ranges of the northern GBM River Basin are barely represented in coarse
2290 resolution GCMs (Fig. 4.2a-c). A more detailed representation of topography in the

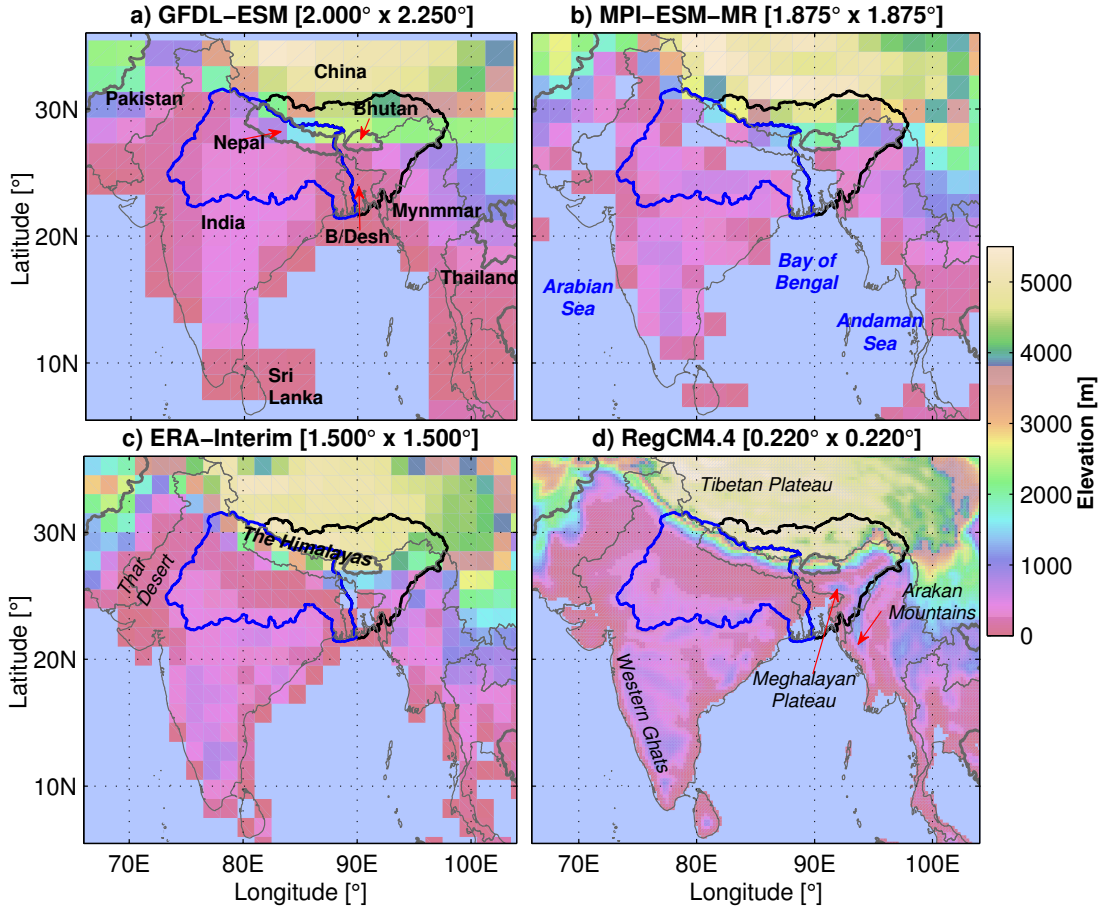


Figure 4.2: Elevation maps of the RegCM4.4 domain at various spatial resolutions: (a) GFDL-ESM, (b) MPI-ESM-MR, (c) ERA-Interim, and (d) RegCM4.4. Note that the nominal resolution of ERA-Interim is $0.79^\circ \times 0.79^\circ$. The Ganges and Brahmaputra–Meghna River Basins are shown in blue and black (thick) polygons.

2291 RCMs (Fig. 4.2d) in particular, improve orographic precipitation along the Himalayan
 2292 mountains (Sinha et al., 2014, Dash et al., 2015).

2293 Before conducting the long-term simulation, a preliminary sensitivity experiment was
 2294 done for a five year period (1998–2012) with boundary conditions supplied by the Eu-
 2295 ropean Centre for Medium-Range Weather Forecasts (ECMWF) retrospective analysis
 2296 (ERA-Interim, Dee et al., 2011) and observed weekly sea surface temperature (SST)
 2297 fields supplied by the National Oceanic and Atmospheric Administration (NOAA, see,
 2298 <http://www.esrl.noaa.gov/psd/data/gridded/data.noaa.oisst.v2.html>). This is
 2299 done to assess the model’s sensitivity to a mixture of two (i.e., Grell and Emanuel
 2300 schemes) cumulus convective schemes. It must be mentioned here that there are clear
 2301 preferences between the various schemes, for instance, the Grell scheme in some cases
 2302 generate very little precipitation over land (e.g., Dash et al., 2006, Sinha et al., 2013,
 2303 Raju et al., 2015), while Emanuel-only scheme tends to produce excess precipitation.
 2304 Following this sensitivity experiment, the Emanuel (over land) and Grell (over ocean)

Table 4.1: Summary of RegCM4.4. and PRECIS model settings.

| Model characteristics | RegCM4.4 | PRECIS |
|---------------------------------|--|--|
| 1. Domain | Indian monsoon region (Figure 4.2) | South Asia (with rotated pole coordinates of 260° longitude, and 70° latitude (Caesar et al., 2015)) |
| 2. Simulation period | 1981–2012 | 1949–2012 |
| 3. Resolution | 25 km | 25 km |
| 4. Vertical layers | 18 [1000 hPa–50 hPa] | 19 [1000 hPa–5 hPa] |
| 5. Topography | GTOPO30 (~ 1.0 km) | US Navy 10 min |
| 6. Boundary condition | ERA-Interim, Weekly SST data, GFDL-ESM, MPI-ESM-MR | QUMP (HadCM3Q0-16) |
| 7. Resolved scale precipitation | Subgrid explicit moisture scheme (SUBEX, Pal et al., 2000) | Smith (1990) |
| 8. Land surface | Biosphere-Atmosphere Transfer scheme (BAT, Dickinson et al., 1993) | Met Office 12. Surface Exchange Scheme (MOSES-I, Cox et al., 1999) |
| 9. Convection Scheme | Emanuel (Land) and Grell (Ocean) | Mass flux penetrative (Gregory and Rowntree, 1990) |

2305 scheme was adopted in this chapter (see, Table 4.1) as this mixed scheme provided better
 2306 simulation of precipitation distribution over the Indian monsoon region (see also, Raju
 2307 et al., 2015). The land surface model used in this experiment Biosphere-Atmosphere
 2308 Transfer scheme (BATS, Dickinson et al., 1993), which has a soil depth of 1 m. Other
 2309 details are provided in Table 4.1, and the same experimental setting has been adopted for
 2310 long-term simulation (1981–2012) using boundary conditions from ERA-Interim (and
 2311 observed SST datasets) and two Earth System Models (ESMs) from the Coupled Model
 2312 Intercomparison Project Phase 5 (CMIP5, Taylor et al., 2012).

2313 Reanalysis systems such as ERA-Interim are termed near-perfect boundary condi-
 2314 tions for RCMs as intended to produce realistic state of the atmosphere at any given
 2315 time-period (e.g. 6 hours). ERA-Interim was chosen as lateral boundary condition (LBC)
 2316 for RegCM4.4 as it is found to provide the most realistic precipitation estimates over the
 2317 GBM River Basin (see, Khandu et al., 2016c). To differentiate between the original ERA-
 2318 Interim fields and those simulated by RegCM4.4, the latter is denoted by RegCM4.4-
 2319 ERAI in the tables and figures presented hereafter. On the other hand, CMIP5 GCMs are
 2320 based on both natural (e.g., solar variations) and anthropogenic (e.g., CO₂, CH₄) condi-
 2321 tions consistent with observed climate variations between 1850 and 2005, and are largely
 2322 based on four pathways of greenhouse gas concentrations (GHGs), referred to as Repre-
 2323 sentative Concentrative Pathways (RCP, Moss et al., 2010) from 2006 onwards. The two
 2324 CMIP5 GCMs include one realisation (RCP4.5 from 2006–2012) each from (i) Geophys-
 2325 ical Fluid Dynamics Laboratory Earth System Model (ESM) (GFDL-ESM2M, hereafter
 2326 as GFDL-ESM, Dunne et al., 2012) and (ii) Max-Planck-Institute ESM medium res-
 2327 olution (MPI-ESM-MR, Giorgetta et al., 2013) for the period 1981 to 2012. The two
 2328 models have been shown to provide reasonable estimation of the Indian monsoon by

2329 numerous previous studies (see e.g., [McSweeney et al., 2015](#)). A basic description of the
2330 two GCMs are presented in Table 4.2.

Table 4.2: Lists of global reanalyses and GCMs that are used to drive the RegCM4.4.

| LBC | Modelling Center | Spatial Resolution | Realisation | Calender |
|-----------------------------|---|--------------------------------------|-------------|-------------|
| ERA-Interim (reanalyses) | ECMWF | $1.500^{\circ} \times 1.500^{\circ}$ | - | 365.25 days |
| MPI-ESM- MR (CMIP5) | Center Max-Planck-Institut für Meteorologie | $1.875^{\circ} \times 1.875^{\circ}$ | r1i1p1 | 365 days |
| GFDL-ESM (CMIP5) | NOAA Geophysical Fluid Dynamics Laboratory | $2.000^{\circ} \times 2.250^{\circ}$ | r1i1p1 | 365 days |

2331 4.3.2 PRECIS model data

2332 Providing REgional Climate Information for Impact Studies (PRECIS, [Jones et al.,](#)
2333 [2004](#)) is an atmospheric and land surface model developed at the Hadley Centre, Met
2334 Office, UK, in order to provide high-resolution future climate scenarios for developing
2335 countries under the framework of United Nations Framework Convention on Climate
2336 Change (UNFCCC). PRECIS climate modelling system is based on the third generation
2337 regional model (HadRM3P) ([Jones et al., 2004](#)), which is a high-resolution version of
2338 the atmospheric general circulation model (HadAM3H) ([Gordon et al., 2000](#)). It is a
2339 hydrostatic model with a terrain following vertical coordinate and uses an Arakawa B-
2340 grid scheme. The standard version of PRECIS can be run at a maximum grid resolution
2341 of 25 km with 19 vertical levels with the lowest and highest limit at $\sim 50\text{m}$ and $\sim 30\text{ km}$
2342 (see, Table 4.1). PRECIS has been applied over the Indian monsoon by several studies
2343 to generate future climate scenarios for various countries (see e.g., [Kumar et al., 2006](#),
2344 [Islam et al., 2008](#), [Lucas-Picher et al., 2011](#), [NEC, 2011](#), [Mathison et al., 2013](#)).

2345 The PRECIS model data used in this study was obtained from the UK Met Of-
2346 fice. It includes six sets of perturbed physics ensemble (PPE) simulations conduced
2347 over the South Asian continent (see, [Caesar et al., 2015](#)) from 1949 to 2099 to esti-
2348 mate model uncertainties and internal climate variability for an assumed pathway of
2349 future anthropogenic projections with boundary conditions from Hadley Centre’s cou-
2350 pled GCM (HadCM3) with various combination of parameter settings. Their original
2351 experiment involved 17 PPE members, which are collectively referred to as QUMP
2352 (Quantifying Uncertainties in Model Projections, see, [Murphy et al., 2007](#), [McSweeney](#)
2353 [et al., 2012](#), for more details). The model parameters used in the 17 member HadCM3
2354 are provided in [Collins et al. \(2006\)](#) and the references therein, and are identified by an
2355 alphanumeric character representing the Hadley Centre’s HadCM3 and the PPE mem-
2356 bers (0-16) representing the various set of parameter samplings discussed in [Collins et al.](#)
2357 [\(2006\)](#). HadCM3Q-0 represents a standard (unperturbed) HadCM3 model, which then
2358 goes from a very low sensitivity model (Q1) to very high sensitivity model (Q16).

2359 Based on a preliminary study by [McSweeney et al. \(2012\)](#) over South and Southeast
2360 Asia, six PPE members (namely, HadCMQ0, HadCMQ9, HadCMQ10, HadCMQ14,

2361 HadCMQ15, and HadCMQ16) simulated by PRECIS model at $0.25^\circ \times 0.25^\circ$ grid reso-
2362 lution over South Asia were obtained for this study. The QUMP members used here
2363 are based on Special Report on Emission Scenarios (SRES, IPCC, 2000) A1B storyline
2364 (IPCC, 2000). The A1B scenario describes a future world of very rapid economic growth,
2365 global population that peaks in mid 21st century and declines thereafter. The major dif-
2366 ference between standard HadCM3 (used in CMIP3) and QUMP is that the later uses
2367 flux adjustments to correct for biases in SSTs and salinity. The use of flux adjustments
2368 is seen to minimize warm biases QUMP models and enabled stable simulations to be
2369 run with a wide range of physics (see, McSweeney et al., 2012). Note that the SRES
2370 A1B is equivalent to RCP6.0 in terms of the future trajectory of global temperature
2371 change and thus, the two RCMs may differ slightly in the region. RCP scenarios also
2372 include more physical and chemical processes and adopts slightly different mitigation
2373 approaches (see, Moss et al., 2010) as opposed to SRES.

2374 4.4 Observational datasets and methods

2375 4.4.1 Observational datasets

2376 Precipitation and surface temperature (at 2 m) derived from various RCM simula-
2377 tions are evaluated with respect to daily SRS-based TMPAv7 (Huffman et al., 2007)
2378 version 7 (hereinafter as TMPAv7) and observational-based monthly GPCCv7 (Becker
2379 et al., 2013) precipitation products (for the period 1998–2012) and monthly tempera-
2380 ture datasets from the CRU_TS3.22 (Harris et al., 2013) for the period 1982–2012. Note
2381 that GPCCv7 and CRU_TS3.22 products are generated at $0.50^\circ \times 0.50^\circ$ grid resolu-
2382 tion. The easy accessibility, better latency period, and its comparable spatial resolution
2383 ($0.25^\circ \times 0.25^\circ$) with RCMs considered here makes it appropriate to use the TMPAv7
2384 product. Daily precipitation datasets from APHRODITE (Yatagai et al., 2012) is used
2385 to indicate the spatial pattern of onset and withdrawal of monsoon together with daily
2386 TMPAv7 products. Reanalysis fields from ERA-Interim (for precipitation and winds)
2387 and MERRA (Rienecker et al., 2011) (for temperature) were also included for compar-
2388 ison to give a wide range of uncertainties across different datasets. As such, a detailed
2389 evaluation of these datasets and the two reanalyses has been conducted in Chapter 2
2390 (see also, Khandu et al., 2016c).

2391 4.4.2 Evaluation methods

2392 The simulated RCM datasets are assessed for their wintertime (DJF) and monsoon
2393 (JJAS) precipitation (1998–2012) and temperature (1982–2012) climatology as well as
2394 their associated mean large-scale circulation, onset and retreat of the monsoon, and
2395 their ability to simulate low-frequency variations associated with ENSO (Trenberth,
2396 1997) and IOD (Saji et al., 1999). PRECIS results are plotted only for the ensemble
2397 mean (from six members), although results from individual members are shown in tables
2398 for discussion. Additionally, the model’s ability to simulate the onset and withdrawal

2399 process of the Indian monsoon is an important criteria. There are various approaches
 2400 for detecting the onset/withdrawal timing of the Indian monsoon based on standardised
 2401 indices developed from daily precipitation or moisture fluxes (e.g., Zeng and Lu, 2003,
 2402 Lucas-Picher et al., 2011), or from combination of different indices (Prasad and Hayashi,
 2403 2005). Each of these methods has its own merits and limitations, and are only meant to
 2404 be used as working guidelines. As such the results tend to agree well among the different
 2405 approaches (see e.g., Prasad and Hayashi, 2005, Lucas-Picher et al., 2011).

2406 Here, the onset/withdrawal timings are calculated by estimating the gradients from
 2407 5-day mean (or pentad) precipitation climatology. The advantage of introducing the
 2408 gradient is that it allows for automatic identification of the high and low peaks, cor-
 2409 responding to onset and withdrawal of the Indian monsoon, without requiring to set a
 2410 threshold. The method is demonstrated in Fig. 4.3 using mean daily precipitation (P)
 2411 estimates of APHRODITE and TMPAv7 for the period 1998–2007. Figure 4.3a–b shows
 2412 the cumulative sums of pentad rainfall (P_{sum}) between January 1 and December 31 for
 2413 the two river basins: (a) Ganges, and (b) Brahmaputra–Meghna. The frequency of rainy
 2414 days increases substantially, and remains high from mid-May until the end of monsoon
 2415 period (approximately falling on the first week of October). The gradients are estimated
 2416 by computing the inverse tangent of cumulative sums (P in %) of pentad rainfalls and
 2417 time (t) as shown in Eqn. 4.1.

$$y_i = \text{atan2}(P_{\text{sum}_i}, t_i) \quad (4.1)$$

$$\Delta m_i = \nabla y_i, \quad (4.2)$$

2418 where $i = 1, 2, 3, \dots, 73$ pentad numbers in a year.

2419 Based on the gradients calculated in Eqn. 4.2, the onset and withdrawal periods
 2420 are fixed to the pentads that correspond to the maximum and the minimum slope
 2421 in Fig. 4.3c–d, respectively. As shown in Fig. 4.3, the onset (withdrawal) timings of
 2422 Brahmaputra–Meghna River Basin falls approximately on pentad 30 or 29th of May
 2423 (pentad 57 or 11th of October) (Fig. 4.3b–d), while the Ganges River Basin has a
 2424 shorter period of monsoon by about 3–4 weeks (see Fig. 4.3a and 4.3c–d). The results
 2425 are consistent with the overall rainfall climatology for the two river basins and other
 2426 published sources (e.g., Rao, 1976, Krishnamurthy and Kinter III, 2003, Lucas-Picher
 2427 et al., 2011). It can be also seen that APHRODITE and TMPAv7 are consistent in
 2428 showing the onset and withdrawal timings of the Indian monsoon. The pentad numbers
 2429 differ by one or two based on how it is being calculated. The example shown here is
 2430 calculated based on the basin-averaged daily precipitation climatology.

2431 4.5 Results

2432 4.5.1 Seasonal precipitation and temperature mean climatology

2433 In order to understand the basic climate characteristics over the model domain, the
 2434 spatial distribution of mean winter (December–February, DJF) and summer monsoon

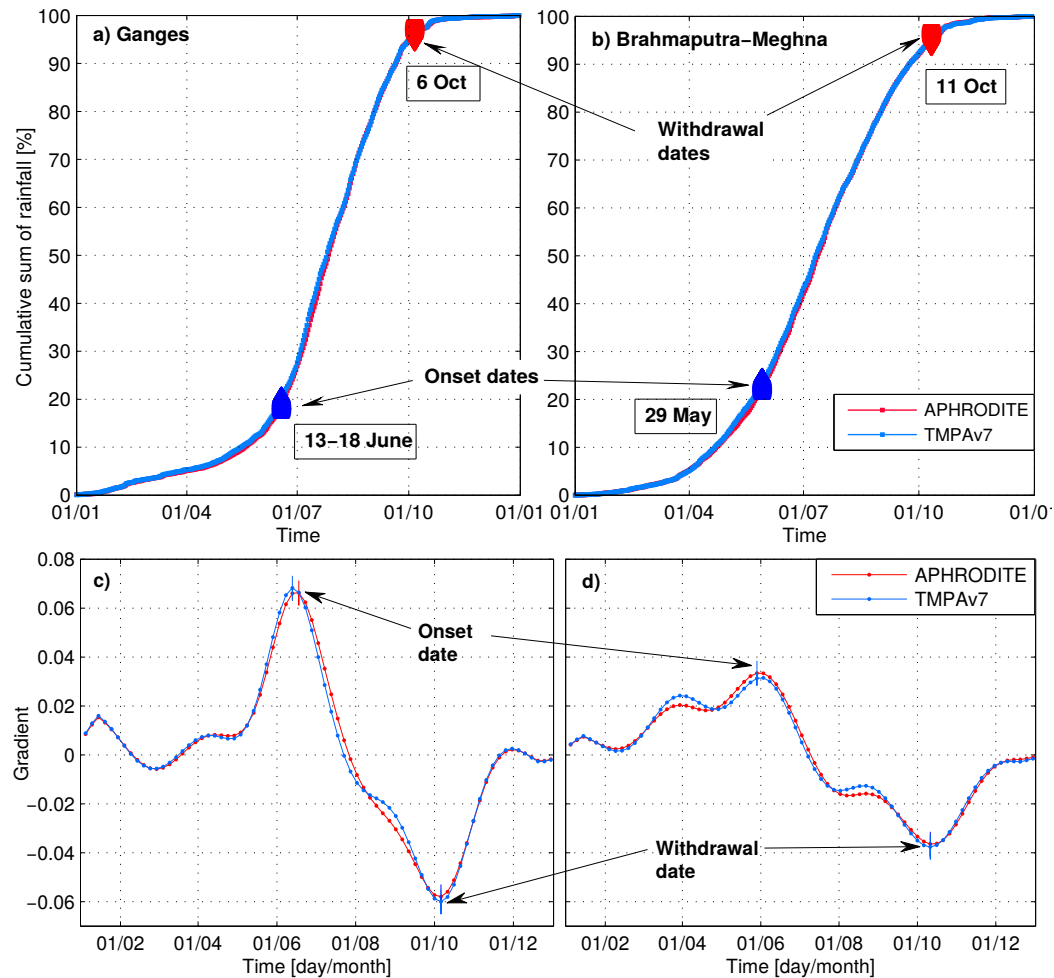


Figure 4.3: Cumulative sums of 5-day average precipitation (in %) based on APHRODITE (red) and TMPAv7 (blue) for (a) Ganges and (b) Brahmaputra–Meghna River Basins indicating their respective mean onset and retreat dates for the period 1998–2007. Gradients derived from (a & b) are shown in (c & d), respectively. The maxima and minima corresponds to the onset and withdrawal period of the Indian monsoon. A low-pass filter of approximately 30 days is applied to the pentad rainfall.

2435 (June–September, JJAS) precipitation (1998–2012) and temperature (1982–2012) de-
 2436 rived from various observations and reanalysis products are shown in Figure 4.4. The
 2437 wintertime precipitation is mainly influenced by extra-tropical storms, otherwise known
 2438 as the Western Disturbances originating from the Mediterranean (Lang and Barros,
 2439 2004, Dimri et al., 2015). These extra-tropical westerlies carry moisture over the west-
 2440 ern Himalayan regions, and frequently move further east towards the Gangetic Plains
 2441 and are ultimately precipitated in the form of snow and rain (Fig. 4.4a–c). As a result,
 2442 strong precipitation patterns are evident along the western Himalayas (covering north-
 2443 ern Pakistan and India, and Nepal) and northeast Indian states of Arunachal Pradesh
 2444 (located in the eastern Himalayas). The westerlies at 850 hPa pressure level shown in
 2445 Fig. 4.4c appears to gain strength over the Ganges River Basin and turn southerly to-

2446 wards the Bay of Bengal or northeasterly towards the Brahmaputra River Basin. Note
 2447 that all three precipitation datasets (TMPAv7, GPCCv7, and ERA-Interim) tend to
 2448 agree very well in the GBM River Basin (Fig. 4.4a–c).

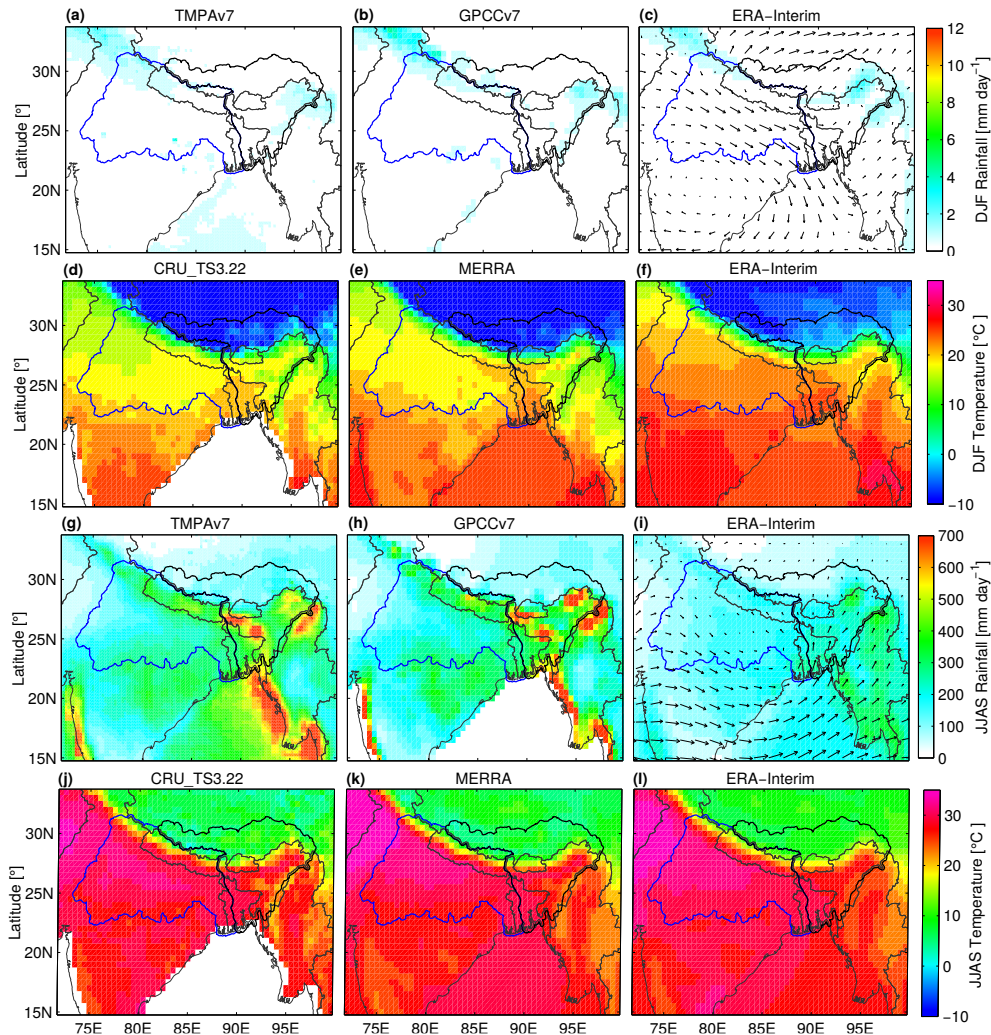


Figure 4.4: (a–f) DJF and (g–l) JJAS precipitation and temperature climatology based on observed and reanalysis dataset. Mean precipitation is computed from TMPAv7, GPCCv7, and ERA-Interim between 1998 and 2012, and mean DJF temperature is computed from CRU_TS3.22, MERRA, and ERA-Interim for the period 1982–2012.

2449 Based on the CRU_TS3.22 dataset, the mean DJF temperature varies from high
 2450 ($\sim 20^\circ\text{C}$) over Bangladesh to low ($\sim 10^\circ\text{C}$) in the Himalayas (especially, at the origin
 2451 of Brahmaputra River), with very sharp changes along the Himalayan Foothills (Fig.
 2452 4.4d). The Himalayas have a profound effect on the climate of the southern plains
 2453 by blocking the freezing dry Arctic winds. While MERRA appears to be particularly
 2454 skilful in reproducing the spatial temperature pattern (Fig. 4.4e), ERA-Interim indicates
 2455 substantial warm bias in the GBM River Basin (Fig. 4.4f), and are consistent with the
 2456 results presented in [Khandu et al. \(2016c\)](#).

2457 Although the Indian monsoon contributes to about 60–90% of the annual total pre-
2458 cipitation in the GBM River Basin, the spatial distribution of precipitation is highly
2459 influenced by the local topographic regimes as shown in Fig. 4.4g–i. In the GBM River
2460 Basin, the Himalayas form the final barrier of the monsoon flow resulting in record
2461 orographic rainfalls along its foothills, particularly across northeast India, Bhutan, and
2462 eastern Nepal. For example, Cherrapunji in Meghalaya (northeast India) receives one of
2463 the highest annual precipitation ($\sim 10,824$ mm) followed by southwest of Bhutan (4,000–
2464 6,000 mm) and Darjeeling (2,000–4,000 mm) (Soja and Starkel, 2007, Galvin, 2008). The
2465 Indian monsoon also undergoes seasonal changes in response to slow variations of the
2466 equatorial Indian Ocean and the equatorial Pacific Ocean that drive large-scale climate
2467 variations (e.g., ENSO and IOD). However, influences from ENSO and IOD events are
2468 considered to be relatively low (about 10–20%) compared to the overall JJAS rain-
2469 fall variation (Krishnamurthy and Kinter III, 2003, Ashok and Saji, 2007). During the
2470 monsoon, majority of the GBM River Basin experiences considerably high tempera-
2471 ture, including the Himalayan Range (~ 8 – 10°C , Fig. 4.4j–l). These patterns are well
2472 depicted by both MERRA and ERA-Interim (Fig. 4.4k–l), although ERA-Interim tend
2473 to indicate a significantly higher temperature in the Ganges River Basin (see, Table
2474 4.3).

2475 In order to assess the mean seasonal skills of the two RCMs, the simulated pre-
2476 cipitation and temperature datasets are compared with daily TMPAv7 precipitation
2477 estimates (1998–2012) and monthly CRU_TS3.22 temperature datasets (1982–2012).
2478 Fig. 4.5 shows the spatial patterns of precipitation and temperature biases of various
2479 RCM simulations in the GBM River Basin for the DJF. The 850 hPa level wind differ-
2480 ences between various RCM simulations and those of ERA-Interim fields are overlayed
2481 to understand their role in simulating precipitation. During winter, all RCM simula-
2482 tions overestimate precipitation in the eastern and western Himalayas by about 5–10
2483 mm day^{-1} , potentially due to slightly stronger westerlies in the RCM simulations (Fig.
2484 4.5a–d). While the bias patterns are similar across all the model simulations, the MPI-
2485 ESM-MR driven RegCM4.4 and QUMP driven PRECIS simulation tends to show the
2486 largest wet bias (Fig. 4.5c–d). Table 4.3 presents a summary of mean seasonal bias for
2487 the two river basins, where the magnitude of bias is higher in the Brahmaputra–Meghna
2488 River Basin.

2489 As shown in Fig. 4.5e–h, all RCM simulations show very cold bias in the Himalayas
2490 and the Tibetan Plateau, and warm bias in the Gangetic Plains. Although the magnitude
2491 of cold bias in the Himalayas is relatively small in the perfect boundary case (RegCM4.4
2492 driven by ERA-Interim), it shows a substantially warmer temperature in the central
2493 Ganges River Basin (Fig. 4.5e). The two CMIP5 driven RegCM4.4 simulations indicate
2494 significant cold bias in the Himalayas and Tibetan Plateau, with very minimal warm
2495 bias in the Ganges River Basin (Fig. 4.5f–g). The QUMP driven PRECIS simulations,
2496 on the other hand, exhibit a much reduced temperature bias across the Himalayan
2497 Range (Fig. 4.5h), although the warm bias in the Ganges River Basin vary among
2498 the six members. In summary, both reanalysis-based temperature products and RCM
2499 simulations show considerable bias in the GBM River Basin, with a relatively high cold
2500 bias in the northern Brahmaputra–Meghna River Basin. The magnitude of bias in the
2501 Brahmaputra–Meghna River Basin ranges from -2.7°C in the PRECIS simulations to

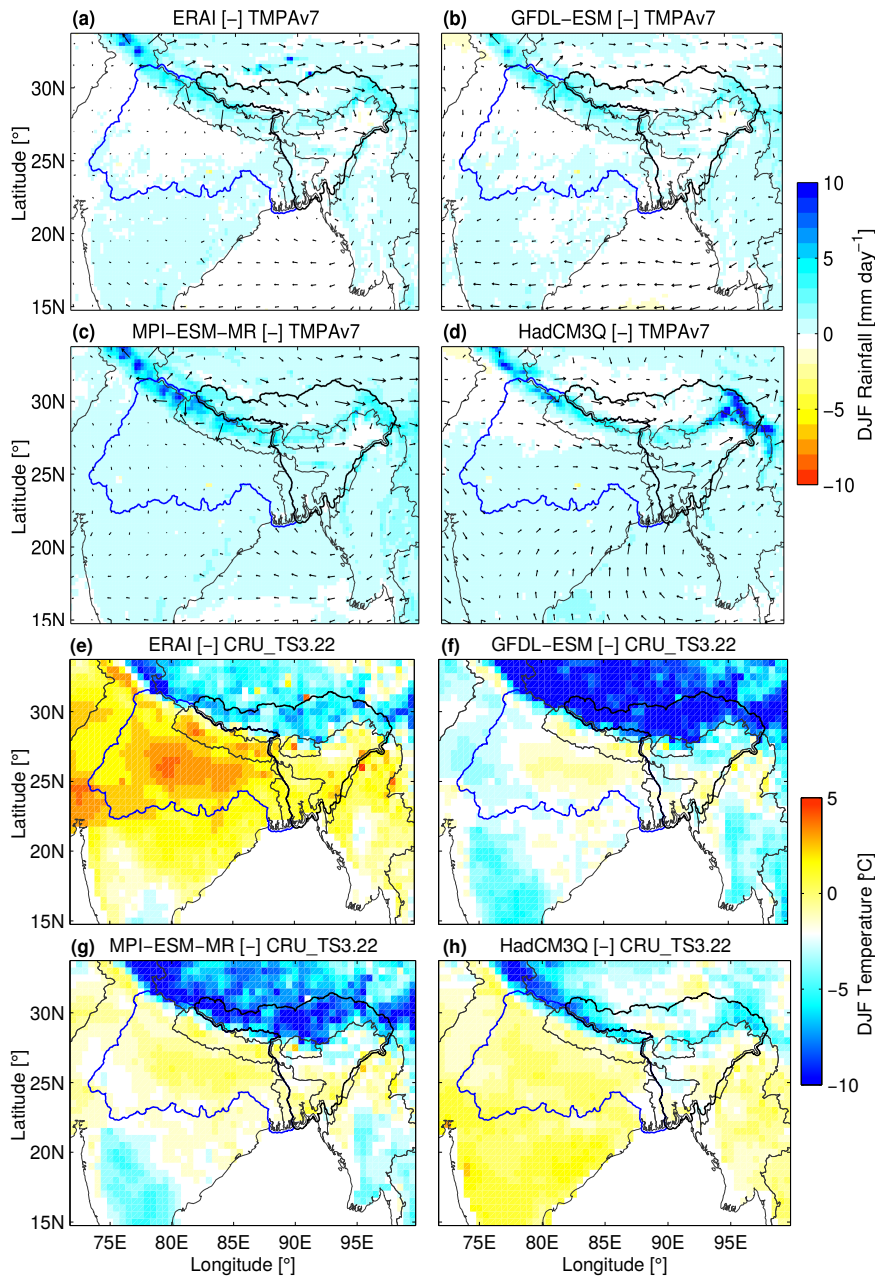


Figure 4.5: (a–d) Mean precipitation (as well as 850 hPa circulation) bias during DJF between various RCM simulations and TMPAv7 (and ERA-Interim) for the period 1998–2012. The corresponding temperature biases with respect to CRU_TS3.22 for the period 1982–2012 are shown from (e–h). Note that the 850 hPa wind differences are plotted as vectors.

Table 4.3: Mean biases in DJF and JJAS precipitation (1998–2012) and temperature (1982–2012) between various RCM simulations and TMPAv7 precipitation and CRU_TS3.22 temperature datasets for the Ganges and Brahmaputra–Meghna River Basins

| Rainfall Data [1998–2012] | DJF [% (°C)] | | JJAS [% (°C)] | |
|------------------------------|--------------|--------------------|---------------|--------------------|
| | Ganges | Brahmaputra–Meghna | Ganges | Brahmaputra–Meghna |
| MERRA | (0.8) | (-1.1) | (0.5) | (-0.4) |
| ERA-Interim | -25 (4.3) | 25 (3.6) | -38 (1.2) | -38 (0.9) |
| RegCM4.4-ERA1 | 75 (1.8) | 125 (-2.3) | 27 (0.3) | 33 (-1.4) |
| RegCM4.4-GFDL-ESM | 75 (-2.4) | 75 (-6) | 27 (-1.2) | 5 (-3) |
| RegCM4.4-MPI-ESM-MR | 250 (-1.2) | 250 (-4.7) | 25 (-1) | 5 (-2.4) |
| PRECIS-HadCM3Q0 | 100 (-1.9) | 275 (-3.4) | -8 (-0.4) | 10 (-0.9) |
| PRECIS-HadCM3Q9 | 100 (-0.9) | 275 (-2.8) | -4 (0.2) | 24 (-0.5) |
| PRECIS-HadCM3Q10 | 50 (-0.7) | 225 (-2.1) | -9 (0.7) | 19 (-0.4) |
| PRECIS-HadCM3Q14 | 175 (-1.6) | 300 (-2.8) | -1 (0.2) | 15 (-0.2) |
| PRECIS-HadCM3Q15 | 250 (-1.5) | 350 (-3.2) | -10 (0.4) | 9 (-0.3) |
| PRECIS-HadCM3Q16 | 50 (0.2) | 325 (-1.7) | -11 (1.6) | 18 (0.3) |
| PRECIS-ENSEMBLE | 121 (-1.1) | 292 (-2.7) | -7 (0.5) | 16 (-0.3) |

2502 -6.0°C in the CMIP5 driven RegCM4.4 simulations (Table 4.3). It should be indicated
 2503 that besides precipitation, the choice of land surface model also affects the surface air
 2504 temperature variations. For instance, [Tiwari et al. \(2015\)](#), in their RegCM4 sensitivity
 2505 experiment, indicated that the Community Land Model (CLM, [Oleson et al., 2013](#))
 2506 with better representation of soil and vegetation layers show improved temperature
 2507 simulation during winter. However, it is also seen that CMIP5 models are generally
 2508 colder over the Himalayan region (see, [Su et al., 2012](#), [Sengupta and Rajeevan, 2013](#)).

2509 Figure 4.6 shows the mean bias for summer monsoon precipitation (and its associated
 2510 850 hPa level circulation) between various RCM simulations and TMPAv7 (and ERA-
 2511 Interim) over the period 1998–2012. It is observed that although RCM simulations are
 2512 able to fairly reproduce the observed spatial patterns of the Indian monsoon rainfall and
 2513 local circulation features, they exhibit significant wet bias along the Himalayan Range
 2514 (Fig. 4.6a–d), with a magnitude of about 20 mm day⁻¹ across eastern Nepal, Bhutan,
 2515 and northern parts of Arunachal Pradesh (northeast India) in the ERA-Interim driven
 2516 simulation (Fig. 4.6a). As such, most RCMs still fail to properly simulate the orographic
 2517 precipitation features along the Himalayan Foothills, in particular, the RegCM4.4 sim-
 2518 ulations tend to underestimate the monsoon circulation features over the Bay of Bengal
 2519 (shown as easterlies in the 850 hPa level wind differences in Fig. 4.6a–d), leading to
 2520 anomalously low precipitation over the sea and Bangladesh. While the PRECIS QUMP
 2521 ensemble mean shown in Fig. 4.6d indicates relatively lower precipitation bias across
 2522 the Ganges River Basin compared to RegCM4.4 simulations, they still fail to represent
 2523 the low orographic features of the Meghalayan Plateau. In general, RegCM4.4 simulates
 2524 higher precipitation (by ~25%) in the Ganges River Basin, whereas PRECIS simula-
 2525 tions show higher precipitation (by ~16%) in the Brahmaputra–Meghna River Basin
 2526 (Table 4.3).

2527 All RCM simulations exhibit cold bias across the Himalayan region (i.e., in the
 2528 northern Brahmaputra River Basin) during the Indian monsoon season as shown in
 2529 Fig. 4.6e–h. However, there are important differences in the low altitude areas, with
 2530 warm biases in the perfect boundary case (RegCM4.4 driven by ERA-Interim, Fig.

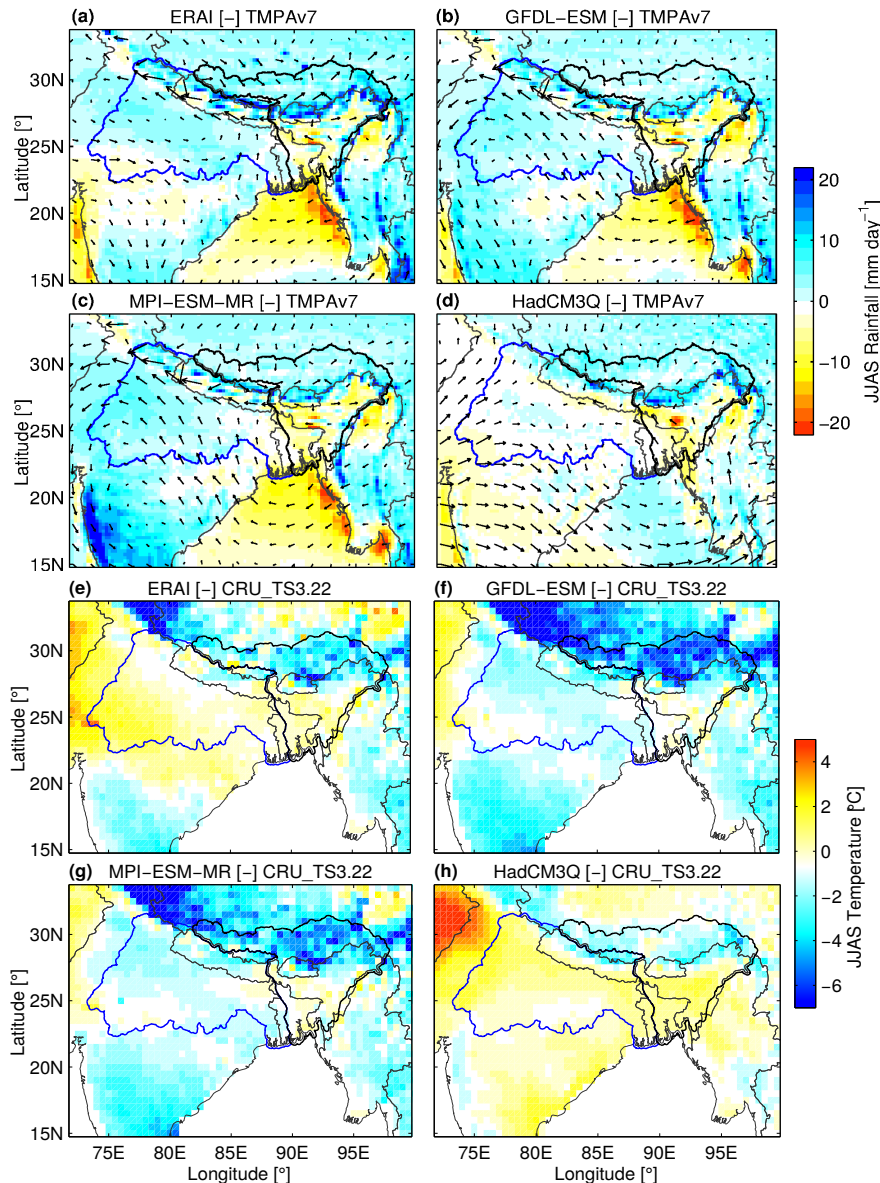


Figure 4.6: (a–d) Mean precipitation (as well as 850 hPa circulation) bias during JJAS between various RCM simulations and TMPAv7 (and ERA-Interim) for the period 1998–2012. The corresponding temperature biases with respect to CRU_TS3.22 for the period 1982–2012 are shown from (e–h). Note that the 850 hPa wind differences are plotted as vectors.

2531 4.6e) and PRECIS simulations and cold bias in the CMIP5 driven RegCM4.4 simu-
 2532 lations (Fig. 4.6f–g). Overall, the CMIP5 driven simulations indicate a cold bias of about
 2533 1.0°C, whereas the PRECIS simulations exhibit a warm bias of 0.5°C in the Ganges
 2534 River Basin when compared to CRU_TS3.22 (Table 4.3). The better results shown
 2535 by PRECIS simulations could be due to the use of flux adjustments in QUMP GCMs
 2536 (McSweeney et al., 2012). The PRECIS model itself has a deeper (2 m) land surface
 2537 model and a higher capacity of water storage to moderate evaporation and latent heat
 2538 (Cox et al., 1999). Warmer temperatures over northern India (including Ganges River

Basin) has been attributed to excessive soil moisture drying and omission of the impact of irrigation (Saeed et al., 2009, Tiwari et al., 2015). Saeed et al. (2009) showed that proper representation of irrigation in RCMs can potentially cool surface temperatures by up to 5°C.

4.5.2 Annual Cycles of precipitation and temperature

Figure 4.7 presents the basin-averaged annual cycle of precipitation (1998–2012) and temperature (1982–2012) for the Ganges and Brahmaputra–Meghna River Basin. The two river basins have very similar annual cycle of precipitation, indicating maximum precipitation in July ($\sim 10.5 \text{ mm day}^{-1}$) and minimum in December (near zero). The precipitation in the Ganges River Basin rise sharply from May–July and reduces sharply from September–October (Fig. 4.7a), while differences in June–August precipitation are smaller for the Brahmaputra–Meghna River Basin (Fig. 4.7b) compared to the Ganges River Basin. RegCM4.4 simulations exhibit substantially higher precipitation (by about 2 mm day^{-1} from April–June in the Ganges River Basin compared to the observed products (i.e., TMPAv7 and GPCCv7) (Fig. 4.7a), while QUMP PPE members indicate a similar pattern in the Brahmaputra–Meghna River Basin (Fig. 4.7b). Interestingly, the QUMP PPE members indicate the peak rainfall in June in the Brahmaputra–Meghna River Basin, while ERA-Interim driven RegCM4.4 simulation exhibits anomalously high peak monsoon rainfall (by about 4 mm day^{-1}) in the same river basin.

Compared to precipitation, climate models are generally able to better simulate the annual cycle of temperature, which has been intensively discussed in successive IPCC reports (see, IPCC, 2007, 2013). Here, it is observed that QUMP PPE members generally exhibit a significantly higher temperature in spring (April–May) in the Ganges River Basin compared to both observed CRU_TS3.22 and RegCM4.4 simulations, although their temporal patterns agree very well with the corresponding observed patterns (Fig. 4.7c). In the Brahmaputra–Meghna River Basin however, the temperature pattern is reversed whereby CMIP5-driven RegCM4.4 simulations tend to exhibit cold bias, while QUMP PPE members mainly differ in the winter months. Note that, HadCM3Q16 has a larger warm bias compared to the rest of QUMP members. Figure 4.7e–f shows the spatially averaged mean annual cycle of lower (at 850 hPa) and higher (at 200 hPa) tropospheric zonal (u) wind components, respectively, over land-only over the RCM domain. It is observed that all RCM simulations tend to provide very good representation of the key large-scale characteristics of tropospheric flow and do not deviate significantly from the parent GCMs (e.g., ERA-Interim). However, there are small differences at 850 hPa level circulation, which may potentially impact large-scale precipitation over the Indian monsoon region.

4.5.3 Onset and withdrawal of monsoon

Precipitation and temperature biases, as well as differences in magnitude and direction of monsoon flow may affect the onset/withdrawal timing of the Indian monsoon. It

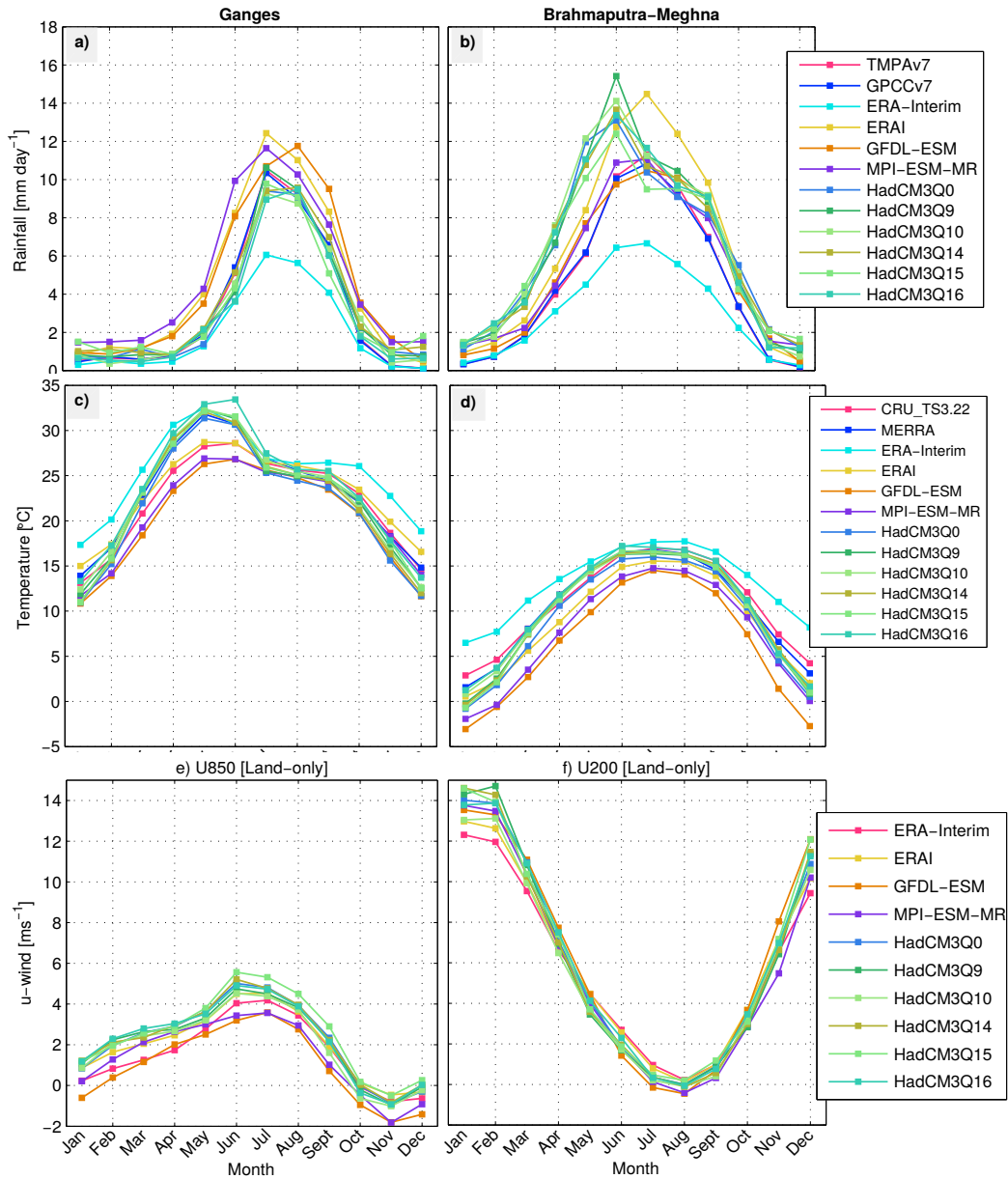


Figure 4.7: The annual cycle of precipitation and temperature based on observations, reanalysis products, and various RCM simulations spatially averaged over the Ganges and Brahmaputra–Meghna River Basins. Mean annual cycle of (a & b) precipitation over the period 1998–2012 and (c & d) temperature over the period 1982–2012. The annual cycle of low level (850 hPa level) and mid-level (200 hPa level) zonal winds shown in (e & f) are computed over land-only for the RegCM4.4 domain.

2578 is seen from Fig. 4.3 that the resulting onset/withdrawal periods from TMPAv7 and
 2579 APHRODITE datasets match very well over the GBM River Basin, and thus, only TM-
 2580 PAv7 products are shown here for comparison. Using the method described in Section
 2581 4.4.2, the onset and withdrawal periods are derived from daily precipitation climatology

(1998–2012) computed from TMPAv7, ERA-Interim, and the RCM simulations and are shown in Fig. 4.8. The mean May–June (corresponding to the onset period) 850 hPa level wind vectors from ERA-Interim and various RCM simulations are also shown. In the RCM domain shown in Fig. 4.8, the monsoon rainfall is first experienced by the coastal regions of Myanmar at around pentad 29–30 (towards the end of May) with the deepening of moist southwesterlies over northern India. Based on the TMPVv7 product (Fig. 4.8a), parts of Assam (northeast India) and few areas across Bangladesh receives earlier monsoon rainfall (at around pentad 30) than the rest of the GBM River Basin. The monsoon onset is estimated at pentad 32 along the Himalayan Foothills, which stretches from northeast India to western Nepal, whereas much of the Gangetic Plains and the northern Brahmaputra River Basin indicate a late monsoon arrival (between pentad 35–36 based on the TMPAv7 product). On average, the monsoon onset is estimated at pentad 34 and 33 for the Ganges and Brahmaputra–Meghna River Basins (see, Table 4.4), which falls between the second and third week of June.

The ERA-Interim precipitation dataset indicates a very similar spatial pattern of monsoon onset in the GBM River Basin, although with a slightly earlier arrival on monsoon rainfall (i.e., pentad 33 and 31 in the Ganges and Brahmaputra–Meghna River Basin, respectively) as indicated in Fig. 4.8b and Table 4.4. The corresponding mean May–June 850 hPa level circulation patterns show intensification of southwesterlies over the Bay of Bengal, Bangladesh, and the western Ganges River Basin, that ultimately turn northwards and drastically loses their strength over the Himalayan Range (Fig. 4.8b). The RegCM4.4 simulations tend to show early (late) onset of the monsoon across the Ganges (Brahmaputra–Meghna) River Basin, which may be associated with wet and dry biases in the river basins (see, Fig. 4.6c–e). Overall, the estimated monsoon onset is found to be around pentad 33 in the CMIP5 driven simulations for the Ganges and Brahmaputra–Meghna River Basins (Table 4.4). Additionally, all RegCM4.4 simulations exhibit a much delayed monsoon onset over Bay of Bengal and are associated with earlier onset over Bangladesh and southern parts of Nepal, which may be attributed to a general under-representation of low level circulation features across the region.

The spatial patterns of onset periods and 850 hPa level circulation patterns shown by QUMP driven PRECIS simulations (Fig. 4.8f) tend to match fairly well with TMPAv7 and ERA-Interim datasets, albeit with a slightly earlier (latter) onset in the Brahmaputra–Meghna (pentad 32) and the Ganges (pentad 35) River Basin (see, Table 4.4). The onset patterns are highly varied among the individual QUMP outputs with some members (e.g., HadCM3Q10 and HadCM3Q16) depicting substantially delayed monsoon (by about 3 weeks) in the western Ganges River Basin, while most members (HadCM3Q9, HadCM3Q10, HadCM3Q14, and HadCM3Q16) simulate early onset over the Brahmaputra–Meghna River Basin.

The monsoon rainfall gradually starts to retreat by the second week of September (at about pentad 50) starting from the western Ganges River Basin, with the weakening of the southwesterlies as indicated in Fig. 4.8g–i. Bangladesh, northeast India, parts of eastern Bhutan experience an extended period of monsoon rainfall compared to the rest of the GBM River Basin (Fig. 4.8g), and sees a complete withdrawal of monsoon by the end of October (at around pentad 60). Other regions such as central Myanmar, southern

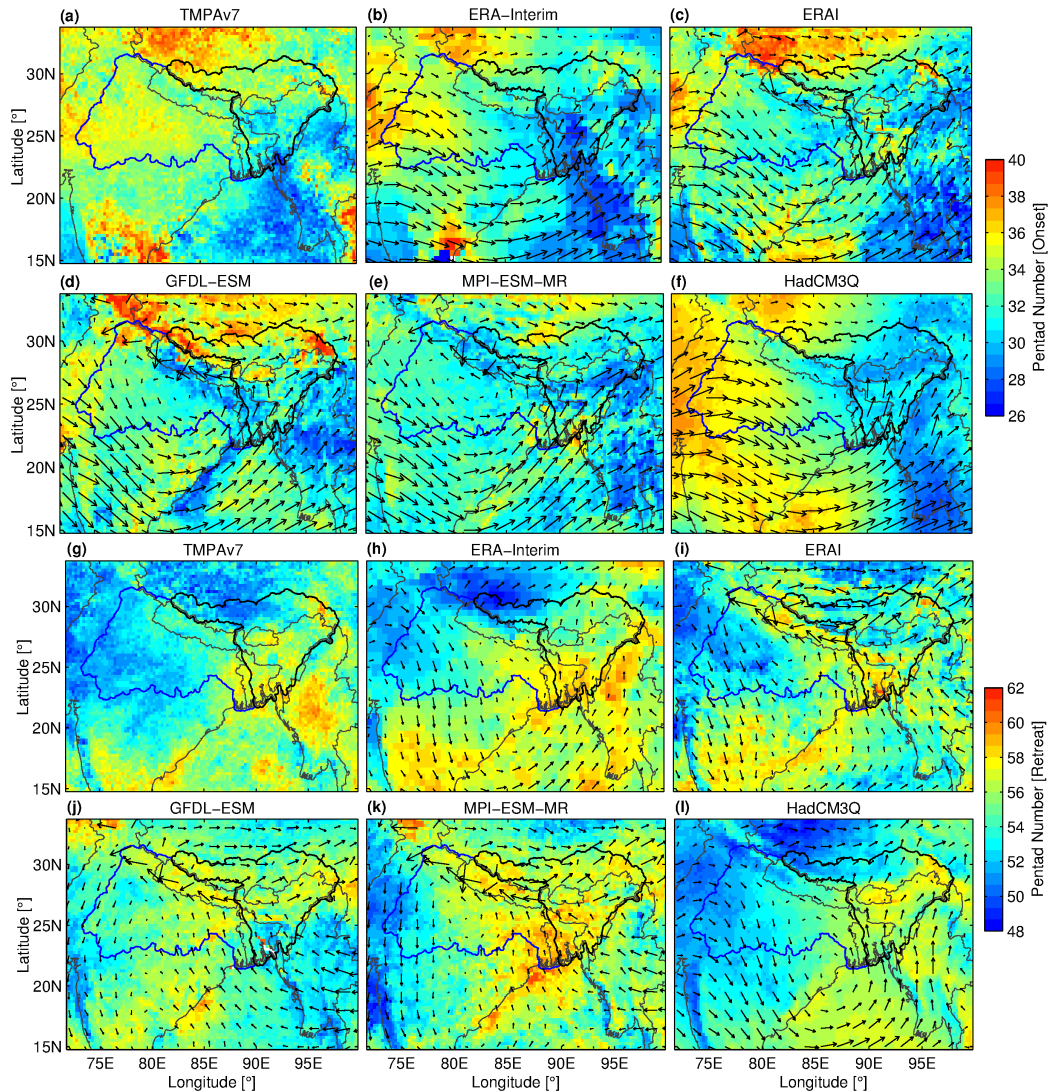


Figure 4.8: Spatial patterns of pentad number representing the onset and withdrawal of the Indian monsoon. These pentads are derived from daily precipitation datasets from TMPAv7, ERA-Interim, and simulated RCM outputs for the period 1998–2012. The May–June mean 850 hPa level circulation patterns are plotted to indicate the monsoon flow during the onset period.

2626 India, and the Bay of Bengal also indicate a late monsoon withdrawal, which are worth
 2627 discussing here. The mean September–October 850 hPa level circulation patterns shown
 2628 by ERA-Interim in Fig. 4.8h indicates a substantial change in magnitude and direction
 2629 of the monsoon, especially over western India where it finally forms a cyclonic zone over
 2630 the Bay of Bengal. It is understood that the reversal of monsoon circulation leads to
 2631 frequent cyclones in the Bay of Bengal and the Andaman Sea during the early months of
 2632 October (see, <https://www.st-andrews.ac.uk/~dib2/asia/monsoon.html>). However,
 2633 it is observed that the southwesterlies still remain very strong over Bangladesh and
 2634 northeast India, which are consistent with the delayed monsoon withdrawal in the region.
 2635 Another important observation in ERA-Interim is the development of strong low level

2636 westerlies over the Tibetan Plateau from September–October, which may be responsible
2637 for excess precipitation amounts over southern China.

Table 4.4: Pentad numbers representing the onset and withdrawal of the Indian monsoon based on observed datasets and various RCM simulations over the period 1998–2012.

| Rainfall data | Onset period | | Withdrawal period | |
|---------------------------------|---------------|--------------------|-------------------|--------------------|
| | Ganges | Brahmaputra–Meghna | Ganges | Brahmaputra–Meghna |
| | Pentad number | Pentad number | Pentad number | Pentad number |
| APHRODITE [1982–2007] | 35 | 32 | 53 | 55 |
| TMPAv7 [1998–2012] | 34 | 33 | 53 | 55 |
| ERA-Interim [1998–2012] | 33 | 31 | 54 | 55 |
| RegCM4.4-ERA1 [1998–2012] | 33 | 33 | 54 | 55 |
| RegCM4.4-GFDL-ESM [1998–2012] | 33 | 34 | 56 | 55 |
| RegCM4.4-MPI-ESM-MR [1998–2012] | 32 | 32 | 56 | 57 |
| PRECIS-HadCM3Q0 [1998–2012] | 34 | 31 | 54 | 56 |
| PRECIS-HadCM3Q9 [1998–2012] | 34 | 30 | 53 | 55 |
| PRECIS-HadCM3Q10 [1998–2012] | 34 | 31 | 54 | 55 |
| PRECIS-HadCM3Q14 [1998–2012] | 33 | 30 | 54 | 56 |
| PRECIS-HadCM3Q15 [1998–2012] | 34 | 32 | 52 | 55 |
| PRECIS-HadCM3Q16 [1998–2012] | 35 | 32 | 53 | 55 |

2638 While the ERA-Interim driven simulation seems to reasonably reproduce the spatial
2639 patterns of monsoon withdrawal across the GBM River Basin (Fig. 4.8i), the CMIP5
2640 driven outputs are not very skillful in reproducing the observed withdrawal features (Fig.
2641 4.8j–k) and are associated with strong westerlies in the Tibetan region. The GFDL-
2642 ESM driven simulation in particular, fail to capture the withdrawal timings across
2643 Bangladesh, Myanmar, and the Bay of Bengal (Fig. 4.8k), which could be related to
2644 their underestimation of monsoon flow over the region (see, Fig. 4.7e–f). In general, the
2645 CMIP5 driven simulations exhibit a delayed monsoon withdrawal by about 2–3 weeks
2646 time in both the river basins (see, Table 4.4). Similar to the onset results, the PRECIS
2647 outputs vary considerably among the six QUMP members (see, Table 4.4), especially
2648 across the western Ganges River Basin. But their ensemble mean appears to provide
2649 a fair representation of the withdrawal pattern (Fig. 4.8l), and its spatially averaged
2650 results are very much consistent with the observed TMPAv7 estimates (see, Table 4.4).
2651 It should be noted however that, PRECIS simulations tend to overestimate the strong
2652 cyclonic features in the Bay of Bengal, when compared to ERA-Interim datasets. The
2653 differences between RCM simulations and TMPAv7 are within one to three pentads over
2654 the GBM River Basin, which could be useful for investigating future changes in onset
2655 and withdrawal of the Indian monsoon.

2656 4.5.4 Trends and interannual variations in precipitation and temper- 2657 ature

2658 The second half of the 20th century saw a period of unprecedented increase in GHG and
2659 aerosol concentrations, leading to increased surface and tropospheric warming across the
2660 globe (IPCC, 2007, 2013). While global warming is expected to produce more rainfall
2661 over the Indian monsoon region (Kumar et al., 2006, Kripalani et al., 2007), the monsoon
2662 rainfall is considered to be decreasing in the recent decades, likely attributed to increas-
2663 ing aerosol affects (Ramanathan et al., 2005, Chung and Ramanathan, 2006). The rain-
2664 fall decrease is found to be particularly significant over the Brahmaputra–Meghna River

Basin since 1998 (Khandu et al., 2016c). By improving the representation of aerosol and biogeochemistry components in climate model's (both GCMs and RCMs), their potential to simulate such affects are likely to improve. The models ability to simulate regional climate trends and changes in response to either external forcings or interdecadal variability modes provides additional confidence in their future climate projections. In this section, the RCM simulations of precipitation (1998–2012) and temperature (1982–2012) are evaluated for their seasonal (DJF and JJAS) trends and interannual variations.

Figure 4.9 shows the spatially averaged DJF and JJAS precipitation anomalies (in mm/month) derived from TMPAv7 and various RCM simulations in the Ganges and Brahmaputra–Meghna for the period 1998–2012. The seasonal precipitation anomalies show substantial interannual variations over the last 15-year period (1998–2012). For instance, the DJF precipitation exhibits high interannual variability from 2000 to 2007 in the Ganges River Basin, whereas the Brahmaputra–Meghna River Basin has experienced increased precipitation variations between 2006 and 2010 (Fig. 4.9a–b). Similar temporal patterns are found during the Indian monsoon season, but with a much higher amplitude. In particular, the Ganges River Basin has seen a sharp increase in monsoon rainfall in 2011 (Fig. 4.9a), which is not observed in the Brahmaputra–Meghna River Basin (see, Fig. 4.9b). These anomalous variations are likely associated with large-scale ocean-atmospheric fluctuations such as ENSO and IOD, which have been shown to have varying impacts on rainfall anomalies in the Ganges and Brahmaputra–Meghna River Basin (e.g., Pervez and Henebry, 2015, Khandu et al., 2016c). For example, the large negative JJAS precipitation anomaly in the Brahmaputra–Meghna River Basin in 2006 had a strong influence from a negative IOD mode (Fig. 4.9d), while ENSO is shown to have a larger impact on precipitation in the Ganges River Basin, with strong negative anomalies in 2002, 2009, and 2011 (Fig. 4.9c).

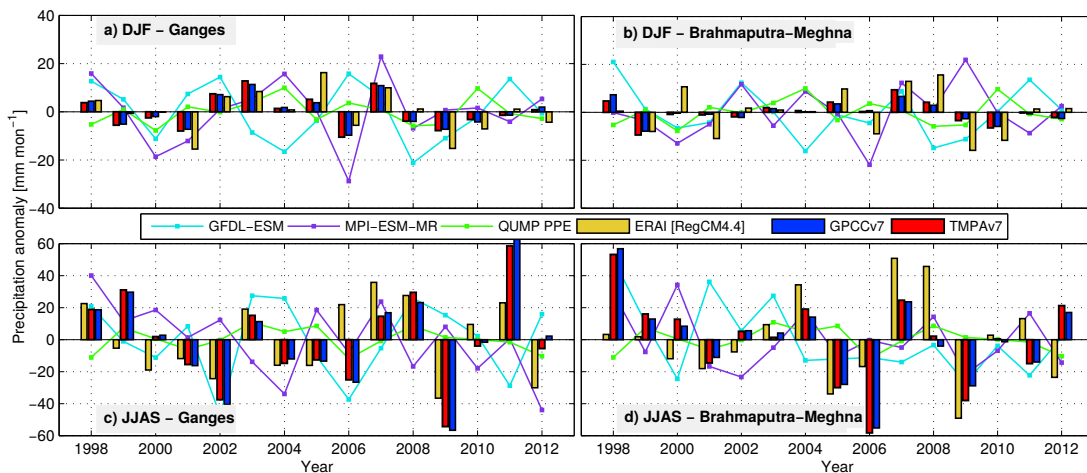


Figure 4.9: Monthly precipitation anomalies (1998–2012) for the GBM River Basin based on observed datasets, ERA-Interim, and RCM simulations. (a & c) DJF and JJAS precipitation anomalies for the Ganges River Basin, and (b & d) DJF and JJAS precipitation anomalies for the Brahmaputra–Meghna River Basin.

The RCM simulations are able to reproduce the high interannual variations in the two river basins, but tend to either miss or underestimate the ENSO and IOD induced

2692 variations, especially during the monsoon season (Fig. 4.9a–d). Compared to the GCM
2693 driven outputs, the ERA-Interim driven simulation shows a much improved represen-
2694 tation of seasonal precipitation anomalies in the GBM River Basin, although there are
2695 large differences, especially between 1998 and 2004 in the Brahmaputra–Meghna River
2696 Basin (Fig. 4.9d). As a result, it is shown to have a higher correlation (i.e., 0.6) for both
2697 seasons with TMPAv7 precipitation anomalies. This indicates that regional climate re-
2698 sponses are well reproduced by RCMs when forced by perfect boundary conditions (e.g.,
2699 ERA-Interim and observed SSTs). Among the GCM driven outputs, the MPI-ESM-
2700 MR-driven simulation appears to be closer to TMPAv7 datasets, while QUMP driven
2701 PRECIS simulations indicate a poor representation of seasonal variation, likely due to
2702 their inability to simulate the changing phase of ENSO and IOD. In terms of the precip-
2703 itation trend, RCMs (particularly, RegCM4.4 simulations) tend to exhibit a decreased
2704 monsoon rainfall in both river basins, particularly in the Brahmaputra–Meghna River
2705 Basin, which are in agreement with the observed trends (see, [Khandu et al., 2016c](#)).

2706 Figure 4.10 shows the spatially averaged DJF and JJAS temperature anomalies based
2707 on CRU_TS3.22, ERA-Interim, MERRA, and RCM simulations for the two river basins
2708 for the period 1982–2012. The corresponding temperature trends are presented in Ta-
2709 ble 4.5. In general, all the datasets indicate a positive temperature trend in the GBM
2710 River Basin for both the seasons from 1982–2012. The temperature variations (both
2711 observed and RegCM4.4 simulations) are well within one standard deviation of six
2712 QUMP members. The largest temperature variations are seen during the winter period
2713 (Fig. 4.10a–b), whereas lowest variations are seen in the Brahmaputra–Meghna River
2714 Basin during the monsoon season, varying by only about 0.5°C. The surface tempera-
2715 ture over the GBM River Basin has increased considerably over the past three decades
2716 and the Brahmaputra–Meghna River Basin has warmed more than the Ganges River
2717 Basin (Table 4.5). Note that ERA-Interim and MERRA indicates reduced temperature
2718 trends during JJAS in the Ganges River Basin, which are not consistent with the ob-
2719 served CRU_TS3.22 dataset (Fig. 4.10c–d). The observed DJF and JJAS temperature
2720 trends are reproduced by most of the RCM simulations (see, Table 4.5). Similarly, using
2721 RegCM3 ([Pal, 2007](#)) with boundary conditions from CMIP3 GCMs, [Dash et al. \(2012\)](#)
2722 found increasing temperature trends over northeast India between 1975 and 2005.

2723 In order to assess the impacts of SST variations on surface temperatures over the
2724 GBM River Basin, the temperature anomalies from Fig. 4.9 are correlated with observed
2725 SST anomalies (obtained from the UK Met Centre, <http://www.metoffice.gov.uk/hadobs/hadisst/>) for the period 1982–2012. The DJF and JJAS SST anomalies (50°S–
2726 50°N) are first decomposed into two major leading modes of variability by applying the
2727 PCA decomposition technique (see, [Preisendorfer, 1988](#)). Figure 4.11 shows the spatial
2728 patterns (or EOFs) and temporal components (PCs) of the first two leading modes of
2729 variability, which explains about 50% of the variations. The first mode (Fig. 4.11a &
2730 c) shows the familiar features of ENSO mode, with strong (positive) SST anomalies
2731 over the equatorial Pacific Ocean during both the seasons. The second mode appears to
2732 indicate a bipolar pattern with positive (negative) anomalies in the northern (southern)
2733 hemisphere during winter (Fig. 4.11b), and strong positive anomalies east of the Niño.3.4
2734 region (Fig. 4.11d).
2735

Table 4.5: DJF and JJAS temperature trends (in °C/decade) estimated from observed, reanalyses, and RCM simulated temperature datasets for the Ganges and Brahmaputra–Meghna River Basins from 1982–2012. The trend values significant at 95% confidence level are highlighted in bold.

| Temperature data | DJF temperature trend [°C/dec] | | JJAS temperature trend [°C/dec] | |
|--------------------|--------------------------------|--------------------|---------------------------------|--------------------|
| | Ganges | Brahmaputra–Meghna | Ganges | Brahmaputra–Meghna |
| CRU_TS3.22 | 0.28 | 0.53 | 0.17 | 0.31 |
| MERRA | 0.07 | 0.40 | -0.31 | 0.22 |
| ERA-Interim | 0.20 | 0.29 | -0.08 | 0.07 |
| RegCM4-ERA-Interim | 0.30 | 0.25 | 0.02 | 0.06 |
| RegCM4-GFDL-ESM | 0.40 | 0.21 | 0.28 | 0.30 |
| RegCM4-MPI-ESM-MR | 0.30 | 0.53 | 0.17 | 0.24 |
| PRECIS [ensemble] | 0.28 | 0.40 | 0.34 | 0.33 |

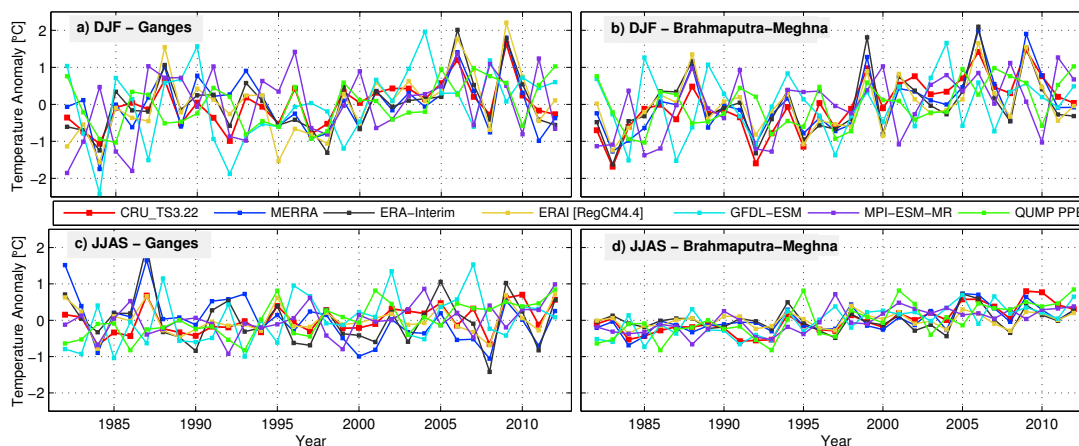


Figure 4.10: Basin-averaged temperature anomalies (1982–2012) for the GBM River Basin based on observed datasets, MERRA, ERA-Interim, and RCM simulations. (a & c) DJF and JJAS temperature anomalies for the Ganges River Basin, and (b & d) DJF and JJAS temperature anomalies for the Brahmaputra–Meghna River Basin.

2736 Accordingly, the leading temporal patterns in Fig. 4.11e & g resembles the ENSO
 2737 index (represented by SST variations in the Niño3.4 region), while the second mode
 2738 (Fig. 4.11f & h) largely depicts a trend-like pattern, which is found to be statistically
 2739 significant (at 95% confidence level) for the monsoon season (Fig. 4.11h). Thus, it should
 2740 be noted here that SST has warmed considerably in the equatorial and northern Indian
 2741 in JJAS between 1982 and 2012. Roxy et al. (2014) found that western Indian Ocean
 2742 has experienced anomalous warming of 1.2°C during the JJAS between 1901 and 2012.
 2743 Such anomalous warming in the Indian Ocean affects the zonal SST gradients, and has
 2744 the potential to alter the behaviour of Indian monsoon circulation and rainfall (Turner
 2745 and Annamalai, 2012, Roxy et al., 2014).

2746 The observed surface temperature anomalies in both river basins are found to be
 2747 significantly correlated with global SST anomalies as shown in Table 4.6. The correlation
 2748 coefficients are higher especially during the monsoon season over the northern Indian

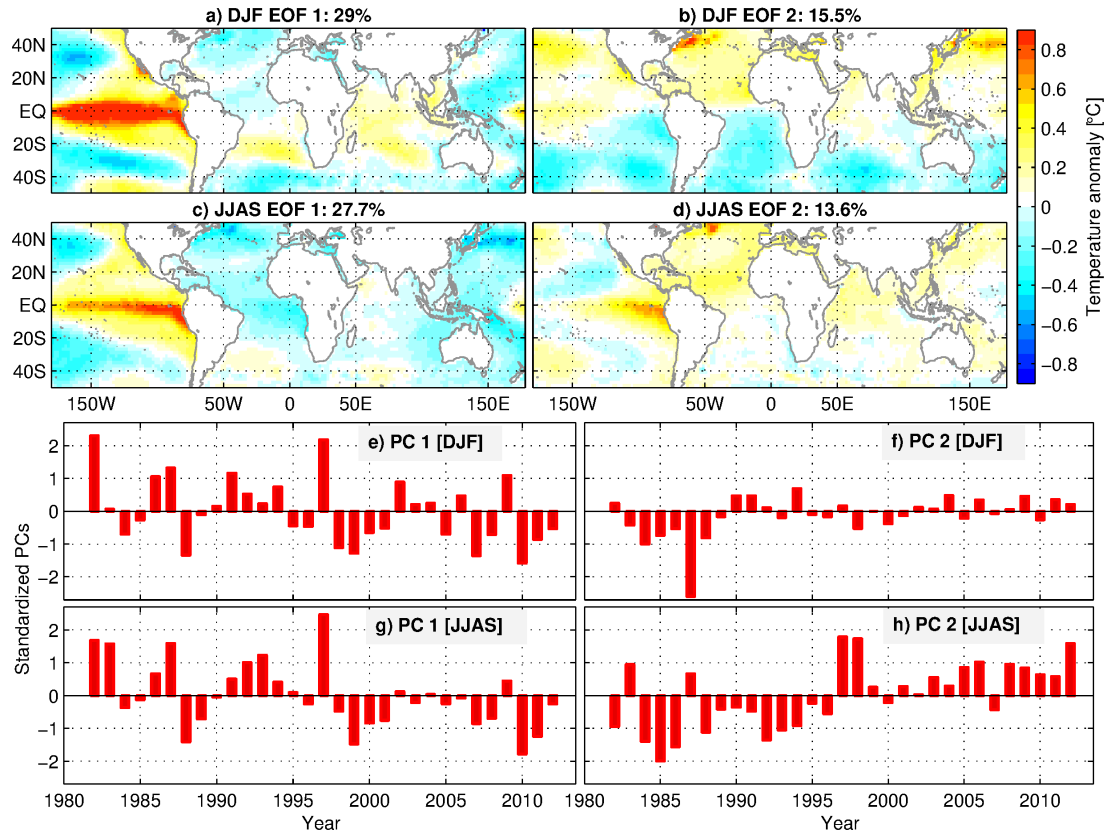


Figure 4.11: PCA decomposition of the DJF and JJAS global (50°N–50°S) SST anomalies. Spatial patterns (or EOFs) of the first two leading modes of DJF (**a** & **b**) and JJAS (**c** & **d**) SST anomalies. The corresponding temporal patterns (or PCs) are shown in (**e** & **f**) for DJF and (**g** & **h**) for JJAS.

Table 4.6: Correlation between PC 2 (Fig. 4.11h) and basin-averaged temperature anomalies of the Ganges and Brahmaputra–Meghna River Basin for the period 1982–2012. The correlation coefficients presented here are found to be significant at 95% confidence level.

| Temperature data | Ganges | Brahmaputra–Meghna |
|-------------------|--------|--------------------|
| CRU_TS3.22 | 0.46 | 0.60 |
| ERA-Interim | 0.32 | 0.49 |
| MERRA | 0.42 | 0.55 |
| RegCM-ERA-Interim | 0.34 | 0.40 |
| RegCM4-GFDL-ESM | 0.30 | 0.39 |
| MPI-ESM-MR | 0.37 | 0.65 |
| PRECIS (ensemble) | 0.43 | 0.63 |

2749 Ocean. The surface temperature anomalies are correlated with PC 2 (Fig. 4.11h) of the
 2750 global SST for the JJAS in order to show how RCMs respond to the warming Indian
 2751 ocean. The results are presented in Table 4.6. Both CRU_TS3.22 and MERRA indicated
 2752 very similar magnitude of correlation with SST datasets, both of which are significant
 2753 at 95% confidence level. Similarly, all RCM simulations exhibit significant correlation

with SST datasets, albeit with varying magnitudes (see, Table 4.6), indicating that the models are able to simulate the response of the warming Indian Ocean. This is consistent with most previous studies of e.g., Chung and Ramanathan (2006), Roxy et al. (2014). Chung and Ramanathan (2006) reported a Indian Ocean warming of about 0.6–0.8°C since the 1950s, while Roxy et al. (2014) reported an anomalous warming of 1.2°C since 1901.

4.6 Concluding remarks

High-resolution Regional Climate Models (RCMs), through improved representation of topography and land surface process, has been shown to provide realistic local and regional circulation and precipitation features suitable for regional climate impact studies. There is renewed interest in applying RCMs over the Indian sub-continent and the Himalayan region, partly driven by the challenges of simulating the Indian monsoon and the strong spatial variability caused by the complex topographic features. In this chapter, various RCM outputs simulated by Regional Climate Model version 4.4 (RegCM4.4) and Providing REgional Climate Information for Impact Studies (PRECIS) are evaluated against observed precipitation and temperature datasets to assess for ability to reproduce the seasonal variations, onset/withdrawal of the Indian monsoon, and long-terms in the Ganges–Brahmaputra–Meghna (GBM) River Basin. The GBM River Basin represents a spatially diverse hydrological regime and is one of the most populated and climate-vulnerable hydrological river basins in the world.

RegCM4.4 simulations are carried out over the Indian monsoon region [2°N–37°N, 61°E–108°E] for the period 1982–2012, with boundary conditions from ERA-Interim and two Global Climate Models (GCMs) from the Coupled Model Intercomparison Project phase 5 (CMIP5), while PRECIS datasets contain six perturbed physics ensemble (PPE) simulations conducted by the UK Met office over the South Asian continent. The results indicated that in general, all RCM simulations sufficiently capture the seasonal spatial and temporal distribution of precipitation and temperature across the GBM River Basin. In particular, the high precipitation amounts in the Western Himalayas during December–January (DJF), and along the Himalayan Foothills during June–September (JJAS) or the monsoon season are reproduced reasonably well, with substantial wet bias across these regions. The wet (dry) bias along the Himalayan Foothills (Bay of Bengal) in RegCM4.4 simulations are found to be associated with strong (wet) southwesterlies in RegCM4.4 simulations, whereas PRECIS fails to represent the key orographic features of the Meghalayan Plateau. Overall, GCM-driven RegCM4.4 simulations overestimate monsoon precipitation by about 26% and 5% in the Ganges and Brahmaputra–Meghna River Basin, respectively, while the QUMP driven PRECIS simulations indicate a dry (about 7%) and wet (about 16%) bias for the two river basins.

Both RegCM4.4 and PRECIS simulations indicate an intense cold bias (by up to 10°C) in the Himalayas, potentially due to strong northerlies and intense precipitation in the region. The cold bias is generally stronger in the GCM driven RegCM4.4 simulations, whereas PRECIS simulations had a similar magnitude of bias to those shown

2795 by ERA-Interim driven RegCM4.4 simulations. The annual cycle of precipitation and
2796 temperature are reproduced fairly well by most of the RCM simulations, except that
2797 they tend to show high precipitation amounts between April and May in the Ganges
2798 (RegCM4.4 simulations) and Brahmaputra–Meghna (PRECIS simulations) River Basin.
2799 Accordingly, RegCM4.4 simulations tend to indicate an early Indian monsoon onset in
2800 the Ganges River Basin, while PRECIS simulations exhibit a delayed monsoon with-
2801 drawal in the Brahmaputra–Meghna River Basin. Despite large spatial variations in
2802 onset and withdrawal periods across the GBM River Basin, the basin-averaged results
2803 agree reasonably well with the observed timings. Nevertheless, there are substantial dif-
2804 ferences in the September–October circulation (at 850 hPa level) patterns corresponding
2805 to the withdrawal period over the basin.

2806 Although GCM driven simulations are generally poor in representing the interannual
2807 variability of precipitation and DJF temperature variations, the ERA-Interim-driven
2808 simulations agree well with observed precipitation anomalies, indicating a correlation of
2809 about 0.6 in both the river basins. The precipitation variations associated with El Niño
2810 Southern Oscillation (ENSO) and Indian Ocean Dipole (IOD) are also well-captured by
2811 ERA-Interim driven RegCM4.4 simulation. It is also seen that all GCM driven simula-
2812 tions feature significant positive surface temperature trends in the GBM River Basin,
2813 which are consistent with the observed temperature trends. The surface warming in the
2814 GBM River Basin appears to be partly driven by the warming Indian Ocean, as surface
2815 temperature variations show significant correlation with sea surface temperature (SST)
2816 anomalies in the equatorial and northern Indian Ocean. GCM-driven simulations are
2817 also able to reproduce the correlation results, indicating that regional SST responses
2818 are well simulated by the RCMs.

2819 5. Future projection of droughts and 2820 wet events

2821 5.1 Introductory remarks

2822 The ongoing climate change impacts and rapidly increasing population has placed enormous
2823 pressure on the sustainability of freshwater in the GBM River Basin. Various
2824 global, continental, and regional studies have reported that warming over South Asia is
2825 likely to be above global average (see, [IPCC, 2007, 2012, 2013](#), and references therein).
2826 As climate warms, the AOGCM studies have generally suggested an increase in Indian
2827 monsoon rainfall ([Kripalani et al., 2007](#)), which will be further characterized by
2828 an increase in frequency and intensity of extreme rainfall events ([Seneviratne et al.,
2829 2012, Mittal et al., 2014, Whitehead et al., 2015](#)). As such, the IPCC Special Report on
2830 Extremes (SREX, [IPCC, 2012](#)) noted that flood risk is heavily concentrated in India,
2831 Bangladesh, and China, and in particular, flooding in Bangladesh and parts of north
2832 and northeastern India, is a normal and frequently recurrent phenomenon. On the other
2833 hand, with global warming, there is a potential for more drying that is being fuelled by
2834 an increase in potential evapotranspiration. More specifically, climate models suggest
2835 strong tendency for wet areas to get wetter and dry areas to become drier ([Dai, 2013,
2836 Trenberth et al., 2014](#)), even though the IPCC SREX report ([IPCC, 2012](#)) has been
2837 more cautious on interpreting their long-term observed and projected trends at the re-
2838 gional level. While extreme wet conditions can have wide humanitarian impacts (e.g.,
2839 mortality, diseases, and homelessness), prolonged dry conditions will lead to droughts
2840 and severe water shortages. For a region, that is heavily dependent on rain-fed water
2841 supply, prolonged dry spells during the monsoon season will substantially reduce surface
2842 and groundwater resources.

2843 The GBM River Basin, which is located within the geographical domain of climate
2844 extremes, exhibits a broad range of characteristics such as (i) in topography, from the
2845 world's highest mountains to the largest deltas, (ii) in precipitation, from arid to semi-
2846 arid areas of western Ganges River Basin to the vast alluvial plains subject to flooding
2847 due to intense orographic rains along the Himalayan Foothills, (iii) large snow/glacial
2848 areas that are highly vulnerable to warming, and (iv) in population, with over 650 mil-
2849 lion people. Many recent studies have indicated that the GBM River Basin has been
2850 experiencing significant decline in freshwater availability (surface and groundwater) over
2851 the last few decades as a result of a general decline in monsoon rainfall and excessive
2852 withdrawal of surface and groundwater to meet it's increasing socio-economic activi-
2853 ties ([Tiwari et al., 2009, Shamsudduha et al., 2009a, Papa et al., 2015, Shahid et al.,
2854 2015, Khandu et al., 2016b](#)). Except for some isolated areas of glacier stability, the Hi-
2855 malayan glaciers are at a rapid decline, directly impacting surface water availability in
2856 the downstream areas during winter and spring ([Barnett et al., 2005, Bates et al., 2008,
2857 Immerzeel et al., 2012, Bajracharya et al., 2015](#)). Several studies have investigated the
2858 climate extremes on various spatial domains within the GBM River Basin, specifically

2859 focussing on the Indian monsoon season (e.g., Roy and Balling, 2004, Baidya et al.,
2860 2008, Rajeevan et al., 2008, Goswami et al., 2010, Singh and Ranade, 2010, Shahid,
2861 2011, Singh et al., 2014, Vinnarasi and Dhanya, 2016, among others). In particular,
2862 Goswami et al. (2010) found that the heavy rainfall events have largely declined in the
2863 Brahmaputra–Meghna River Basin (particulary in northeast Inda) between 1975 and
2864 2006, while Vinnarasi and Dhanya (2016) also reported a significant reduction of wet
2865 spells during the monsoon over major parts of the GBM River Basin based on 113 years
2866 of high-resolution observed daily rainfall data. These studies suggest that is an appar-
2867 ent shift in the monsoon rainfall distribution with wet regions becoming drier and dry
2868 regions becoming wetter, contrary to most climate model projections.

2869 Based on the projected increase in rainfall simulated by CMIP5 (Taylor et al., 2012)
2870 GCMs, Masood et al. (2015) estimated an increased runoff by about 16%, 33%, and
2871 39.7% in the Ganges, Brahmaputra, and Meghna River Basins, respectively, by 2100
2872 (2075–2099) compared to the base period 1979–2003. Like many GCM projections,
2873 regional climate models based on CMIP3 GCMs also project an increase in Indian
2874 monsoon rainfall with potential for more floods (e.g., Kumar et al., 2006, Ahmed and
2875 Suphachalasai, 2014, Mittal et al., 2014, Whitehead et al., 2015). Large-scale water
2876 transfers in the upstreams of the GBM river system may have the potential to reduce
2877 flows further downstream, which will enhance salt water intrusion, reduce water supply
2878 and agricultural yields, and affect other crucial ecosystems in the delta region. De-
2879 spite projections of increased rainfall, the Indian monsoon is found to be weakening
2880 in response to the warming Indian Ocean (Chung and Ramanathan, 2006, Rao et al.,
2881 2008, Roxy et al., 2014) and radiative cooling effects from the increasing aerosol con-
2882 centrations over South Asia (Ramanathan et al., 2005, Lau et al., 2009). Under current
2883 projections, this weakening response is likely to continue for the next two decades, which
2884 will inevitably be associated with more dry conditions. Prolonged dry conditions due
2885 to insufficient precipitation and/or high evapotranspiration can lead to meteorological
2886 droughts, which may result in severe water scarcity under the current trend of over-
2887 exploitation of water resources. Regional climate models (RCMs) predict an increase
2888 in duration and intensity of droughts, particularly in the arid and semi-arid areas of
2889 Bangladesh and India (Ahmed and Suphachalasai, 2014). Regional models also project
2890 a decrease (or drying) in stream flow that currently have low stream flows, potentially
2891 causing extended hydrological drought conditions (e.g., Ahmed and Suphachalasai, 2014,
2892 Whitehead et al., 2015).

2893 Although many studies have examined the various characteristics of extreme wet
2894 and dry conditions (in terms of past and future variations of intensity, spell, onset,
2895 withdrawal, etc.) based on observed and modelled precipitation, the general conclusions
2896 drawn from the studies are often contradictory and not coherent enough for put them
2897 into policy decisions in managing the transboundary water management. Considering
2898 the spatial variability of precipitation and its associated extremes, the lack of adequate
2899 *in-situ* gauge networks and substantial model uncertainties resulting from inaccurate
2900 representation of orographic precipitation patterns along the Himalayas, can have con-
2901 siderable impact on the results. On the other hand, most studies focus exclusively on the
2902 wet and dry spells during the Indian monsoon season. Given the general nature of the
2903 GBM River Basin and increasing societal demands for more freshwater resources, it is

crucial to highlight the important characteristics of extreme wet and dry conditions and their expected probability of occurrences (in terms of return periods) for the remaining 21st century. Therefore, this chapter will primarily focus on examining the probability of occurrences of extreme wet and dry events using simulated monthly precipitation data from two RCMs: (i) RegCM4.4 (Giorgi et al., 2012) and PRECIS (Jones et al., 2004) driven by coarse scale GCMs and an ensemble of eight CMIP5 GCMs under various warming and socio-economic scenarios in the GBM River Basin.

The characteristics of extremes are usually derived from standardized anomalies of, for example precipitation time-series (either based on daily or monthly), with a statistically sound threshold value (e.g., based on percentiles). Most studies have adopted a specific threshold value to identify extreme precipitation events (e.g., Goswami et al., 2006, Klein Tank et al., 2006, Baidya et al., 2008, Rajeevan et al., 2008, Shahid, 2011) following the recommendations of Expert Team on Climate Change Detection and Indices (ETCCDI) of the World Climate Research Programme (WCRP), while others determine the length of wet and dry spells of the Indian monsoon season to study the changes in extreme wet and dry spells (e.g., Singh and Ranade, 2010, Singh et al., 2014, Vinnarasi and Dhanya, 2016). Standardized indices developed from monthly precipitation time-series and/or water storage components (such soil moisture, runoff, and TWS) are most commonly used to relate the impacts of extreme dry and wet spells to water resources management. For instance, the popular Palmer Drought Severity Index (PDSI, Palmer, 1965) and its derivatives incorporate multiple climatic variables (e.g. evapotranspiration, soil moisture) with monthly precipitation time-series to monitor the impacts of prolonged deficit precipitation on various hydrological systems at various time-scales. While such an inclusive system is desirable to understand the hydrological process and its associated impacts (e.g., agricultural, hydrological and socio-economic), interpretation of such a system remains a challenge (Awange et al., 2016b).

For consistent interpretation of wet and dry spells and study their impacts on various systems (e.g., hydrological, agricultural), the World Meteorological Organization (WMO, 2012) recommends to use the Standardized Precipitation Index (SPI, McKee et al., 1993). As such, SPI can be applied to both daily and monthly precipitation and other water storage components and is a powerful tool for analysing wet and dry spells on various time-scales. Therefore, in this chapter, the wet and dry spells are categorized into severe and extreme wets or droughts based on the duration of wet and dry spells estimated using the SPI derived from monthly precipitation datasets of various climate model outputs. It should be noted, however that wet and drought are not quite the opposite and wet events could imply either abundant water or widespread flooding or both, while droughts imply prolonged periods of deficit rainfall or dry spell and can be highly catastrophic in terms of water availability.

This chapter is organized as follows: the datasets used and analysis methods are discussed in Section 5.2. Section 5.3 presents the results and Section 5.4 discusses the key impacts of future droughts in the GBM River Basin and its water resources.

2945 5.2 Data and methods

2946 5.2.1 Model and observational data used

2947 The model data used here include monthly precipitation and temperature data simu-
2948 lated by RegCM4.4 (Giorgi et al., 2012) and PRECIS (Jones et al., 2004) model over
2949 the Indian monsoon region for the period 1982 to 2100, whose detailed description is
2950 provided in Section 4.3. Both regional models are hydrostatic in nature and consists of
2951 very similar dynamics and physics but are coupled with different land surface models.
2952 For the historical period (1982-2012), RegCM4.4 is run at a 25 km grid resolution over
2953 the core Indian monsoon region covering most of South Asia and parts of the Tibetan
2954 Plateau and Southeast Asia (2°N – 37°N, 61°E–108°E). The model is forced by ERA-
2955 Interim (Dee et al., 2011) and two CMIP5 models: (i) GFDL-ESM2M (Dunne et al.,
2956 2012) and (ii) MPI-ESM-MR (Giorgetta et al., 2013) between 1981 and 2012 but only
2957 the MPI-ESM-MR is used for the future period (2013–2099). CMIP5 ESMs are fully
2958 coupled ocean-atmospheric models with added capability to explicitly represent biogeo-
2959 chemical processes that interact with the physical climate (Flato, 2011, Taylor et al.,
2960 2012). In the CMIP5 experiment, the historical simulations (1850–2005) are forced by
2961 both natural and anthropogenic conditions derived from observational datasets whereas
2962 the future projections (2006–2100) are largely based on four prescribed pathways of
2963 GHG concentrations, referred to as Representative Concentrative Pathways (RCP, Moss
2964 et al., 2010). The two ESMs used here are based on RCP4.5, which represents a modest
2965 warming scenario with a radiative forcing of 4.5 Wm^{-2} by 2100.

2966 The PRECIS model data used here include six PPE members for the period 1982–
2967 2100 that were previously simulated over the South Asian CORDEX domain at 25
2968 km grid by the UK Met Office (see details in, Collins et al., 2011, McSweeney et al.,
2969 2012, Caesar et al., 2015). The six PPE members (namely, HadCMQ0, HadCMQ9,
2970 HadCMQ10, HadCMQ14, HadCMQ15, and HadCMQ16) have been forced by the widely
2971 used IPCC SRES (IPCC, 2000) A1B emission scenario that describes a future world
2972 of very rapid economic growth, in which global population that peaks in 2050 and
2973 declines thereafter, and rapid introduction of new and more efficient technologies. A1B
2974 is a medium-high emission scenario with a projected warming of around 2.5°C by 2100
2975 as opposed to a 2.0°C warming in the RCP4.5 (see, Knutti and Sedláček, 2013). In
2976 addition, eight CMIP5 models with RCP4.5 are also used to supplement the findings in
2977 this chapter. A general description of the CMIP5 models are given in Table 5.1.

2978 Both the GCMs and RCM outputs are assessed for their ability to simulate ba-
2979 sic drought characteristics by comparing them with available observational dataset for
2980 the most recent period (1982-2012). Observational datasets used here include monthly
2981 precipitation products from the GPCC version 7 (hereinafter referred to as GPCCv7,
2982 Becker et al., 2013), and CRU version TS3.22 (hereinafter as CRU_TS3.22, Harris et al.,
2983 2013). The GPCC dataset uses up to 40,000 gauge stations from across the world and
2984 is considered the most comprehensive global-land precipitation record available, while
2985 CRU typically consists of precipitation and temperature records from 5,000 to 10,000
2986 stations globally. Over the GBM River Basin, the station density per grid ranges from

Table 5.1: Basic descriptions of 8 CMIP5 ESMs including their modelling group, name, and their horizontal (grid dimension) and vertical (number of atmospheric levels, L) resolution of atmospheric model. All models are based on the initial realistaion (r1i1p1) and forced by RCP4.5 scenario.

| Modelling Centre | Model Name | Horizontal (vertical) resolution |
|---|------------|----------------------------------|
| Canadian Centre for Climate Modelling and Analysis | CanESM2 | 128 × 64(L35) |
| National Center for Atmospheric Research | CCSM4 | 280 × 200(L27) |
| Centre National de Recherches Meteorologiques/Centre Europeen de Recherche et de Formation Avancees | CNRM-CM5 | 256 × 128(L31) |
| Geophysical Fluid Dynamics Laboratory | GFDL-ESM2M | 144 × 90(L24) |
| Met Office Hadley Centre | HadGEM2-ES | 192 × 145(L38) |
| Institute for Numerical Mathematics | INM-CM4 | 180 × 120(L21) |
| Japan Agency for Marine-Earth Science and Technology, Atmosphere and Ocean Research Institute | MIROC-ESM | 128 × 64(L80) |
| Max Planck Institute for Meteorology | MPI-ESM-MR | 192 × 96(L40) |

2987 one station over majority of the region to eight stations over central Nepal (see, Chapter
 2988 2. To be consistent with observed datasets, the RCM outputs are linearly interpolated
 2989 to a $0.5^\circ \times 0.5^\circ$ grid resolution and CMIP5 precipitation datasets are interpolated to a
 2990 $1.0^\circ \times 1.0^\circ$ horizontal resolution. Subsequent analysis of PRECIS and CMIP5 datasets
 2991 are based on their ensemble mean, unless otherwise specified.

2992 5.2.2 Sea surface temperature data

2993 Simulation of extreme dry and wet conditions require realistic representation of seasonal
 2994 and annual mean surface air temperature and precipitation. It is also important for
 2995 climate models to accurately simulate seasonal, interannual, long-term variability in
 2996 order to reproduce key features of climate extremes including drought behaviors. Climate
 2997 models (both GCMs and RCMs) have been extensively evaluated to simulate the Indian
 2998 monsoon circulation (Kumar et al., 2006, Kripalani et al., 2007, Sperber et al., 2013,
 2999 Turner and Annamalai, 2012). Chapter 4 provided an indepth evaluation of two RCMs
 3000 on how various metrics are represented. It is understood from Chapter 4 and several
 3001 other studies that both GCMs and RCMs have a reasonable skill in reproducing the
 3002 spatial distribution of the Indian monsoon rainfall, with a much greater detail in the
 3003 latter owing to its high spatial resolution and better representation of local climate
 3004 forcings.

3005 Sustained dry and wet conditions have been linked to periodic fluctuations in tropi-
 3006 cal SSTs. Such SST fluctuations include the well-known ENSO (Trenberth, 1997) that
 3007 occurs in the equatorial Pacific Ocean, and the IOD (Saji et al., 1999, Webster et al.,
 3008 1999) that occurs in the equatorial Indian Ocean. Ashok et al. (2001) found that IOD
 3009 modulates the Indian summer monsoon rainfall (ISMR) and therefore, perturbs the cor-
 3010 relation between ISMR and ENSO. Although many previous studies have shown that

climate models, particularly the GCMs, are able to reproduce the observed relationships between Niño3.4 SST anomalies and ISMR (e.g., Kripalani et al., 2007, Sperber et al., 2013), its impact on regional climate extremes are not well examined. In order to assess how well RCM outputs reproduce the observed relationships between SST anomalies and precipitation across the GBM River Basin, the 12 month time-scale SPI from various precipitation products are correlated with the Niño3.4 index (Trenberth, 1997) and the DMI (Saji et al., 1999). This climate indices have been described in Section 2.3.3.

5.2.3 Identification of extreme dry and wet events

In general, prolonged dry spells result from a marked deficiency of precipitation, which may lead to various types of droughts. According to the American Meteorological Society (1997) drought can be classified as: (i) meteorological or climatological, (ii) agricultural, (iii) hydrological, and (iv) socio-economic. Meteorological drought mainly describes the prolonged deficit of precipitation, agricultural drought relates to moisture deficits in the root-zone (1 m) layer that impacts crops, hydrological drought describes to below-normal stream flow, lake and groundwater levels, and socio-economic drought relates the supply and demand of water linking the previous three drought conditions. The relationship between these droughts is complex but the latter three drought categories originate in one way or the other from a deficiency of precipitation (Heim, 2002).

The standardized precipitation index (SPI) developed by McKee et al. (1993) using monthly precipitation data provides an effective statistical measure of both dry (and wet) spells on various time scales (1, 2, 3, ..., 48 months), which can ultimately be used to characterize various categories of meteorological droughts either based on intensity (e.g., McKee et al., 1993) or duration (e.g., Awange et al., 2016b). A basic description of SPI is provided in Section 3.3.4. To provide an assessment about how wet and dry spells evolve in the next 80–90 years, a drought or a wet event for a given time-scale is defined here as a period in which SPI is continuously below (above) a threshold of -0.9 (+0.9) for three consecutive months (Awange et al., 2016b). This includes the duration of the event and a series of intensities for the duration of the event. Based on this definition, the frequency of drought or wet events are calculated for all the grid cells inside the GBM River Basin.

Following Awange et al. (2016b), the probability of a drought year is estimated based on a 50-year period by calculating the ratio based on the number of drought years to the total number of years (i.e., ~50) between for example, April 2001–March 2050 and April 1950–March 2099. A year is considered to be in drought (or wet) when one or more months in a year falls within the definition of drought or wet (i.e., SPI remains below -0.9 or above +0.9 for three consecutive months) as defined above. Drought years are searched between April and March of next year, which is chosen to synchronize with the ENSO cycle. Subsequently, the probability of a drought (or wet) year is calculated as a ratio of total number of drought (or wet) events to the total number of years between the time range (e.g., April 2001 to March 2050). The probability (P) of severe (SD) and extreme droughts (ED)- (and wet) are then estimated by:

$$P_{SD} = \frac{\text{Number of severe drought events}}{\text{Number of drought events}} \times \frac{\text{Number of drought years}}{\text{Total Number of years}}, \quad (5.1)$$

3052 where a drought (wet) event is deemed to be severe (SD) if it lasts for a period of 6 to 12
3053 months and is deemed extreme if the duration exceeds more than 12 months. It should be
3054 mentioned here that SPI is solely based on precipitation and does not account for water
3055 loss due to evapotranspiration, where the latter is a function of both precipitation and
3056 air temperature. With the increase in surface air temperature, the evapotranspiration
3057 is projected to increase significantly over the next few decades based on the Clausius–
3058 Clapeyron relation, which may lead to more extreme precipitation events and lesser
3059 droughts in the future. To calculate the spatial extent (or coverage) of drought and wet
3060 conditions over the entire time period for the two river basins, individual time-series of
3061 area fraction with SPI below (above) -0.9 (+0.9) are plotted for all the climate model
3062 outputs and observational products.

3063 5.3 Results

3064 5.3.1 Model evaluation

3065 To examine how well RCMs driven by various GCMs simulate the ENSO- and IOD-
3066 related dry and wet conditions across various parts of the GBM River Basin, Niño3.4
3067 index and DMI are correlated with monthly precipitation anomalies (represented by
3068 SPI at 12 month time-scale) derived from RegCM4.4 and PRECIS model outputs for
3069 the period 1982–2012. The spatial distribution of correlation coefficients of ENSO and
3070 IOD are shown in Fig. 5.1 and 5.2, respectively. Based on the observed precipitation
3071 products (GPCCv7 and CRU_TS3.22), Niño3.4 SST anomalies show large negative
3072 correlations with SPI over large portions of the GBM River Basin, mainly above 25°N
3073 between 1982 and 2012 (Fig. 5.1a–b), indicating that El Niño (La Niña) events are
3074 associated with drier (wetter) than normal conditions in the GBM River Basin. While
3075 the ERA-Interim (and observed SST) driven RegCM4.4 output indicates a very similar
3076 spatial pattern with respect to GPCCv7 (Fig. 5.1c), specifically in the northern parts
3077 of GBM River Basin, model outputs driven by two CMIP5 models shows somewhat
3078 a contrasting pattern over the region (Fig. 5.1d–e). The GFDL-ESM driven output
3079 shows a very poor representation of ENSO mode in the western Ganges River Basin
3080 and Bangladesh (Fig. 5.1d), while the MPI-ESM-MR driven output indicates a fairly
3081 comparable spatial pattern with GPCCv7 and CRU_TS3.22 (Fig. 5.1e). There are small
3082 variations among the six QUMP ensemble members and are considerable different from
3083 the observed patterns, especially in the Ganges River Basin as indicated by the ensemble
3084 mean in Fig. 5.1f.

3085 The IOD mode is mainly associated with positive correlations with SPI mainly in the
3086 high rainfall regions of northeast India and northern Bangladesh (Fig. 5.2a–b) indicating
3087 increased rainfall amounts in these regions. The IOD has a negative impact on rainfall
3088 across the Ganges River Basin, which may further exacerbate droughts during the El
3089 Niño years. The increasing trend in DMI over the last few decades, particularly due
3090 to warming of the equatorial Indian Ocean is an important phenomenon that has been
3091 linked to the current weakening of the Indian monsoon circulation. The spatial patterns

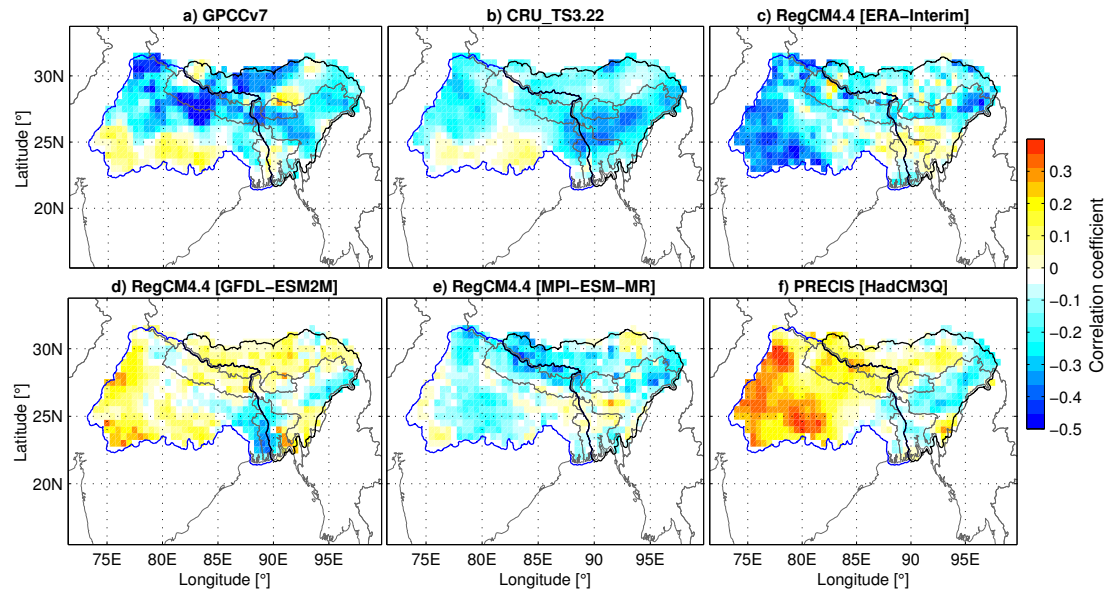


Figure 5.1: Correlation between Niño3.4 index and gridded 12-month SPI derived from (a) GPCCv7, (b) CRU_TS3.2, (c) RegCM4.4 (driven by ERA-Interim and observed SST data), (d) RegCM4.4 (driven by GFDL-ESM), (e) RegCM4.4 (driven by MPI-ESM-MR), and (f) PRECIS ensemble mean (driven by six QUMP GCMs)..

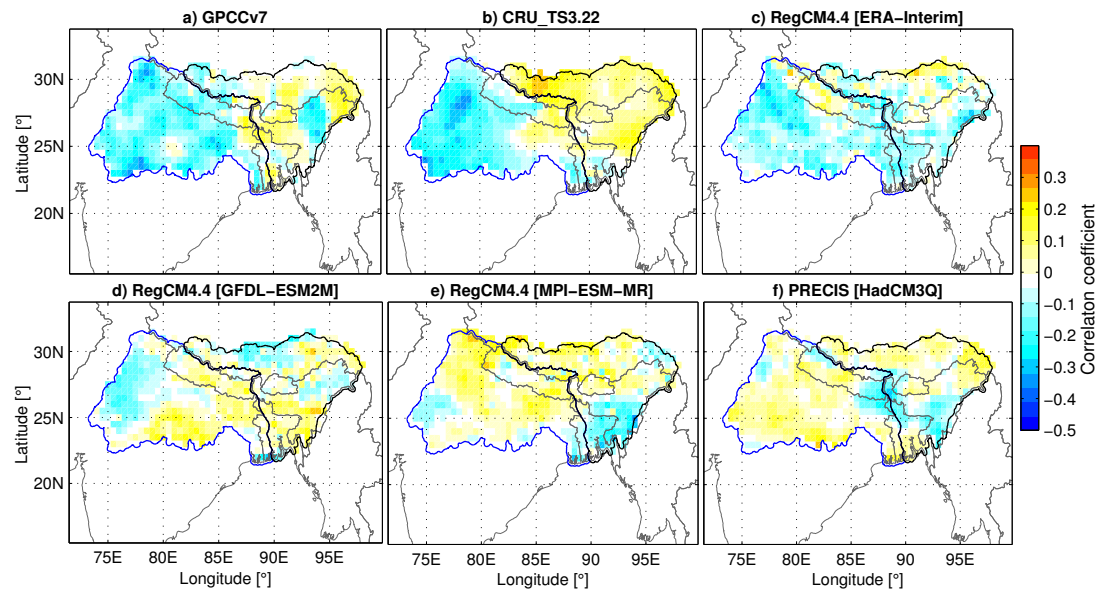


Figure 5.2: Correlation between DMI and gridded 12-month SPI derived from (a) GPCCv7, (b) CRU_TS3.2, (c) RegCM4.4 (driven by ERA-Interim and observed SST data), (d) RegCM4.4 (driven by GFDL-ESM), (e) RegCM4.4 (driven by MPI-ESM-MR), and (f) PRECIS ensemble mean (driven by six QUMP GCMs).

3092 of correlation coefficients is well-reproduced by the original ERA-Interim data (results
 3093 not shown) but those positive correlations observed over northeast India and Bangladesh
 3094 are not captured well when downscaled by the RegCM4.4 model (Fig. 5.2c). The GCM-

3095 driven outputs (Fig. 5.2d–f) tend to show almost an opposite pattern with positive
3096 (negative) effects over the Ganges (Brahmaputra–Meghna) River Basin, especially in the
3097 MPI-ESM-MR- and QUMP-driven outputs, indicating that the regional SST forcings
3098 are not well simulated in the current state-of-the-art RCMs. While it is evident from
3099 the correlation results that ENSO plays a dominant role on precipitation in the GBM
3100 River Basin, the increasing IOD anomalies due to rising SST in the equatorial Indian
3101 Ocean may weaken the ENSO-monsoon relationship.

3102 Although it is possible that RCMs poorly simulate the ENSO/IOD precipitation
3103 relationships, especially due to the poor representation of the warming Indian Ocean
3104 and the changing lead-lag relationships with the monsoon rainfall, models may be able
3105 to reflect the basic characteristics of dry and wet events. Figure 5.3 shows the spatial
3106 variation of a number of drought events as indicated by the RCM outputs and observed
3107 precipitation products. The central Ganges River Basin (covering Madhya Pradesh)
3108 and parts of Brahmaputra–Meghna River Basin (mainly over northeast India) have
3109 recorded up to 9–11 droughts on a 12 month time-scale during the past three decades
3110 (Fig. 5.3a–b). Overall, at least 4–8 drought events have occurred in the entire GBM
3111 River Basin, although few areas have experienced relatively low number of droughts. The
3112 difference between GPCCv7 and CRU_TS3.22 is mainly observed in the eastern parts of
3113 Ganges River Basin (eastern Nepal and the Indian state of Bihar and Jharkhand) where
3114 CRU_TS3.22 tends to show considerably lower number of drought events compared
3115 to GPCCv7. This could be a data interpolation problem in CRU_TS3.22 as it has
3116 substantially lower number of rain gauges in the region (especially in the Indian region),
3117 whereas the GPCCv7 has up to 2–8 stations per grid cell in the same region (Khandu
3118 et al., 2016c).

3119 The spatial pattern of drought events are reasonably captured by the two models (Fig.
3120 5.3c–f). In particular, the RegCM4.4 model when driven by perfect boundary conditions
3121 (ERA-Interim and observed SST datasets) shows a fair spatial representation of drought
3122 events in the arid and semi-arid regions (e.g., central Ganges and northeast India, Fig.
3123 5.3c). The RegCM4.4 outputs driven by two CMIP5 GCMs are also able to indicate
3124 spatial variation of drought events in the GBM River Basin (Fig. 5.3d–e), except that
3125 the MPI-ESM-MR driven output shows significantly lower (higher) number of drought
3126 events over southern (northern) Brahmaputra–Meghna River Basin (Fig. 5.3e). The
3127 PRECIS model outputs on the other hand, highly overestimates the number of drought
3128 events in the northern GBM River Basin with respect to the widely used GPCCv8
3129 and CRU_TS3.22 even though the spatial patterns are well-reproduced in the southern
3130 parts of the basin (Fig. 5.3f).

3131 The number of wet events tend to occur more frequently in the Ganges River Basin
3132 and major portions of Bangladesh, indicating a maximum of 8–10 events from April
3133 1983–March 2012. It is also indicative of the fact that dry areas are also prone to
3134 more wet events. It is also observed that there are substantial differences in GPCCv7
3135 and CRU_TS3.22 (Fig. 5.3g–h) especially in terms of the number of wet events in the
3136 Ganges River Basin and northeast India and northern Bangladesh. While the ERA-
3137 Interim driven RegCM4.4 output indicates reasonably good agreement with observed
3138 precipitation products (Fig. 5.3i), there are noticeable differences in the CMIP5 driven

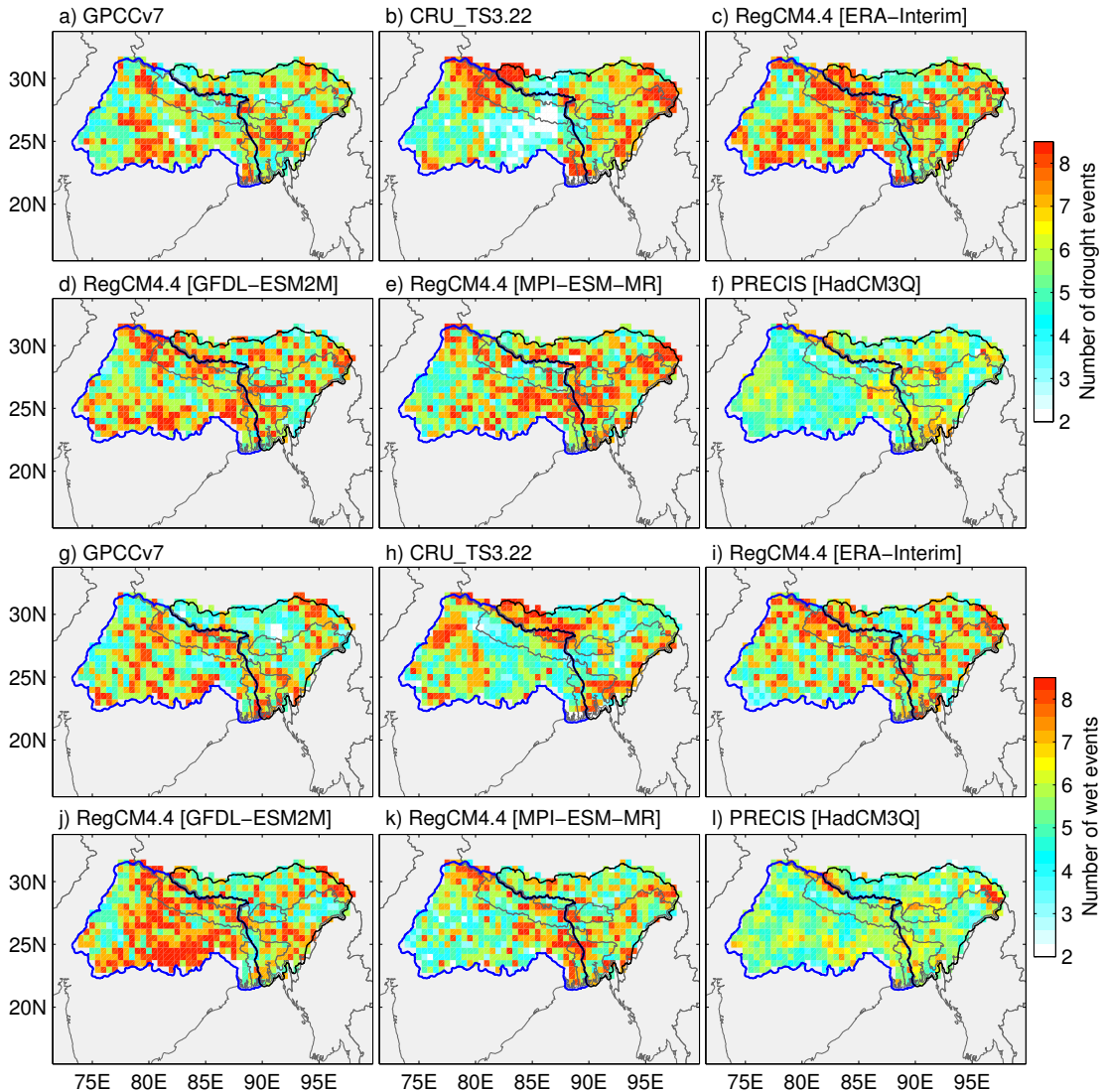


Figure 5.3: Number of drought events between April 1983 to March 2012 as shown by (a) GPCCv7, (b) CRU_TS3.22, (c) RegCM4.4 (driven by ERA-Interim and observed SST data), (d) RegCM4.4 (driven by GFDL-ESM), (e) RegCM4.4 (driven by MPI-ESM-MR), and (f) PRECIS ensemble mean (driven by six QUMP GCMs). These events were calculated from a 12 month time-scale SPI.

3139 output (Fig. 5.3j–k). The unusually high number of wet events in MPI-ESM-MR driven
 3140 output over Bangladesh is consistent with the relatively lower number of drought events
 3141 (Fig. 5.3k). Similar results are shown by the PRECIS model outputs but with a relatively
 3142 lower number of wet events for the entire GBM River Basin compared to the observed
 3143 products (Fig. 5.3l).

3144 Eight CMIP5 models are also included in this study and are compared with GPCCv7
 3145 and CRU_TS3.22 for the period 1950–2012. Figure 5.4 shows the frequency of droughts
 3146 and wet events from April 1951 to March 2012, with observed precipitation products

3147 showing a maximum of about 18 drought and wet events (Fig. 5.4a–b and d–e). The
 3148 spatial distribution drought events are very similar to those seen between 1983–2012
 3149 except that more drought events have occurred over northern Bangladesh and Meghalaya
 3150 (in India), which did not feature in the observed precipitation products between 1983 and
 3151 2012. The CMIP5 models tend to overestimate (underestimate) drought (wet) events
 3152 across the GBM River Basin, especially in the eastern half of the GBM River Basin
 3153 (Fig. 5.4c and f).

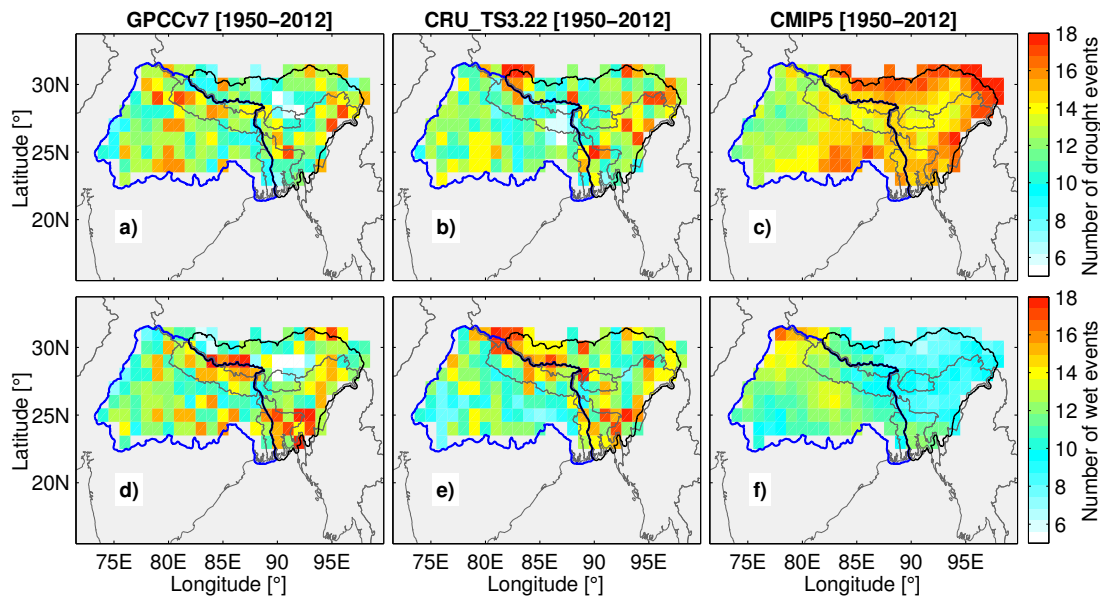


Figure 5.4: Number of drought events between April 1950 to March 2012 as shown by (a) GPCCv7, (b) CRU_TS3.22, and (c) ensemble mean of 8 CMIP5 models. Number of wet events for the same period as shown by (d) GPCCv7, (e) CRU_TS3.22, and (f) CMIP5 ensemble mean of 8 CMIP5 models. These events are calculated from the 12 month time-scale SPI.

3154 5.3.2 Seasonal projections of precipitation and temperature

3155 Projected changes in seasonal precipitation and temperature can have a large influ-
 3156 ence on the future trajectory of dry and wet conditions. Although winter (December–
 3157 February, DJF) precipitation is likely to remain unchanged, many previous modelling
 3158 studies have projected an increase in monsoon rainfall (Kumar et al., 2006, Kripalani
 3159 et al., 2007, Turner and Annamalai, 2012), possibly as a result of enhanced moisture
 3160 transport from the warming Indian Ocean (Chung and Ramanathan, 2006). The pro-
 3161 jected rainfall increase may lead to more frequent wet events and lesser drought events,
 3162 although it is highly likely that their pattern of change vary from region to region. This
 3163 section examines the projected changes in monsoon (June–September, JJAS) precipita-
 3164 tion and temperature based on one RegCM4.4 output (i.e., driven by MPI-ESM-MR)
 3165 and ensemble mean of six PRECIS model outputs.

3166 Figure 5.5 shows the spatial pattern and basin-averaged changes in monsoon (JJAS)
 3167 rainfall in the GBM River Basin based on the two model outputs (RegCM4.4 and

3168 PRECIS). Based on RegCM4.4 model (i.e., forced by MPI-ESM-MR), only few regions
 3169 in the northern GBM River Basin (Nepal and northern Brahmaputra–Meghna River
 3170 Basin) indicate an increase in monsoon rainfall. Large decreases are projected over
 3171 Bangladesh, Bhutan and parts of northeast India with a declining rate of up to 10–
 3172 25 mm decade⁻¹ (Fig. 5.5a). It should be mentioned here that more recent modelling
 3173 studies based on CMIP5 models have also projected a minimal rainfall increase in the
 3174 region under RCP4.5 (e.g. Hsu et al., 2012, Lee and Wang, 2014). In particular, the
 3175 results shown here are consistent with those from Sharmila et al. (2015), who showed
 3176 a rainfall decrease in the MPI-ESM-MR ESM even under the highest warming scenario
 3177 (i.e., RCP8.5). On the other hand, PRECIS projects a large increase in monsoon rainfall
 3178 over majority of the GBM River Basin with a rate of up to 24 mm decade⁻¹ along the
 3179 Himalayan Foothills (Fig. 5.5b) and are consistent with the previous studies on CMIP3
 3180 modelling projections and their downscaled results (Kumar et al., 2006, Kripalani et al.,
 3181 2007, Mathison et al., 2013, Whitehead et al., 2015).

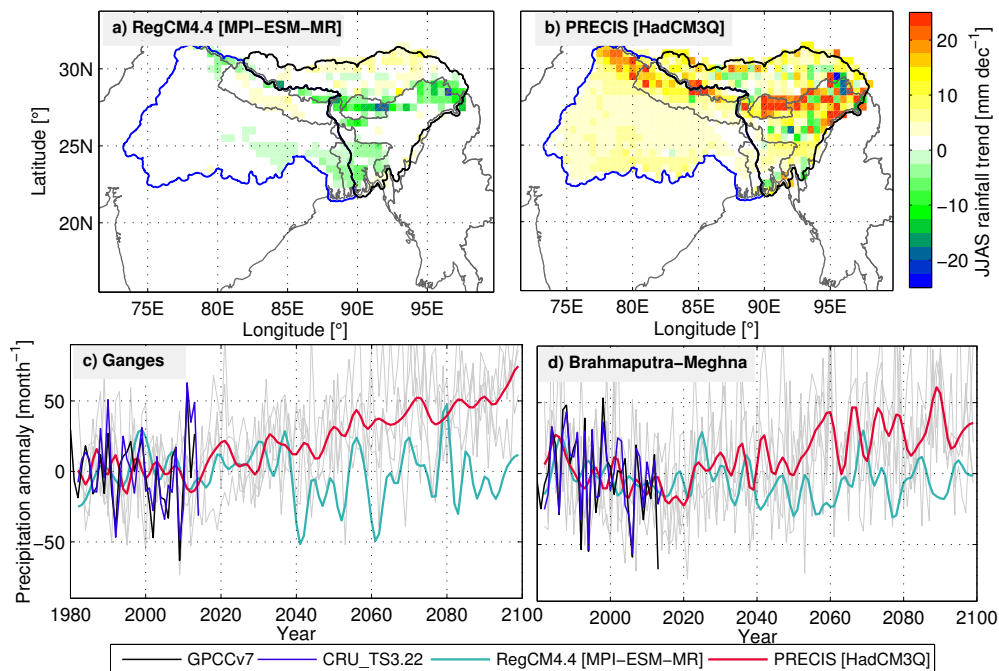


Figure 5.5: Spatial distribution of JJAS precipitation changes (mm per decade) over the GBM River Basin based on (a) RegCM4.4 (driven by MPI-ESM-MR) and (b) PRECIS (driven by 6 QUMP GCMs) between 1982–2099 including the spatially-averaged temporal anomalies based on observations (GPCCv7 and CRU_TS3.22) and two RCMs (RegCM4.4 and PRECIS) for the (c) Ganges and (d) Brahmaputra–Meghna River Basins.

3182 Using an ensemble of all 17 QUMP models, McSweeney et al. (2012) showed that
 3183 monsoon rainfall increase is associated with increase in 850 hPa level wind speeds sug-
 3184 gesting that monsoon circulation may strengthen under enhanced warming. However,
 3185 other studies based on CMIP3 and CMIP5 models indicate that the intensified mon-
 3186 soon rainfall is associated with enhanced moisture transport over the monsoon region
 3187 from the warmer Indian Ocean, while large-scale monsoon circulation is projected to
 3188 weaken as a result of reduction in meridional thermal gradient across Asia (Chung and

3189 Ramanathan, 2006, Ueda et al., 2006). The RCM results presented here are more coherent
 3190 with previous GCM results under A1B scenario (e.g., Turner and Annamalai, 2012,
 3191 Menon et al., 2013, Sharmila et al., 2015), except that RCMs show enhanced rainfall
 3192 increases along the Himalayan Foothills.

3193 The spatially-averaged JJAS precipitation anomalies derived from the simulated
 3194 model outputs (1982-2100) for the Ganges and Brahmaputra–Meghna River Basins
 3195 are shown in Fig. 5.5c–d, together with those from GPCCv7 and CRU_TS3.22 for
 3196 the period 1982–2012. Consistent with the spatial patterns (Fig. 5.5a–b), RegCM4.4
 3197 (driven by MPI-ESM-MR) do not show any future trends in precipitation but feature
 3198 high interannual variability after 2040, whereas PRECIS shows a significant increase in
 3199 monsoon rainfall in the GBM River Basin (Fig. 5.5c–d). The rate of increase is projected
 3200 to be higher in the Ganges River Basin by a factor of two (Fig. 5.5c) than those
 3201 projected for the Brahmaputra–Meghna River Basin. The model results agree very well
 3202 with the observed precipitation datasets for the recent period 1982–2012 (Fig. 5.5c–d),
 3203 with both models indicating the monsoon rainfall decline in the Brahmaputra–Meghna
 3204 River Basin, where it has declined significantly since the early 1990s (Fig. 5.5d).

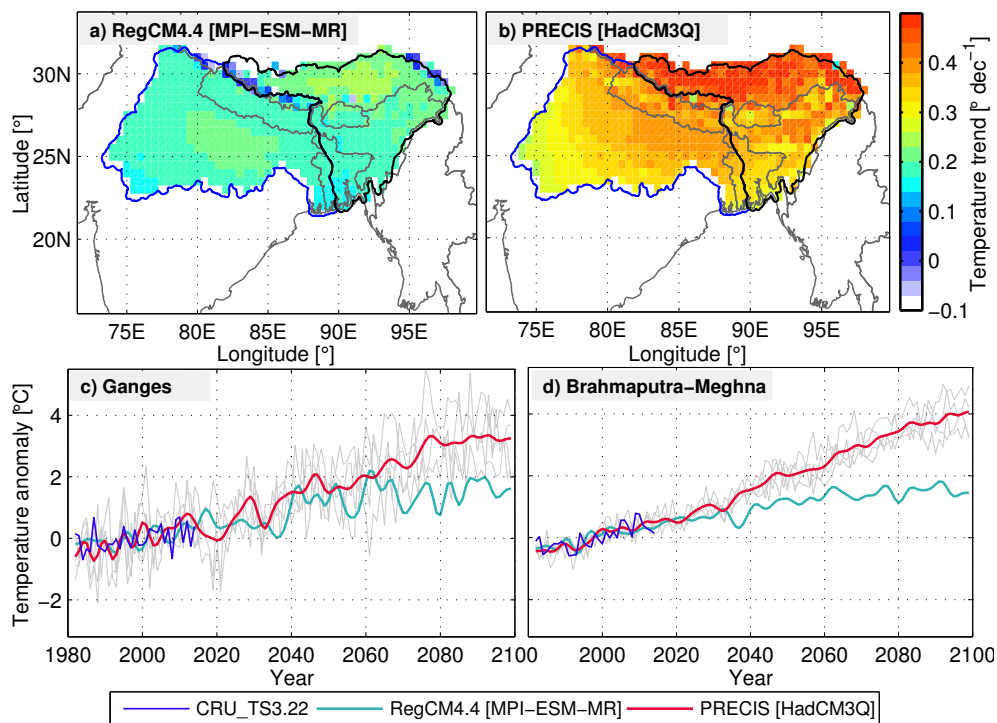


Figure 5.6: Spatial distribution of JJAS temperature changes ($^{\circ}\text{C}$ per decade) over the GBM River Basin based on (a) RegCM4.4 (driven by MPI-ESM-MR) and (b) PRECIS (driven by 6 QUMP GCMs) between 1982–2099 including the spatially-averaged temporal anomalies based on observed CRU_TS3.22 data and two RCMs (RegCM4.4 and PRECIS) for the (c) Ganges and (d) Brahmaputra–Meghna River Basins.

3205 Figure 5.6a & b show the spatial distribution of rate of JJAS temperature changes
 3206 between 1982 and 2100 based on RegCM4.4 (forced by MPI-ESM-MR under RCP4.5)
 3207 and PRECIS (forced by QUMP under SRES A1B), respectively, over the GBM River

3208 Basin. It is evident that both models show significant increase in surface air temperature
3209 with substantially higher rate of increase in the northern Brahmaputra River Basin
3210 (Tibetan region) with a rate of about 0.25°C per decade (in RegCM4.4, Fig. 5.6a) and
3211 0.42° per decade (in PRECIS, Fig. 5.6b). While both models agree on the warming
3212 pattern across the GBM River Basin, the magnitude of warming is substantially higher
3213 in PRECIS (ensemble mean of six QUMP members) by almost a factor of two (Fig. 5.6c–
3214 d). RegCM4.4 shows a consistent warming of about 2°C in both the River Basins by the
3215 end of 21st century, whereas the QUMP ensemble shows a slightly higher warming in the
3216 Brahmaputra–Meghna River Basin (4°C) compared to the Ganges River Basin (3.5°C).
3217 The model temperature datasets agree well with CRU_TS3.22 for the most recent
3218 period (1982–2012) although it must be noted that the driving GCMs (e.g., QUMP,
3219 CMIP5) are forced by emission scenarios (e.g., SRES, RCPs) for the most recent decade
3220 (e.g., from 2005 onwards in the RCP-based scenarios).

3221 5.3.3 Future projection of drought and wet conditions

3222 Future temperature projections based on two RCMs under different climate scenarios
3223 indicate a warming climate (with different rates), which is expected to warm by at least
3224 2°C by 2100. Even though RegCM4.4 (driven by MPI-ESM-MR) predicts almost no
3225 change over majority of the GBM River Basin, PRECIS (driven by QUMP) projects a
3226 much more uniform rainfall increase across the GBM River Basin indicating that the
3227 region is expected to become wetter in the coming decades. Nevertheless, precipitation
3228 is highly variable in time and space across the GBM River Basin and consists of a
3229 sequence of active and break periods on a seasonal scale and is subject to considerable
3230 interannual variation in response to global and local SST variations (e.g., ENSO and
3231 IOD). Previous studies have suggested that the interannual variability of rainfall could
3232 either increase (decrease) owing to increased (decreased) ENSO amplitudes (see, Meehl
3233 et al., 2006, Turner et al., 2007), which may influence the occurrences of dry and wet
3234 spells and their location and spatial coverage.

3235 To assess the future occurrences of wet and dry spells, two important risk-based
3236 metrics are studied. The number of drought (and wet) events are extracted from the 12
3237 month time-scale SPI derived from monthly precipitation time-series of two RCMs and 8
3238 CMIP5 GCMs to examine the (i) probability of drought (and wet) occurrences, and (ii)
3239 spatial coverage in terms of the basin area affected by either drought or wet events on a
3240 monthly basis. These two key characteristics will provide crucial information for regional
3241 risk management and mitigation strategies, particularly if there is high risk of severe
3242 or extreme drought events. In order to remove the trend effects, the SPI time-series are
3243 detrended before counting the number of events as mentioned above.

3244 5.3.3.1 Frequency of drought and wet events

3245 Figure 5.7 shows the number of drought events for the two periods: 2001–2050 and 2050–
3246 2099 based on RegCM4.4 (driven by MPI-ESM-MR), ensemble mean of six PRECIS

3247 simulations (driven by QUMP) and ensemble mean of 8 CMIP5 models. The two RCMs
 3248 indicate a maximum of about 14 drought events for the two 50-year period. For the first
 3249 half century (2001-2050), RegCM4.4 predicts the highest number of droughts in the
 3250 Brahmaputra–Meghna River Basin, mostly concentrating in Bangladesh and northeast
 3251 India (Fig. 5.7a), while PRECIS shows higher drought occurrences in the eastern Ganges
 3252 River Basin (Fig. 5.7b). On the other hand, the CMIP5 GCMs exhibits maximum
 3253 drought occurrences in the central Ganges and northeast India (Fig. 5.7c). As the climate
 3254 warms, the drought pattern shifts towards the west. The Ganges River Basin is likely to
 3255 experience more droughts between 2050 and 2100, as shown by RegCM4.4 and CMIP5
 3256 models (Fig. 5.7d and f), although such patterns are not shown by PRECIS (Fig. 5.7e).
 3257 It should be noted however that, PRECIS projects a much wetter scenario when taking
 3258 into account the wetting trend (Fig. 5.5b).

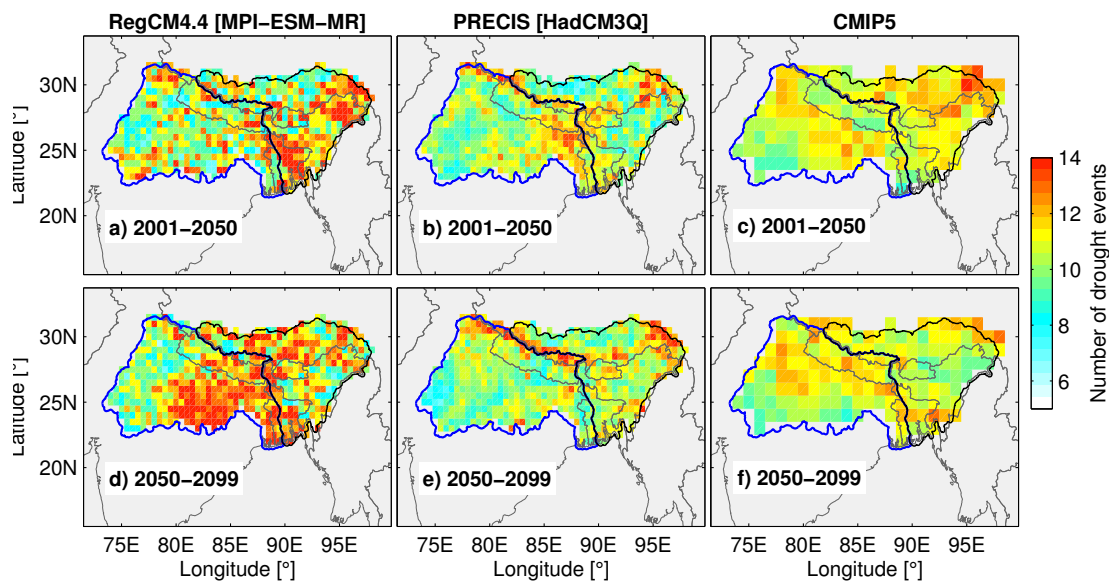


Figure 5.7: Number of drought events for the periods 2001–2050 and 2050–2099 based on (a & d) RegCM4.4 (driven by MPI-ESM-MR), (b & e) PRECIS ensemble mean (driven by 6 QUMP GCMs), and (c & f) CMIP5 ensemble mean (based on 8 GCMs).

3259 The projected number of wet events are shown in Fig. 5.8. Unlike the drought events,
 3260 the models tend to agree on the spatial variation of number of wet events in GBM
 3261 River Basin for the first half century (2001–2050, Fig. 5.8a–c). All three models exhibit
 3262 maximum wet occurrences in the Ganges River Basin, mainly covering the central and
 3263 southern parts of the basin. The spatial pattern of wet occurrences are not very ho-
 3264 mogeneous between 2050 and 2100, particularly in the low altitude areas (Fig. 5.8d–f).
 3265 While the Ganges River Basin and parts of northeast India as expected to become sub-
 3266 stantially wetter under a higher warming scenario, the number of wet events in PRECIS
 3267 simulations after removing the wetting trend do not reveal any significant change (Fig.
 3268 5.8e).

3269 Figure 5.9 shows the number of drought and wet events decade⁻¹ derived from the
 3270 two RCMs (1983–2099) and observed precipitation products (1983–2012). Although
 3271 there are small differences between GPCCv7 and CRU_TS3.22, the number of drought

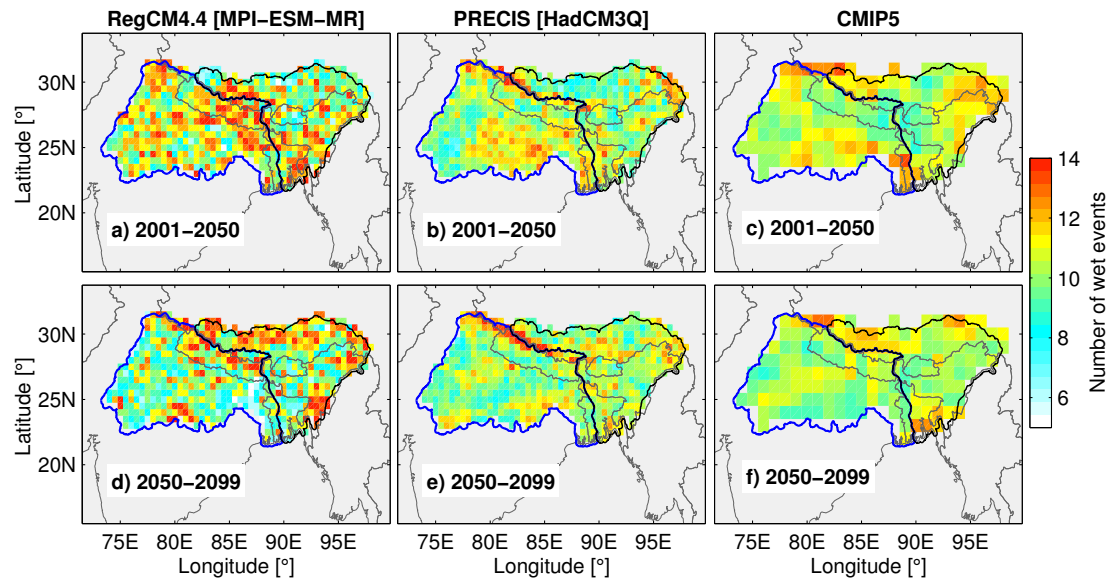


Figure 5.8: Number of wet events for the periods 2001–2050 and 2050–2099 based on (a & d) RegCM4.4 (driven by MPI-ESM-MR), (b & e) PRECIS ensemble mean (driven by 6 QUMP GCMs), and (c & f) CMIP5 ensemble mean (based on 8 GCMs).

3272 events have increased substantially in the past three decades (Fig. 5.9a and c), especially
 3273 in the Ganges River Basin as indicated by the CRU_TS3.22 dataset (Fig. 5.9a), while
 3274 the number of wet events have also increased (decreased) slightly in the Ganges and
 3275 Brahmaputra–Meghna River Basin during the last 30 years (Fig. 5.9b and d). The
 3276 models tend to show a higher number drought and wet events but generally agree on the
 3277 trend with observed datasets between 1982 and 2012. The two RCMs appears to indicate
 3278 an increasing trend in the number of drought events for the next two–three decades in
 3279 the Ganges River Basin, while the number of wet events a likely to remain unchanged.
 3280 On the other hand, the Brahmaputra–Meghna River Basin is likely to experience more
 3281 wet events from the next decade (Fig. 5.8d), although there is no visible trend in the
 3282 number of drought events (Fig. 5.8c). However, it should be mentioned here that no
 3283 significant changes are predicted.

3284 The RCM results agree very well with CMIP5 simulations in terms of the overall
 3285 pattern (Fig. 5.10) although it should be noted that CMIP5 models have low reliability
 3286 in simulating decadal to multi-decadal variability. For example, CMIP5 amplified the
 3287 overestimated the drought events of 1970s and 1980s in the Ganges River Basin, while
 3288 they completely missed the drought events of 1950s and 1960s in the Brahmaputra–
 3289 Meghna River Basin. In general, the number of droughts have increased gradually since
 3290 the 1950s in both the river basins (Fig. 5.10a and c) but has been shown to decrease in
 3291 the Brahmaputra–Meghna River Basin since 1990s. In the CMIP models, the number
 3292 of drought events decade⁻¹ in the Ganges River Basin increases substantially till the
 3293 2060s, before it declines for the next three–four decades (Fig. 5.10a), while the number
 3294 of drought events in the Brahmaputra–Meghna River Basin are found to be stable till
 3295 the 2080s, after which both river basins exhibit no major drought events (Fig. 5.10c).

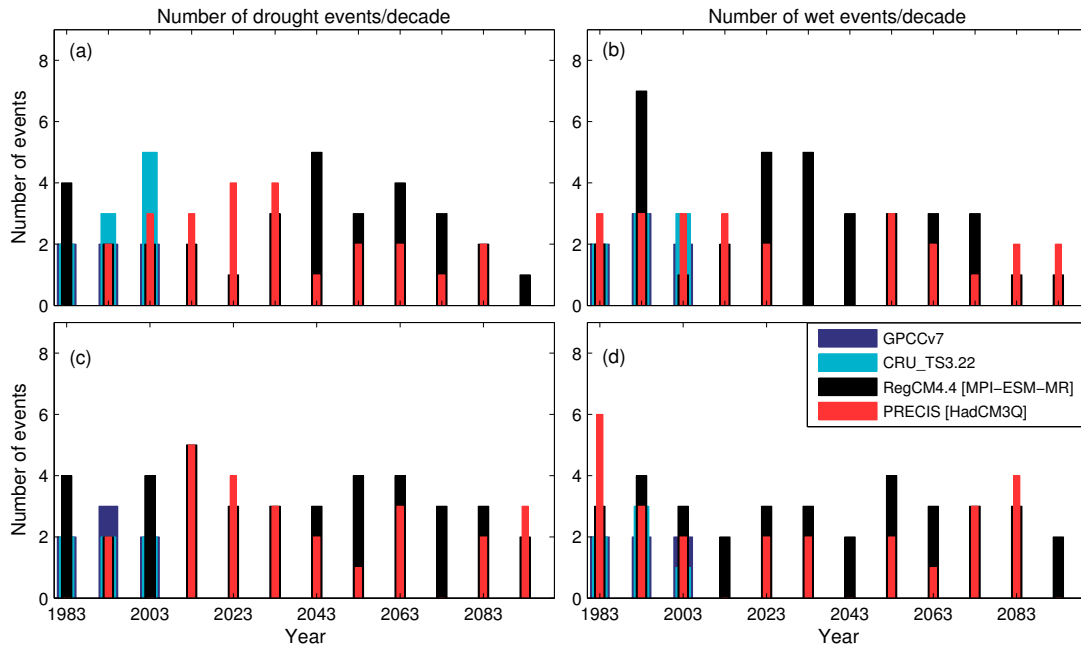


Figure 5.9: Number of drought and wet events per decade based on observed (1983–2012) and RCM simulated (1983–2099) precipitation on a 12 month time-scale: (a & b) for drought events and (c & d) for wet events for the Ganges and Brahmaputra–Meghna River Basin, respectively.

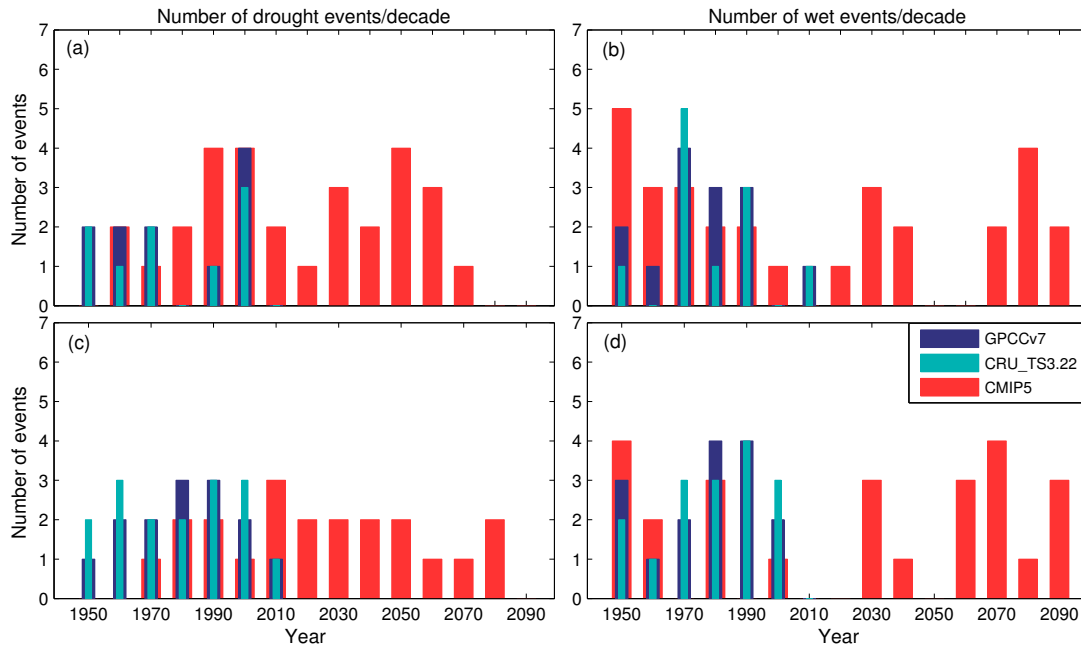


Figure 5.10: Number of drought and wet events per decade based on observed (1951–2012) and CMIP5 (1951–2099) precipitation on a 12 month time-scale: (a & b) for drought events and (c & d) for wet events for the Ganges and Brahmaputra–Meghna River Basin, respectively.

3296 Consistent with time-series of drought events, higher number of wet events are likely to
 3297 be occur towards the end of the century in both the river basins (Fig. 5.10b and d).

3298 5.3.3.2 Drought and wet occurrences

3299 In order to provide more detailed information on the severity of wet and dry spells for
3300 the two time periods (2001–2050 and 2050–2099), the probability of drought (and wet)
3301 years and their associated severe and extreme events are determined based on Eq. 5.1.
3302 Figure 5.11 shows the probability of drought years, severe and extreme droughts in the
3303 GBM River Basin based on RegCM4.4 (driven by MPI-ESM-MR) and PRECIS (driven
3304 by QUMP) based on the 12 month time-scale SPI. Both RCMs project a high probability
3305 of drought years in the Ganges River Basin for both the time periods (2001–2050 and
3306 2050–2099). RegCM4.4 tend to exhibit substantially higher probability of drought years
3307 between 2001 and 2050 (Fig. 5.11a) than PRECIS (Fig. 5.11g), ranging from 15% to
3308 about 31%, with low values mainly in the eastern Ganges River Basin. Occurrences of
3309 severe and extreme droughts are also higher in the western Ganges River Basin, with
3310 a maximum probability of about 18% and 8%. PRECIS, on the other hand, exhibits
3311 relatively lower probability of all drought categories between 2001 and 2050 (Fig. 5.11g–
3312 i).

3313 Further, the Ganges River Basin is likely to experience more droughts for the second
3314 half century, with both the RCMs predicting a higher probability of drought years than
3315 the first half. RegCM4.4 shows that the probability of 12-month time-scale droughts in
3316 the GBM River Basin ranges from 20–35% (~ 1 in 3 years, Fig. 5.11d), with maximum
3317 probability mostly concentrating in the southern GBM River Basin. Fig. 5.11d–f shows
3318 maximum probability of severe ($\sim 20\%$ or ~ 1 in 5 years) and extreme ($\sim 8\%$ or ~ 1 in 13
3319 years) in the southern and northern Ganges River Basin, respectively. Note that there
3320 are some isolated regions in the Brahmaputra–Meghna River Basin that depict similar
3321 drought occurrences. The drought patterns are much more homogeneous and lesser in
3322 PRECIS simulations, indicating a probability of drought years of about 28% and severe
3323 droughts of 16%, mostly concentrated in the western Ganges River Basin (Fig. 5.11j–k).
3324 PRECIS, however, shows a higher probability of extreme droughts in the Ganges River
3325 Basin than RegCM4.4, which extends further east into Bangladesh (Fig. 5.11l).

3326 Similarly, the probability of wet years are shown in Fig. 5.12 based on a 12 month
3327 time-scale SPI, where the RCMs project a greater probability of severe wet events for
3328 both the time periods (2001–2050 and 2050–2099). Both RegCM4.4 and PRECIS shows
3329 a overall increase in wet probability from 2001–2050 (Figure 5.12a and g) to 2050–
3330 2099 (Fig. 5.12d and j). RegCM4.4 shows maximum probability ($\sim 32\%$) of wet years
3331 in the western and northern parts of the GBM River Basin between 2001 and 2050,
3332 while PRECIS indicates higher probability ($\sim 25\%$) of wet years in the central GBM
3333 River Basin, covering Nepal, Bhutan, Bangladesh, and few Indian states. The severe
3334 wet probability ranges from 5–18% with high values mainly over western Ganges River
3335 Basin, Bangladesh, and Nepal in RegCM4.4 (Fig. 5.12b) and over majority of the GBM
3336 River Basin in PRECIS (Fig. 5.12h). The probability of extreme wets show some isolated
3337 areas of high probability ($\sim 8\%$) in the western and northern parts of the GBM River
3338 Basin and low values (less than 4%) in the southern regions.

3339 The spatial pattern of wet probability changes considerably during the second half
3340 century (2050–2099). While RegCM4.4 indicates high probability ($\sim 32\%$) of wet years

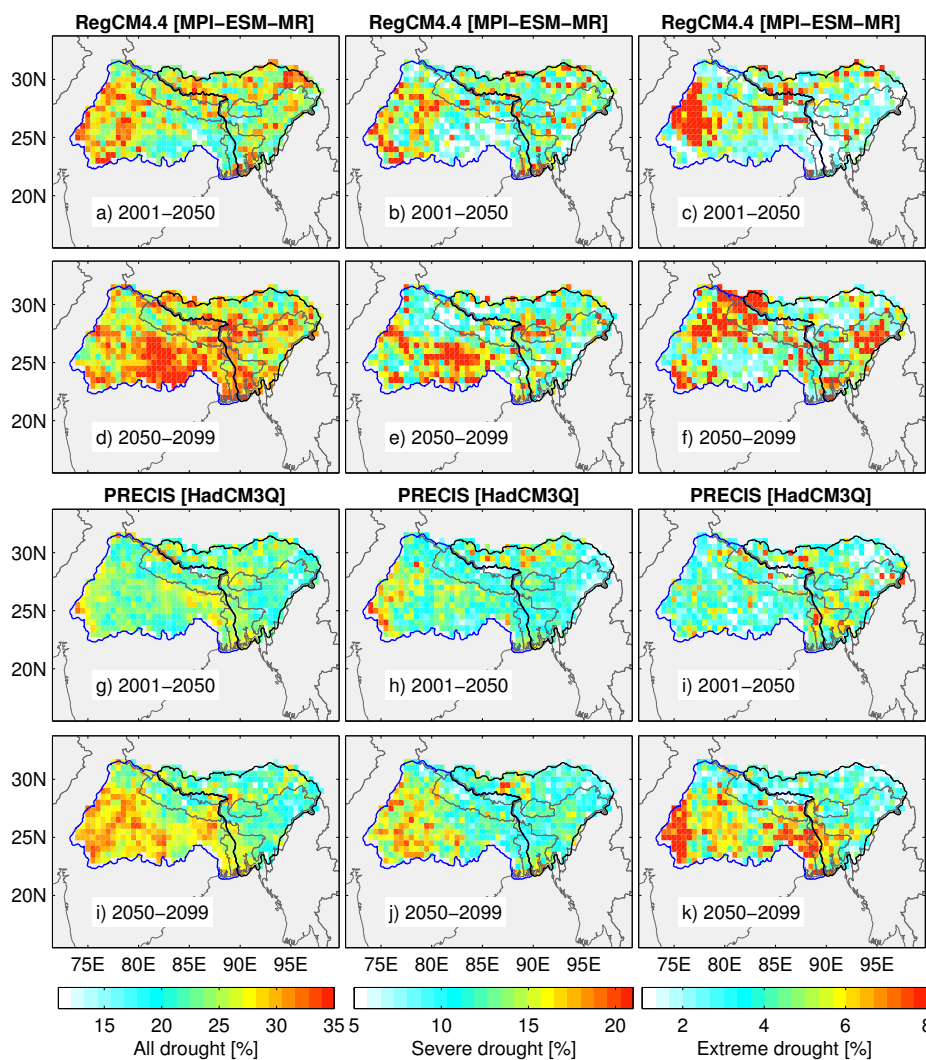


Figure 5.11: Probability (in %) of drought year on a 12 month time-scale for (a & d) all drought, (b & e) severe drought, and (c & f) extreme drought based on PRECIS ensemble mean for the periods 2001–2050 and 2050–2099. g–l represents the same but for RegCM4.4 model..

3341 over majority of the GBM River Basin (Fig. 5.12d), with higher values of severe wet
 3342 (~16%) in the central Ganges and eastern Brahmaputra–Meghna River Basin, and ex-
 3343 treme wet (~8%) in the southern and eastern parts of GBM River Basin than elsewhere
 3344 (Fig. 5.12e–f). In PRECIS, the wet probability ranges from 22–26% in the Ganges River
 3345 Basin and western Bangladesh, with higher values of severe wet (12–17%) and extreme
 3346 wet (6–8%) in the southern and central parts the GBM River Basin (Fig. 5.12j–l).

3347 The probability of drought and wet occurrences estimated from CMIP5 GCMs shown
 3348 in Fig. 5.13a–l are very similar to those shown by the RegCM4.4 and PRECIS. Like
 3349 the two RCMs, CMIP5 GCMs predict a higher probability of droughts and wets in the
 3350 western GBM River Basin (Fig. 5.13a–c and g–i). Apart from western Ganges River
 3351 Basin, parts of Bangladesh and Nepal also sees higher values of severe (~15%) and

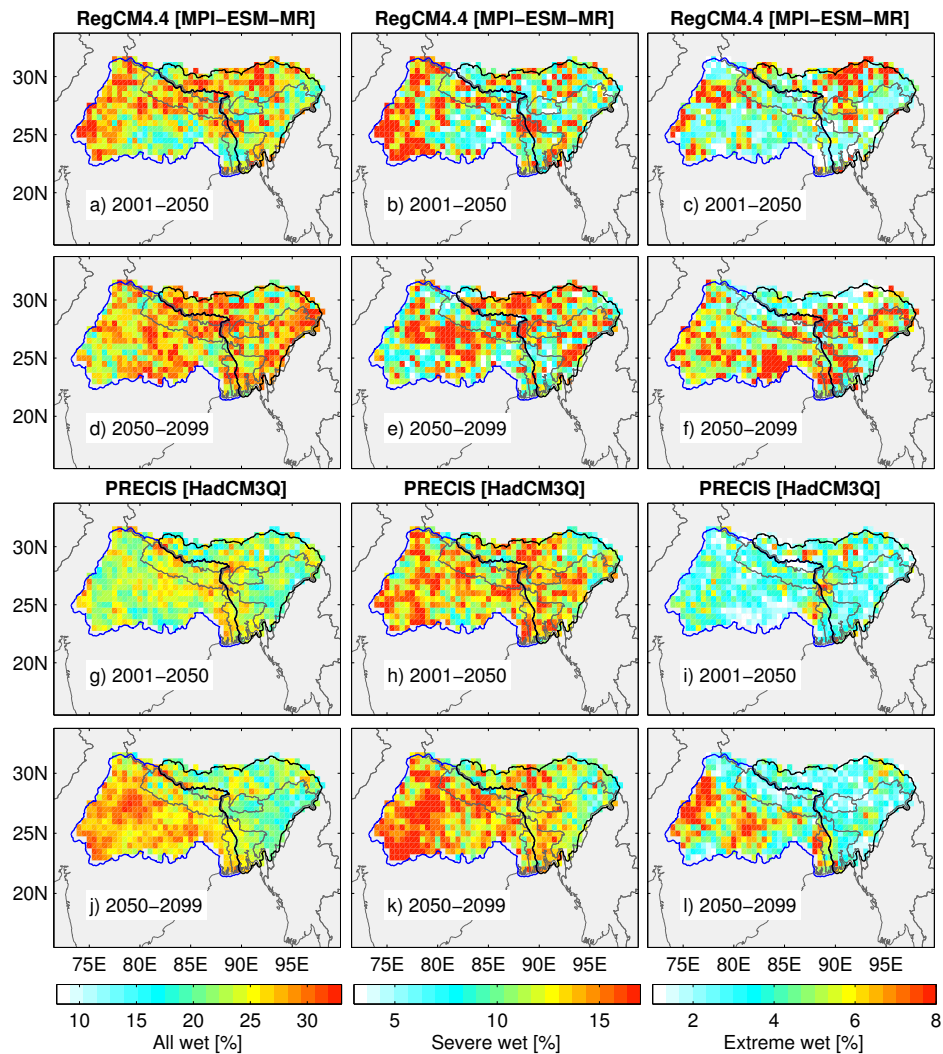


Figure 5.12: Probability (in %) of wet year on a 12 month time-scale for (a & d) all wet, (b & e) severe wet, and (c & f) extreme wet based on PRECIS ensemble mean for the periods 2001–2050 and 2050–2099. g–l represents the same but for RegCM4.4 model.

3352 extreme (7%) droughts during the first half century (Fig. 5.13b–c) than other areas of
 3353 the GBM River Basin, while few regions in northeast India are likely to experience more
 3354 extreme droughts (6–8%) during the second half century (Fig. 5.13f). Wet probabilities
 3355 have a very similar pattern, although with higher values in the southwestern and central
 3356 parts of the basin than elsewhere (Fig. 5.12j–l). These patterns suggest that areas which
 3357 are likely to experience more droughts are also likely to experience more extreme wet
 3358 events.

3359 In summary, both RCMs and GCMs predict an overall higher likelihood of drought
 3360 years in the western Ganges River Basin, with an estimated probability of about 25% (or
 3361 ~ 1 in 4 years) between 2001 and 2050 and 27–35% (~ 1 in 3 years) between 2050–2099.
 3362 The probability of severe and extreme droughts are found to be about 12–16% (~ 1 in

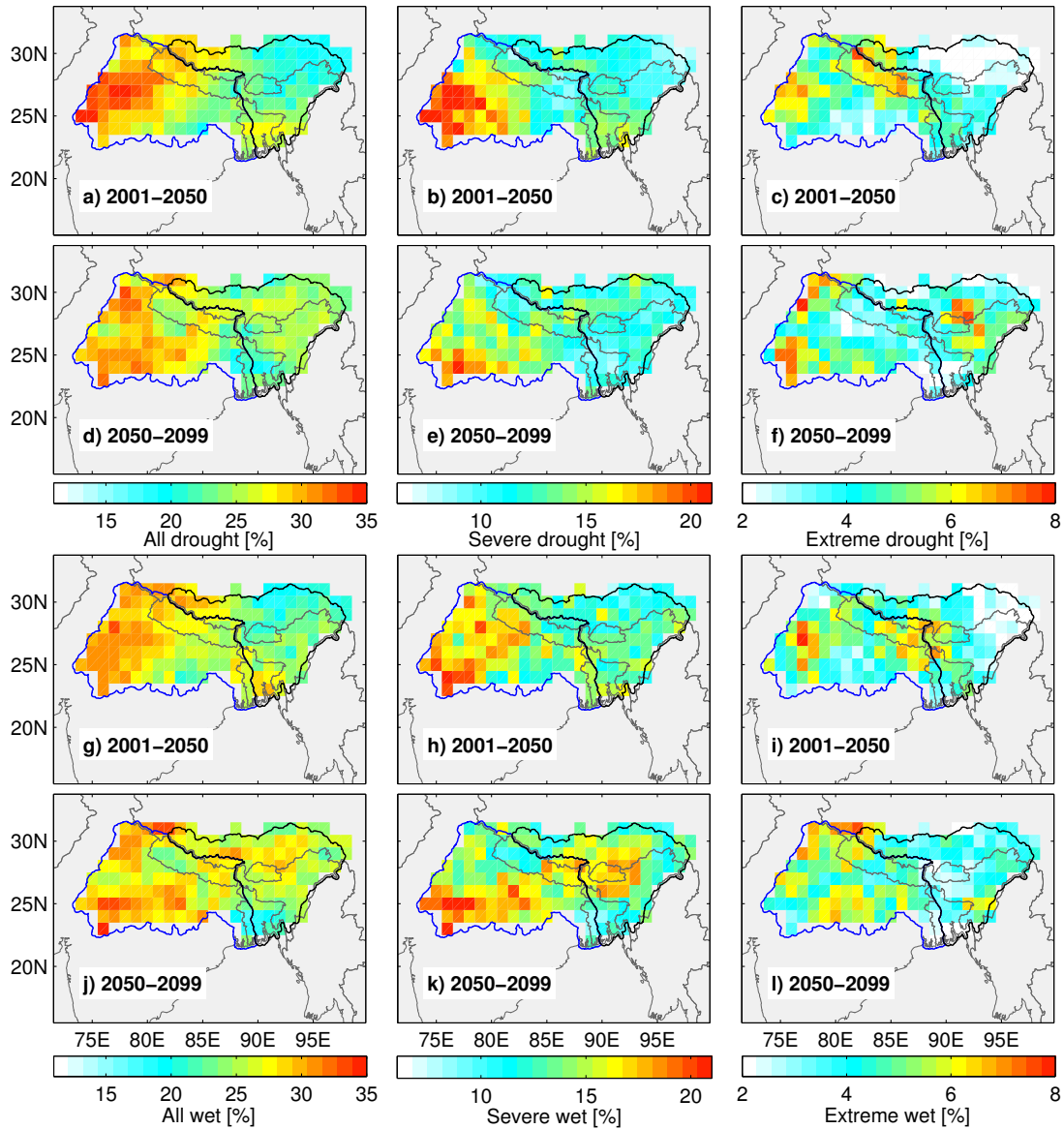


Figure 5.13: Probability (in %) of drought-year on a 12 month time-scale for (a & d) all drought, (b & e) severe drought, and (c & f) extreme drought. The probability of wet-year is plotted in (g & j) for all wet, (h & k) severe wet, and (i & l) extreme wet, each representing for the periods 2001–2050 and 2050–2099.

3363 7 years) and about 5–8% (~ 1 in 17 years), respectively, mostly covering the western
 3364 Ganges River Basin, Bangladesh and northeast India, although there are noticeable
 3365 differences in the two RCMs for severe and extreme droughts. Both RCMs and GCMs
 3366 predict an overall increase in spatial extent of drought areas, specifically in the western
 3367 Ganges GBM River Basin and northeastern parts of the GBM River Basin. On the
 3368 other hand severe and extreme wets are more likely in the southern and central parts of
 3369 the GBM River Basin, with an estimated probability of about 15–20% (~ 1 in 6 years)
 3370 and 5–8% (~ 1 in 17 years).

3371 5.3.3.3 Area affected by dry and wet spells

3372 The percentage area affected by wet and dry spells are calculated for the two river basins
 3373 (Ganges and Brahmaputra–Meghna) separately. It is estimated as a fraction area with
 3374 respect to the total number of grid cells under dry (and wet) spell (with a threshold
 3375 of ± 0.9 based on a 12 month time-scale SPI without removing the linear trend) to the
 3376 total number of grid cells in a basin for each month. Figure 5.14 shows the observed
 3377 (1983–2012) and RCM simulated (1983–2099) changes in dry and wet areas based on a 12
 3378 month times-scale in the Ganges and Brahmaputra–Meghna River Basin. The simulated
 3379 results are found to be temporally consistent with the observed patterns capturing the
 3380 high interannual variability for the period 1983–2012, especially in Ganges River Basin
 3381 (Fig. 5.14a).

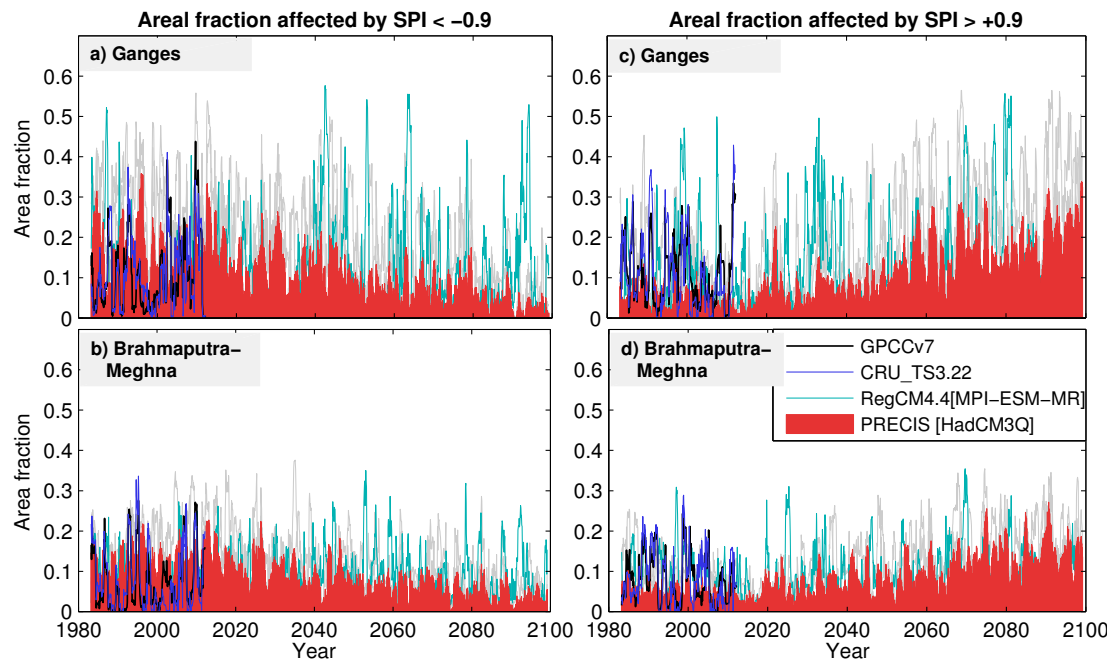


Figure 5.14: RCM projections drought and wet areas (as a fraction) in the Ganges and Brahmaputra–Meghna River Basin based on RegCM4.4 and PRECIS ensemble mean. The results from GPCCv7 and CRU_TS3.22 are also shown for the period 1983–2012. Area affected by drought (a & b) and wet events (c & d) in the Ganges and Brahmaputra–Meghna River Basin, respectively. The individual QUMP members outputs are plotted in grey colors.

3382 The area affected by dry spells in the Ganges River Basin between 1983 and 2012
 3383 varies from high (30–35%) in the mid-1980s and late 2000s to low (0–10%) in the late
 3384 1990s coinciding with extreme drought and wet periods (Fig. 5.14a). The Brahmaputra–
 3385 Meghna River Basin shows a very similar pattern but shows a much lower % area affected
 3386 by dry spells (with a high of around 20%). While the RegCM4.4 model agrees well for
 3387 the historical period, it shows high variability from 2040 onwards indicating abrupt
 3388 increases in dry areas (up to 60% and 40% in the two basins). On the other hand,
 3389 PRECIS model projects about decline–fold decline in dry areas in both the River Basins
 3390 from the current level. However, after removing the linear trend effects due to monsoon

3391 rainfall increases, it may be possible that that both river basins may be affected by dry
 3392 spells as indicated by their probabilities.

3393 On the other hand, both RCMs project a gradual increase in wet areas from 2020
 3394 ($\sim 5\text{--}10\%$) onwards and reaches a peak ($\sim 20\text{--}30\%$) by the end of the century (Fig. 5.14c).
 3395 Even though there are periods of enhanced wetness in both RCMs, especially between
 3396 2050 and 2080, the wetting trend is much higher in the Ganges River Basin in PRECIS
 3397 as it is likely to suffer from more wet events. The Brahmaputra–Meghna River Basin
 3398 on the other hand, sees a modest, but still significant increase in the wet areas with
 3399 both RCMs projecting a two-fold increase in wet areas by the end of 21st century (Fig.
 3400 5.14d) under a temperature increase of 1.8°C (in RegCM4.4) and 4.0°C (in PRECIS).
 3401 The changes are consistent after removing the linear trend effects, but the trends are
 3402 much lowered in Brahmaputra–Meghna River Basin.

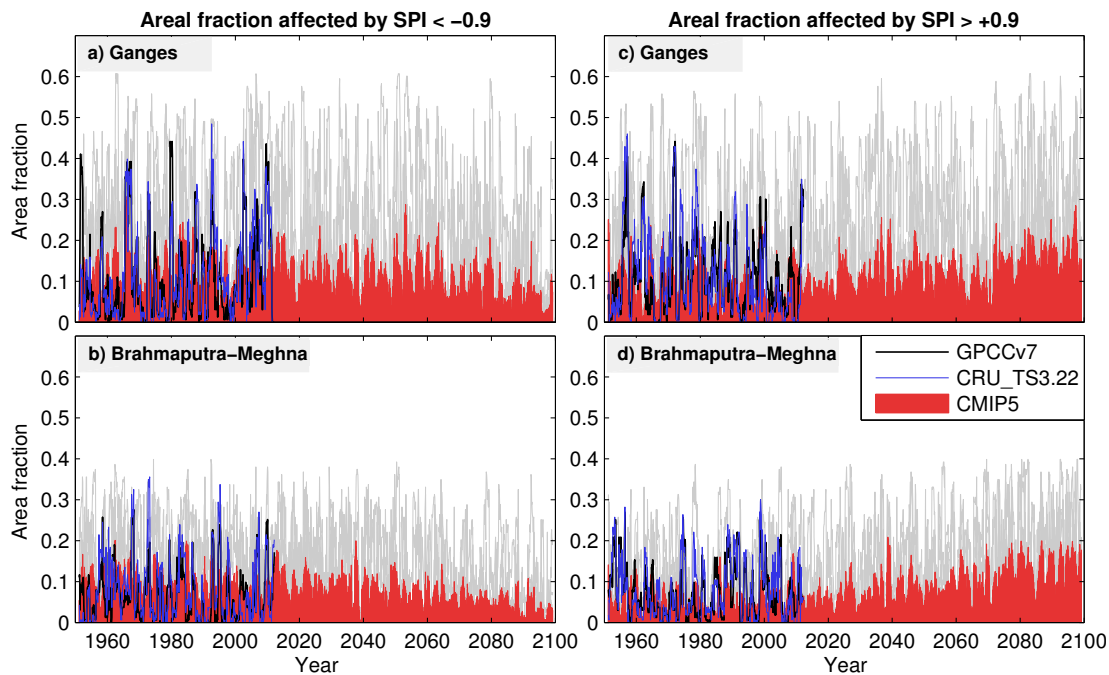


Figure 5.15: Multimodel mean projections of drought and wet areas (as a fraction) in the Ganges and Brahmaputra–Meghna River Basin based on CMIP5 models. The results from GPCCV7 and CRU_TS3.22 are also shown for the period 1951–2012. Area affected by drought (a & b) and wet events (c & d) in the Ganges and Brahmaputra–Meghna River Basin, respectively. The individual CMIP5 outputs are plotted in grey colors.

3403 RCM results are supported by ensemble mean of eight CMIP5 ESMs that predict a
 3404 very similar scenario under RCP4.5 as shown in Fig. 5.15a–d. However, it is observed
 3405 that drying and wetting trends in the Ganges River Basin is not exactly linear as
 3406 indicated by the RCMs (Fig. 5.15a and c). In CMIP5 models, the amount of dry areas
 3407 start to decline only in 2060s in the Ganges River Basin (Fig. 5.15a) and 2040s in the
 3408 Brahmaputra–Meghna River Basin (Fig. 5.15c).

3409 5.4 Discussion and summary

3410 There is growing confidence that the recent global warming is a result of anthropogenic
3411 causes, particularly due to increasing emission of GHGs and land use change. With an
3412 increase in global and regional surface temperatures, the near-surface evaporation (and
3413 atmospheric water vapour) over ocean is expected to rapidly rise ($\sim 6\text{--}7\%^\circ\text{C}^{-1}$) due
3414 to the Clausius-Clapeyron relation and that global mean precipitation is projected to
3415 increase by roughly about $1\text{--}3\%^\circ\text{C}^{-1}$ (e.g., [Allan and Soden, 2007](#), [Lorenz et al., 2010](#),
3416 [Wild and Liepert, 2010](#)). The generally lower precipitation increase as compared to
3417 the precipitable water (or atmospheric water) is being explained by the energy-balance
3418 concept (see, e.g., [Allan and Soden, 2007](#), [Lambert and Webb, 2008](#), [Lorenz et al.,](#)
3419 [2010](#), [Schneider et al., 2010](#), [Wild and Liepert, 2010](#)). The Indian monsoon precipitation
3420 has decreased considerably since the 1950s possibly as a result of increased aerosol
3421 concentration ([Ramanathan et al., 2005](#), [Bollasina et al., 2011](#)) and the weakening of
3422 meridional northern Indian Ocean SST gradient ([Chung and Ramanathan, 2006](#), [Roxy](#)
3423 [et al., 2014](#)). However, most climate models suggest an increase in the Indian monsoon
3424 precipitation as well as the interannual variability under an enhanced warming scenario
3425 (e.g., [Kumar et al., 2006](#), [Kripalani et al., 2007](#), [Turner and Annamalai, 2012](#), [Menon](#)
3426 [et al., 2013](#), [Ahmed and Suphachalasai, 2014](#)), although few CMIP3 and CMIP5 models
3427 project a declining trend (e.g., [Turner and Annamalai, 2012](#), [Sharmila et al., 2015](#)).
3428 Under the SRES A1B scenario, monsoon precipitation is projected to increase by 10–25
3429 mm per decade in the GBM River Basin for a temperature increase of about 2–4°C at
3430 the end of 21st century.

3431 The mechanism for this increase has been explained in a number of ways ([Kripalani](#)
3432 [et al., 2007](#), [Sperber et al., 2013](#), [Menon et al., 2013](#)), which can be summarized as:
3433 (i) increase in moisture convergence over northern India due to intensification of heat
3434 low, (ii) anomalous easterly flow over Bay of Bengal despite weakening monsoon cir-
3435 culation, (iii) weakening relationship between ENSO and Indian monsoon rainfall, and
3436 (iv) dominant effect of rising SST on Indian monsoon rainfall despite negative feed-
3437 back from increasing CO₂. Together with 2–4°C increase in surface air temperature,
3438 the GBM River Basin is predicted to become wetter due to increase in monsoon rain-
3439 fall. However, after accounting for the precipitation trend, both RCMs project a higher
3440 probability (25–35%) of droughts in western GBM River Basin than elsewhere, with
3441 extreme droughts shifting towards Bangladesh and northeast India by the second half
3442 century (2050–2099). While these results are in agreement with the current observa-
3443 tions indicating a shift in rainfall distribution (e.g., [Goswami et al., 2010](#), [Vinnarasi and](#)
3444 [Dhanya, 2016](#)), further examinations are required using most up-to-date RCM projec-
3445 tions. During the second half century, the probability of severe and extreme droughts
3446 range between 15–20% (~ 1 in 6 years) and 6–8 years (~ 1 in 17 years) in these regions.
3447 Although the impacts of short-term droughts (less than 6 months) are mainly limited to
3448 surface water flows, which serves as primary water supplies for agriculture, hydropower
3449 production, and ecosystem, among others, reduced water availability will place greater
3450 reliance on groundwater resources. As such groundwater is already a main source of
3451 water for irrigation in the GBM River Basin ([Shamsudduha et al., 2009b](#), [Mukherjee](#)
3452 [et al., 2015](#)).

3453 Severe and extreme droughts (more than 6 months) can have detrimental effect on
3454 all types of water resources, including surface water, soil moisture, and groundwater.
3455 During long-term droughts, excessive groundwater abstraction can cause aquifer systems
3456 to compact, which can ultimately lead to a permanent loss of groundwater storage. For
3457 example, over pumping in California San Joaquin Valley aquifer system has resulted
3458 in a large drop in ground elevation and has caused serious structural issues to the
3459 surface water delivery networks (Sneed et al., 2013). Prolonged droughts can cause
3460 reversal of groundwater flows to the Indian Ocean, leading to salt water intrusion,
3461 and subsequently degrade water quality. Additionally, high arsenic contamination of
3462 groundwater resources across Bangladesh and Gangetic plains has become a serious
3463 problem with increasing number of tube wells over the past 40 years (see, Yunus et al.,
3464 2016, and references therein). The CMIP5 models project a similar drought occurrence
3465 for the next 80–90 years, with low values of severe and extreme droughts mainly over
3466 the eastern Brahmaputra–Meghna River Basin covering northeast India and parts of
3467 southern China.

3468 The wet frequencies are also predicted to occur in the same areas where higher
3469 drought frequencies are expected, suggesting that western Ganges River Basin will ex-
3470 perience both dry and wet regimes for the next 80–90 years. The likely increase in
3471 wet spells mainly due to severe and extreme wets are likely to enhance water storage
3472 in the GBM River Basin, although it does not necessarily account for the increasing
3473 atmospheric water demands due to increasing surface air temperatures. Additionally,
3474 more extreme wet events would imply increased risks from flooding, particularly across
3475 northern Bangladesh and northeast India. Nevertheless, both RCM and CMIP5 models
3476 do not project any significant change in the mean decadal duration and intensity of
3477 drought and wet events, which may perhaps point to the diminishing role of ENSO in
3478 the future climate (Turner and Annamalai, 2012). Despite showing consistent spatial
3479 patterns of drought and wet frequencies, the poor representation of dominant climate
3480 drivers such as ENSO and IOD in RCMs, provides a big challenge for predicting future
3481 climate extremes (e.g., droughts and extreme wet events) in the GBM River Basin.
3482 Both RegCM4.4 and PRECIS are incapable of reproducing the ENSO/IOD rainfall re-
3483 lationship, except when forced by perfect boundary conditions. Thus, there is a need to
3484 synchronize model simulations with ENSO/IOD time-series to simulate more realistic
3485 patterns of wet and dry spells.

3486 As a primary source of water, projected increase in monsoon rainfall may relieve water
3487 shortage in the GBM River Basin, but there are other factors to consider, especially on
3488 a seasonal scale. Higher warming in winter and spring would enhance glacier melt and
3489 cause higher runoffs during spring. This will perhaps trigger more glacial lake outburst
3490 floods (GLOFs) and landslides, which will be highly catastrophic to the Himalayan
3491 nations such as Bhutan, Nepal, and north India (ICIMOD, 2007, Bajracharya et al.,
3492 2015). However, as climate warms, more winter precipitation are expected to fall as
3493 rain to curb snow water equivalent in the Himalayas. In the upstream Himalayas, the
3494 potential risks of GLOFs and increased runoffs on hydropower can be very damaging.
3495 Countries like Bhutan, Nepal, and India have invested significant amount of capital
3496 on the development of hydropower projects that are intended for long-term use. As
3497 glaciers and snowlines begin to retreat more rapidly and with more deforestation, the

3498 Himalayan inhabitants will potentially lose their local springs and streams through
3499 drying of watersheds ([Bates et al., 2008](#)). Precipitation increases during the summer as
3500 shown by both GCMs and RCMs will also lead to increased runoffs in the GBM river
3501 system and its Himalayan nations, which will likely cause widespread flooding in the
3502 deltaic plains ([Ahmed and Suphachalasai, 2014](#), [Whitehead et al., 2015](#)).

6. Spatio-temporal variability of UTLS temperature based on COSMIC GNSS RO

6.1 Introductory remarks

The upper troposphere–lower stratosphere (UTLS) region (400–30 hPa) is characterized by steep changes in static stability (temperature lapse rate) with large gradients in a number of radiatively active trace gases, including ozone and water vapour (Reid and Gage, 1985, Randel et al., 2000). The variability and changes in UTLS temperature play an important role in regulating the exchange of water vapour, ozone, and other trace gases between the troposphere and the stratosphere, as well as in climate research. The troposphere is projected to warm consistently with increase in GHG concentrations, with an enhancement of warming (cooling) in the upper troposphere (lower stratosphere). Observational evidence suggests that the troposphere has warmed considerably over the past decades with substantial cooling in the lower stratosphere (Karl et al., 2006, Lott et al., 2013, Thorne et al., 2011). The *tropopause*, a region that marks the separation between the troposphere and the stratosphere in the UTLS region, is of special importance for understanding the transport of water vapour into the stratosphere and exchange of ozone between the two layers (Randel et al., 2000). The height of the tropopause is affected by the heat balance of both the troposphere (e.g., warming as a result of increasing greenhouse gas concentration) and the stratosphere (e.g., warming as a result of absorption of aerosols) (Santer et al., 2003a,b, 2008).

Many studies have analyzed the seasonal and interannual variations of UTLS temperature using observations from global network of radiosondes, SRS-based measurements, and global reanalyses (e.g., Reid and Gage, 1985, Randel et al., 2000, Gettelman et al., 2001, Santer et al., 2003a,b, Wilcox et al., 2011, Lott et al., 2013). Large-scale variation of the tropopause is dominated by an annual cycle and longer-term interannual variability associated with the ENSO mode (Trenberth, 1990) and the quasi-biennial oscillation (QBO, Baldwin et al., 2001). While the global characteristics of UTLS temperature is widely studied, much remains to be known in terms of its regional behaviour and how it influences the regional climate (e.g., rainfall). Large observational uncertainties still exist over South Asia, specifically over the GBM River Basin due to poor quality of radiosonde networks (e.g., Das Gupta et al., 2005, Sun et al., 2010, Krishna Kumar et al., 2011, Ansari et al., 2015). Some stations have been recently updated by the Indian Meteorological Department (IMD) with Global Positioning System (GPS)-based radiosondes to improve their accuracy (see Krishna Kumar et al., 2011, Ansari et al., 2015). Our analysis over the GBM basin between August 2006 and December 2013 shows that GPS-based radiosondes have been significantly improved over the previous versions and exhibit negligible bias against the highly accurate Constellation Observing

3541 System for Meteorology, Ionosphere, and Climate (COSMIC, [Anthes et al., 2008](#)) radio
3542 occultation (RO) data sets.

3543 The GBM river River Basin is located in a region where the UTLS is characterized
3544 by large-scale anticyclonic circulation that is dynamically active and coupled to the
3545 Indian monsoon circulation ([Rao et al., 2008](#), [Kunze et al., 2010](#)). As a dominant source
3546 of seasonal and interannual variability, the Indian monsoon is also a major source of
3547 moisture in the UTLS as well as an important mode of transport for many trace gases
3548 and other pollutants over the region. The temperature changes in the UTLS affects
3549 static stability (e.g., increase with respect to global warming) with the potential to
3550 alter global and region weather/climate. The recent weakening of the Indian monsoon
3551 has been attributed to the upper-tropospheric cooling (warming) over the anticyclonic
3552 region (equatorial Indian Ocean) ([Rao et al., 2008](#), [Kunze et al., 2010](#)). With increasing
3553 population and rapid industrialization, the GBM River Basin has witnessed a dramatic
3554 increase in atmospheric pollution and aerosols that has been found to influence rainfall
3555 patterns ([Gautam et al., 2009](#), [Lau et al., 2009](#)).

3556 Since the launch of GPS/Meteorology (GPS/MET) mission in 1995 ([Rocken et al.,](#)
3557 [1997](#)), Global Navigation Satellite Systems (GNSS) RO has demonstrated immense po-
3558 tential to provide improved spatio-temporal (and vertical) resolution in the probing of
3559 the Earth's atmosphere including pressure, temperature, and water vapour ([Schmidt](#)
3560 [et al., 2010](#), [Anthes, 2011](#)). Several studies have demonstrated the usefulness of GNSS
3561 RO in improving numerical weather prediction forecasts (e.g., [Healy and Thépaut, 2006](#),
3562 [Cucurull et al., 2007](#), [Poli et al., 2008, 2010](#)), climate changes studies ([Foelsche et al.,](#)
3563 [2008](#), [Schmidt et al., 2010](#), [Steiner et al., 2013](#)), and space weather/ionospheric research
3564 and operations (e.g., [Lee et al., 2012](#), [Zhang et al., 2014](#)) over the past 2 decades.
3565 The number of RO profiles has increased substantially over the past years with the
3566 launch of several GNSS RO missions enabling wider applications in regional studies
3567 (see, e.g., [Anthes, 2011](#)). For instance, the joint Taiwan–US six-satellite mission, COS-
3568 MIC/FORMOSA Satellite Mission 3 (COSMIC/FORMOSAT-3, hereafter COSMIC)
3569 ([Anthes et al., 2008](#)), has provided about 1500–2000 RO soundings per day globally
3570 with 70–90% of the soundings since August 2006. It is now possible to infer decadal
3571 temperature trends in the UTLS and the tropopause with a structural uncertainty of
3572 less than 0.06°C in the tropics and mid-latitudes ([Steiner et al., 2013](#)). Using ~ 9 years of
3573 RO data from CHALLENGING Minisatellite Payload (CHAMP, 2001–2008, [Wickert et al.,](#)
3574 [2001](#)), Gravity Recovery And Climate Experiment (GRACE, 2006–2009, [Wickert et al.,](#)
3575 [2009](#)), and COSMIC (2006–2009), [Schmidt et al. \(2010\)](#) found an increase of global
3576 tropopause height ($5\text{--}9\text{ m year}^{-1}$), which is consistent with the current global warming
3577 trends.

3578 In the context of growing GNSS RO mission and its ability to provide high spatio-
3579 temporal (and vertical) resolution vertical profiles, this study examines the potential
3580 benefits in the GBM River Basin by studying interannual variability of temperature
3581 in the UTLS region using ~ 8 years of monthly accumulated COSMIC RO data from
3582 August 2006 to December 2013. Two global reanalysis fields from ECMWF reanalysis
3583 (ERA-Interim, [Dee et al., 2011](#)) and MERRA ([Rienecker et al., 2011](#)) are also included
3584 here to assess their consistency in the region with respect to the high quality GNSS

RO data. Reanalysis systems are backbone to many climate research studies and in understanding the various dynamics of the tropospheric–stratospheric exchange process. Both ERA-Interim and MERRA were developed primarily to improve on various aspects of the hydrologic cycle that were not adequately described in previous generations of reanalyses (Dee et al., 2011, Rienecker et al., 2011). ERA-Interim also assimilates refractivity profiles from various GNSS RO missions from 2001 to reduce temperature biases (Poli et al., 2010, Dee et al., 2011). Thus, modern reanalyses such as MERRA and ERA-Interim are expected to accurately capture the interannual variability of temperature in the UTLS for the most recent decade. The findings of this study have been published in the *Atmospheric Measurement Technique* and only minor changes have been made in this Chapter.

Section 6.2 describes the various temperature datasets used and methods applied to compare and assess the temperature variations in the UTLS region. The results are presented and discussed in Section 6.3, and Section 6.4 presents a brief summary of this study.

6.2 Data and methods

6.2.1 FORMOSAT/COSMIC RO data

COSMIC is a highly successful RO mission that has demonstrated wide scientific applications in operational weather forecasts (see, e.g., Anthes et al., 2008, Ho et al., 2010, Anthes, 2011) and global atmospheric studies (see, e.g., Foelsche et al., 2008, Schmidt et al., 2010). In the RO data retrieval process, the bending angle (α) derived from Doppler shift measurements onboard low earth orbiting (LEO) satellites can be inverted to recover refractivity (N) based on the Abel transform, which is related to total pressure (P), temperature (T), and water vapour pressure (P_w) (Melbourne et al., 1994). In a dry atmosphere (with $P_w = 0$), density profiles are obtained from the known relationship between refractivity and density, while pressure and dry temperature can be derived using the hydrostatic equation and equation of state for ideal gas (see, e.g., Melbourne et al., 1994). In the presence of water vapour (especially in the lower troposphere), humidity and temperature profiles should be complemented with a priori information (e.g., numerical weather forecasts).

Alternatively, wet profiles can be generated using a one-dimensional variational (1D-Var) method implemented at the COSMIC Data Analysis and Archive Center (CDAAC) at the University Corporation for Atmospheric Research (UCAR). These atmospheric profiles are provided as Level 2 RO data by various data retrieval centers including CDAAC (see <http://cdaac-www.cosmic.ucar.edu/cdaac/status.html>). In this study, COSMIC Level 2 RO data (both wet and dry profiles) covering the GBM River Basin between April 2006 and December 2013 are used. The wet and dry profiles mainly differ in the lower troposphere due to presence of water vapour but are similar and highly accurate between 8 and 20 km (for more details, see, Anthes et al., 2008). The wet profiles are used for evaluating the accuracy of radiosonde observations whereas dry profiles

3625 (i.e., temperature only) are used for examining the interannual variations of UTLS tem-
 3626 perature over the GBM River Basin. The GBM River Basin received 59 419 COSMIC
 3627 profiles from April 2006 to December 2013, out of which $\sim 14\%$ were found to be of bad
 3628 quality (see, [Khandu et al., 2016b](#)).

3629 Figure 6.1a shows the number of monthly accumulated COSMIC RO profiles re-
 3630 trieved within the GBM River Basin during the study period, with an average of
 3631 ~ 576 profiles per month. The number of profiles decreased considerably between late
 3632 2010 and 2012 (Fig. 6.1a) due to problems in some COSMIC satellites (see <http://cdaac-www.cosmic.ucar.edu/cdaac/status.html>). Figure 6.1b shows the distribu-
 3633 tion of RO data points at various pressure (altitude) levels indicating that most COSMIC
 3634 profiles penetrate deep into the lower troposphere with more than 56% of the profiles
 3635 reaching at least 850 hPa (~ 1.5 km above mean sea level). The geographical distribu-
 3636 tion of COSMIC profiles at 850 hPa (~ 1.5 km), 700 hPa (~ 3.1 km), 500 hPa (~ 6.0
 3637 km), and 400 hPa (~ 7.5 km) levels in Fig. 6.2a–d indicate the effect of high topography
 3638 over the region (Fig. 6.3), i.e., the blockage of GNSS radio waves. A near-complete cov-
 3639 erage of the RO data can be seen at 400 hPa (~ 7.5 km), corresponding to the highest
 3640 altitude of the Himalayas.
 3641

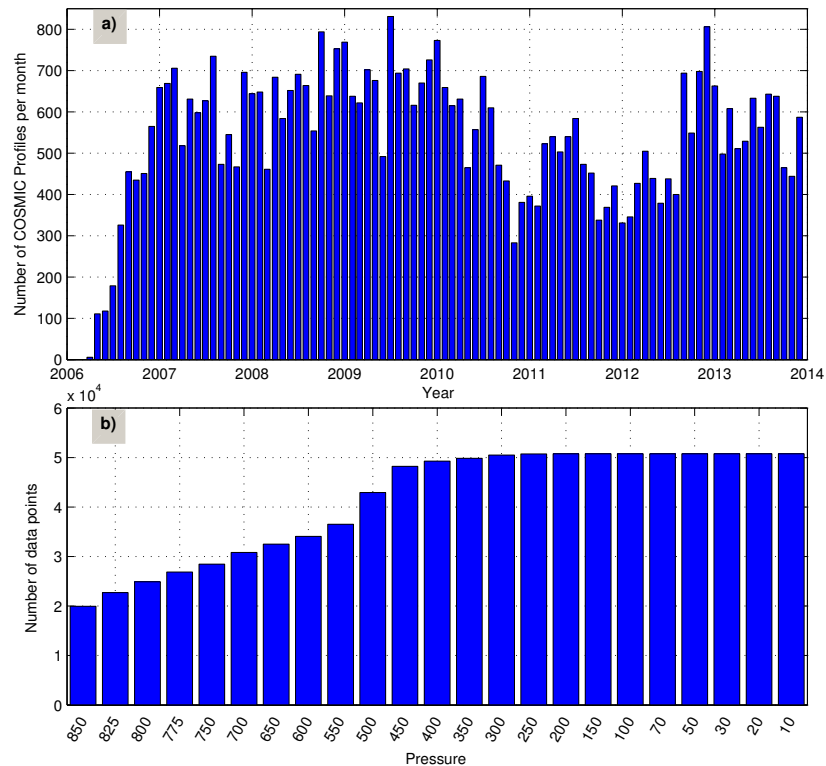


Figure 6.1: (a) Total number of monthly COSMIC RO profiles reported in and around the GBM River Basin between April 2006 and December 2013, and (b) the corresponding number of data points at each pressure levels 850–30 hPa (1.5–24.0 km).

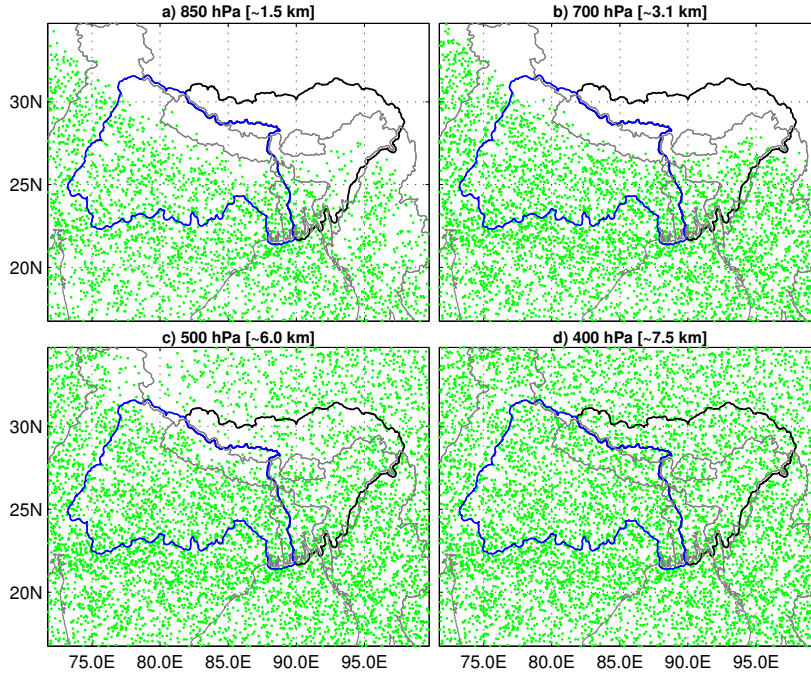


Figure 6.2: Spatial distribution of COSMIC data points in the lower troposphere for the year 2012: (a) 850 hPa (~ 1.5 km), (b) 700 hPa (~ 3.1 km), (c) 500 hPa (~ 5.8 km), and (d) 400 hPa (~ 7.5 km).

3642 6.2.2 Radiosonde data

3643 CDAAC also maintains radiosonde records from around the globe that are collocated
 3644 with atmospheric profiles from most of the RO missions (e.g., COSMIC, CHAMP,
 3645 GRACE). These radiosonde profiles are extracted from National Center for Atmospheric
 3646 Research (NCAR) mass store (see details in, Sun et al., 2010). There are 24 opera-
 3647 tional or synoptic radiosonde stations within or around the GBM basin, with most of
 3648 them (18) located within the Indian territory and operated by the Indian Meteorolog-
 3649 ical Department (IMD) (see, Fig. 6.3), whereas three of them are located in Tibet or
 3650 southern China (or the upper Brahmaputra basin) and the rest are located in southern
 3651 Bangladesh. Based on the country of location, these radiosondes differ in their sensor
 3652 types and design (Table 6.1). The accuracy of IMD operated radiosondes have been a
 3653 concern for many years due to their poor observational qualities (see, e.g., Das Gupta
 3654 et al., 2005, Kumar et al., 2010, Sun et al., 2010) and has been undergoing substantial
 3655 upgrades in the past 6–7 years.

A detailed evaluation of 12 different radiosonde types globally by Sun et al. (2010) from April 2008 to October 2009 showed relatively poor skills (in temperature, water vapour, and refractivity) by IMD radiosondes with respect to COSMIC RO data, while the ShangE sondes from China suffered from large negative refractivity biases in the mid-troposphere. However, Kumar et al. (2010) reported significant reduction in daily temperature fluctuations at 10 stations, which were prominent before they were upgraded in 2009, suggesting that newly upgraded instruments could be of better quality.

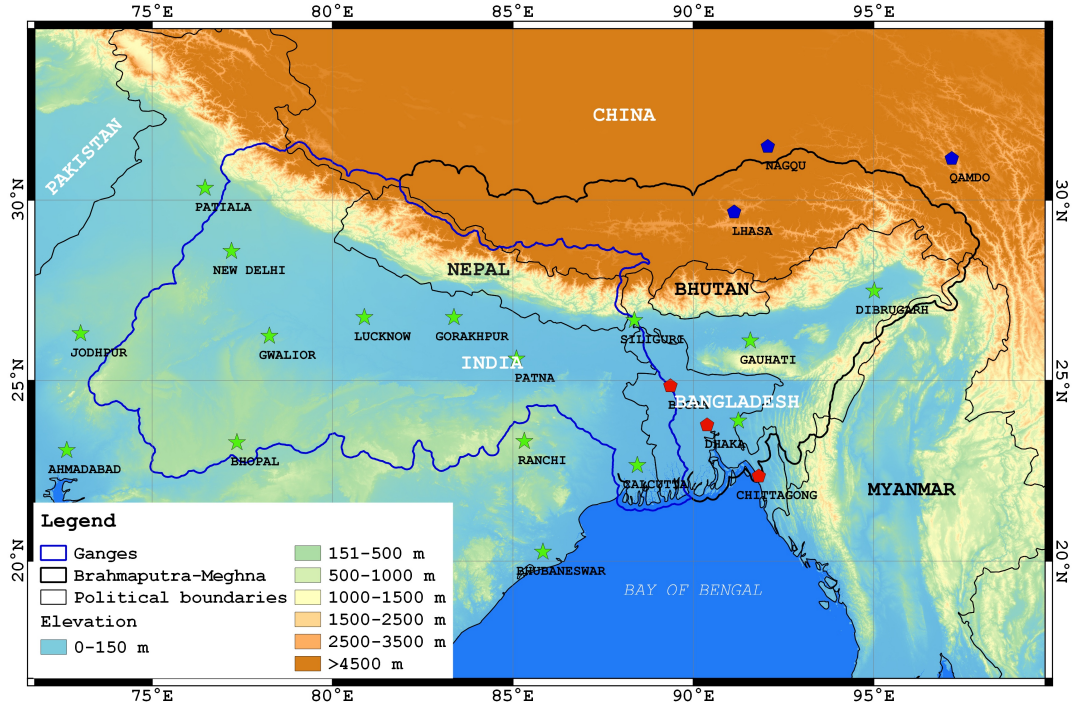


Figure 6.3: The general topography and locations of the radiosonde stations in the GBM River Basin. The radiosondes are shown in different colors- green for IMD/MK4 (India), red for those over Bangladesh (unknown), and blue for ShangE/ShangM (China)

To make an overall assessment and to understand the magnitude of improvements in the newly upgraded systems, radiosonde profiles of temperature, water vapour pressure, and refractivity extracted from CDAAC are compared with collocated COSMIC RO profiles. Refractivity (N) is a derived quantity, calculated from observed temperature (T) and water vapour pressure (p_w) at various pressure (p) levels based on the relation (Smith and Weintraub, 1953):

$$N = 77.6 \frac{p}{T} + 3.73 \times 10^5 \frac{p_w}{T^2}. \quad (6.1)$$

3656 6.2.3 Reanalysis products

3657 Global reanalyses have long played an important role in climate monitoring and research
 3658 applications due to their complete spatial coverage and temporal consistency with phys-
 3659 ical models. However, despite many efforts to integrate millions of observational data,
 3660 reanalyses completed to date have undesirable and sometimes very obvious and time-
 3661 varying biases, depending on the region, variable of interest, and application (Thorne
 3662 et al., 2011). Chapter 2–3 presented the skills of recent high global resolution reanalyses
 3663 over the satellite-era (1979 onwards), mainly with respect to precipitation, tempera-
 3664 ture, and soil moisture variables in the GBM River Basin. In this Chapter, their skills
 3665 in representing the upper air temperature and interannual variations at various altitude
 3666 levels within the UTLS region are assessed with respect to the spatially interpolated

Table 6.1: Details of radiosondes shown in Fig. 6.3 and the total number of profiles recorded from 2006 to 2013 at each radiosonde stations. The upgraded IMD radiosondes are named as IMD GPS. The radiosondes within Bangladesh are categorized as “unknown”.

| SL/No | WMO ID | Make | Location/Country | Latitude | Longitude | MSL [m] | # Profiles |
|-------|--------|---------|-------------------|----------|-----------|---------|------------|
| 1 | 42101 | IMD MK4 | PATIALA/INDIA | 30°20'N | 76°28'E | 251 | 1354 |
| 2 | 42182 | IMD GPS | NEW DELHI/INDIA | 28°35'N | 77°12'E | 216 | 2937 |
| 3 | 42314 | IMD GPS | DIBRUGARH/INDIA | 27°29'N | 95°1'E | 111 | 1687 |
| 4 | 42339 | IMD MK4 | JODHPUR/INDIA | 26°18'N | 73°1'E | 224 | 1142 |
| 5 | 42361 | IMD MK4 | GWALIOR/INDIA | 26°14'N | 78°15'E | 207 | 245 |
| 6 | 42369 | IMD MK4 | LUCKNOW/INDIA | 26°45'N | 80°53'E | 128 | 1244 |
| 7 | 42379 | IMD MK4 | GORAKHPUR/INDIA | 26°45'N | 83°22'E | 77 | 864 |
| 8 | 42397 | IMD MK4 | SILIGURI/INDIA | 26°40'N | 88°22'E | 123 | 432 |
| 9 | 42410 | IMD MK4 | GAUHATI/INDIA | 26°6'N | 91°35'E | 54 | 810 |
| 10 | 42492 | IMD GPS | PATNA/INDIA | 25°36'N | 85°6'E | 60 | 1066 |
| 11 | 42647 | IMD MK4 | AHMADABAD/INDIA | 23°4'N | 72°38'E | 55 | 1366 |
| 12 | 42667 | IMD MK4 | BHOPAL/INDIA | 23°17'N | 77°21'E | 523 | 1011 |
| 13 | 42701 | IMD MK4 | RANCHI/INDIA | 23°19'N | 85°19'E | 652 | 1248 |
| 14 | 42724 | IMD MK4 | AGARTALA/INDIA | 23°53'N | 91°15'E | 16 | 681 |
| 15 | 42809 | IMD MK4 | CALCUTTA/INDIA | 22°39'N | 88°27'E | 6 | 2537 |
| 16 | 42867 | IMD MK4 | NAGPUR /INDIA | 21°6'N | 79°3'E | 310 | 908 |
| 17 | 42874 | IMD MK4 | RAIPUR/INDIA | 21°14'N | 81°39'E | 298 | 655 |
| 18 | 42971 | IMD MK4 | BHUBANESWAR/INDIA | 20°15'N | 85°50'E | 46 | 1662 |
| 19 | 41923 | VRS92G | DHAKA/BDESH | 23°46'N | 90°23'E | 9 | 843 |
| 20 | 41977 | Unknown | CHITTAGONG/BDESH | 22°21'N | 91°49'E | 34 | 210 |
| 21 | 41883 | Unknown | BOGRA/BDESH | 24°51'N | 89°22'E | 20 | 21 |
| 22 | 56137 | Shang/M | QAMDO/CHINA | 31°9'N | 97°10'E | 3307 | 908 |
| 23 | 55591 | Shang/E | LHASA/CHINA | 29°40'N | 91°8'E | 3650 | 264 |
| 24 | 55299 | Shang/E | NAGQU/CHINA | 31°29'N | 92°4'E | 4508 | 2664 |

3667 COSMIC RO data. This is important especially given that observational systems have
3668 been relatively poor in the region (Das Gupta et al., 2005, Kumar et al., 2011).

3669 COSMIC temperature profiles over the GBM region are compared with two high-
3670 resolution modern reanalysis products, (a) MERRA-I (hereinafter as MERRA) (Rie-
3671 necker et al., 2008) and (b) ERA-Interim (Dee et al., 2011), both of which have been
3672 described in Chapter 2. The state-of-the-art Goddard Earth Observing System Data
3673 Assimilation System version 5 (GOES-5), used in MERRA, assimilates data from a
3674 wide variety of observing systems (e.g., *in-situ*, satellites) to produce a consistent set of
3675 spatio-temporal meteorological and climatic variables since the start of the satellite era
3676 (i.e., 1979). MERRA products are generated on a $1/2^\circ \times 2/3^\circ$ (or $\sim 50 \times 70$ km) grid
3677 with 72 vertical layers extending from the surface through to the stratosphere. Atmo-
3678 spheric variables (e.g., temperature, humidity) are produced at various temporal scales
3679 ranging from 3 hourly at $1.5^\circ \times 1.5^\circ$ (or $\sim 150 \times 150$ km grid) to monthly scales at the
3680 nominal horizontal resolution.

3681 ERA-Interim (Dee et al., 2011) builds on the previous generation of reanalyses (e.g.,
3682 ERA-15 and ERA-40) with improved model aspects, more advanced assimilation tech-
3683 niques (e.g., 4-D Variational Schemes) and better land surface model, and assimilates
3684 atmospheric profiles retrieved from the GNSS RO data. The atmospheric variables (e.g.,
3685 temperature and water vapour) are simulated at 6-hourly time-scales over 60 vertical
3686 levels at a $\sim 79 \times \sim 79$ km grid. Because ERA-Interim assimilates GNSS RO data,
3687 ERA-Interim and COSMIC RO data are not completely independent. Poli et al. (2010)
3688 found that GNSS RO data help to reduce temperature bias of ERA-Interim in the

3689 UTLS but are found to produce drying effects in the tropics. Monthly mean temper-
 3690 atures at 14 pressure levels from 500 to 10 hPa are obtained for both MERRA (see
 3691 <http://disc.sci.gsfc.nasa.gov/daac-bin/FTPSubset.pl>) and ERA-Interim (see
 3692 <http://apps.ecmwf.int/datasets/data/interim-full-daily/levtype=sfc/>) to as-
 3693 sess UTLS temperature over the GBM River Basin.

3694 6.2.4 Ocean–atmospheric indices

3695 Three climate indices are used in this here, representing (a) ENSO, (b) IOD, and
 3696 (c) QBO, which are commonly associated with significant fluctuations in UTLS tem-
 3697 peratures, i.e., large-scale ocean-atmospheric phenomena lead to variations in UTLS
 3698 temperature. ENSO and IOD indices have already been described in Section 2.3.3 of
 3699 Chapter 2 and the indices used here are extracted from the same data source. QBO
 3700 is stratospheric phenomenon characterized by an east–west oscillation in stratospheric
 3701 winds over a period of approximately 28 months (Baldwin et al., 2001). The QBO dom-
 3702 inates variability of the equatorial stratosphere and is easily identified as downward
 3703 propagating easterly (negative) and westerly (negative) wind regimes. It is commonly
 3704 characterized by an index derived based on zonal winds at 30 or 50 hPa. Here, the
 3705 QBO index at 30 hPa level covering the period 2006–2013 is obtained from NOAA
 3706 (<http://www.esrl.noaa.gov/psd/data/correlation/qbo.data>).

3707 6.2.5 Comparison of radiosonde and COSMIC RO datasets

3708 The collocated radiosondes and COSMIC RO profiles are compared at 13 pressure levels
 3709 (i.e., 850 hPa, 700 hPa, 500 hPa, 400 hPa, 300 hPa, 250 hPa, 200 hPa, 150 hPa, 100
 3710 hPa, 70 hPa, 50 hPa, 30 hPa, and 20 hPa) with respect to temperature (T), water
 3711 vapour pressure (p_w), and refractivity (R) by averaging over the period 2006–2013.
 3712 Mean biases and standard deviations are expressed relative to COSMIC RO data in
 3713 terms of temperature differences (ΔT), relative errors of water vapour pressure (RE p_w)
 3714 and refractivity (RE N) at each pressure level based on Eq. 6.2–6.4:

$$\Delta T = T^{\text{radiosonde}} - T^{\text{COSMIC}} \quad (6.2)$$

$$\text{RE } p_w = \frac{p_w^{\text{radiosonde}} - p_w^{\text{COSMIC}}}{p_w^{\text{COSMIC}}} \quad (6.3)$$

$$\text{RE } N = \frac{N^{\text{radiosonde}} - N^{\text{COSMIC}}}{N^{\text{COSMIC}}} \quad (6.4)$$

3715 It should be noted here that several studies have addressed the use of collocation
 3716 criteria (relating to the radial distance and time difference between a pair of radiosonde
 3717 and RO profile) in comparing radiosonde and GNSS RO measurements (e.g., Sun et al.,
 3718 2010, Anthes, 2011, Khandu et al., 2011, Zhang et al., 2011). These studies have found
 3719 insignificant differences in the UTLS region within a difference of 3 hours and 300 km.
 3720 However, in the troposphere (850–200 hPa), Sun et al. (2010) found that collocation
 3721 mismatch significantly impacts their measurement precisions, i.e., 0.35°C per 3 hour

3722 and 0.42°C per 100 km, and 3.3% per 3 hour and 3.1% per 100 km in relative humidity.
 3723 Considering the limited number of radiosonde stations in the GBM River Basin, a
 3724 collocation criteria of 200 km and 2-hour time difference is applied here.

3725 6.2.6 Tropopause temperatures and heights

3726 The high vertical resolution of GNSS RO retrieval enables near-accurate changes in the
 3727 tropopause, through its high vertical resolution, which is important for understanding
 3728 the physical and chemical processes, including temperature variations that affect these
 3729 processes. Since the inception of GNSS RO technique, several studies have presented the
 3730 added values of GNSS RO in understanding the variability of the tropopause (Steiner
 3731 et al., 2007, Schmidt et al., 2010, Anthes, 2011) and the UTLS region. High observational
 3732 quality and data stability among various RO systems provide stable climate data in the
 3733 UTLS region required for climate change studies (Steiner et al., 2011, 2013, Ho et al.,
 3734 2014). To estimate the regional temporal variations in tropopause properties such as
 3735 tropopause heights and temperatures, the spatially interpolated COSMIC RO-derived
 3736 *lapse rate tropopause* (LRT) heights and temperatures are examined in this Chapter.
 3737 Among various tropopause definitions (see Pan et al., 2004), many previous studies
 3738 have found LRT to be more sensitive to tropospheric warming and most relates to
 3739 the underlying effect of climate change (see Santer et al., 2003a, Sausen and Santer,
 3740 2003). LRT or (hereinafter as tropopause) can be derived from a temperature profile
 3741 by applying the World Meteorological Organisation (WMO, 1957) definition, wherein
 3742 it is defined as “the lowest level at which the lapse rate decreases to 2°C km⁻¹ or less,
 3743 provided also the average lapse rate between this level and all higher levels within 2 km
 3744 does not exceed 2°C km⁻¹”.

COSMIC RO data extracted from CDAAC contain the derived tropopause heights and temperatures. Following the introduction of ERA-Interim and MERRA, it is also important to compare them with the COSMIC RO data, in order to quantify their spatio-temporal differences over the GBM River Basin. The WMO (1957) definition is applied to MERRA temperature profiles to calculate the tropopause temperatures, whereas the tropopause heights are interpolated using the pressure levels and their approximate heights are estimating using the following relationship (PSAS, 2004):

$$h_{\text{LRT}} \equiv 44\,330.8 - 4946.54 \times P^{0.1902632}. \quad (6.5)$$

3745 6.3 Results and discussion

3746 6.3.1 Evaluation of radiosonde observations

3747 Temperature, water vapour pressure and refractivity profiles observed at various ra-
 3748 diosondes in the GBM River Basin (see, Table 6.1) are compared with those derived
 3749 from COSMIC RO between August 2006 and December 2013. Of particular interest is

3750 the performance of the recently upgraded radiosondes at three stations in India: New-
 3751 Delhi, Patna, and Dirbugarh, where major concerns have been raised prior to upgrading
 3752 to a new GPS-based system (e.g., Das Gupta et al., 2005, Krishna Kumar et al., 2011,
 3753 Ansari et al., 2015). Figure 6.4 shows the total number of data pairs at each pressure
 3754 level where COSMIC RO data are found within a radial distance of 200 km and 2 hours
 3755 time difference from a nearest radiosonde station over the entire period of study. The
 3756 number of data pairs varied at each pressure level for both temperature and humid-
 3757 ity (i.e., water vapour pressure) and tend to decrease rapidly with increasing altitude,
 3758 which is particularly true for the IMD radiosondes (Fig. 6.4). Majority of the IMD ra-
 3759 diosondes have burst out between 14.2 km and 18.8 km, leading to a drastic decline in
 3760 meteorological data in the UTLS region.

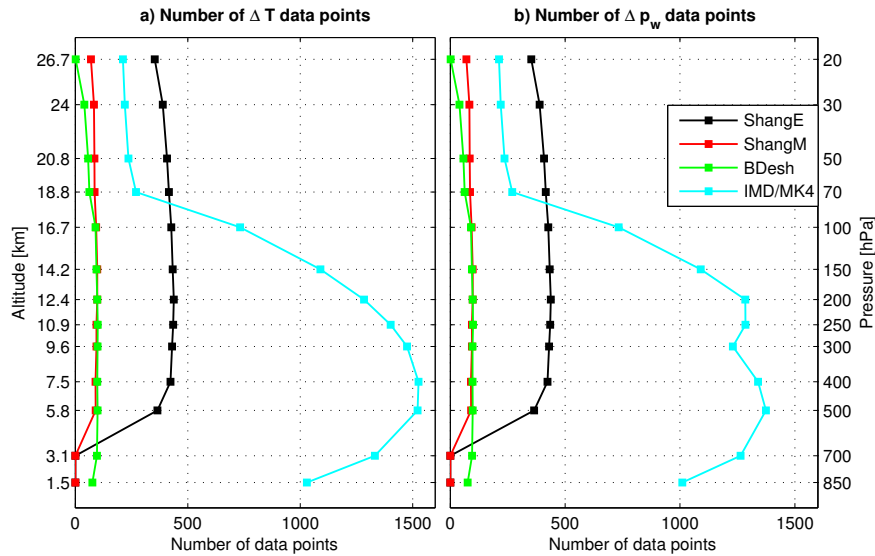


Figure 6.4: Number of data pairs at each pressure level for temperature and humidity (water vapour pressure) for all the radiosonde types (see, Table 6.1) from August 2006 to December 2013.

3761 6.3.1.1 Temperature

3762 Figure 6.5 shows the mean temperature bias and their standard deviations for various
 3763 radiosondes with respect to the COSMIC RO data. The quality of radiosondes differ
 3764 considerably within the altitude range compared. Radiosondes generally show cold bias
 3765 in the troposphere (below 14.2 km) and the lower stratosphere (above the tropopause
 3766 level), warm bias in the tropopause region (with the exception of radiosondes over
 3767 Bangladesh). While the three radiosondes over the Bangladesh territory (labelled as
 3768 “Bdesh”) exhibit significantly large (warm) bias within the UTLS region (including the
 3769 tropopause), biases are generally less than $\pm 0.5^\circ\text{C}$ in the Chinese territory (labelled as
 3770 “ShangE” and “ShangM”). ShangE appears to perform better than ShangM both in
 3771 terms of biases (Fig. 6.5a) and standard deviations (Fig. 6.5b) in the tropopause region
 3772 although it also shows a substantial bias in the stratosphere and in the lower most
 3773 troposphere (Fig. 6.5a). On the other hand, the radiosondes in the Indian territory

3774 (labelled as “IMD/MK4”) exhibit the largest bias above 7.5 km (or 400 hPa level) with
 3775 a standard deviation of more than 2°C (Fig. 6.5b). These results are consistent with
 3776 most previous studies (e.g., Sun et al., 2010, Krishna Kumar et al., 2011, Ansari et al.,
 3777 2015).

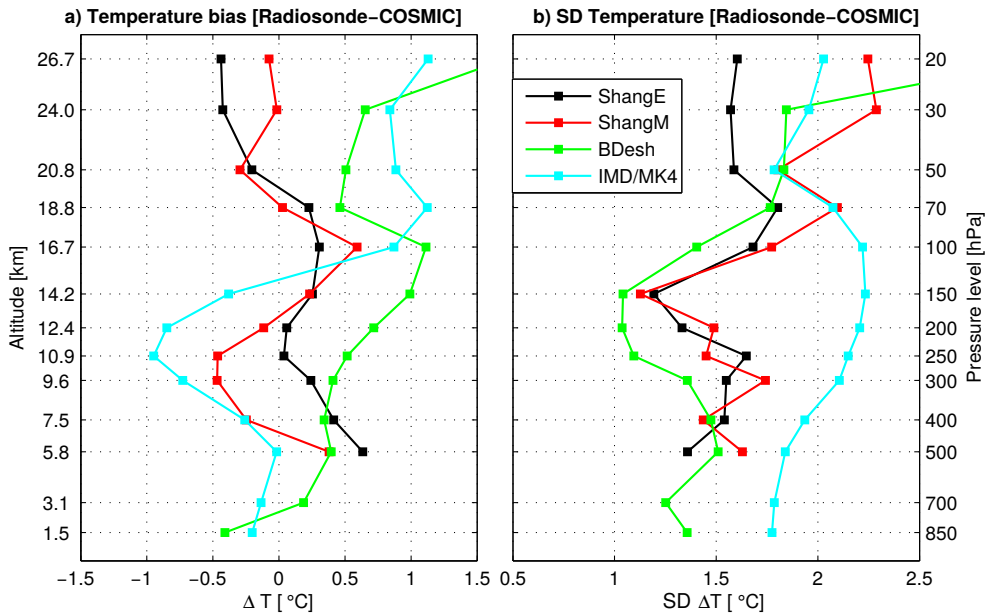


Figure 6.5: (a) Mean temperature bias and (b) standard deviations of various radiosondes (refer to Table 6.1) over the GBM River Basin with respect to COSMIC RO data between August 2006 and December 2013.

3778 The spatially averaged mean biases and standard deviations of various radiosonde
 3779 observations calculated for the entire GBM River Basin are given in Table 6.2. Biases
 3780 and standard deviations are estimated separately for the UT (400–150 hPa level) and the
 3781 lower stratosphere (70–20 hPa level) in order to avoid the cancellation of errors caused
 3782 by opposite signs. As discussed, ShangE and ShangM exhibit the least temperature
 3783 bias (even though of opposite signs) for both the layers. IMD/MK4 sondes show a cold
 3784 (warm) bias of 0.6°C (1.0°C) in the upper troposphere (lower stratosphere), while Bdes
 3785 sondes indicate warm bias of 0.6°C and 0.8°C in the UT and LS layers, respectively
 3786 (Table 6.2).

3787 In order to examine if there are any improvements in the measurements obtained
 3788 from three recently upgraded radiosondes (at New Delhi, Patna, and Dilbugarh), a sep-
 3789 arate analysis is carried out using observations before (August 2006–May 2009) and
 3790 after (June 2009–May 2013) upgrading to the new GPS-based system. The comparison
 3791 results shown in Fig. 6.6 are based on more than 200 data pairs for both time periods.
 3792 The results show substantial improvement in temperature bias and standard deviations
 3793 (see, Fig. 6.6a–b). The large cold (warm) bias in the troposphere (stratosphere) has been
 3794 largely eliminated (Fig. 6.6a) and their variance have also been reduced substantially in
 3795 the new GPS-based radiosondes. GPS receivers onboard radiosondes helps to provide
 3796 better estimation of pressure (in addition to geographical position) resulting in an overall

3797 improvement in its measurements. Overall, the temperature biases have reduced from -
 3798 0.8°C
 3799 in T
 3800 Shar
 3801 resu.
 3802 port
 3803 2013

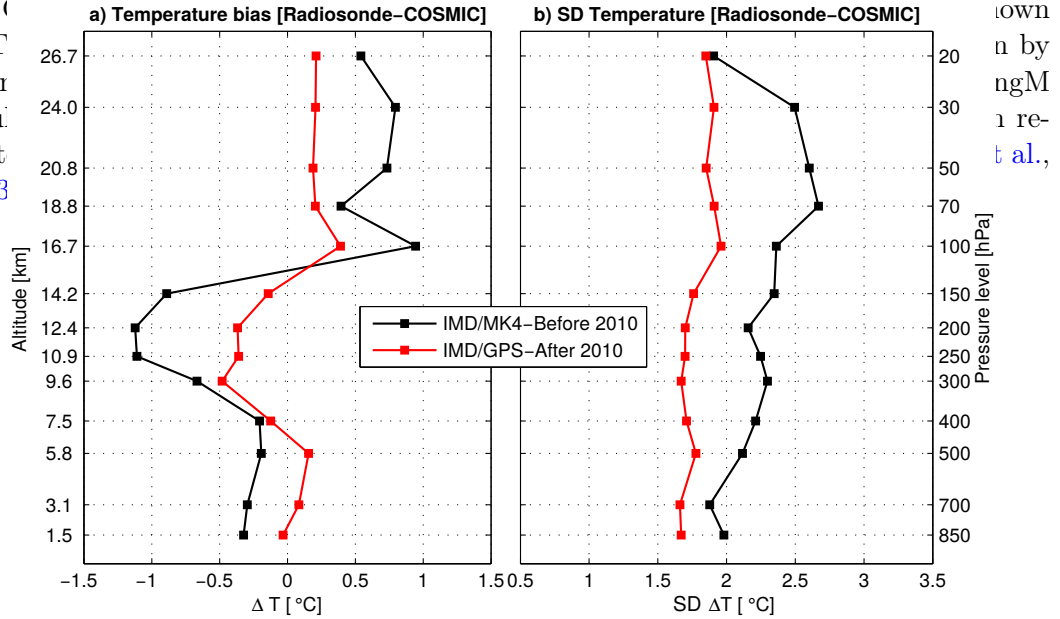


Figure 6.6: (a) Mean temperature bias and (b) standard deviations of IMD/MK4 and IMD-GPS (refer to Table 6.1) with respect to COSMIC RO data over the GBM Basin. The temperature biases are plotted for two periods based on three radiosonde stations (New Delhi, Patna, and Dilbugarh), one between August 2006 and May 2009 (labelled as “IMD/MK4”) and the other between May 2009 and December 2013 (labelled as “IMD/GPS”).

Table 6.2: Mean biases and standard deviations in temperature, water vapour pressure, and refractivity of various existing radiosondes in the GBM River Basin with to COSMIC RO data (“wet profiles”). The statistics are computed separately for the upper troposphere (400–150 hPa) and the lower stratosphere (70–20 hPa) for the period 2006–2013.

| Radiosondes | Upper Troposphere [400–150 hPa] | | | Lower Stratosphere [70–20 hPa] | |
|-------------|---------------------------------|--------------|------------|--------------------------------|------------|
| | ΔT [°C] | RE p_w [%] | RE N [%] | ΔT [°C] | RE N [%] |
| ShangE | 0.2±1.5 | -45.0±50.4 | -0.4±0.9 | -0.2±1.6 | 0.1±0.8 |
| ShangM | -0.2±1.4 | -35.2±47.7 | -0.1±0.8 | -0.1±0.1 | 0±0 |
| IMD/MK4 | -0.6±2.1 | -54.5±43.1 | -0.1±1.2 | 1.0±2.0 | -0.5±0.9 |
| Bdesh | 0.6±1.2 | -42.4±44.4 | -0.3±0.8 | 0.8±2.1 | -0.4±1.0 |

Table 6.3: Mean biases and standard deviations in temperature, water vapour pressure, refractivity of three IMD/GPS-based radiosondes in reference to COSMIC RO data (“wet profiles”). Biases and standard deviations are estimated from Fig. 6.6.

| Radiosondes | Upper Troposphere [400–150 hPa] | | | Lower Stratosphere [70–20 hPa] | |
|-------------|---------------------------------|------------------|----------------|--------------------------------|----------------|
| | ΔT [°C] | RE p_w [%] | RE N [%] | ΔT [°C] | RE N [%] |
| IMD/MK4 | -0.8 ± 2.3 | -50.6 ± 47.6 | 0.1 ± 1.2 | 0.6 ± 2.2 | -0.3 ± 1.0 |
| IMD/GPS | -0.3 ± 1.7 | -35.5 ± 50.5 | -0.1 ± 0.9 | 0.2 ± 1.9 | -0.1 ± 0.9 |

3804 6.3.1.2 Water vapour

3805 Water vapour plays an important role in the global and regional weather, climate,
 3806 and hydrology and is a major source of uncertainty in the lower troposphere (e.g., [Kuo
 3807 et al., 2004](#), [Danzer et al., 2014](#)). CDAAC uses a 1D-Var assimilation system with coarse
 3808 grid ECMWF operational forecast analysis to disaggregate the most optimal fields of
 3809 pressure, temperature, and moisture contribution to refractivity ([Anthes et al., 2008](#),
 3810 [Anthes, 2011](#)). The retrieved profiles are called “wet profile”. Figure 6.7 shows the relative
 3811 errors in water vapour pressure of various radiosondes with respect to the COSMIC RO
 3812 (“wet profiles”) data. Considering that water vapour is negligible in the stratosphere,
 3813 the errors are plotted only for the troposphere (below 100 hPa level) and their basin-
 3814 averaged statistics are provided in Table 6.2 and 6.3. All the radiosondes show dry bias
 3815 against the COSMIC RO data and their magnitudes tend to increase with altitude (Fig.
 3816 6.7a). The biases in ShangE and ShangM sondes are found to be consistent below 200
 3817 hPa with a mean bias of -39% and 23%, respectively. Note that the relative errors shown
 3818 in Table 6.2 are calculated between 400 hPa and 150 hPa level and it should be noted
 3819 that these two radiosondes are anomalously biased at the tropopause (100 hPa) level.
 3820 On the other hand, IMD/GPS radonsonde exhibit relatively low biases above 500 hPa
 3821 level (Fig. 6.7a) and their standard deviations are also found to be consistent around
 3822 50% (Fig. 6.7b). The relative error has been reduced by about 15% after upgrading to
 3823 the GPS-based sondes at the three stations over India (see, Table 6.3).

3824 6.3.1.3 Refractivity

3825 Errors in refractivity are directly related to errors in observed temperatures and water
 3826 vapour with the latter contributing largest in the lower troposphere. The comparison
 3827 results shown in Tables 6.2 and 6.3 indicated relatively large errors for temperature and
 3828 water vapour pressure by the IMD/MK4 and BdesH radiosondes corresponding to very
 3829 cold (warm) biases in the troposphere and stratosphere (tropopause region) (see, Fig.
 3830 6.5a). The refractivity errors are consistent with the errors in temperature and water
 3831 vapour pressure with IMD/MK4 and BdesH radiosondes indicating the largest relative
 3832 refractivity bias above 300 hPa level (Fig. 6.8a). However, it is seen that BdesH radioson-
 3833 des indicate the smallest standard deviation between 300 hPa to 70 hPa level. Thus,
 3834 very large refractivity errors in IMD/BdesH sondes in the upper troposphere may have
 3835 resulted from large temperature bias (see, Fig. 6.5a). Consistent with the temperature
 3836 and water vapour pressure measurements, refractivity errors are greatly reduced in the

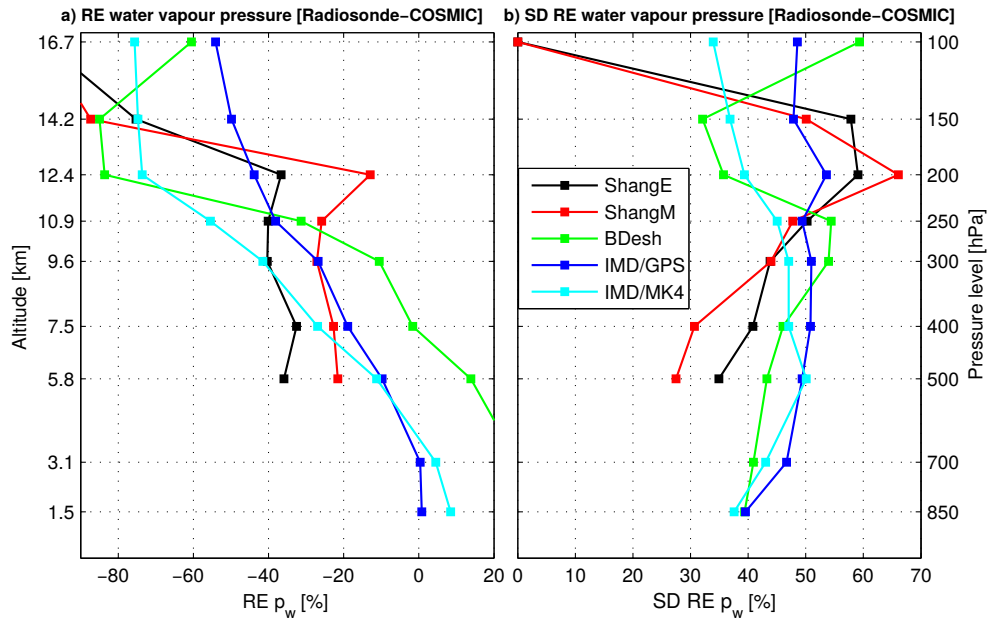


Figure 6.7: (a) Relative errors and (b) standard deviations of water vapour pressure (hPa) of various radiosondes over the GBM River Basin with respect to COSMIC RO data.

3837 IMD/GPS-based radiosondes both in terms of biases and standard deviations, which is
 3838 now at par with ShangE and ShangM sondes (see, Table 6.2 and 6.3).

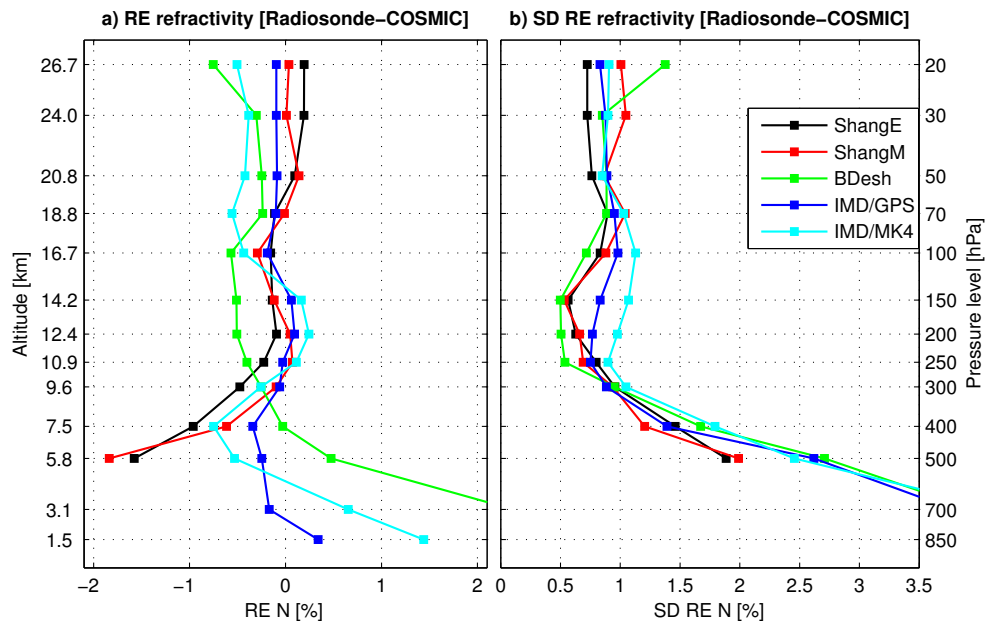


Figure 6.8: (a) Relative errors and (b) standard deviations of refractivity (in %) of various radiosondes with respect to COSMIC RO data over the GBM River Basin between August 2006 and December 2013.

3839 **6.3.2 Seasonal and interannual variability of UTLS temperature**

3840 In this section, the COSMIC RO temperature datasets (from “dry profile”) are compared
 3841 with those simulated by two widely used reanalysis systems: MERRA and ERA-Interim.
 3842 The COSMIC RO temperature datasets are firstly linearly interpolated to the standard
 3843 pressure level of MERRA and ERA-Interim between 500 hPa and 10 hPa, are then
 3844 spatially interpolated to a $0.5^\circ \times 0.5^\circ$ grid at each level using the ordinary kriging
 3845 interpolation algorithm (Goovaerts, 2000). Figure 6.9 shows the spatially averaged tempo-
 3846 ral evolution of UTLS temperature anomalies (time mean removed) over the GBM
 3847 River Basin. The temperature anomalies of COSMIC RO data are plotted in Fig. 6.9a.
 3848 The temperature anomalies range between $\pm 6^\circ\text{C}$, with large anomalies in the upper tro-
 3849 posphere and lower troposphere, suggesting strong seasonal variations in these regions.
 3850 As a result a strong seasonal cycle is evident in the troposphere below 200 hPa level
 3851 and the stratosphere (above 70 hPa level). The three datasets (COSMIC, MERRA, and
 3852 ERA-Interim) agree very well above 200 hPa where water vapour is negligible. Below
 3853 200 hPa level, however, COSMIC data (Fig. 6.9a) are found to be colder than the two
 3854 reanalyses (Fig. 6.9b–c) as the effect of water vapour becomes more significant.

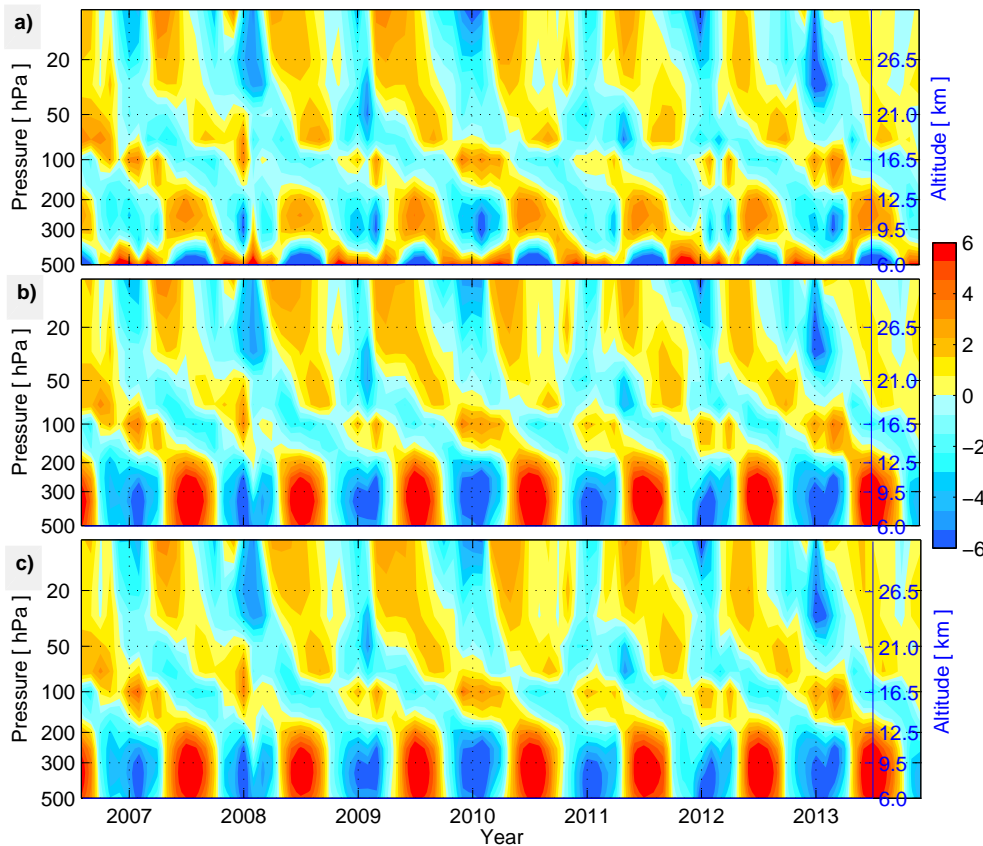


Figure 6.9: Temporal evolution of temperature ($^\circ\text{C}$) with the time mean removed at each pressure level (500–10 hPa) based on (a) COSMIC RO, (b) MERRA, and (c) ERA-Interim. Data span between August 2006 and December 2013 and contain area-average over the region ($16\text{--}35^\circ\text{N}$, $71\text{--}100^\circ\text{E}$) covering the GBM River Basin.

3855 Both MERRA and ERA-Interim show quantitatively similar biases with respect to
 3856 the COSMIC RO data, indicating a mean bias of 1.23°C and 1.22°C , respectively, when
 3857 averaged over 200 to 70 hPa level, whereas the difference between MERRA and ERA-
 3858 Interim is found to be relatively small (within $\pm 0.5^{\circ}\text{C}$) over the same layer during the
 3859 last 89 months. The annual cycle of temperature at (a) 200 hPa, (b) 100 hPa, (c) 70 hPa,
 3860 and (d) 50 hPa levels are shown in Fig. 6.10. Both MERRA and ERA-Interim exhibit
 3861 warm bias at all the pressure levels with varying magnitudes over different seasons.
 3862 Both reanalysis products are found to be warmer by $\sim 1^{\circ}\text{C}$ in June at 200 hPa level
 3863 (Fig. 6.10a), $\sim 1.5^{\circ}\text{C}$ at 100 hPa level (Fig. 6.10b), and up to 2°C at 70 hPa level from
 3864 November to May (Fig. 6.10c).

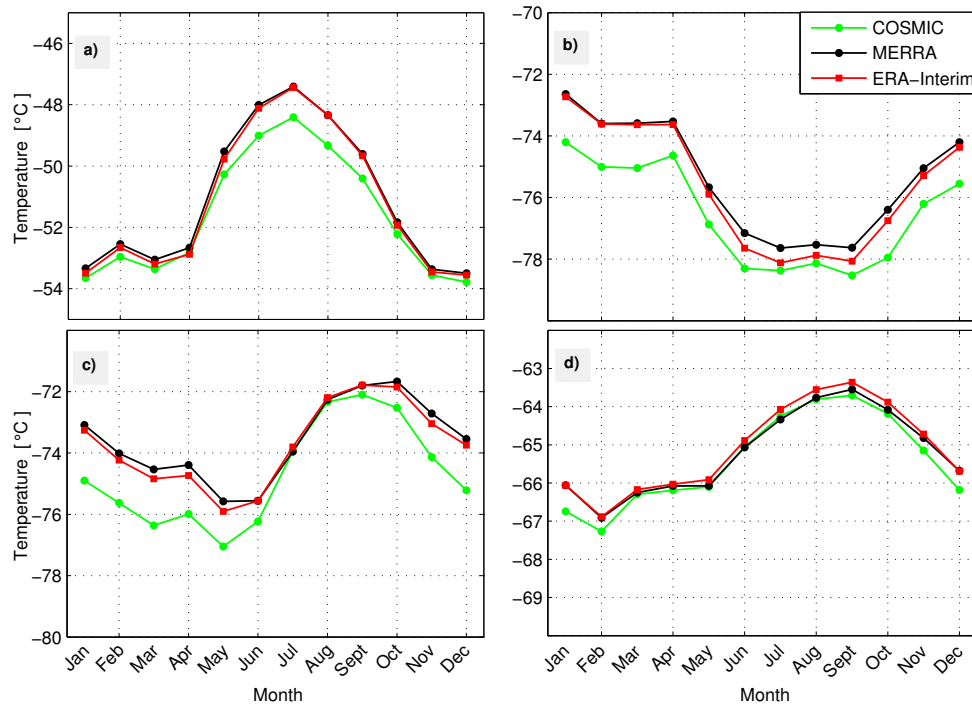


Figure 6.10: Seasonal cycle of temperature ($^{\circ}\text{C}$) at (a) 200 hPa, (b) 100 hPa, (c) 70 hPa, and (d) 50 hPa from August 2006 to December 2013 based on COSMIC RO, MERRA, and ERA-Interim averaged over the GBM River Basin.

3865 Figure 6.11 shows the detrended (as well as deseasonalized) time-series of temper-
 3866 ature anomalies at four pressure levels mentioned above. The temperature anomalies
 3867 show considerable interannual variability from 2006 to 2013, indicating large negative
 3868 anomalies in the troposphere during the 2009/2010 and 2012/2013 winter, and during
 3869 2007/2008, 2008/2009, and 2011/2012 winters in the lower stratosphere. The 100 hPa
 3870 level was warmer by $\sim 1.5^{\circ}\text{C}$ during the period 2006/2007, 2009/2010, and 2012/2013,
 3871 and this is consistent in all the three data sets (Fig. 6.11a-c). The warm anomalies at
 3872 the 100 hPa level for all three periods coincide with warm (i.e., El Niño) ENSO phase,
 3873 while anomalously cold temperatures at 50 hPa level during 2009/2010 and 2010/2011
 3874 coincides with the recent stratospheric sudden warming (SSW) events. The stratospheric
 3875 planetary waves in the winter Northern Hemisphere can become so intense that they

3876 can rapidly disrupt the northern polar vortex, replacing the westerly winds with east-
 3877 erly winds at high latitudes, leading to a dramatically warm polar stratosphere. This
 3878 phenomenon is called SSW (Baldwin et al., 2001) and has a tendency to cool the strato-
 3879 sphere in the tropics and subtropics (e.g., 50 hPa level in Fig. 6.11). The temperature
 3880 decreased by about 5°C during the 2008/2009 SSW event at 50 hPa level (see also
 3881 Resmi et al., 2013). The SSW events can occur during both westerly and easterly phase
 3882 of the QBO, in which both 2008/2009 and 2010/2011 events occurred during the west-
 3883 erly phase. The warm temperature anomalies from 2006–2007 in the UTLS are likely
 3884 associated with El Niño (warm ENSO phase) and positive IOD phase, whereas positive
 3885 temperature anomalies above 50 hPa possibly indicate a weak SSW event.

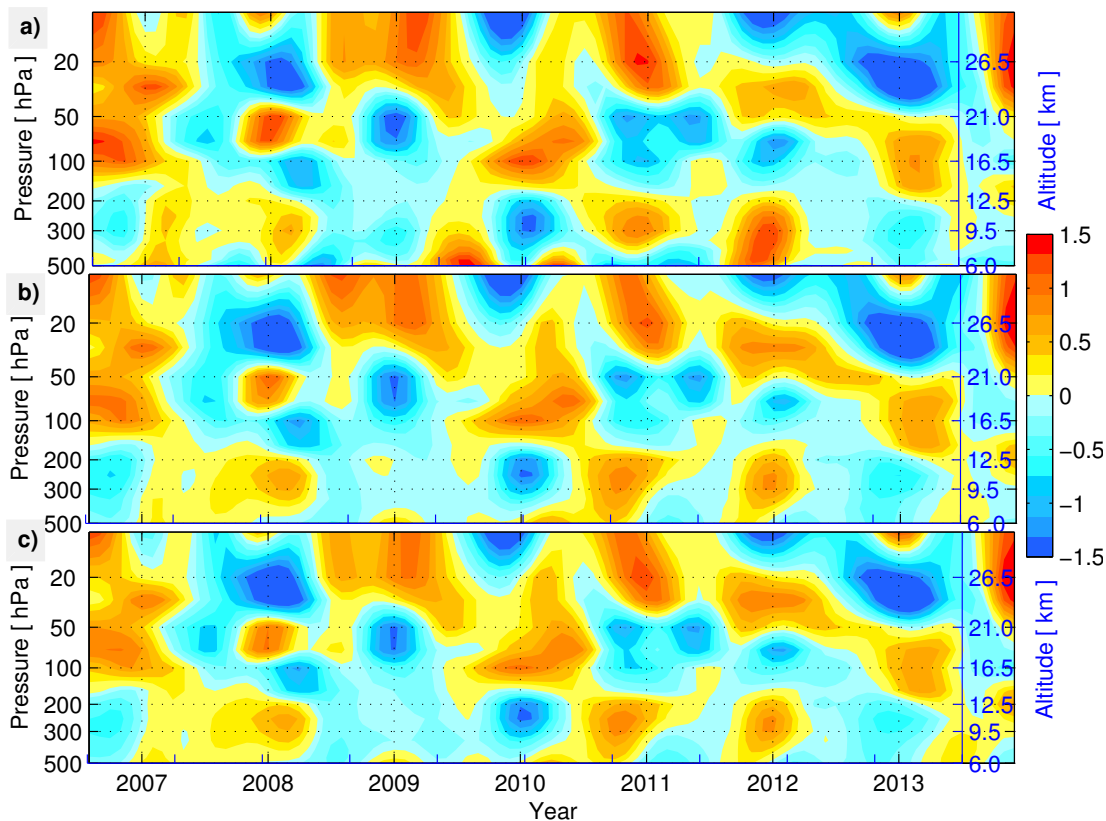


Figure 6.11: Interannual variability of temperature (°C) in the UTLS region based on (a) COSMIC RO, (b) MERRA, and (c) ERA-Interim from August 2006 to December 2013.

3886 In order to relate them to the three climate indices described in Sect. 6.2.4, the tem-
 3887 perature anomalies at (a) 200 hPa, (b) 100 hPa, (c) 70 hPa, and (d) 50 hPa are plotted
 3888 in Fig. 6.12a–d together with the three indices in Fig. 6.12e. The 200 hPa level temper-
 3889 ature anomalies clearly indicate the influence of 2009/2010 El Niño event (Fig. 6.12a)
 3890 where temperature decreased by $\sim 1.5^\circ\text{C}$ when El Niño was at its peak in January
 3891 2010 (Fig. 6.12a). The 200 hPa level temperatures are negatively correlated with ENSO
 3892 (Fig. 6.12e) and the 100 hPa level temperature variations (Fig. 6.12b). The 100 hPa level,
 3893 whose temperatures are highly correlated with ENSO (see Table 6.4), also appears to be
 3894 closely associated with the QBO anomalies especially during 2008/2009 and 2010/2011

3895 (Fig. 6.12b). The temperature anomalies at 70 and 50 hPa levels (Fig. 6.12c–d) primar-
 3896 ily depict the structure of recent major SSW events (see also, Fig. 6.11), both of which
 3897 occurred during the westerly phase of the QBO cycle. Correlation coefficients between
 3898 temperature anomalies at these four pressure levels and three atmospheric/ocean in-
 3899 dices are given in Table 6.4. Significance of the correlation coefficients are tested at 95%
 3900 confidence level using the Students t -test with a reduced degree of freedom calculated
 3901 by dividing the total number of months (i.e., 89) by 3 (i.e., averaging window), that is
 3902 used to smooth the time-series. Thus, the degree of freedom becomes $n-2 = 27$.

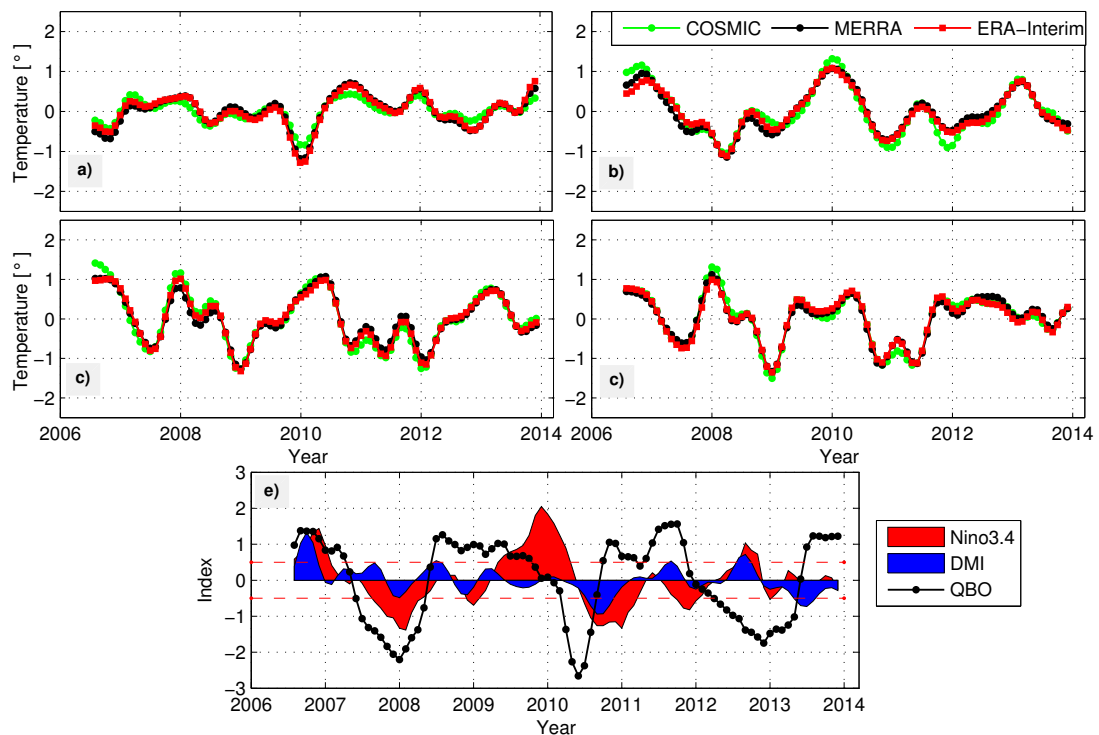


Figure 6.12: Interannual variability of temperature ($^{\circ}\text{C}$) at (a) 200 hPa, (b) 100 hPa, (c) 70 hPa, and (d) 50 hPa from August 2006 to December 2013 based on COSMIC RO, MERRA, and ERA-Interim. (e) Ocean–atmospheric indices: Niño3.4, DMI, and QBO are also plotted for reference.

3903 As shown in Fig. 6.12, ENSO is highly correlated (0.82 at 1-month time lag)
 3904 with temperatures at 100 hPa level and tend to be insignificant above 70 hPa level.
 3905 Warmer (colder) SST leads to stronger (weaker) convection resulting in colder (warmer)
 3906 tropopause temperatures and are also negatively correlated with temperatures at 200
 3907 hPa level. Both MERRA and ERA-Interim indicate very similar correlation values and
 3908 hence, are not shown. IOD is found to be significantly correlated with temperatures
 3909 in the lower troposphere with a correlation of -0.53 at 400 hPa level (see Table 6.4).
 3910 This is obvious because the correlation between IOD and ENSO between 2006 and 2013
 3911 was substantially higher (0.42) than the long-term value (of ~ 0.3). At the 200 hPa
 3912 level, its correlation decreased to -0.42 (see, Table 6.4) but is still significant at 95%
 3913 confidence level. Temperatures at 100 hPa level over the tropics have been shown as an
 3914 approximation of the QBO signal in Liang et al. (2011) due their very high correlation

Table 6.4: Correlation coefficients between various climate indices and temperature anomalies at 200 hPa, 100 hPa, 70 hPa, and 50 hPa for the period August 2006 to December 2013. The values that are significant at 95% confidence level based on the reduced degree of freedom are bolded. Positive time lag indicate ENSO/IOD/QBO fluctuating UTLS temperature and vice versa.

| Pressure levels | ENSO | | IOD | | QBO | |
|-----------------|--------------|--------------|--------------|--------------|--------------|--------------|
| | Correlation | Lag (months) | Correlation | Lag (months) | Correlation | Lag (months) |
| 200 hPa | -0.70 | 0 | -0.42 | 0 | 0.39 | 1 |
| 100 hPa | 0.82 | 1 | 0.27 | 2 | 0.47 | 0 |
| 70 hPa | 0.40 | 3 | -0.35 | -4 | -0.45 | 2 |
| 50 hPa | 0.27 | 1 | 0.34 | 2 | 0.42 | 6 |

3915 (0.86) between 2004 and 2010. However, their relationship did not hold steady (with
 3916 a correlation of 0.47 at 100 hPa level) as the QBO westerly phase slowed dramatically
 3917 lasting for about 21 months (i.e., 1 and 1/2 cycle) from June 2008 to January 2010,
 3918 which is then followed by a steep easterly phase in June 2010.

3919 Temperature changes estimated at the four pressure levels (Fig. 6.12) from 2006 to
 3920 2013 are given in Table 6.5. The linear trends are estimated from the deseasonalized tem-
 3921 perature anomalies using non-parametric Sen’s slope estimator (Sen, 1968). Significance
 3922 of trends are tested at 95% confidence level based on the Mann–Kendall non-parametric
 3923 test (Mann, 1945, Kendall, 1962). Consistent with the time-series shown in Fig. 6.12a,
 3924 there is a slight increase (but not significant) in temperature ($0.02 \pm 0.02^\circ\text{C year}^{-1}$ based
 3925 on COSMIC RO) at 200 hPa level and a decrease in temperature ($-0.04 \pm 0.05^\circ\text{C year}^{-1}$
 3926 based on COSMIC RO) at the 100 hPa level. It also confirms the recent stratospheric
 3927 cooling trends (Seidel et al., 2011), indicating a temperature decrease at the rate of
 3928 $0.07 \pm 0.05^\circ\text{C year}^{-1}$ based on COSMIC RO at 70 hPa level during the past 8 years.
 3929 These trends are also consistently estimated by the two reanalysis products (MERRA
 3930 and ERA-Interim) except at 100 hPa level where MERRA data did not show any trend
 3931 (see Table 6.5). The uncertainties in trend estimates were relatively larger than the trend
 3932 themselves due to the short time span but nevertheless the trends are clearly visible at
 3933 various pressure levels in the UTLS region (see, Fig. 6.12).

Table 6.5: Trends in temperature ($^\circ\text{C}/\text{yr}$) at 200 hPa, 100 hPa, 70 hPa, and 50 hPa for the period August 2006 to December 2013. Uncertainties in trend estimates are reported at 95% confidence interval.

| Pressure levels | COSMIC | MERRA | ERA-Interim |
|-----------------|------------------|------------------|------------------|
| 200 hPa | 0.02 ± 0.02 | 0.03 ± 0.03 | 0.03 ± 0.05 |
| 100 hPa | -0.04 ± 0.05 | 0.00 ± 0.00 | -0.02 ± 0.04 |
| 70 hPa | -0.07 ± 0.05 | -0.04 ± 0.05 | -0.05 ± 0.05 |
| 50 hPa | -0.02 ± 0.04 | -0.01 ± 0.01 | -0.01 ± 0.02 |

3934 6.3.3 Trends and variability of tropopause heights and temperatures

3935 This section examines the spatio-temporal variations in tropopause temperatures and
 3936 heights using MERRA and spatially interpolated COSMIC RO data between August
 3937 2006 and December 2013. The annual mean and standard deviation of tropopause tem-
 3938 peratures and heights are plotted in Figs. 6.13 and 6.14. The tropopause is generally
 3939 colder (higher) in south (closer to the equator), reaching a minimum (maximum) tem-
 3940 perature (height) of -81.5°C (16.9 km) over southern Myanmar (Figs. 6.13a and 6.14a).
 3941 While the temperature gradually increases from south to north (from -81.5 to -69.5°C ,
 3942 based on COSMIC RO in Fig. 6.13a), its heights are more or less homogenous at around
 3943 16.8 km below 29°N with its boundary roughly falling on the northern boundaries of
 3944 Bhutan. However, its height changes steeply by around 2 km from 29 to 35°N , which
 3945 also shows the largest standard deviation (~ 1.8 km, Fig. 6.14b). The standard deviation
 3946 of tropopause temperatures reaches up to $\pm 6^{\circ}\text{C}$ over the region based on COSMIC
 3947 RO data (Fig. 6.13b).

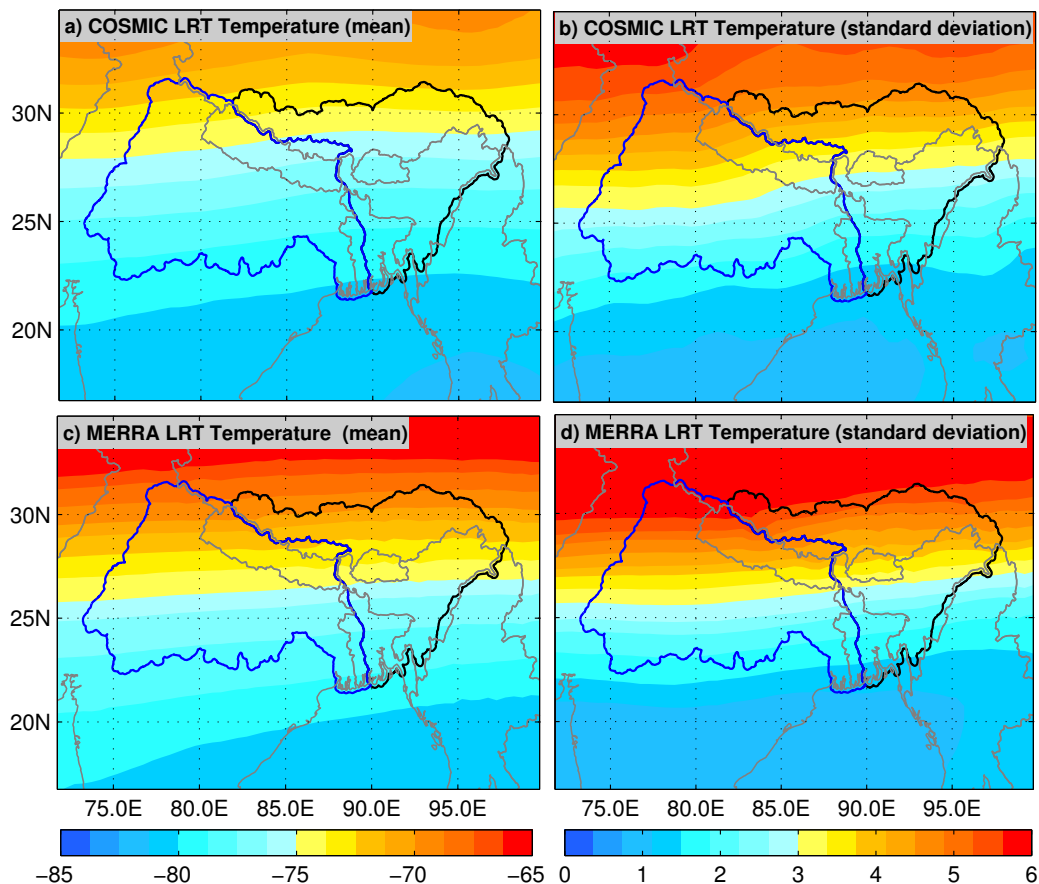


Figure 6.13: Spatial variation of mean and standard deviation of tropopause temperatures ($^{\circ}\text{C}$) derived from COSMIC RO and MERRA product based on 89 months from August 2006 to December 2013. (a) Mean and (b) standard deviation of tropopause temperatures ($^{\circ}\text{C}$) from COSMIC RO, (c) mean and (d) standard deviation of tropopause temperatures ($^{\circ}\text{C}$) from MERRA product.

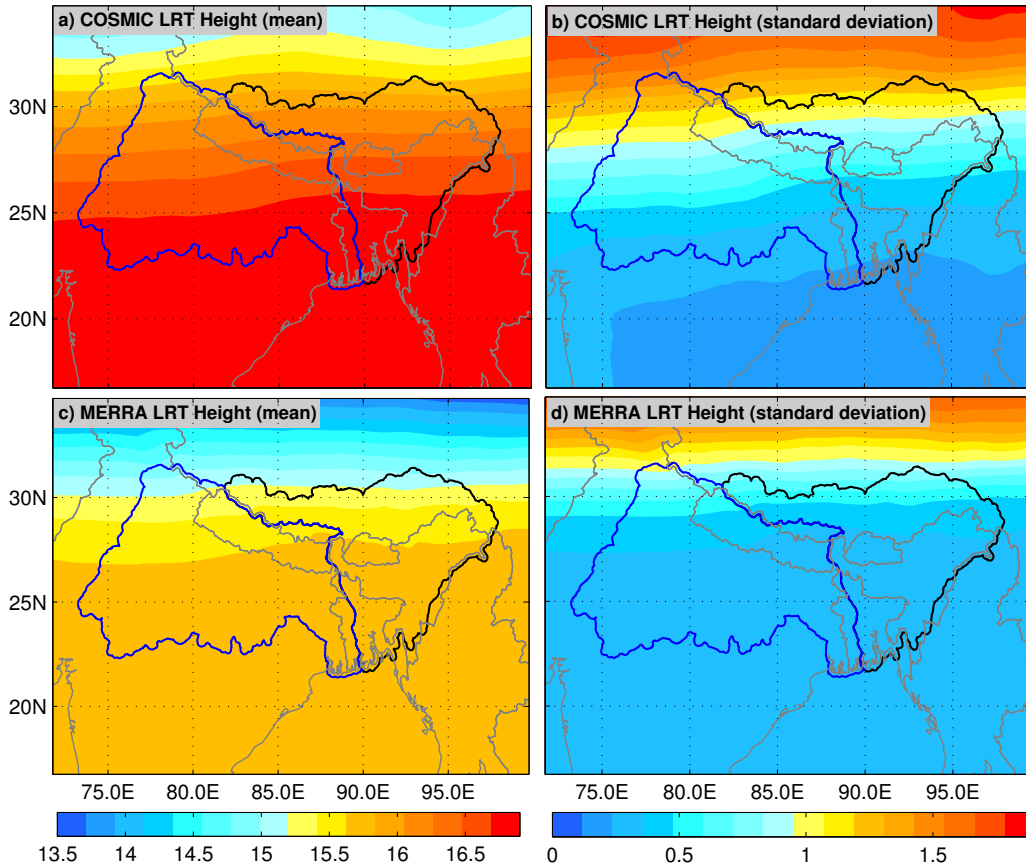


Figure 6.14: Spatial variation of mean and standard deviation of tropopause heights (km) derived from COSMIC RO and MERRA datasets based on 89 months from August 2006 to December 2013. (a) Mean and (b) standard deviation of tropopause heights (km) from COSMIC RO, (c) mean and (d) standard deviation of tropopause heights (km) estimated based on MERRA temperature data.

3948 The tropopause over the GBM River Basin often reaches as high as 18 km in response
 3949 to the Indian summer monsoon, when intense convective activities occur, and as low
 3950 as 10 km during winter. The spatial patterns of tropopause shown by MERRA are
 3951 consistent with those from COSMIC RO but are found to be more zonally homogenous,
 3952 warmer (by up to 4°C in the north) and lower (by ~ 1 km) over the region. This warm
 3953 bias (against COSMIC RO data) is also observed in ERA-Interim at 100 hPa level (see
 3954 Fig. 6.10b) but is relatively lower than MERRA, especially during the monsoon. The
 3955 annual cycle of spatially averaged (over the spatial domain covering 71.5–99.5°E, 16.5–
 3956 34.5°N) tropopause temperatures and heights of COSMIC RO and MERRA are shown
 3957 in Fig. 6.15. The tropopause temperatures (heights) of COSMIC RO reach minimum
 3958 (maximum) in June but are warmer (lower) in MERRA by 1.0–2.5°C (~ 1.2 km from
 3959 May to December). MERRA also shows tropopause temperature minimum during July
 3960 instead of June (Fig. 6.15a). The large differences in MERRA could partly be related to
 3961 the approximation in Eq. (6.5), but it should be noted that errors in tropopause heights
 3962 may cause large errors in temperature due to the lapse-rate criterion. The warm bias

3963 (against COSMIC RO data) observed in reanalysis products is thought to mainly stem
 3964 from assimilation of radiance observations from aircrafts and satellites (see, e.g., [Dee](#)
 3965 [et al., 2011](#), and the references therein). Large variations in tropopause temperatures and heights in Fig. 6.15 (indicated by error bars) during winter and spring could be
 3966 related to high diurnal temperature variations ([Mehta et al., 2010](#)).
 3967

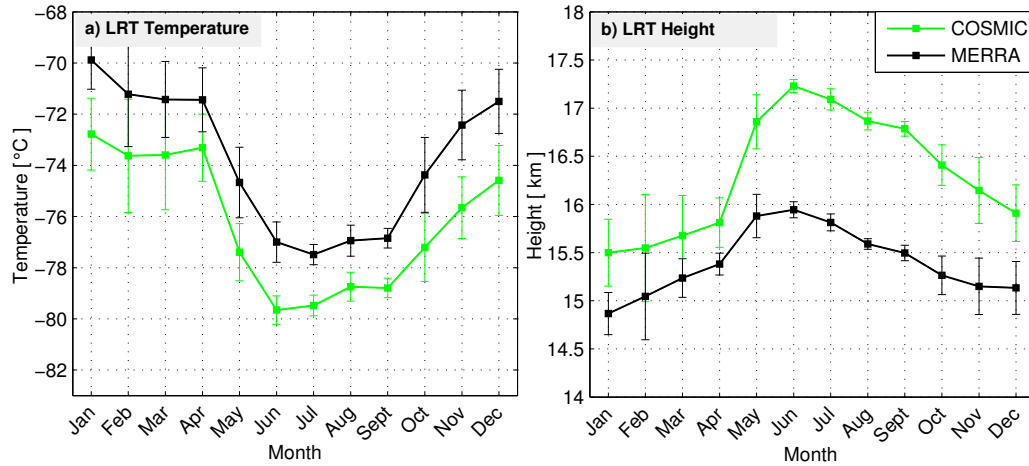


Figure 6.15: Annual cycle of tropopause over the GBM River Basin computed from MERRA and COSMIC RO data for the period between August 2006 and December 2013: (a) tropopause temperatures and (b) tropopause heights.

3968 The annual cycle was removed from each grid cell to examine the interannual vari-
 3969 ability of tropopause temperatures and heights as well as to estimate linear trends over
 3970 the period August 2006 to December 2013. The linear trends and their uncertainties are
 3971 presented in Table 6.6. In general, based on the COSMIC RO data, the tropopause ap-
 3972 pears to be cooling (increasing in height) at a rate of $-0.039 \pm 0.05^\circ\text{C year}^{-1}$ (6.01 ± 5.02
 3973 m year^{-1}) during the period (see Table 6.6), which to some degree is also estimated by
 3974 MERRA. However, MERRA shows negligible cooling compared to COSMIC RO data.
 3975 Nevertheless, the increase in heights are not consistent with the temperature decline.
 3976 The increasing (decreasing) tropopause heights (temperatures) has been consistently ob-
 3977 served in GNSS RO data over the years at both global and regional scale (e.g., [Schmidt](#)
 3978 [et al., 2008, 2010, Khandu et al., 2011](#)), which is evidently in response to enhanced
 3979 warming in the upper troposphere and substantial cooling in the lower stratosphere.

Table 6.6: Trends in tropopause temperatures ($^\circ\text{C}/\text{yr}$) and heights (m/yr) based on the area-averaged time-series anomalies derived from COSMIC RO and MERRA. Data span between August 2006 and December 2013. Uncertainties in trend estimates are reported at 95% confidence interval. Note that the temperature trend estimates are not found to be significant at 95% confidence interval.

| Data | Temperature ($^\circ\text{C year}^{-1}$) | Height (m year^{-1}) |
|-----------|--|---------------------------------|
| COSMIC RO | -0.039 ± 0.05 | 6.01 ± 5.02 |
| MERRA | -0.005 ± 0.03 | 17.00 ± 10.20 |

3980 To assess their spatio-temporal variability over the GBM River Basin, PCA is ap-
 3981 plied to the deseasonalized time-series of tropopause temperatures and heights. PCA

is particularly relevant here because tropopause is a transitional layer that responds to perturbations from both the troposphere and stratosphere, which makes it difficult to understand their variability modes. Figure 6.16 shows the EOFs (or spatial maps) of the first three leading modes of variability. The first EOF accounts for a variability of $\sim 73\%$ (COSMIC RO) and $\sim 63\%$ (MERRA) indicating positive anomalies (up to 1.1°C) across the GBM River Basin. EOF 1 appears to be rather symmetric around 29°N in COSMIC RO, but seems to be shifted slightly southwards in MERRA (Fig. 6.16a and d). Their corresponding PCs are shown in Fig. 6.17. PC 1 (Fig. 6.17a) is found to be highly correlated with Niño3.4 index with a correlation of 0.77 (COSMIC RO) and 0.78 (MERRA) with a time lag of 1 month, indicating that ENSO dominates tropopause variability over the region (see Table 6.7). IOD is also moderately correlated (0.35) with PC 1 of both COSMIC RO and MERRA (with a lag of 2 months), indicating that warmer SSTs in the equatorial Indian ocean might be having some influence on the regional tropopause variability.

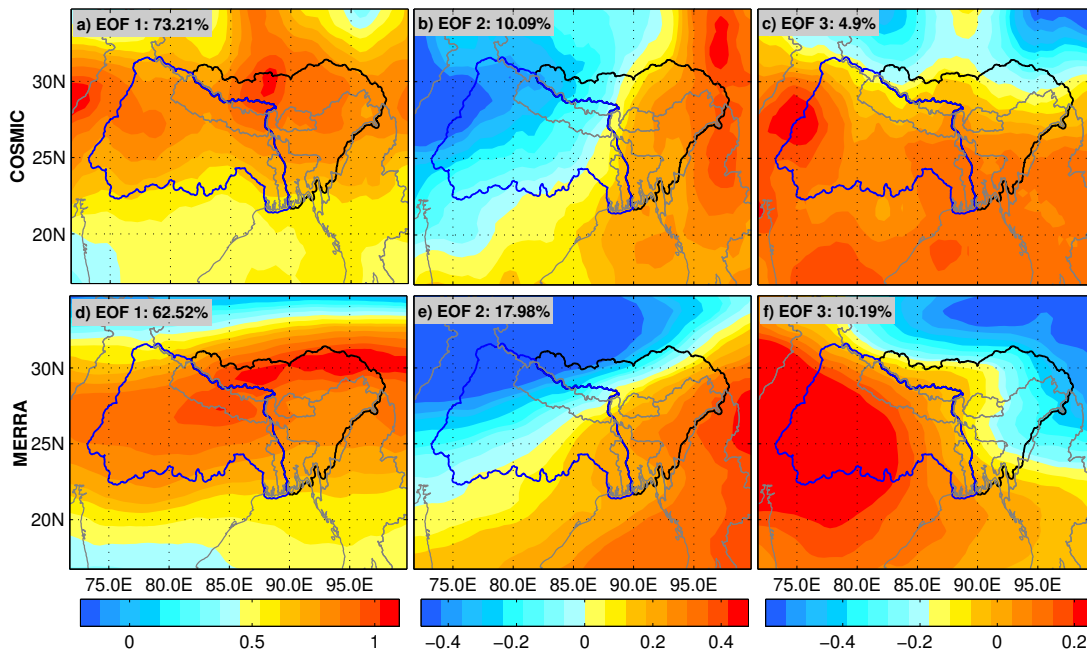


Figure 6.16: The first three leading EOFs of tropopause temperature ($^\circ\text{C}$) based on MERRA data and COSMIC RO data for the period August 2006 to December 2013.

The second EOF shown in Fig. 6.16b and e indicate a diagonal (dipole) pattern with positive (negative) anomalies in the northwest (southeast), accounting for variance of $\sim 10\%$ (COSMIC) and $\sim 18\%$ (MERRA). The corresponding PC is significantly correlated with the QBO index with a correlation coefficient of 0.40 (COSMIC RO) and 0.53 (MERRA) (at zero lag). It is therefore, not surprising that the relationship between PC 2 and QBO is relatively low compared to the equatorial (or tropical) tropopause since QBO is a tropical phenomenon (e.g., Reid and Gage, 1985, Randel et al., 2000, Gettelman et al., 2001, Liang et al., 2011). It also stems from the fact that QBO westerly phase prolonged for an extended period of 21 months before changing to a westerly phase in January 2010. The third EOF (Fig. 6.16c and f) explains about 5% (COSMIC RO)

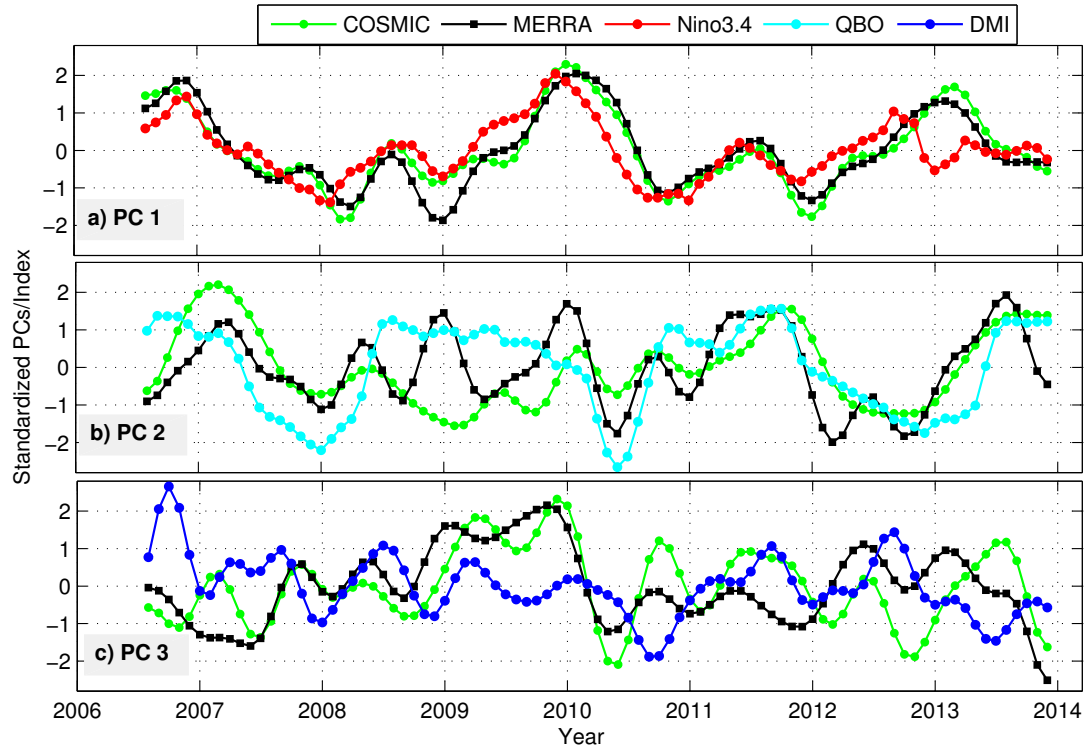


Figure 6.17: The corresponding PCs (temporal components) based on the three leading orthogonal modes shown in Fig. 6.16.

4006 and 10% (MERRA) of the variability and shows positive (negative) anomalies below
 4007 (above) 30°N , although MERRA shows a diagonal dipole pattern similar to EOF 2.
 4008 Their corresponding PCs are found to be moderately correlated with ENSO and IOD.
 4009 The tropopause heights are negatively correlated with their temperatures and, therefore,
 4010 vary inversely with their temperatures, i.e., increase in tropopause heights with decrease
 4011 in temperatures. The correlation coefficient between the PCs of three leading modes of
 4012 tropopause heights and the ocean-atmospheric indices indicate similar magnitudes of
 4013 correlations but with opposite signs (see Table 6.7).

Table 6.7: Correlation coefficients between tropopause parameters (temperature and height) derived from COSMIC RO and MERRA and ocean-atmospheric indices for the period August 2006 to December 2013. The values that are significant at 95% confidence level based on the reduced degree of freedom are bolded.

| Data | COSMIC RO | | MERRA | |
|----------------|-------------|--------------|-------------|--------------|
| | Temperature | Height | Temperature | Height |
| Nino3.4 & PC 1 | 0.77 | -0.74 | 0.78 | -0.75 |
| IOD & PC 1 | 0.35 | 0.37 | 0.35 | 0.38 |
| QBO & PC 2 | 0.36 | 0.36 | 0.53 | 0.54 |

4014 To show the influence of ENSO mode on the tropopause, the seasonal mean area-
 4015 averaged anomalies of tropopause temperatures and heights are plotted in Fig. 6.18.

4016 Seasonal mean anomalies are obtained by averaging the products of EOF 1 and PC
 4017 1 (of the COSMIC RO data). The ENSO effect is found to be maximum during the
 4018 winter period (e.g., 2009–2010, 2012–2013) when ENSO was at its peak. Its effects are
 4019 also felt during autumn (in 2007 and 2011) and spring (in 2008) and during the El Niño
 4020 and La Niña periods, respectively. The largest tropopause anomaly occurred during the
 4021 major El Niño event of 2009/2010 when tropopause temperatures (heights) increased
 4022 (decreased) by about 1.5°C (300 m) in the winter (Fig. 6.18a–b). La Niña periods (e.g.,
 4023 2007/2008, 2010/2011) are mainly associated with deep convections in the troposphere
 4024 leading to a wider troposphere or higher tropopause heights (see Fig. 6.18b).

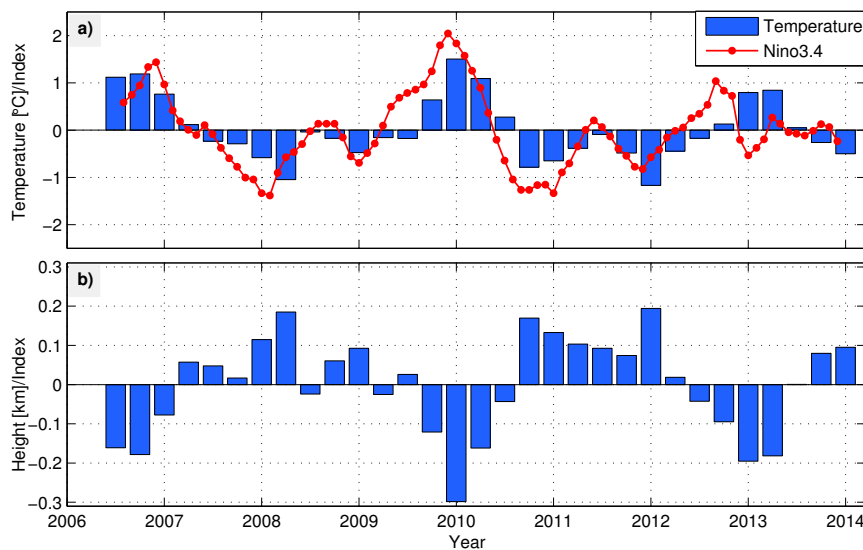


Figure 6.18: Seasonal mean tropopause temperature and height anomalies due to ENSO mode together with the Niño3.4 index. The area-averaged time-series were obtained by multiplying EOF 1 and PC 1, i.e., basically showing the replication of ENSO mode.

4025 6.4 Concluding remarks

4026 This study assess the spatio-temporal variations of temperature in the UTLS region over
 4027 the GBM River Basin using 89 months (August 2006 to December 2013) of COSMIC
 4028 RO data and two global reanalyses (MERRA and ERA-Interim). The GBM River Basin
 4029 received an average of ~ 576 well-distributed COSMIC RO profiles/month during the
 4030 period with more than 56% of the profiles reaching at least 1.5 km above the mean sea
 4031 level height. Even though the reanalysis products such as MERRA and ERA-Interim
 4032 are significantly warmer (by up to 2°C) than COSMIC RO data at 200–50 hPa level,
 4033 the warm bias is found to be consistent over time. The UTLS temperature showed
 4034 considerable interannual variability during the past 8 years (2006–2013) with modest
 4035 trends in the troposphere and stratosphere. ENSO is found to have the largest effect at
 4036 the 100 hPa level with a correlation of 0.82 (at 1-month lag) while SSW signals tend
 4037 to dominate the lower stratospheric temperature anomalies (e.g., at 50 hPa level). The
 4038 temperature at 200 hPa level decreased by $\sim 1.5^\circ\text{C}$ during the last major El Niño event

4039 of 2009/2010. The SSW events that occurred in 2008/2009 and 2010/2011 winters are
4040 marked by pronounced cooling at 50 hPa level.

4041 The relationship between ENSO and QBO has been reported to be strong between
4042 2004 and 2008 (Liang et al., 2011) but has weakened substantially over the years due to
4043 a persistent westerly phase that lasted for 21 months from June 2008 to January 2010.
4044 The IOD mode plays a significant role on the tropospheric temperature warming over
4045 the GBM River Basin as enhanced upwellings in the equatorial Indian ocean drives more
4046 convection in the region. However, their role seems to be limited within the troposphere
4047 as the magnitude of correlation between IOD and temperature decreases from -0.53 at
4048 400 hPa level to -0.42 hPa at 200 hPa level. Consistent with previous global warming
4049 trends, there is a warming (cooling) trend in the upper troposphere (lower stratosphere)
4050 (see, e.g., IPCC, 2007, 2013, and references therein).

4051 The tropopause temperatures and heights derived from COSMIC RO and MERRA
4052 were investigated in detail due to their importance in climate change and attribution
4053 studies (see, e.g., Santer et al., 2003a, 2008, IPCC, 2007). The interannual variability
4054 of tropopause temperatures and heights over the GBM River Basin was studied by
4055 applying the PCA method. The results indicate a dominant effect of ENSO, accounting
4056 for a variance of about 73% (COSMIC RO) and 63% (MERRA) of the first variability
4057 mode. PC 1 shows a near-accurate representation of the ENSO mode (represented by
4058 the Niño3.4 index) with a correlation of 0.77 (COSMIC RO) and 0.78 (MERRA). The
4059 QBO accounts for $\sim 10\%$ (COSMIC RO) and $\sim 18\%$ (MERRA) of the variability, as
4060 indicated by the correlation between PC 2 and the QBO index. The largest temperature
4061 anomaly was recorded in 2009/2010 winter corresponding to a major El Niño event. The
4062 tropopause temperatures (heights) increased (decreased in heights) by about 1.5°C (300
4063 m) during this period. Because IOD effects are generally found to be concentrated within
4064 the troposphere, its correlations with tropopause (temperatures and heights) are found
4065 to be low but, nevertheless, require further examination using longer time-series.

4066 Additionally, this study compared radiosonde observations from various stations in
4067 the GBM River Basin with high quality COSMIC RO data. Evaluation results for the
4068 period between August 2006 and December 2013 confirmed that radiosondes in the
4069 Indian and Bangladesh territory exhibit substantial biases in the UTLS region. Further,
4070 the results from three newly upgraded radiosondes in India indicated that the new
4071 GPS-based radiosondes significantly reduced temperature bias and standard deviations
4072 in the UTLS region. This suggests that incorporating GPS receivers in conventional
4073 radiosondes helps to provide better estimates of air temperature through more accurate
4074 measurement of pressure at various altitude levels. However, there are still problems
4075 with IMD radiosondes in regard to their ability to ascend to higher altitudes thus,
4076 limiting their usage in investigating the UTLS region.

4077 7. Conclusion and future outlook

4078 In this Chapter, the main findings are summarized, and suggestions are provided for
4079 future research to study the combined impacts of climate change and increasing water
4080 use on water availability in the Ganges–Brahmaputra–Meghna (GBM) River Basin.

4081 7.1 Summary of the findings

4082 7.1.1 Quality assessment of climate datasets

4083 Quantifying the climate change impacts on various aspects of water resources (e.g., wa-
4084 ter availability, storage, quality) require high-quality up-to-date observational datasets
4085 and climate and hydrological modelling approaches based on well-established physical
4086 laws. Unfortunately, it is hard to achieve such an ideal scenario, and uncertainties in ob-
4087 servational datasets can propagate into physical models, which are in fact build based on
4088 empirical theories and observational evidences. Much of this thesis has been dedicated to
4089 assessing the skills of various climate datasets by using novel statistical techniques, in-
4090 cluding both parametric such as cross-correlation, multiple linear regression approaches,
4091 and generalized three-cornered-hat (TCH) methods (e.g., [Awange et al., 2015](#)), and non-
4092 parametric methods such as Sen’s slope estimation ([Sen, 1968](#)) and Principle Component
4093 Analysis (PCA, [Preisendorfer, 1988](#)). In particular, statistical decomposition of climate
4094 data using PCA provides both spatial and temporal components in the order of their
4095 maximum variability for comparison. The TCH algorithm on the other hand, can be ex-
4096 tended to include several datasets for estimating relative uncertainties, consistent with
4097 other conventional methods, but without having to specify a reference dataset ([Awange
4098 et al., 2015](#), see also, Chapter 3).

4099 In Chapter 2, the strengths and weaknesses of the commonly used data as inputs to
4100 land surface and hydrological models, including monthly precipitation and temperature,
4101 are evaluated by comparing with existing regional and global *in-situ* gauge datasets from
4102 Asian Precipitation- Highly Resolved Observational Data Integration Towards Evalu-
4103 ation (APHRODITE, [Yatagai et al., 2012](#)), Global Precipitation Climatology Center
4104 (GPCC version 6 and 7, [Becker et al., 2013](#), [Schneider et al., 2014](#)), Climate Research
4105 Unit (CRU version TS3.22, [Harris et al., 2013](#)), and University of Delaware (UDEL,
4106 [Legates and Willmott, 1990](#)). The results indicate that among the three global reanaly-
4107 ses: (i) the European Centre for Medium-Range Weather Forecasts (ECMWF) reanalysis
4108 (ERA-Interim, [Dee et al., 2011](#)), (ii) Modern-Era Retrospective Analysis for Research
4109 and Applications (MERRA, [Rienecker et al., 2011](#)), and (iii) Climate Forecast System
4110 (CFS) Reanalysis (CFSR, [Saha et al., 2010](#)), ERA-Interim is found to be more accurate
4111 in reproducing the observed interannual variations and long-term precipitation trends,
4112 while MERRA tend to perform better in terms of reproducing the observed amplitudes,
4113 variations, and to some degree long-term trends of temperature for the period 1980–2010.
4114 Given that ERA-Interim provides consistent precipitation patterns, it is considered as

4115 the primary driving data for the Regional Climate Model version 4.4 (RegCM4.4, [Giorgi](#)
4116 [et al., 2012](#)) simulation conducted in Chapter 4.

4117 Additionally, several satellite remote sensing (SRS) precipitation products have also
4118 been evaluated for their seasonal variations and decadal trends, including those from
4119 Tropical Rainfall Measuring Mission (TRMM) Multisatellite Precipitation Analysis
4120 (TMPA, [Huffman et al., 2007](#)), Climate Hazards Group InfraRed Precipitation (CHIRP,
4121 [Funk et al., 2014](#)), Climate Predict Center (CPC) MORPHing technique, and Precipi-
4122 tation Estimation from Remotely Sensed Information using Artificial Neural Networks
4123 (PERSIAN, [Sorooshian et al., 2000](#)), with the latter three products assessed mainly over
4124 the eastern Himalayan regions of Bhutan (see, [Khandu et al., 2015, 2016c](#)). Among the
4125 SRS-based products, while both microwave- and infra-based precipitation estimates ad-
4126 equately describe the larges-scale precipitation variations across the GBM River Basin,
4127 their footprints are found to be too large for small countries such as Bhutan ([Khandu](#)
4128 [et al., 2015](#)), making them unsuitable for any applications. The SRS-only products still
4129 significantly underestimate monsoon precipitation over high precipitation regions (e.g.,
4130 the Himalayan Foothills), and require bias correction measures to reproduce the cor-
4131 rect amplitudes and seasonal means. A multi-step algorithm implemented by TMPA
4132 to merge SRS with high density gauge products such as GPCP version 6, provides the
4133 most consistent precipitation estimates in the GBM River Basin (e.g., [Xue et al., 2013](#),
4134 [Prakash et al., 2014, Khandu et al., 2015, 2016c](#)).

4135 Given the lack of sufficient ground-based soil moisture observations, climate change
4136 impact assessments on water resources mainly rely on distributed and semi-distributed
4137 land surface and hydrological models, with inputs from high quality precipitation and/or
4138 temperature datasets. However, modelling various water storage components requires
4139 considerable parameterization and regional understanding, and requires complex data
4140 assimilation techniques to combine observations and modelled outputs, thus requiring
4141 careful evaluation before applying them for impact analysis. In Chapter 3, the gener-
4142 alized TCH method is applied to quantify the relative uncertainties in soil moisture
4143 products derived from various reanalyses and land surface hydrological models such as
4144 Global Land Data Assimilation System (GLDAS, [Rodell et al., 2004](#)) following [Awange](#)
4145 [et al. \(2015\)](#). The results for the period 2002–2015 indicated that ERA-Interim exhibits
4146 the largest uncertainties compared to CPC (Climate Prediction Center, [van den Dool](#)
4147 [et al., 2003](#)) and MERRA with a magnitude of about 20 mm, while GLDAS Noah ex-
4148 hibits the smallest magnitude of error (~ 12 mm). When the same algorithm is applied to
4149 total water storage (TWS) changes derived from three official GRACE (Gravity Recov-
4150 ery and Climate Experiment, [Tapley et al., 2004](#)) data processing centers, the Center for
4151 Space Research (CSR) product indicated the smallest magnitude of error (of less than 1
4152 cm), which are consistent with most previous studies (e.g., [Chambers and Bonin, 2012](#)).

4153 Further, in Chapter 6, the reanalysis products and observed atmospheric profiles
4154 from conventional radiosondes are assessed for their temperature accuracy in the upper
4155 troposphere lower stratosphere (UTLS region) region over the GBM River Basin using
4156 high-quality atmospheric profiles derived from the state-of-the-art COSMIC (Constella-
4157 tion Observing System for Meteorology, Ionosphere, and Climate, [Anthes et al., 2008](#))
4158 radio occultation (RO) measurements for the period 2006–2013. It is understood most

reanalyses do not use radiosonde observations from the region due to their poor observational quality (Das Gupta et al., 2005, Kumar et al., 2010). Nevertheless, this is being currently addressed by the Indian Meteorological Department and present analysis from three newly upgraded radiosondes in the GBM River Basin showed significant reduction in temperature bias and standard deviation in the UTLs region compared to RO datasets (see, Khandu et al., 2016c). While the reanalyses products such as ERA-Interim and MERRA show substantial seasonal biases, especially during the winter months, they are able to reproduce the interannual variations and linear trends between 2006 and 2013, suggesting that their atmospheric components are well represented. In particular, the quality of ERA-Interim is believed to have improved upon assimilation of RO datasets (see, Poli et al., 2008, 2010).

7.1.2 Key improvements in Regional Climate Models (RCMs)

Due to fundamental limitations posed by Global Climate Models (GCMs) for providing more detailed representation of key regional processes, RCMs are increasingly used to dynamically downscale the former to generate high-resolution climate information for regional impact studies. However, RCMs apply very similar principles that are used in GCMs, and some form of systematic bias is unavoidable, albeit considerably reduced compared to the GCMs (Rummukainen, 2009). Additionally, long-term RCM simulations require careful examination of various model parameters through various validation procedures. Despite considerable improvement of model physics in RCMs, most existing RCMs still suffer from large systematic biases in the GBM River Basin, particularly in the Himalayan region (e.g., Dash et al., 2006, Ahmed and Suphachalasai, 2014). To further contribute to RCM development in the GBM River Basin, two widely used state-of-the-art high-resolution RCMs are evaluated in Chapter 4 by comparing their simulated precipitation and temperature with observed datasets for the period 1982–2012. The evaluation mainly focuses on examining the precipitation variability and change over the Indian monsoon region covering the Indian subcontinent and parts of the Tibetan Plateau and Southeast Asia (2°N – 37°N , 61°E – 108°E) on a 25 km horizontal resolution (see, Fig. 4.2 in Chapter 4). The two RCMs: (i) RegCM4.4 (Giorgi et al., 2012) and (ii) Providing REgional Climate Information for Impact Studies (PRECIS, Jones et al., 2004) are driven by coupled ocean-atmospheric global climate models (AOGCMs) with prescribed greenhouse gas (GHG) concentrations.

The evaluation results indicate that, in general, the two RCMs exhibited reasonable skills in simulating the seasonal spatial patterns of the Indian monsoon rainfall in the GBM River Basin, albeit with substantial biases. The RCMs also poorly reproduce the observed onset and withdrawal timing and spatial representation of the Indian monsoon. The RCM simulations driven by GCMs failed to reproduce the observed interannual variability of precipitation, but tended to reproduce the observed temperature trends in the GBM River Basin. In particular, the RegCM4.4 model, when driven by perfect boundary conditions (e.g., ERA-Interim) captured the precipitation variations likely associated with ENSO and IOD. This was confirmed by correlating the ENSO and IOD indices with monthly precipitation anomalies derived from various RCM outputs

4201 for the period 1982–2012 in Chapter 5. In summary, although RCMs provided more re-
4202 alistic spatial representations of precipitation and temperature in the GBM River Basin
4203 needed to assess the potential impacts of climate change on the basin’s hydrology, there
4204 still persists significant biases in these two variables, particularly, along the Himalayan
4205 Foothills and high rainfall areas. These biases can largely be reduced by applying bias
4206 correction techniques (see, e.g., Piani et al., 2010) but such techniques require up-to-
4207 date records of observed datasets, which is seldom available for a transboundary river
4208 basin. Until such long-term records are achieved with efficient data sharing and further
4209 improvement in SRS-based estimates, bias corrected climate datasets may still reveal
4210 significant differences in variations and trends.

4211 7.1.3 Impacts of climate variability and change on water resources

4212 Climate variability and change plays a key role in driving water resources in the GBM
4213 River Basin. In particular, any abnormal changes in the Indian monsoon can be catas-
4214 trophic to the region that is heavily reliant on the monsoon rainfall. Extreme climate
4215 events resulting from droughts and flooding can exert additional pressure on the al-
4216 ready water-stressed region, which is being excessively abstracted to meet its rapidly
4217 increasing population and their associated socio-economic activities. Chapter 2 provides
4218 an improved understanding of climate change and variability in the GBM River Basin
4219 based on the last three decades of observational evidences (gauge- and SRS-based) and
4220 modelling approaches, particularly in terms of temperature and precipitation. Based on
4221 the observed temperature records from CRU and UDEL, it is observed that the GBM
4222 River Basin has warmed significantly over the past three decades with maximum warm-
4223 ing in the Himalayan region with a warming rate of of $0.6^{\circ}\text{C decade}^{-1}$. Additionally,
4224 the observed surface temperature records also show substantial interannual variations,
4225 most of which appears to be driven by large-scale sea-surface temperature fluctuations
4226 such as El Niño Southern Oscillation (ENSO) and Indian Ocean Dipole (IOD). Ob-
4227 served precipitation records from APHRDITE, CRU, and GPCP indicate decreasing
4228 precipitation trends in the core monsoon regions of Bangladesh, northeast India, and
4229 Bhutan, with significant declines particularly during the last 10–15 years. Interestingly,
4230 the western Ganges River Basin has recorded a surplus in monsoon precipitation during
4231 the last decade, especially following two continuous major La Niña events after 2010.
4232 Overall, ENSO and IOD contributed to about 10–20% and 8–10% of the annual total
4233 rainfall in the GBM River Basin, respectively (see, Khandu et al., 2016c).

4234 In Chapter 6, the upper troposphere-lower stratosphere (UTLS) temperature vari-
4235 ations are studied using monthly accumulated atmospheric profiles from the ongoing
4236 COSMIC (Constellation Observing System for Meteorology, Ionosphere, and Climate)
4237 RO mission (Anthes et al., 2008) between 2006 and 2013. The UTLS region, in partic-
4238 ular, the tropopause layer, presents an important metric for detecting climate change
4239 due to its sensitivity to tropospheric warming (Santer et al., 2003a, Sausen and Santer,
4240 2003, Karl et al., 2006, Steiner et al., 2013, Thorne et al., 2011), and as such RO offsets
4241 limitations in conventional radiosonde observation systems. The inception of six-satellite
4242 COSMIC RO mission enabled high spatial coverage in the GBM River Basin, which pro-
4243 vided about 576 atmospheric profiles on a monthly scale since August 2006. More than

4244 56% of the recorded profiles reached at least 1.5 km above the mean sea level. These
4245 profiles when combined with *a priori* information from ground-based observations, will
4246 help improve the understanding of the lower atmospheric process, climate feedbacks, and
4247 ultimately improve representation of the hydrological cycle (Anthes, 2011). This study
4248 found clear indication of tropospheric warming, albeit over a very short period of time.
4249 The tropopause height increased by 6 m year⁻¹ in response to a temperature decrease
4250 of $\sim 0.04^\circ\text{C year}^{-1}$, which is consistent with the global trends estimated by Schmidt
4251 et al. (2010) from 2001–2009. This may not be significant but corresponds well with the
4252 surface temperature trends examined in Chapter 2. Additionally, ENSO accounted for
4253 73% of the interannual variability (tropopause temperature and height) for the period
4254 with the largest anomaly occurring during the major El Niño event of 2009/2010 (see
4255 also, Khandu et al., 2016b). The tropopause temperature (height) increased (decreased)
4256 by about 1.5°C (300 m) between 2009 and 2010, which clearly reflected its sensitivity
4257 to large-scale ocean-atmospheric circulation.

4258 The observed impacts of precipitation variability on the available freshwater storages
4259 (mainly groundwater, soil moisture, and surface water) is investigated in Chapter 3.
4260 The assessment is conducted between 1980 and 2015, with particular emphasis on last
4261 decade from 2002–2015, by taking into account the large-scale observations of total
4262 water storage (TWS) changes estimated by the state-of-the-art GRACE (Tapley et al.,
4263 2004) mission. The results indicate that both Ganges and Brahmaputra–Meghna River
4264 Basins have suffered a significant loss of water mass since 2002, at a declining rate of
4265 $9.1 \pm 4.5 \text{ km}^3 \text{ year}^{-1}$ and $10.5 \pm 3.2 \text{ km}^3 \text{ year}^{-1}$, respectively, in spite of a general increase
4266 in simulated soil moisture (see, also Khandu et al., 2016a). While the alarming rate of
4267 TWS decline ($\sim 20 \text{ km}^3 \text{ year}^{-1}$) in the Ganges River Basin has subsided since 2010, with
4268 an increase ($\sim 8 \text{ km}^3 \text{ year}^{-1}$) in the last five years due to a significant surplus of monsoon
4269 precipitation, TWS continued to decline in the Brahmaputra–Meghna River Basin in
4270 response to decreasing precipitation. As a primary driver of water resources in the region,
4271 prolonged meteorological droughts exerts a profound impact on the basin water storage,
4272 which can be seen especially from the recent meteorological droughts of 2005/2006
4273 and 2009/2010. As such, TWS and soil moisture variations strongly respond to the
4274 precipitation anomalies (represented by drought indices), with a correlation coefficient
4275 of 0.6 or higher across the GBM River Basin, with low values mainly across eastern
4276 Bangladesh, Bhutan, and northeast India.

4277 7.1.4 Impacts of excessive water abstraction on various water storage 4278 components

4279 Besides climate variability such as meteorological droughts and extreme wet events, the
4280 water storage changes across many parts of the GBM River Basin have been under
4281 enormous pressure from increasing demands for freshwater. For instance, agriculture
4282 only, uses about 60–90% of the groundwater, and available surface water continued to
4283 be extracted even at higher rates (Papa et al., 2015). In-situ observations from relatively
4284 sparse ground-level wells and global hydrological models have consistently shown that
4285 groundwater declines have been caused by excessive withdrawals of surface/groundwater

4286 across the GBM River Basin (Shamsudduha et al., 2009b, Central Ground Water Board,
4287 2014, Shahid et al., 2015). The integrated global water resources and use model Water-
4288 GAP (Water- Global Analysis and Prognosis) Global Hydrology Model (WGHM, Döll
4289 et al., 2003, 2014, Müller Schmied et al., 2014) developed at the University of Kassel and
4290 the University of Frankfurt, Germany, attempts to estimate the impacts of demographic,
4291 socio-economic and technological changes on water use, as well as the impact of climate
4292 change and variability on irrigation water use. WGHM provides several model variants
4293 representing various water storage components (TWS, groundwater, sub- and surface
4294 water storages) based on natural variability-only and variations due to contributions
4295 from varying amounts of water consumption (e.g., agriculture, industry, cities).

4296 The TWS and surface water storage outputs simulated by WGHM (WaterGAP ver-
4297 sion 2.2a) are analyzed in Chapter 3 to quantify the contributions from increasing pop-
4298 ulation in the GBM River Basin. By assuming that 70% of is water being used for
4299 irrigation with daily groundwater recharge rate of 10 mm, the model shows high con-
4300 centrations of groundwater withdrawal in the western Ganges River Basin, covering
4301 the Indian states of Haryana, Punjab, Rajasthan, and northwestern Bangladesh, that
4302 are consistent with GRACE-derived TWS trends. These estimates are obtained after
4303 accounting for the natural variability. A separate analysis in the Ganges River Basin
4304 revealed a declining trend of $15 \text{ km}^3 \text{ year}^{-1}$ in TWS between 1979 and 2009. It revealed
4305 a much greater trend ($22 \text{ km}^3 \text{ year}^{-1}$) for the most recent period (2002–2009) compared
4306 to a decline of $13 \text{ km}^3 \text{ year}^{-1}$ for the period (1979–2001) (see also, Khandu et al., 2016a),
4307 suggesting a rise in freshwater consumption.

4308 In Chapter 5, the possible future impacts of increasing frequency of dry and wet
4309 spells on water resources are discussed, by analyzing the drought and wet frequencies
4310 calculated from a range of RCM and GCM simulations. The characteristics of drought
4311 and wet frequencies are identified by applying a threshold of ± 0.9 on the Standardized
4312 Precipitation Index (SPI, McKee et al., 1993) generated from the monthly precipitation
4313 datasets. A drought (wet) event is said to occur if SPI continuously falls (rises) below
4314 (above) -0.9 ($+0.9$) for three months, and are classified as severe and extreme if it
4315 persists for 6–12 months and more than 12 months, respectively, adopting a risk-based
4316 assessment approach e.g., in Awange et al. (2016b). As such, the PRECIS ensemble mean
4317 (of six PPE simulations) predict a general increase in monsoon rainfall, especially along
4318 the Himalayan Foothills, with a maximum increasing rate of $10\text{--}25 \text{ mm decade}^{-1}$ over
4319 a temperature increase of $2\text{--}4^\circ\text{C}$ by 2100 (see, Fig. 5.5b in Chapter 5), while RegCM4.4
4320 simulations show declining rainfall trends in the same region, which are consistent with
4321 recent CMIP5 (Climate Model Intercomparison Project Phase 5, Taylor et al., 2012)
4322 projections (e.g., Sharmila et al., 2015). These increasing (declining) trends in monsoon
4323 rainfall may suggest a wetter (drier) regime in the future.

4324 However, after accounting for the precipitation trend, both RCM and GCM simula-
4325 tions project a higher probability of severe $15\text{--}20\%$ (~ 1 in 6 years) and extreme $6\text{--}8\%$
4326 (~ 1 in 17 years) droughts in the western GBM River Basin for the second half of the
4327 21st century than the first half. This region is also likely to experience more severe and
4328 extreme wet events for the second half of the 21st century with varying return periods.
4329 Their likely impacts on various water storage components are discussed (see, Chapter
4330 5).

4331 7.2 Future outlook

4332 This work offers several research avenues, which can be briefly summarized as follows:

4333 7.2.1 Simulating future hydrological droughts using RCM projected 4334 temperature and precipitation

4335 The future drought occurrences assessed in Chapter 5 was based on meteorological
4336 droughts and as such are not adequate enough to represent climate change impacts on
4337 water resources. Meteorological droughts due to deficit in precipitation and hydrological
4338 drought indices based on actual water availability (e.g., soil moisture, surface water, and
4339 groundwater) must be incorporated to assess the overall impacts of climate change. This
4340 has been partly studied in Chapter 3 using observational datasets and readily available
4341 hydrological model outputs but has not been addressed for the future period. Several
4342 studies have simulated various components of the global land hydrology including soil
4343 moisture and (sub-) surface runoffs using existing hydrological models with inputs from
4344 coarse scale GCMs. Both GCMs and RCMs provide crude estimates of soil moisture and
4345 runoff, but their applications to drought monitoring are currently limited due to their
4346 poor representation of for example, soil moisture. These variables should be added by
4347 adopting high global and regional resolution macro-scale hydrological models to study
4348 regional and basin-scale hydrological droughts (see, e.g., Johnston and Smakhtin, 2014,
4349 Mishra et al., 2014).

4350 7.2.2 Improving spatial representation of climate datasets

4351 In Chapters 2 and 3, various observational (both *in-situ* and SRS-based) and re-
4352 analysis precipitation products have revealed substantial seasonal differences. Long-
4353 term and high-resolution precipitation data are limited in the region, particularly at
4354 daily time-scale. The present research mainly employs monthly global high-resolution
4355 datasets and TMPAv7 precipitation estimates are used to evaluate RCMs at daily time-
4356 scales, which are in itself substantially biased in terms of seasonal averages. As a pri-
4357 mary input data for hydrological modelling and impact studies (e.g., water availabil-
4358 ity), it is inevitable therefore that, climate datasets be harmonized specifically for the
4359 river basin by efficient data sharing. With new algorithm and further accumulation
4360 of SRS-based products, it may help reduce biases and dependency on ground-based
4361 observations. The recently launched Global Precipitation Measurement (GPM, Hou
4362 et al., 2014) mission provides next-generation global observations of rain and snow
4363 from nine independent satellites at three-hourly time-scales, that will significantly ad-
4364 vance the regional hydrological understanding. Further, the GRACE Follow on mission
4365 (<https://decadal.gsfc.nasa.gov/grace2.html>) is expected to be launched in late
4366 2017 and continue GRACE observations with likely higher spatio-temporal accuracy as
4367 the K-band range rating system will be replaced by a much precise laser system.

4368 7.2.3 Towards an integrated drought monitoring system

4369 Drought is a recurrent feature of climate variability that occurs almost everywhere across
4370 the world. Besides adverse impacts from a slow shift in climate, drought affects virtu-
4371 ally all parts of life from regular freshwater supply–agriculture–to complex industries
4372 (Heim, 2002). Hao et al. (2014) presented a Global Integrated Drought Monitoring and
4373 Prediction System (GIDMaPS) that addresses meteorological and agricultural drought
4374 information by integrating precipitation and soil moisture from multi-satellites and land
4375 surface models. Given that water resources in the GBM River Basin are under mounting
4376 pressure from rapidly growing demands from a growing population and its associated
4377 socio-economic development, there is a need to develop a more comprehensive drought
4378 monitoring system to inform decision making and future drought risk management. Re-
4379 gion specific drought monitoring systems with near real-time forecasting will provide
4380 near-perfect information at high spatial scale that can be helpful for allocating available
4381 water resources and proper management of food crops. Agriculture accounts for up to
4382 80–90% of the groundwater and surface water use, and as such, a comprehensive drought
4383 monitoring systems may prevent large-scale drought risks.

References

- 4384
- 4385 Ahmed, M., and S. Suphachalasai (2014). *Climate Change Scenario in South Asia*. In:
4386 *Assessing the Costs of Climate Change and Adaptation in South Asia*, 16–28. Asian
4387 Development Bank. ISBN 978-92-9254-511-6.
- 4388 Alcamo, J., P. Döll, T. Henrichs, F. Kaspar, B. Lehner, T. Rösch and S. Siebert (2003).
4389 *Development and testing of the WaterGAP 2 global model of water use and availability*.
4390 Hydrol. Sci. J., 48(3):317–337. doi:[10.1623/hysj.48.3.317.45290](https://doi.org/10.1623/hysj.48.3.317.45290).
- 4391 Allan, R. P., and B. J. Soden (2007). *Large discrepancy between observed and sim-*
4392 *ulated precipitation trends in the ascending and descending branches of the tropical*
4393 *circulation*. Geophys. Res. Lett., 34(L18705). doi:[10.1029/2007GL031460](https://doi.org/10.1029/2007GL031460).
- 4394 American Meteorological Society (1997). *Meteorological drought- Policy statement*. Bull.
4395 Amer. Meteor. Soc., 78:847–849.
- 4396 Andermann, C., S. Bonnet and R. Gloaguen (2011). *Evaluation of precipitation data sets*
4397 *along the Himalayan front*. Geochem. Geophys., 7(12). doi:[10.1029/2011GC003513](https://doi.org/10.1029/2011GC003513).
- 4398 Annamalai, H., K. Hamilton and K. R. Sperber (2007). *The South Asian Summer*
4399 *Monsoon and Its Relationship with ENSO in the IPCC AR4 Simulations*. J. Clim.,
4400 20(6):1071–1092. doi:[10.1175/JCLI4035.1](https://doi.org/10.1175/JCLI4035.1).
- 4401 Ansari, M. I., R. Madan and S. Bhaita (2015). *Verification of quality of GPS*
4402 *based radiosonde data*. Mausam, 66(3):367–374. Available at: [metnet.ind.gov.in/
4403 mausamdocs/16632_F.pdf](http://metnet.ind.gov.in/mausamdocs/16632_F.pdf).
- 4404 Anthes, R. A. (2011). *Exploring Earth's atmosphere with radio occultation: Contri-*
4405 *butions to weather, climate and space weather*. Atmos. Meas. Tech., 4:1077–1103.
4406 doi:[10.5194/amt-4-1077-2011](https://doi.org/10.5194/amt-4-1077-2011).
- 4407 Anthes, R. A., D. Ector, D. C. Hunt, Y. H. Kuo, C. Rocken, W. S. Schreiner, S. V.
4408 Sokolovskiy, S. Syndergaard, T. K. Wee, Z. Zeng, P. A. Bernhardt, K. F. Dymond,
4409 Y. Chen, H. Liu, K. Manning, W. J. Randel, K. E. Trenberth, L. Cucurull, S. B.
4410 Healy, S. P. Ho, C. McCormick, T. K. Meehan, D. C. Thompson and N. L. Yen
4411 (2008). *The COSMIC/FORMOSAT-3 Mission: Early Results*. Bull. Am. Meteorol.
4412 Soc., 89:313–333. doi:[10.1175/BAMS-89-3-313](https://doi.org/10.1175/BAMS-89-3-313).
- 4413 Ashok, K., and N. H. Saji (2007). *On the impacts of ENSO and Indian Ocean dipole*
4414 *events on sub-regional Indian summer monsoon rainfall*. Nat. Hazards, 42(2):273–285.
4415 doi:[10.1007/s11069-006-9091-0](https://doi.org/10.1007/s11069-006-9091-0).
- 4416 Ashok, K., Z. Guan, and T. Yamagata (2001). *Impact of the Indian Ocean dipole on the*
4417 *relationship between the Indian monsoon rainfall and ENSO*. Geophys. Res. Lett., 28
4418 (23):4499–4502. doi:[10.1029/2001GL013294](https://doi.org/10.1029/2001GL013294).

- 4419 Asian Development Bank (2012). In: *Climate Change in South Asia- Strong responses for*
4420 *building a sustainable future*, 1–28. Asian Development Bank, Metro Manila, Philip-
4421 pines.
- 4422 Awange, J. L., F. H. Mpelasoka and R. M. Goncalves (2016b). *When every drop counts:*
4423 *Analysis of Droughts in Brazil for the 1901–2013 period*. *Sci. Total Environ.*, 566–567:
4424 1472–1488. doi:[10.1016/j.scitotenv.2016.06.031](https://doi.org/10.1016/j.scitotenv.2016.06.031).
- 4425 Awange, J.L., M.A. Sharifi, O. Baur, W. Keller, W.E. Featherstone and M. Kuhn
4426 (2009). *GRACE Hydrological Monitoring of Australia: Current Limitations and Fu-*
4427 *ture Prospects*. *J. Spat. Sci.*, 54(1):23–36.
- 4428 Awange, J.L., V.G. Ferreira, Khandu, S.A. Andam-Akorful, E. Forootan, N.O. Agutu
4429 and X.F. He (2015). *Uncertainties in remotely-sensed precipitation data over Africa*.
4430 *Int. J. Climatol.*, 36(1):303–323. doi:[10.1002/joc.4346](https://doi.org/10.1002/joc.4346).
- 4431 Awange, J.L., Khandu, M. Schumacher, E. Forootan and B. Heck (2016a). *Explor-*
4432 *ing hydro-meteorological drought patterns over the Greater Horn of Africa (1979–*
4433 *2014) using remote sensing and reanalysis products*. *Adv. Water Res.*, 94:45–59.
4434 doi:[10.1016/j.advwatres.2016.04.005](https://doi.org/10.1016/j.advwatres.2016.04.005).
- 4435 Baidya, S., M. L. Shrestha and M. M. Sheikh (2008). *Trends in Daily Climatic Extremes*
4436 *of Temperature and Precipitation in Nepal*. *Soc. Hydrol. Meteo. (Nepal)*, 5:37–51.
- 4437 Bajracharya, S. R., S. B. Maharjan, F. Shrestha, W. Guo, S. Liu, W. Immerzeel and
4438 B. Shrestha (2015). *The glaciers of the Hindu Kush Himalayas: current status and*
4439 *observed changes from the 1980s to 2010*. *Int. J. Water Resour. Dev.*, 13(2):161–173.
4440 doi:[10.1080/07900627.2015.1005731](https://doi.org/10.1080/07900627.2015.1005731).
- 4441 Baldwin, M. P., L. J. Gray, T. J. Dunkerton, K. Hamilton, P. H. Haynes, W. J. Randel,
4442 J. R. Holton, M. J. Alexander, I. Hirota, T. Horinouchi, D. B. A. Jones, J. S. Kinner-
4443 sley, C. Marquardt, K. Sato and M. Takahashi (2001). *The quasi-biennial oscillation*.
4444 *Rev. Geophys.*, 39(2):179–229. doi:[10.1029/1999RG000073](https://doi.org/10.1029/1999RG000073).
- 4445 Balsamo, G., C. Albergel, A. Beljaars, S. Boussetta, E. Brun, H. Cloke, D. Dee, E. Dutra,
4446 J. Muñoz-Sabater, F. Pappenberger, P. de Rosnay, T. Stockdale and F. Vitart (2015).
4447 *ERA-Interim/Land: A global land surface reanalysis data set*. *Hydrol. Earth Syst. Sci.*,
4448 19:389–407. doi:[10.5194/hess-19-389-2015](https://doi.org/10.5194/hess-19-389-2015).
- 4449 Barnett, T. P., J. C. Adam and D. P. Lettenmaier (2005). *Potential impacts of a*
4450 *warming climate on water availability in snow-dominated regions*. *Nature*, 438:303–
4451 309. doi:[10.1038/nature04141](https://doi.org/10.1038/nature04141).
- 4452 Barros, A. P., G. Kim, E. Williams and S. W. Nesbitt (2004). *Probing orographic controls*
4453 *in the Himalayas during the monsoon using satellite imagery*. *Nat. Hazards Earth*
4454 *Syst. Sci.*, 4(1):29–51. doi:[10.5194/nhess-4-29-2004](https://doi.org/10.5194/nhess-4-29-2004).
- 4455 Bates, B., Z. W. Kundzewicz, S. Wu and J. Palutikof (2008). *Climate change and water*.
4456 In: *IPCC Technical Paper VI*, 210 pp. Intergovernmental Panel on Climate Change
4457 (IPCC), IPCC Secretariat, Geneva. ISBN 978-92-9169-123-4.

- 4458 Becker, A., P. Finger, A. Meyer-Christoffe, B. Rudolf, K. Schamm, U. Schneider, and
4459 M. Ziese (2013). *A description of the global land-surface precipitation data prod-*
4460 *ucts of the Global Precipitation Climatology Centre with sample applications includ-*
4461 *ing centennial (trend) analysis from 1901–present.* Earth Syst. Sci. Data, 5:71–99.
4462 doi:[10.5194/essd-5-71-2013](https://doi.org/10.5194/essd-5-71-2013).
- 4463 Berry, P. A. M., J. D. Garlick, J. A. Freeman and E. L. Mathers (2005). *Global in-*
4464 *land water monitoring from multi-mission altimetry.* Geophys. Res. Lett., 32(16).
4465 doi:[10.1029/2005GL022814](https://doi.org/10.1029/2005GL022814).
- 4466 Bhaskaran, B., R. G. Jones, J. M. Murphy and M. Noguer (1996). *Simulations of the*
4467 *Indian summer monsoon using a nested regional climate model: domain size experi-*
4468 *ments.* Clim. Dyn., 12(9):573–587. doi:[10.1007/BF00216267](https://doi.org/10.1007/BF00216267).
- 4469 Bhaskaran, B., A. Ramachandran, R. Jones and W. Moufouma-Okia (2012). *Regional*
4470 *climate model applications on sub-regional scales over the Indian monsoon region:*
4471 *The role of domain size on downscaling uncertainty.* J. Geophys. Res., 117(D10).
4472 doi:[10.1029/2012JD017956](https://doi.org/10.1029/2012JD017956).
- 4473 Biemans, H., L.H. Speelman, F. Ludwig, E.J. Moors, A.J. Wiltshire, P. Kumar,
4474 D. Gerten and P. Kabat (2013). *Future water resources for food production in five*
4475 *South Asian river basins and potential for adaptation- A modeling study.* Sci. Total
4476 Environ., 468-469:S117–S131. doi:[10.1016/j.scitotenv.2013.05.092](https://doi.org/10.1016/j.scitotenv.2013.05.092).
- 4477 Bolch, T., A. Kulkarni, A. Kääb, C. Huggel, F. Paul, J. G. Cogley, H. Frey, J. S. Kargel,
4478 K. Fujita, M. Scheel, S. Bajracharya and M. Stoffel (2012). *The State and Fate of*
4479 *Himalayan Glaciers.* Science, 336:310–314. doi:[10.1126/science.1215828](https://doi.org/10.1126/science.1215828).
- 4480 Bollasina, M. A., Y. Ming and V. Ramaswamy (2011). *Anthropogenic Aerosols and*
4481 *the Weakening of the South Asian Summer Monsoon.* Science, 334(6055):502–505.
4482 doi:[10.1126/science.1204994](https://doi.org/10.1126/science.1204994).
- 4483 Caesar, J., T. Janes, A. Lindsay and B Bhaskaran (2015). *Temperature and precipita-*
4484 *tion projections over Bangladesh and the upstream Ganges, Brahmaputra and Meghna*
4485 *systems.* Environ. Sci. Process Impacts, 17:1047–1056. doi:[10.1039/c4em00650j](https://doi.org/10.1039/c4em00650j).
- 4486 Central Ground Water Board (2014). *Dynamic Ground Water Resources of India (as*
4487 *on 31st March 2011).* Technical Report, Ministry of Water Resources, River Devel-
4488 opment and Ganga Rejuvenation, Government of India, Faridabad, India.
- 4489 Chambers, D. P. (2004). *Preliminary observations of global ocean mass variations with*
4490 *GRACE.* Geophys. Res. Lett., 31(13). doi:[10.1029/2004GL020461](https://doi.org/10.1029/2004GL020461).
- 4491 Chambers, D. P. (2006). *Observing seasonal steric sea level variations with GRACE*
4492 *and satellite altimetry.* J. Geophys. Res., 111(C3). doi:[10.1029/2005JC002914](https://doi.org/10.1029/2005JC002914).
- 4493 Chambers, D. P., and J. A. Bonin (2012). *Evaluation of Release-05 GRACE time-*
4494 *variable gravity coefficients over the ocean.* Ocean Sci., 8:859–868,. doi:[10.5194/os-8-](https://doi.org/10.5194/os-8-859-2012)
4495 [859-2012](https://doi.org/10.5194/os-8-859-2012).

- 4496 Chambers, D. P., M. E. Tamisiea, R. S. Nerem and J. C. Ries (2007). *Effects of ice*
4497 *melting on GRACE observations of ocean mass trends*. *Geophys. Res. Lett.*, 34(5).
4498 doi:[10.1029/2006GL029171](https://doi.org/10.1029/2006GL029171).
- 4499 Chaturvedi, R. K., A. Kulkarni, Y. Karyakarte, J. Joshi and G. Bala (2014). *Glacial*
4500 *mass balance changes in the Karakoram and Himalaya based on CMIP5 multi-model*
4501 *climate projections*. *Clim. Change*, 123(2):315–328. doi:[10.1007/s10584-013-1052-5](https://doi.org/10.1007/s10584-013-1052-5).
- 4502 Chen, F., K. Mitchell, J. Schaake, Y. Xue, H.-L. Pan, V. Koren, Q. Y. Duan, M. Ek and
4503 A. Betts (1996). *Modeling of land surface evaporation by four schemes and comparison*
4504 *with FIFE observations*. *J. Geophys. Res.*, 101:7251–7268. doi:[10.1029/95JD02165](https://doi.org/10.1029/95JD02165).
- 4505 Chen, J., J. Li, Z. Zhang and S. Ni (2014a). *Long-term groundwater variations in*
4506 *Northwest India from satellite gravity measurements*. *Glob. Planet. Chang.*, 116:130–
4507 138. doi:[10.1016/j.gloplacha.2014.02.007](https://doi.org/10.1016/j.gloplacha.2014.02.007).
- 4508 Chen, J., J. S. Famiglietti, B. R. Scanlon and M. Rodell (2014b). *Groundwater Storage*
4509 *Changes: Present Status from GRACE Observations*. *Surveys in Geophysics*, 35:1–21.
4510 doi:[10.1007/s10712-015-9332-4](https://doi.org/10.1007/s10712-015-9332-4).
- 4511 Chen, J. L., and C. R. Wilson (2008). *Low degree gravity changes from GRACE, Earth*
4512 *rotation, geophysical models, and satellite laser ranging*. *J. Geophys. Res.*, 113(B6).
4513 doi:[10.1029/2007JB005397](https://doi.org/10.1029/2007JB005397).
- 4514 Chen, J. L., C. R. Wilson, B. D. Tapley and J. C. Ries (2004). *Low degree gravitational*
4515 *changes from GRACE: Validation and interpretation*. *Geophys. Res. Lett.*, 31(22).
4516 doi:[10.1029/2004GL021670](https://doi.org/10.1029/2004GL021670).
- 4517 Chen, J. L., M. Rodell, C. R. Wilson and J. S. Famiglietti (2005). *Low degree spherical*
4518 *harmonic influences on Gravity Recovery and Climate Experiment (GRACE) water*
4519 *storage estimates*. *Geophys. Res. Lett.*, 32(L14405). doi:[10.1029/2005GL022964](https://doi.org/10.1029/2005GL022964).
- 4520 Chen, J. L., C. R. Wilson and K. W. Seo (2006). *Optimized smoothing of Gravity*
4521 *Recovery and Climate Experiment (GRACE) time-variable gravity observations*. *J.*
4522 *Geophys. Res.*, 111(B6). doi:[10.1029/2005JB004064](https://doi.org/10.1029/2005JB004064).
- 4523 Cheng, M. K., and B. D. Tapley (2004). *Variations in the Earth's oblateness during the*
4524 *past 28 years*. *Geophys. Res. Lett.*, 109(B9). doi:[10.1029/2004JB003028](https://doi.org/10.1029/2004JB003028).
- 4525 Cheng, M. K., J. C. Ries and B. D. Tapley (2013). *Geocenter Variations from Analysis*
4526 *of SLR Data*. In: *Reference Frames for Applications in Geosciences*, Vol. 138 Series
4527 *International Association of Geodesy Symposia*, 19–25. Springer Berlin Heidelberg.
- 4528 Chowdary, J. S., N. John and C. Gnanaseelan (2014). *Interannual variability of surface*
4529 *air-temperature over India: impact of ENSO and Indian Ocean Sea surface tempera-*
4530 *ture*. *Int. J. Climatol.*, 34(2):416–429. doi:[10.1002/joc.3695](https://doi.org/10.1002/joc.3695).
- 4531 Chowdhury, M. D. R., and N. Ward (2004). *Hydro-meteorological variability in the*
4532 *greater Ganges-Brahmaputra-Meghna basins*. *Int. J. Climatol.*, 24(12):1495–1508.
4533 doi:[10.1002/joc.1076](https://doi.org/10.1002/joc.1076).

- 4534 Chowdhury, M. R. (2003). *The El Niño-Southern Oscillation (ENSO) and seasonal*
4535 *flooding- Bangladesh*. Theor. Appl. Climatol., 76(1–2):105–124. doi:[10.1007/s00704-](https://doi.org/10.1007/s00704-003-0001-z)
4536 [003-0001-z](https://doi.org/10.1007/s00704-003-0001-z).
- 4537 Christensen, J. H., B. Hewitson, A. Busuioc, A. Chen, X. Gao, I. Held, R. Jones, R.K.
4538 Kolli, W. T. Kwon, R. Laprise, V. M. Rueda, L. Mearns, C.G. Menéndez, J. Räisä-
4539 nen, A. Rinke, A. Sarr and P. Whetton (2007). *Regional Climate Projections*. In:
4540 Solomon, S., D. Qin, M. Manning, Z. Chen, M. Marquis, K.B. Averyt, M. Tignor and
4541 H.L. Miller (Hrsg.), *Climate Change 2007: The Physical Science Basis. Contribution*
4542 *of Working Group I to the Fourth Assessment Report of the Intergovernmental Panel*
4543 *on Climate Change*. Cambridge University Press, Cambridge, United Kingdom and
4544 New York, USA.
- 4545 Chung, C. E., and V. Ramanathan (2006). *Weakening of North Indian SST Gra-*
4546 *dients and the Monsoon Rainfall in India and the Sahel*. J. Clim., 19:2036–2045.
4547 doi:[10.1175/JCLI3820.1](https://doi.org/10.1175/JCLI3820.1).
- 4548 Clark, M. P., R. L. Wilby, E. D. Gutmann, J. A. Vano, S. Gangopadhyay, A. W. Wood,
4549 H. J. Fowler, C. Prudhomme, J. R. Arnold and L. D. Brekke (2016). *Characterizing*
4550 *Uncertainty of the Hydrologic Impacts of Climate Change*. Curr. Clim. Change. Rep.,
4551 2:55–64. doi:[10.1175/JHM-D-14-0104.1](https://doi.org/10.1175/JHM-D-14-0104.1).
- 4552 Collins, M., B. B. Booth, G. R. Harris, J. M. Murphy, D. M. H. Sexton and M. J.
4553 Webb (2006). *Towards quantifying uncertainty in transient climate change*. Clim.
4554 Dyn., 27(2):127–147. doi:[10.1007/s00382-006-0121-0](https://doi.org/10.1007/s00382-006-0121-0).
- 4555 Collins, M., B. B. Booth, B. Bhaskaran, G. R. Harris, J. M. Murphy, D. M. H. Sexton
4556 and M. J. Webb (2011). *Climate model errors, feedbacks and forcings: a comparison*
4557 *of perturbed physics and multi-model ensembles*. Clim. Dyn., 36(9–10):1737–1766.
4558 doi:[10.1007/s00382-010-0808-0](https://doi.org/10.1007/s00382-010-0808-0).
- 4559 Cox, P. M., R. A. Betts, C. B. Bunton, R. L. H. Essery, P. R. Rowntree and J. Smith
4560 (1999). *The impact of new land surface physics on the GCM simulation of climate*
4561 *and climate sensitivity*. Clim. Dyn., 15(3):183–203. doi:[10.1007/s003820050276](https://doi.org/10.1007/s003820050276).
- 4562 Cucurull, L., J. C. Derber, R. Treadon and R. Purser (2007). *Assimilation of Global*
4563 *Positioning System radio occultation observations into NCEP’s Global Data Assim-*
4564 *ilation System*. Mon. Weather Rev., 35:3174–3193. doi:[10.1175/MWR3461.1](https://doi.org/10.1175/MWR3461.1).
- 4565 Dai, A. (2013). *Increasing drought under global warming in observations and models*.
4566 Nat. Clim. Change, 3:52–58. doi:[10.1038/nclimate1633](https://doi.org/10.1038/nclimate1633).
- 4567 Dai, A., K. E. Trenberth and T. Qian (2004). *A global data set of Palmer Drought*
4568 *Severity Index for 1870-2002: Relationship with soil moisture and effects of surface*
4569 *warming*. J. Hydrometeorol., 5:1117–1130. doi:[10.1175/JHM-386.1](https://doi.org/10.1175/JHM-386.1).
- 4570 Danzer, J., U. Foelsche, B. Scherllin-Pirscher and M. Schwärz (2014). *Influence of*
4571 *changes in humidity on dry temperature in GPS RO climatologies*. Atmos. Meas.
4572 Tech., 7:2883–2896. doi:[10.5194/amt-7-2883-2014](https://doi.org/10.5194/amt-7-2883-2014).

- 4573 Das Gupta, M., S. Das, K. Prasanthi and P. K. Pradhan (2005). *Validation of upper-air*
4574 *observations taken during the ARMEX-I and its impact on the global analysis-forecast*
4575 *system*. *Mausam*, 56(1):139–146.
- 4576 Dash, S. K., M. S. Shekhar and G. P. Singh (2006). *Simulation of Indian summer*
4577 *monsoon circulation and rainfall using RegCM3*. *Theor. Appl. Climatol.*, 86(1–4):
4578 161–172. doi:[10.1007/s00704-006-0204-1](https://doi.org/10.1007/s00704-006-0204-1).
- 4579 Dash, S. K., K. C. Pattnayak, S. K. Panda, D. Vaddi and A. Mangain (2015). *Im-*
4580 *act of domain size on the simulation of Indian summer monsoon in RegCM4 us-*
4581 *ing mixed convection scheme and driven by HadGEM2*. *Clim. Dyn.*, 44:961–975.
4582 doi:[10.1007/s00382-014-2420-1](https://doi.org/10.1007/s00382-014-2420-1).
- 4583 Dash, S.K., N. Sharma, K.C. Pattnayak, X.J. Gao and Y. Shi (2012). *Temperature*
4584 *and precipitation changes in the north-east India and their future projections*. *Glob.*
4585 *Planet. Change*, 98–99:31–44. doi:[10.1016/j.gloplacha.2012.07.006](https://doi.org/10.1016/j.gloplacha.2012.07.006).
- 4586 Dee, D. P., S. M. Uppala, A. J. Simmons, P. Berrisford, P. Poli, S. Kobayashi, U. An-
4587 drae, M. A. Balmaseda, , G. Balsamo, P. Bauer, P. Bechtold, A. C. M. Beljaars,
4588 L. van de Berg, J. Bidlot, N. Bormann, C. Delsol, R. Dragani, M. Fuentes, A. J.
4589 Geer, L. Haimbergere, S. B. Healy, H. Hersbach, E. V. Holm, L. Isaksen, P. Källberg,
4590 M. Köhler, M. Matricardi, A. P. McNally, B. M. Monge-Sanz, J.-J. Morcrette, B.-K.
4591 Park, C. Peubey, P. de Rosnay, C. Tavolato, J.-N. Thépaut and F. Vitarta (2011).
4592 *The ERA-Interim reanalysis: Configuration and performance of the data assimilation*
4593 *system*. *Q. J. R. Meteorolog. Soc.*, 137:553–597. doi:[10.1002/qj.828](https://doi.org/10.1002/qj.828).
- 4594 Deser, C., A. S. Phillips, V. Bourdette and H. Teng (2012). *Uncertainty in cli-*
4595 *mate change projections: the role of internal variability*. *J. Clim.*, 38:527–546.
4596 doi:[10.1007/s00382-010-0977-x](https://doi.org/10.1007/s00382-010-0977-x).
- 4597 Devineni, N., S. Perveen and U. Lall (2013). *Assessing chronic and climate-induced water*
4598 *risk through spatially distributed cumulative deficit measures: A new picture of water*
4599 *sustainability in India*. *Water Resour. Res.*, 49(4):2135–2145. doi:[10.1002/wrcr.20184](https://doi.org/10.1002/wrcr.20184).
- 4600 Dickinson, R. E., A. Henderson-Sellers and P.J. Kennedy (1993). *Biosphere-atmosphere*
4601 *Transfer Scheme (BATS) Version 1e as Coupled to the NCAR Community Climate*
4602 *Model*. NCAR, National Center for Atmospheric Research, Boulder, CO, 422 pp,
4603 1993.
- 4604 Dimri, A. P., D. Niyogi, A. P. Barros, J. Ridley, U. C. Mohanty, T. Yasunari and
4605 D. R. Sikka (2015). *Western Disturbances: A Review*. *Rev. Geophys.*, 53(2):225–246.
4606 doi:[10.1002/2014RG000460](https://doi.org/10.1002/2014RG000460).
- 4607 Döll, P., F. Kaspar and B. Lehner (2003). *A global hydrological model for deriving*
4608 *water availability indicators: model tuning and validation*. *J. Hydrol.*, 207:105–134.
4609 doi:[10.1016/S0022-1694\(02\)00283-4](https://doi.org/10.1016/S0022-1694(02)00283-4).
- 4610 Döll, P., H. Hoffmann-Dobrev, F.T. Portmann, S. Siebert, A. Eicker, M. Rodell,
4611 G. Strassberg and B.R. Scanlon (2012). *Regional and global volumes of glaciers de-*

- 4612 rived from statistical upscaling of glacier inventory data. *J. Geodyn.*, 59–60:143–156.
4613 doi:[10.1016/j.jog.2011.05.001](https://doi.org/10.1016/j.jog.2011.05.001).
- 4614 Döll, P., H. Müller Schmied, C. Schuh, F.T. Portmann and A. Eicker (2014). *Global-scale*
4615 *assessment of groundwater depletion and related groundwater abstractions: Combining*
4616 *hydrological modeling with information from well observations and GRACE satellites.*
4617 *Water Resour. Res.*, 50(7):5698–5720. doi:[10.1002/2014WR015595](https://doi.org/10.1002/2014WR015595).
- 4618 Doms, G., M. Baldauf and U. Schättler (2015). *A Description of the Nonhydrostatic*
4619 *Regional COSMO-Model: Dynamics and Numerics.* Report, Climate Limited-area
4620 Modelling-Community (CLM-Community), Deutscher Wetterdienst, Offenbach, Ger-
4621 many. Available at [http://www.cosmo-model.org/content/model/documentation/](http://www.cosmo-model.org/content/model/documentation/core/cosmoDyncsNumcs.pdf)
4622 [core/cosmoDyncsNumcs.pdf](http://www.cosmo-model.org/content/model/documentation/core/cosmoDyncsNumcs.pdf). Accessed 21 Dec 2014.
- 4623 Duncan, J. M.A., and E. M. Biggs (2012). *Assessing the accuracy and applied use*
4624 *of satellite-derived precipitation estimates over Nepal.* *Appl. Geogr.*, 34:626–638.
4625 doi:[10.1016/j.apgeog.2012.04.001](https://doi.org/10.1016/j.apgeog.2012.04.001).
- 4626 Dunne, J. P., J. G. John, E. Shevliakova, R. J. Stouffer, P. Krasting J, S. L. Malyshev,
4627 P. C. D. Milly, L. T. Sentman, A. J. Adcroft, W. Cooke, K. A. Dunne, S. M. Griffies,
4628 R. W. Hallberg, M. J. Harrison, H. Levy, A. T. Wittenberg, P. J. Phillips and N. Zadeh
4629 (2012). *GFDL's ESM2 Global Coupled Climate-Carbon Earth System Models. Part*
4630 *II: Carbon System Formulation and Baseline Simulation Characteristics.* *J. Clim.*,
4631 26:2247–2267. doi:[10.1175/JCLI-D-12-00150.1](https://doi.org/10.1175/JCLI-D-12-00150.1).
- 4632 Ebert, E. E., J. E. Janowiak and C. Kidd (2007). *Comparison of Near-Real-Time*
4633 *Precipitation Estimates from Satellite Observations and Numerical Models.* *Bull. Am.*
4634 *Meteorol. Soc.*, 88(1):47–64. doi:[10.1175/BAMS-88-1-47](https://doi.org/10.1175/BAMS-88-1-47).
- 4635 Emanuel, K. A. (1991). *A scheme for representing cumulus convection in large-scale*
4636 *models.* *J. Atmos. Sci.*, 48:2313–2335.
- 4637 Emanuel, K. A., and M. Z.-Rothman (1999). *Development and Evaluation of a Con-*
4638 *vection Scheme for Use in Climate Models.* *J. Atmos. Sci.*, 56(11):764–787.
- 4639 Entekhabi, D., E. G. Njoku, P. E. O'Neill, K. H. Kellogg, W. T. Crow, W. N. Edel-
4640 stein, J. K. Entin, S. D. Goodman, T. J. Jackson, J. Johnson, J. Kimball, J. R.
4641 Piepmeier, R. D. Koster, N. Martin, K. C. McDonald, M. Moghaddam, S. Moran,
4642 R. Reichle, J. C. Shi, M. W. Spencer, S. W. Thurman, T. Leung and J. van Zyl
4643 (2010). *The Soil Moisture Active Passive (SMAP) Mission.* *Proc. IEEE*, 98(5).
4644 doi:[10.1109/JPROC.2010.2043918](https://doi.org/10.1109/JPROC.2010.2043918).
- 4645 Eriksson, M., X. Jianchu, A. B. Shrestha, R. A. Vaidya, S. Nepal and K. Sand-
4646 ström (2009). In: *The changing Himalayas: impact of climate change on water re-*
4647 *sources and livelihoods in the greater Himalayas*, 1–22. ICIMOD in cooperation with
4648 UNEP Programme Regional Office Asia and the Pacific (ROAP), International Cen-
4649 tre for Integrated Mountain Development, Khumaltar, Kathmandu, Nepal. ISBN
4650 9789291151141. Available at [http://www.preventionweb.net/publications/view/](http://www.preventionweb.net/publications/view/11621)
4651 [11621](http://www.preventionweb.net/publications/view/11621). Accessed on 24 July 2014.

- 4652 Famiglietti, J. S. (2014). *The global groundwater crisis*. Nat. Clim. Change, 4:945–948.
4653 doi:[10.1038/nclimate2425](https://doi.org/10.1038/nclimate2425).
- 4654 FAO (2011). *Ganges-Brahmaputra-Meghna Basin*. Technical Report, AQUASTAT,
4655 Food and Agriculture Organization of the United Nations, Rome, Italy. available
4656 from: <http://www.fao.org/nr/water/aquastat/basins/gbm/index.stm>. Accessed
4657 on 21 Feb 2015.
- 4658 Flato, G., J. Marotzke, B. Abiodun, P. Braconnot, S.C. Chou, W. Collins, P. Cox, F. Dri-
4659 ouech, S. Emori, V. Eyring, C. Forest, P. Gleckler, E. Guilyardi, C. Jakob, V. Kattsov,
4660 C. Reason and M. Rummukainen (2013). *Evaluation of Climate*. In: Stocker, T. F.,
4661 D. Qin, G.-K. Plattner, M. Tignor, S.K. Allen, J. Boschung, A. Nauels, Y. Xia, V. Bex
4662 and P.M. Midgley (Hrsg.), *Climate Change 2013: The Physical Science Basis. Contri-
4663 bution of Working Group I to the Fifth Assessment Report of the Intergovernmental
4664 Panel on Climate Change*. Cambridge University Press, Cambridge, United Kingdom
4665 and New York, NY, USA.
- 4666 Flato, G. M. (2011). *Earth system models: An overview*. WIREs Clim. Change, 2:
4667 783–800. doi:[10.1002/wcc.148](https://doi.org/10.1002/wcc.148).
- 4668 Foelsche, U., M. Borsche, A. K. Steiner, A. Gobiet, B. Pirscher, G. Kirchengast, J. Wick-
4669 ert and T. Schmidt (2008). *Observing upper troposphere-lower stratosphere climate
4670 with radio occultation data from the CHAMP satellite*. Clim. Dyn., 31(1):49–65.
4671 doi:[10.1007/s00382-007-0337-7](https://doi.org/10.1007/s00382-007-0337-7).
- 4672 Forootan, E. (2014). *Statistical Signal Decomposition Techniques for Analyzing Time-
4673 Variable Satellite Gravimetry Data*. PhD Thesis, Universität Bonn, Bonn, Germany.
- 4674 Forootan, E., Khandu, J. L. Awange, M. Schumacher, R. Anyah, A. van Dijk and
4675 J. Kusche (2015). *Quantifying the impacts of ENSO and IOD on rain gauge and
4676 remotely sensed precipitation products over Australia*. Remote Sens. Environ., 172:
4677 50–66. doi:[10.1016/j.rse.2015.10.027](https://doi.org/10.1016/j.rse.2015.10.027).
- 4678 Forsythe, N., S. Blenkinsop and H. J. Fowler (2014). *Exploring objective climate classi-
4679 fication for the Himalayan arc and adjacent regions using gridded data sources*. Earth
4680 Syst. Dynam., 6:311–326. doi:[10.5194/esd-6-311-2015](https://doi.org/10.5194/esd-6-311-2015).
- 4681 Funk, C., J. Michaelsen and M. T. Marshall (2012). *Mapping Recent Decadal Climate
4682 Variations in Precipitation and Temperature across Eastern Africa and the Sahel*.
4683 In: Wardlow, B. D., M. C. Anderson and J. P. Verdin (Hrsg.), *Remote Sensing of
4684 Drought: Innovative Monitoring Approaches*, chapter 14, 331–357. CRC Press 2012.
4685 ISBN 978-1-4398-3560-9.
- 4686 Funk, C. C., P. J. Peterson, M. F. Landsfeld, D. H. Pedreros, J. P. Verdin, J. D. Rowland,
4687 B. E. Romero, G. J. Husak, J. C. Michaelsen and A. P. Verdin (2014). *A Quasi-Global
4688 Precipitation Time Series for Drought Monitoring*. U.S. Geol. Surv. Data Ser., 27:
4689 1062–1069. doi:[10.1175/JCLI-D-13-00332.1](https://doi.org/10.1175/JCLI-D-13-00332.1).

- 4690 Funk, C. C., P. J. Peterson, M. F. Landsfeld, D. H. Pedreros, J. P. Verdin, S. Shukla,
4691 G. Husak, J. Rowland, A. Hoell L. Harrison and J. C. Michaelsen (2015). *The climate*
4692 *hazards infrared precipitation with stations-A new environmental record for monitor-*
4693 *ing extremes*. Sci. Data, 2(150066):21pp. doi:[10.1038/sdata.2015.66](https://doi.org/10.1038/sdata.2015.66).
- 4694 Gain, A. K., W. W. Immerzeel, F. C. S. Weiland and M. F. P. Bierkens (2011). *Impact*
4695 *of climate change on the stream flow of the lower Brahmaputra: trends in high and*
4696 *low flows based on discharge-weighted ensemble modelling*. Hydrol. Earth Syst., 15:
4697 1537–1545. doi:[10.5194/hess-15-1537-2011](https://doi.org/10.5194/hess-15-1537-2011).
- 4698 Galindo, F. J., and J. Palacio (2013). *Post-processing ROA data clocks for optimal*
4699 *stability in the ensemble timescale*. Metrologia, 40:S237–S244. doi:[10.1088/0026-](https://doi.org/10.1088/0026-1394/40/3/301)
4700 [1394/40/3/301](https://doi.org/10.1088/0026-1394/40/3/301).
- 4701 Galvin, J. F. P. (2008). *The weather and climate of the tropics: Part 6 - Monsoons*.
4702 Weather, 63(5):129–137. doi:[10.1002/wea.230](https://doi.org/10.1002/wea.230).
- 4703 Gautam, D., and N. R. Prajapati (2014). *Drawdown and Dynamics of*
4704 *Groundwater Table in Kathmandu Valley, Nepal*. Open Hydro. J., 8(1).
4705 doi:[10.2174/1874378101408010017](https://doi.org/10.2174/1874378101408010017).
- 4706 Gautam, R., N. C. Hsu, K. M. Lau, S. C. Tsay and M. Kafatos (2009). *Enhanced Pre-*
4707 *Monsoon Warming over the Himalayan-Gangetic Region from 1979 to 2007*. Geophys.
4708 Res. Lett., 36(7). doi:[10.1029/2009GL037641](https://doi.org/10.1029/2009GL037641).
- 4709 Gettelman, A., W. J. Randel, S. Massie, F. Wu, W. G. Read and J. M. Russell (2001). *El*
4710 *Ni no as a Natural Experiment for Studying the Tropical Tropopause Region*. J. Clim.,
4711 14(4B):3375–339. doi:[10.1175/1520-0442\(2001\)014<3375:ENOAAN>2.0.CO;2](https://doi.org/10.1175/1520-0442(2001)014<3375:ENOAAN>2.0.CO;2).
- 4712 Giorgetta, M. A., J. Jungclaus, C. H. Reick, S. Legutke, J. Bader, M. Böttinger,
4713 V. Brovkin, T. Crueger, M. Esch, K. Fieg, K. Glushak, V. Gayler, H. Haak, H. D.
4714 Hollweg, T. Ilyina, S. Kinne, L. Kornblueh, D. Matei, T. Mauritsen, U. Mikolajew-
4715 icz, W. Mueller, D. Notz, F. Pithan, T. Raddatz, S. Rast, R. Redler, E. Roeckner,
4716 H. Schmidt, R. Schnur, J. Segschneider, K. D. Six, M. Stockhause, C. Timmreck,
4717 J. Wegner, H. Widmann, K. H. Wieners, M. Claussen, J. Marotzke and B. Stevens
4718 (2013). *Climate and carbon cycle changes from 1850 to 2100 in MPI-ESM simulations*
4719 *for the Coupled Model Intercomparison Project phase 5*. J. Adv. Model. Earth Sys., 5
4720 (3):643–674. doi:[10.1002/jame.20038](https://doi.org/10.1002/jame.20038).
- 4721 Giorgi, F., and L. O. Mearns (1991). *Approaches to the simulation of regional climate*
4722 *change: A review*. Rev. Geophys., 29(2):191–216. doi:[10.1029/90RG02636](https://doi.org/10.1029/90RG02636).
- 4723 Giorgi, F., M. R. Marinucci and G. T. Bates (1993). *Development of a second*
4724 *generation regional climate model (RegCM2). Part I: Boundary layer and radia-*
4725 *tive transfer processes*. Mon. Weather Rev., 121:2794–2813. doi:[10.1175/1520-](https://doi.org/10.1175/1520-0493(1993)121<2794:DOASGR>2.0.CO;2)
4726 [0493\(1993\)121<2794:DOASGR>2.0.CO;2](https://doi.org/10.1175/1520-0493(1993)121<2794:DOASGR>2.0.CO;2).
- 4727 Giorgi, F., M. R. Marinucci, G. D. Canio and G. T. Bates (1993). *Development of a*
4728 *Second-Generation Regional Climate Model (RegCM2). Part II: Convective Processes*

- 4729 *and Assimilation of Lateral Boundary Conditions*. *Mon. Weather Rev.*, 121:2814–
4730 2832. doi:[10.1175/1520-0493\(1993\)121<2814:DOASGR>2.0.CO;2](https://doi.org/10.1175/1520-0493(1993)121<2814:DOASGR>2.0.CO;2).
- 4731 Giorgi, F., E. Coppola, F. Solmon, L. Mariotti, M. B. Sylla, X. Bi, N. Elguindi, G. T.
4732 Diro, V. Nair, G. Giuliani, U. U. Turuncoglu, S. Cozzini, I. Güttler, T. A. O'Brien,
4733 A. B. Tawfik, A. Shalaby, A. S. Zakey, A. L. Steiner, F. Stordal, L. C. Sloan and
4734 C. Brankovic (2012). *RegCM4: Model description and preliminary tests over multiple*
4735 *CORDEX domains*. *Clim. Res.*, 52:7–29. doi:[10.3354/cr01018](https://doi.org/10.3354/cr01018).
- 4736 Goovaerts, P. (2000). *Geostatistical approaches for incorporating elevation into the*
4737 *spatial interpolation of rainfall*. *J. Hydrol.*, 228(1-2):113–129. doi:[10.1016/S0022-1694\(00\)00144-X](https://doi.org/10.1016/S0022-1694(00)00144-X).
- 4739 Gordon, C., C. Cooper, C. A. Senior, H. Banks, J. M. Gregory, T. C. Johns, J. F. B.
4740 Mitchell and R. A. Wood (2000). *The simulation of SST, sea ice extents and ocean heat*
4741 *transports in a version of the Hadley Centre coupled model without flux adjustments*.
4742 *Clim. Dyn.*, 16(2/3):147–168. doi:[10.1007/s003820050010](https://doi.org/10.1007/s003820050010).
- 4743 Goswami, B. B., P. Mukhopadhyay, R. Mahanta and B. N. Goswami (2010). *Multiscale*
4744 *interaction with topography and extreme rainfall events in the northeast Indian region*.
4745 *J. Geophys. Res.*, 115(D12). doi:[10.1029/2009JD012275](https://doi.org/10.1029/2009JD012275).
- 4746 Goswami, B. N., V. Venugopal, D. Sengupta, M. S. Madhusoodanan and P. K. Xavier
4747 (2006). *Increasing Trend of Extreme Rain Events Over India in a Warming Environ-*
4748 *ment*. *Science*, 314(5804):1442–1445. doi:[10.1126/science.1132027](https://doi.org/10.1126/science.1132027).
- 4749 Gregory, D., and P. R. Rowntree (1990). *A Mass Flux Convection Scheme with Represen-*
4750 *tation of Cloud Ensemble Characteristics and Stability-Dependent Closure*. *Mon. Wea.*
4751 *Rev.*, 118:1483–1506. doi:[10.1175/1520-0493\(1990\)118<1483:AMFCSW>2.0.CO;2](https://doi.org/10.1175/1520-0493(1990)118<1483:AMFCSW>2.0.CO;2).
- 4752 Grell, G. (1993). *Prognostic evaluation of assumptions used by cumulus parameteriza-*
4753 *tions*. *Mon. Weather Rev.*, 121:764–787.
- 4754 Grell, G. A., J. Dudhia and D. R. Stauffer (1994). *Description of the fifth generation*
4755 *Penn State/NCAR Mesoscale Model (MM5)*. NCAR, Boulder, Colorado, 1994.
- 4756 Guo, Z., P. A. Dirmeyer, X. Gao and M. Zhao (2007). *Improving the quality of simulated*
4757 *soil moisture with a multi-model ensemble approach*. *Q. J. R. Meteorolog. Soc.*, 33
4758 (624):731–747. doi:[10.1002/qj.48](https://doi.org/10.1002/qj.48).
- 4759 Hamed, K. H., and A. R. Rao (1998). *A modified Mann-Kendall trend test for autocor-*
4760 *related data*. *J. Hydrol.*, 204(1–4):182–196. doi:[10.1016/S0022-1694\(97\)00125-X](https://doi.org/10.1016/S0022-1694(97)00125-X).
- 4761 Han, S. C., C. K. Shum, C. Jekeli, C. Y. Kuo, C. R. Wilson and K. W. Seo (2005). *Non-*
4762 *isotropic filtering of GRACE temporal gravity for geophysical signal enhancement*.
4763 *Geophys. J. Int.*, 163(1):18–25. doi:[10.1111/j.1365-246X.2005.02756.x](https://doi.org/10.1111/j.1365-246X.2005.02756.x).
- 4764 Hannachi, A., I. T. Jolliffe and D. B. Stephenson (2007). *Empirical orthogonal functions*
4765 *and related techniques in atmospheric science: A review*. *Int. J. Climatol.*, 27(9):1119–
4766 1152. doi:[10.1002/joc.1499](https://doi.org/10.1002/joc.1499).

- 4767 Hao, Z., A. AghaKouchak, N. Nakhjiri and A. Farahmand (2014). *Global in-*
4768 *tegrated drought monitoring and prediction system.* Sci. Data, (140001):1–10.
4769 doi:[10.1038/sdata.2014.1](https://doi.org/10.1038/sdata.2014.1).
- 4770 Harris, I., P.D. Jones, T.J. Osborn and D.H. Lister (2013). *Updated high-resolution grids*
4771 *of monthly climatic observations- the CRU TS3.10 Dataset.* Int. J. Climatol., 34(3):
4772 623–642. doi:[10.1002/joc.3711](https://doi.org/10.1002/joc.3711).
- 4773 Hartmann, D. L., A. M. G. Klein Tank, M. Rusticucci, L. V. Alexander, S. Brönnimann,
4774 Y. Charabi, F. J. Dentener, E. J. Dlugokencky, D. R. Easterling, A. Kaplan, B. J.
4775 Soden, P. W. Thorne, M. Wild and P. M. Zhai (2013). *Observations: Atmosphere and*
4776 *Surface.* In: Stocker, T. F., D. Qin, G.-K. Plattner, M. Tignor, S.K. Allen, J. Boschung,
4777 A. Nauels, Y. Xia, V. Bex and P.M. Midgley (Hrsg.), *Climate Change 2013: The*
4778 *Physical Science Basis. Contribution of Working Group I to the Fifth Assessment*
4779 *Report of the Intergovernmental Panel on Climate Change.* Cambridge University
4780 Press, Cambridge, United Kingdom and New York, NY, USA.
- 4781 Healy, S. B., and J.-N. Thépaut (2006). *Assimilation experiments with CHAMP*
4782 *GPS radio occultation measurements.* Q. J. R. Meteorol. Soc., 132:605–623.
4783 doi:[10.1256/qj.04.182](https://doi.org/10.1256/qj.04.182).
- 4784 Heim, R. R. (2002). *A Review of Twentieth-Century Drought Indices Used in*
4785 *the United States.* Bull. Amer. Meteor. Soc, 83(8):1149–1165. doi:[10.1175/1520-](https://doi.org/10.1175/1520-0477(2002)083<1149:AROTDI>2.3.CO;2)
4786 [0477\(2002\)083<1149:AROTDI>2.3.CO;2](https://doi.org/10.1175/1520-0477(2002)083<1149:AROTDI>2.3.CO;2).
- 4787 Helsel, D.R., and R.M. Hirsch (2002). *Statistical Methods in Water Resources.* In: *Tech-*
4788 *niques of Water Resources Investigations*, Book 4, chapter A3, 522pp. U.S. Geological
4789 Survey.
- 4790 Hingane, L. S., K. Rupa Kumar and B. V. Ramana Murty (1985). *Long-term*
4791 *trends of surface air temperature in India.* Int. J. Climatol., 5(5):521–528.
4792 doi:[10.1002/joc.3370050505](https://doi.org/10.1002/joc.3370050505).
- 4793 Hirsch, R. M., and J. R. Slack (1984). *A Nonparametric Trend Test for*
4794 *Seasonal Data With Serial Dependence.* Water Resour. Res., 6(20):727–732.
4795 doi:[10.1029/WR020i006p00727](https://doi.org/10.1029/WR020i006p00727).
- 4796 Hirschi, M., S. I. Seneviratne, V. Alexandrov, F. Boberg, C. Boroneant, O. B. Chris-
4797 tensen, H. Formayer, B. Orłowsky and P. Stepanek (2011). *Observational evidence*
4798 *for soil-moisture impact on hot extremes in southeastern Europe.* Nature, 4:17–21.
4799 doi:[10.1038/ngeo1032](https://doi.org/10.1038/ngeo1032).
- 4800 Ho, S. P., X. Zhou, Y. H. Kuo, D. Hunt and J. H. Wang (2010). *Global Evaluation of Ra-*
4801 *diosonde Water Vapor Systematic Biases using GPS Radio Occultation from COSMIC*
4802 *and ECMWF Analysis.* Remote Sens., 2(5):1320–1330. doi:[10.3390/rs2051320](https://doi.org/10.3390/rs2051320).
- 4803 Ho, S. P., X. Yue, Z. Zeng, C. O. Ao, C. Y. Huang, E. R. Kursinski and Y. H. Kuo
4804 (2014). *Applications of COSMIC Radio Occultation Data from the Troposphere to*
4805 *Ionosphere and Potential Impacts of COSMIC-2 Data.* Bull. Amer. Meteor. Soc., 95
4806 (1):ES18–ES22. doi:[10.1175/BAMS-D-13-00035.1](https://doi.org/10.1175/BAMS-D-13-00035.1).

- 4807 Hoque, M. A., M. M. Hoque and K. M Ahmed (2007). *Declining groundwater level and*
4808 *aquifer dewatering in Dhaka metropolitan area, Bangladesh: Causes and quantifica-*
4809 *tion*. *Hydrogeol. J.*, 15:1523–1534. doi:10.1007/s10040-007-0226-5.
- 4810 Hou, A. Y., R. K. Kakar, S. Neeck, A.A. Azarbarzin, C. D. Kummerow, M. Kojima,
4811 R. Oki, K. Nakamura and T. Iguchi (2014). *The Global Precipitation Measurement*
4812 *mission*. *Bull. Amer. Meteor. Soc.*, 65(5):701–722. doi:10.1175/BAMS-D-13-00164.1.
- 4813 Hsu, P.- C., T. Li, J.- J. Luo, H. Murakami, A. Kitoh and M. Zhao (2012). *Increase of*
4814 *global monsoon area and precipitation under global warming: A robust signal?* *Geo-*
4815 *phys. Res. Lett.*, 39(6). doi:10.1029/2012GL051037.
- 4816 Huffman, G. J., and D. T. Bolvin (2013). *TRMM and Other Data Precipitation Data*
4817 *Set Documentation*. Technical Report, Mesoscale Atmospheric Processes Laboratory,
4818 NASA Goddard Space Flight Center and Science Systems and Applications, Inc.
- 4819 Huffman, G. J., D. T. Bolvin, E. J. Nelkin, D. B. Wolff, Robert F. Adler, G. Gu,
4820 Y. Hong, K. P. Bowman and E. F. Stocker (2007). *The TRMM Multisatellite Precip-*
4821 *itation Analysis (TMPA): Quasi-Global, Multiyear, Combined-Sensor Precipitation*
4822 *Estimates at Fine Scales*. *J. Hydrometeorol.*, 8(1):38–55. doi:10.1175/JHM560.1.
- 4823 ICIMOD (2007). In: Bajracharya, S. R., P. K. Mool and B. Shrestha (Hrsg.), *Impact of*
4824 *Climate Change on Himalayan Glaciers and Glacial Lakes: Case Studies on GLOF*
4825 *and Associated Hazards in Nepal and Bhutan*, 1–133. ICIMOD in cooperation with
4826 UNEP Programme Regional Office Asia and the Pacific (ROAP), International Centre
4827 for Integrated Mountain Development, Khumaltar, Kathmandu, Nepal. ISBN 978-
4828 92-9115-032-8. Available at <http://lib.icimod.org/record/22442>. Accessed on 24
4829 July 2014.
- 4830 Immerzeel, W. (2008). *Historical trends and future predictions of climate variability in*
4831 *the Brahmaputra basin*. *Int. J. Climatol.*, 28:243–254. doi:10.1002/joc.1528.
- 4832 Immerzeel, W. W., L. P. H. van Beek and M. F. P. Bierkens (2010). *Climate Change Will*
4833 *Affect the Asian Water Towers*. *Science*, 328:1382–1385. doi:10.1126/science.1183188.
- 4834 Immerzeel, W. W., L. P. H. van Beek, M. Konz, A. B. Shrestha and M. F. P. Bierkens
4835 (2012). *Hydrological response to climate change in a glacierized catchment in the*
4836 *Himalayas*. *Clim. Chang.*, 110(3):721–736. doi:10.1007/s10584-011-0143-4.
- 4837 Immerzeel, W. W., L. Petersen, S. Ragetli and F. Pellicciotti (2014). *The importance*
4838 *of observed gradients of air temperature and precipitation for modeling runoff from a*
4839 *glacierized watershed in the Nepalese Himalayas*. *Water Resour. Res.*, 50:2212–2226.
4840 doi:10.1002/2013WR014506.
- 4841 Inman, M. (2010). *Settling the science on Himalayan glaciers*. *Nat. Clim. Change*, 4,
4842 doi:10.1038/climate.2010.19.
- 4843 IPCC (2000). *Special Report on Emissions Scenarios: A Special Report of Working*
4844 *Group III of the Intergovernmental Panel on Climate Change*. Technical Report,
4845 International Panel on Climate Change, Cambridge, United Kingdom and New York,
4846 NY, USA.

- 4847 IPCC (2007). *Summary for Policymakers*. In: Solomon, S., D. Qin, M. Manning,
4848 Z. Chen, M. Marquis, K.B. Averyt, M. Tignor and H.L. Miller (Hrsg.), *Climate Change*
4849 *2007: The Physical Science Basis. Contribution of Working Group I to the Fifth As-*
4850 *essment Report of the Intergovernmental Panel on Climate Change*. Cambridge Uni-
4851 versity Press, Cambridge, United Kingdom and New York, USA.
- 4852 IPCC (2012). *Managing the Risks of Extreme Events and Disasters to Advance Cli-*
4853 *mate Change Adaptation*. 582. Intergovernmental Panel on Climate Change, Geneva,
4854 Switzerland.
- 4855 IPCC (2013). *Summary for Policymakers*. In: Stocker, T. F., D. Qin, G. K. Plattner,
4856 M. Tignor, S. K. Allen, J. Boschung, A. Nauels, Y. Xia, V. Bex and P.M. Midgley
4857 (Hrsg.), *Climate Change 2013: The Physical Science Basis. Contribution of Working*
4858 *Group I to the Fifth Assessment Report of the Intergovernmental Panel on Climate*
4859 *Change*. Cambridge University Press, Cambridge, United Kingdom and New York,
4860 USA.
- 4861 Islam, M. N., M. Rafiuddin, A. U. Ahmed and R. K. Kolli (2008). *Calibration of*
4862 *PRECIS in employing future scenarios in Bangladesh*. *Int. J. Climatol.*, 28:617–628.
4863 doi:[10.1002/joc.1559](https://doi.org/10.1002/joc.1559).
- 4864 Jacob, D., and R. Podzun (1997). *Sensitivity studies with the regional climate model*
4865 *REMO*. *Meteo. Atmo. Phys.*, 63:119–129. doi:[10.1007/BF01025368](https://doi.org/10.1007/BF01025368).
- 4866 Jacob, T., J. Wahr, W. T. Pfeffer and S. Swenson (2012). *Recent contributions of glaciers*
4867 *and ice caps to sea level rise*. *Nature*, 482:514–518. doi:[10.1038/nature10847](https://doi.org/10.1038/nature10847).
- 4868 Jain, S. K., V. Kumar and M. Saharia (2012). *Analysis of rainfall and temperature*
4869 *trends in northeast India*. *Int. J. Climatol.*, 33:968–978. doi:[10.1002/joc.3483](https://doi.org/10.1002/joc.3483).
- 4870 Janowiak, J. E., R. J. Joyce and Yelena Yarosh (2001). *A Real-Time Global Half-Hourly*
4871 *Pixel-Resolution Infrared Dataset and Its Applications*. *Bull. Am. Meteorol. Soc.*, 82:
4872 205–217. doi:[10.1175/1520-0477\(2001\)082<0205:ARTGHH>2.3.CO;2](https://doi.org/10.1175/1520-0477(2001)082<0205:ARTGHH>2.3.CO;2).
- 4873 Jekeli, C. (1981). *Alternative methods to smooth the Earth's gravity field*. Technical
4874 Report, Dep. of Geod. Sci. and Surv., Ohio State Univ., Columbus.
- 4875 Ji, Y., and A. D (1997). *Simulation of the Asian Summer Monsoons of 1987 and*
4876 *1988 with a Regional Model Nested in a Global GCM*. *J. Clim.*, 10:1965–1979.
4877 doi:[10.1175/1520-0442\(1997\)010<1965:SOTASM>2.0.CO;2](https://doi.org/10.1175/1520-0442(1997)010<1965:SOTASM>2.0.CO;2).
- 4878 Jiménez-Cisneros, B. E., T. Oki, N.W. Arnell, G. Benito, J.G. Cogley, P. Döll, T. Jiang
4879 and S.S. Mwakalila (2014). *Freshwater Resources*. In: Barros, V.R., C.B. Field, D.J.
4880 Dokken, M.D. Mastrandrea, K.J. Mach, T.E. Bilir, M. Chatterjee, K.L. Ebi, Y.O.
4881 Estrada, R.C. Genova, B. Girma, E.S. Kissel, A.N. Levy, S. MacCracken, P.R. Mas-
4882 strandrea and L.L. White (Hrsg.), *Climate Change 2014: Impacts, Adaptation, and*
4883 *Vulnerability. Part A: Global and Sectoral Aspects. Contribution of Working Group II*
4884 *to the Fifth Assessment Report of the Intergovernmental Panel on Climate Change*,
4885 229–269. Cambridge University Press, Cambridge, United Kingdom and New York,
4886 USA.

- 4887 Johnston, R., and V. Smakhtin (2014). *Hydrological Modeling of Large river Basins:*
4888 *How Much is Enough?* Water Resour. Manag., 28(10):2695–2730. doi:[10.1007/s11269-](https://doi.org/10.1007/s11269-014-0637-8)
4889 [014-0637-8](https://doi.org/10.1007/s11269-014-0637-8).
- 4890 Jones, R.G., M. Noguer, D.C. Hassel, D. Hudson, S.S. Wilson, G.J. Jenkins and J.F.B.
4891 Mitchell (2004). *Generating High Resolution Climate Change Scenarios using PRE-*
4892 *CIS*. Technical Report, Met Office Hadley Center, UK.
- 4893 Joyce, R. J., J. E. Janowiak, P. A. Arkin and P. Xie (2004). *CMORPH: A Method*
4894 *that Produces Global Precipitation Estimates from Passive Microwave and Infrared*
4895 *Data at High Spatial and Temporal Resolution*. J. Hydrometeorol., 5(3):487–503.
4896 doi:[10.1175/1525-7541\(2004\)005<0487:CAMTPG>2.0.CO;2](https://doi.org/10.1175/1525-7541(2004)005<0487:CAMTPG>2.0.CO;2).
- 4897 Juang, H. M. H., S. C. Chen, S. Hong, H. Kanamaru, T. Reichler, T. Enomoto, D. Pu-
4898 trasahan, B. T. Anderson, S. Gershunov, H. Li, K. Yoshimura, N. Buenning and
4899 D. Boomer (2014). *Regional Spectral Model Workshop in Memory of John Roads and*
4900 *Masao Kanamitsu*. Bull. Amer. Meteor. Soc., 96:ES61–ES65. doi:[10.1175/BAMS-13-](https://doi.org/10.1175/BAMS-13-00124.1)
4901 [00124.1](https://doi.org/10.1175/BAMS-13-00124.1).
- 4902 Justice, C.O., J.R.G Townshend, E.F Vermote, E Masuoka, R.E Wolfe, N Saleous, D.P
4903 Roy and J.T Morisette (2002). *An overview of MODIS Land data processing and*
4904 *product status*. Remote Sens. Environ., 83:3–15. doi:[10.1016/S0034-4257\(02\)00084-6](https://doi.org/10.1016/S0034-4257(02)00084-6).
- 4905 Kalnay, E., M. Kanamitsu, R. Kistler, W. Collins, D. Deaven, L. Gandin, M. Iredell,
4906 S. Saha, G. White, J. Woollen, Y. Zhu, M. Chelliah, W. Ebisuzaki, W. Higgins,
4907 J. Janowiak, K. C. Mo, C. Ropelewski, J. Wang, A. Leetmaa, R. Reynolds, R. Jenne,
4908 and D. Joseph (1996). *The NCEP/NCAR 40-year reanalysis project*. Bull. Am. Meteorol.
4909 Soc., 77(3):437–470. doi:[10.1175/1520-0477\(1996\)077<0437:TNYRP>2.0.CO;2](https://doi.org/10.1175/1520-0477(1996)077<0437:TNYRP>2.0.CO;2).
- 4910 Kanamitsu, M., W. Ebisuzaki, J. Woollen, S.-K. Yang, J. J. Hnilo, M. Fiorino and G. L.
4911 Potter (2002). *NCEP-DOE AMIP-II Reanalysis (R-2)*. Bull. Am. Meteorol. Soc., 83:
4912 1631–1643. doi:[10.1175/BAMS-83-11-1631](https://doi.org/10.1175/BAMS-83-11-1631).
- 4913 Karl, T. R., S. J. Hassol, C. D. Miller and W. L. Murray (eds) (2006). *Temperature*
4914 *Trends in the Lower Atmosphere: Steps for Understanding and Reconciling Differ-*
4915 *ences*. Technical Report, U.S. Climate Change Science Program, Washington, DC.
- 4916 Kendall, M. G. (1962). *Rank correlation methods*. J. Am. Stat. Assoc., 63(324):1379–
4917 1389. doi:[10.1080/01621459.1968.10480934](https://doi.org/10.1080/01621459.1968.10480934).
- 4918 Kerr, Y. H., P. Waldteufel, J. P. Wigneron, J. M. Martinuzzi, J. Font and M. Berger
4919 (2001). *Soil moisture retrieval from space: The Soil Moisture and Ocean Salinity*
4920 *(SMOS) mission*. IEEE Trans. Geosci. Remote Sens., 39(8). doi:[10.1109/36.942551](https://doi.org/10.1109/36.942551).
- 4921 Khandu, J. L. Awange, J. Wickert, T. Schmidt, M. A. Sharifi, B. Heck and K. Fleming
4922 (2011). *GNSS remote sensing of the Australian tropopause*. Clim. Chang., 105(3–4):
4923 597–618. doi:[10.1007/s10584-010-9894-6](https://doi.org/10.1007/s10584-010-9894-6).
- 4924 Khandu, J. L. Awange and E. Forootan (2015). *An evaluation of high-resolution gridded*
4925 *precipitation products over Bhutan (1998-2012)*. Int. J. Climatol., 36(3):1067–1087.
4926 doi:[10.1002/joc.4402](https://doi.org/10.1002/joc.4402).

- 4927 Khandu, E. Forootan, M. Schumacher, J.L. Awange and H. Müller Schmied (2016a).
4928 *Exploring the influence of precipitation extremes and human water use on total water*
4929 *storage (TWS) changes in Brahmaputra-Ganges-Meghna Basin.* Water Resour. Res.,
4930 52(3):2240–2258. doi:[10.1002/2015WR018113](https://doi.org/10.1002/2015WR018113).
- 4931 Khandu, , J. L. Awange and E. Forootan (2016b). *Interannual variability of temperature*
4932 *in the UTLS region over Ganges–Brahmaputra–Meghna river basin based on COSMIC*
4933 *GNSS RO data.* Atmos. Meas. Tech., 9:1685–1699. doi:[10.5194/amt-9-1685-2016](https://doi.org/10.5194/amt-9-1685-2016).
- 4934 Khandu, J. L. Awange, R. Anyah, M. Kuhn and E. Forootan (2016c). *Changes*
4935 *and variability of precipitation and temperature in the Ganges-Brahmaputra-*
4936 *Meghna River Basin based on global high-resolution reanalyses.* Int. J. Climatol.
4937 doi:[10.1002/joc.4842](https://doi.org/10.1002/joc.4842).
- 4938 Kishore, P., S. Jyothi, G. Basha, S. V. B. Rao, M. Rajeevan and I. Velicogna (2016). *Pre-*
4939 *cipitation climatology over India: validation with observations and reanalysis datasets*
4940 *and spatial trends.* Clim. Dyn., 46(1):541–556. doi:[10.1007/s00382-015-2597-y](https://doi.org/10.1007/s00382-015-2597-y).
- 4941 Kitoh, A., and H. Endo (2016). *Changes in precipitation extremes projected by a*
4942 *20-km mesh global atmospheric model.* Weather and Climate Extremes, 11:41–52.
4943 doi:[10.1016/j.wace.2015.09.001](https://doi.org/10.1016/j.wace.2015.09.001).
- 4944 Klein Tank, A. M. G., T. C. Peterson, D. A. Quadir, S. Dorji, X. Zou, H. Tang, K. San-
4945 thosh, U. R. Joshi, A. K. Jaswal, R. K. Kolli, A. B. Sikder, N. R. Deshpande, J. V.
4946 Revadekar, K. Yeleuova, S. Vandasheva, M. Faleyeva, P. Gomboluudev, K. P. Bud-
4947 hathoki, A. Hussain, M. Afzaal, L. Chandrapala, H. Anvar, D. Amanmurad, V. S.
4948 Asanova, P. D. Jones, M. G. New, and T. Spektorman (2006). *Changes in daily tem-*
4949 *perature and precipitation extremes in central and south Asia.* J. Geophys. Res., 111
4950 (D16105). doi:[10.1029/2005JD006316](https://doi.org/10.1029/2005JD006316).
- 4951 Klein Tank, A. M. G., F. W. Zwiers and X. Zhang (2009). *Guidelines on Analysis of*
4952 *extremes in a changing climate in support of informed decisions for adaptation.* World
4953 Meteorological Organization, Geneva 2, Switzerland, June 2009.
- 4954 Knutti, R., and J. Sedláček (2013). *Robustness and uncertainties in the new CMIP5*
4955 *climate model projections.* Nat. Clim. Chang., 3:369–373. doi:[10.1038/nclimate1716](https://doi.org/10.1038/nclimate1716).
- 4956 Knutti, R., R. Furrer, C. Tebaldi, J. Cermak and G. A. Meehl (2010). *Challenges in*
4957 *Combining Projections from Multiple Climate Models.* J. Clim., 23(10):2739–2758.
4958 doi:[10.1175/2009JCLI3361.1](https://doi.org/10.1175/2009JCLI3361.1).
- 4959 Kobayashi, S., Y. Ota, Y. Harada, A. Ebata, M. Moriya, H. Onoda, K. Onogi, H. Kama-
4960 hori, C. Kobayashi, H. Endo, K. Miyaoka and K. Takahashi (2015). *The JRA-55*
4961 *Reanalysis: General Specifications and Basic Characteristics.* Quart. J. R. Meteorol.
4962 Soc., 93(1):5–48. doi:[10.2151/jmsj.2015-001](https://doi.org/10.2151/jmsj.2015-001).
- 4963 Koot, L., O. de Viron and V. Dehant (2006). *Atmospheric angular momentum time-*
4964 *series: characterization of their internal noise and creation of a combined series.* J.
4965 Geod., 79(12):663–674. doi:[10.1007/s00190-005-0019-3](https://doi.org/10.1007/s00190-005-0019-3).

- 4966 Kothawale, D. R., , A. A Munot and K. Krishna Kumar (2010). *Surface air temperature*
4967 *variability over India during 1901-2007, and its association with ENSO*. *Clim. Res.*,
4968 42(1):89–104. doi:[10.3354/cr00857](https://doi.org/10.3354/cr00857).
- 4969 Kripalani, R. H., , J. H. Oh, , A. Kulkarni, , S. S. Sabade and H. S. Chaudhari
4970 (2007). *South Asian summer monsoon precipitation variability: Coupled climate model*
4971 *simulations and projections under IPCC AR4*. *Theor. Appl. Climatol.*, 90:133–159.
4972 doi:[10.1007/s00704-006-0282-0](https://doi.org/10.1007/s00704-006-0282-0).
- 4973 Krishna Kumar, K., K. Kamala, B. Rajagopalan, M. P. Hoerling, J. K. Eischeid,
4974 S. K. Patwardhan, G. Srinivasan, B. N. Goswami and R. Nemani (2011). *The once*
4975 *and future pulse of Indian monsoonal climate*. *Clim. Dyn.*, 36(11–12):4397–4417.
4976 doi:[10.1007/s00382-010-0974-0](https://doi.org/10.1007/s00382-010-0974-0).
- 4977 Krishnamurthy, L., and V. Krishnamurthy (2014). *Influence of PDO on South Asian*
4978 *summer monsoon and monsoon-ENSO relation*. *Clim. Dyn.*, 42(9–10):2397–2410.
4979 doi:[10.1007/s00382-013-1856-z](https://doi.org/10.1007/s00382-013-1856-z).
- 4980 Krishnamurthy, V., and J. L. Kinter III (2003). *The Indian Monsoon and its Relation*
4981 *to Global Climate Variability*. In: Rodó, X., and F. A. Comín (Hrsg.), *Global Climate*,
4982 186–236. Springer Berlin Heidelberg, New York.
- 4983 Kumar, G., R. Madan, K.C. S. Krishnan and P. K. Jain (2010). *UPGRADATION*
4984 *OF INDIAN RADIOSONDE NETWORK: PERFORMANCE & FUTURE PLANS*.
4985 Technical Report, India Meteorological Department, Lodi Road, New Delhi, India.
- 4986 Kumar, G., R. Madan, K.C. Saikrishnan, S. K. Kundu and P. K. Jain (2011). *Technical*
4987 *and operational characteristics of GPS sounding system in the upper air network*
4988 *of IMD*. *Mausam*, 62(3):403–416. Available at: [metnet.imd.gov.in/mausamdocs/](http://metnet.imd.gov.in/mausamdocs/16632_F.pdf)
4989 [16632_F.pdf](http://metnet.imd.gov.in/mausamdocs/16632_F.pdf).
- 4990 Kumar, K. Rupa, A. K. Sahai, K. Krishna Kumar, S. K. Patwardhan, P. K. Mishra,
4991 J. V. Revadekar, K. Kamala and G. B. Pant (2006). *High-resolution climate change*
4992 *scenarios for India for the 21st century*. *Curr. Sci.*, 90(3).
- 4993 Kummerow, C., W. Barnes, T. Kozu, J. Shiue and J. Simpson (1998). *The Tropical*
4994 *Rainfall Measuring Mission (TRMM) Sensor Package*. *J. Atmos. Oceanic Technol.*,
4995 15:809–817. doi:[10.1175/1520-0426\(1998\)015<0809:TTRMMT>2.0.CO;2](https://doi.org/10.1175/1520-0426(1998)015<0809:TTRMMT>2.0.CO;2).
- 4996 Kunze, M., P. Braesicke, U. Langematz, G. Stiller, S. Bekki, C. Brühl, M. Chipperfield,
4997 M. Dameris, R. Garcia and M. Giorgetta (2010). *Influences of the Indian Summer*
4998 *Monsoon on Water Vapor and Ozone Concentrations in the UTLS as Simulated by*
4999 *Chemistry-Climate Models*. *J. Clim.*, 23(13). doi:[10.1175/2010JCLI3280.1](https://doi.org/10.1175/2010JCLI3280.1).
- 5000 Kuo, Y. H., T. K. Wee, S. Sokolovskiy, C. Rocken, W. Schreiner, D. Hunt and R. A.
5001 Anthes (2004). *Inversion and Error Estimation of GPS Radio Occultation Data*. *J.*
5002 *Meteor. Soc. Japan*, 82(1B):507–531. doi:[10.1029/2004GL021443](https://doi.org/10.1029/2004GL021443).
- 5003 Kusche, J. (2007). *Approximate decorrelation and non-isotropic smoothing of*
5004 *time-variable GRACE-type gravity field models*. *J. Geod.*, 81(11):733–749.
5005 doi:[10.1007/s00190-007-0143-3](https://doi.org/10.1007/s00190-007-0143-3).

- 5006 Kusche, J., R. Schmidt, S. Petrovic and R. Rietbroek (2009). *Decorrelated GRACE time-*
5007 *variable gravity solutions by GFZ, and their validation using a hydrological model.* J.
5008 Geod., 83(10):903–913. doi:[10.1007/s00190-009-0308-3](https://doi.org/10.1007/s00190-009-0308-3).
- 5009 Lal, M., J. L. McGregor and K. C. Nguyen (2008). *Very high-resolution climate sim-*
5010 *ulation over Fiji using a global variable-resolution model.* Clim. Dyn., 30:293–305.
5011 doi:[10.1007/s00382-007-0287-0](https://doi.org/10.1007/s00382-007-0287-0).
- 5012 Lambert, F. H., and M. J. Webb (2008). *Dependency of global mean precipitation on*
5013 *surface temperature.* Geophys. Res. Lett., 35(16). doi:[10.1029/2008GL034838](https://doi.org/10.1029/2008GL034838).
- 5014 Landerer, F. W., and S. C. Swenson (2012). *Accuracy of scaled GRACE terrestrial water*
5015 *storage estimates.* Water Resour. Res., 48(W04531). doi:[10.1029/2011WR011453](https://doi.org/10.1029/2011WR011453).
- 5016 Lang, T. J., and A. P. Barros (2004). *Winter storms in the central Himalayas.* J. Meteor.
5017 Soc. Japan, 82(3):829–844. doi:[10.2151/jmsj.2004.829](https://doi.org/10.2151/jmsj.2004.829).
- 5018 Lau, K. M., and K. M. Kim (2006). *Observational relationships between aerosol*
5019 *and Asian monsoon rainfall, and circulation.* Geophys. Res. Lett., 33(21).
5020 doi:[10.1029/2006GL027546](https://doi.org/10.1029/2006GL027546).
- 5021 Lau, W. K. M., K. M. Kim, C. N. Hsu and B. N. Holben (2009). *Possible influences of air*
5022 *pollution, dust- and sandstorms on the Indian monsoon.* Bull. World Meteorological
5023 Organization, 58(1):22–30.
- 5024 Leduc, M., and R. Laprise (2009). *Regional climate model sensitivity to domain size.*
5025 Clim. Dyn., 32(6):833–854. doi:[10.1007/s00382-008-0400-z](https://doi.org/10.1007/s00382-008-0400-z).
- 5026 Lee, I. T., T. Matsuo, A. D. Richmond, J. Y. Liu, W. Wang, C. H. Lin, J. L. Anderson and
5027 M. Q. Chen (2012). *Assimilation of FORMOSAT-3/COSMIC electron density profiles*
5028 *into a coupled thermosphere/ionosphere model using ensemble Kalman filtering.* J.
5029 Geophys. Res., 117(A10). doi:[10.1029/2012JA017700](https://doi.org/10.1029/2012JA017700).
- 5030 Lee, J. Y., and B. Wang (2014). *Future change of global monsoon in the CMIP5.* Clim.
5031 Dyn., 42(1):101–119. doi:[10.1007/s00382-012-1564-0](https://doi.org/10.1007/s00382-012-1564-0).
- 5032 Legates, D. R., and C. J. Willmott (1990). *Mean seasonal and spatial vari-*
5033 *ability in global surface air temperature.* Theor. Appl. Climatol., 41(1):11–21.
5034 doi:[10.1007/BF00866198](https://doi.org/10.1007/BF00866198).
- 5035 Liang, C. K., A. Eldering, A. Gettelman, B. Tian, S. Wong, E. J. Fetzer and K. N.
5036 Liou (2011). *Record of tropical interannual variability of temperature and wa-*
5037 *ter vapor from a combined AIRS-MLS data set.* J. Geophys. Res., 116(D16).
5038 doi:[10.1029/2010JD014841](https://doi.org/10.1029/2010JD014841).
- 5039 Long, D., X. Chen, B. R. Scanlon, Y. Wada, Y. Hong, V. P. Singh, Y. Chen, C. Wang,
5040 Z. Han and W. Yang (2016). *Have GRACE satellites overestimated groundwater*
5041 *depletion in the Northwest India Aquifer?* Sci. Rep., 6:1–10. doi:[10.1038/srep24398](https://doi.org/10.1038/srep24398).

- 5042 Longuevergne, L., B. R. Scanlon and C. R. Wilson (2010). *GRACE Hydrological esti-*
5043 *mates for small basins: Evaluating processing approaches on the High Plains Aquifer,*
5044 *USA.* Water Resour. Res., 46(11). doi:[10.1029/2009WR008564](https://doi.org/10.1029/2009WR008564).
- 5045 Lorenz, D. J., E. T. DeWeaver, and D. J. Vimont (2010). *Evaporation Change and Global*
5046 *Warming: The Role of Net Radiation and Relative Humidity.* J. Geophys. Res., 115
5047 (D20). doi:[10.1029/2010JD013949](https://doi.org/10.1029/2010JD013949).
- 5048 Lott, F. C., P. A. Stott, D. M. Mitchell, N. Christidis, N. P. Gillett, L. Haimberger,
5049 J. Perlwitz and P. W. Thorne (2013). *Models versus radiosondes in the free atmo-*
5050 *sphere: A new detection and attribution analysis of temperature.* J. Geophys. Res.,
5051 118(1–11). doi:[10.1002/jgrd.50255](https://doi.org/10.1002/jgrd.50255).
- 5052 Lucas-Picher, P., J. H. Christensen, F. Saeed, P. Kumar, S. Asharaf, B. Ahrens, A. J.
5053 Wiltshire, D. Jacob and S. Hagemann (2011). *Can Regional Climate Models Represent*
5054 *the Indian Monsoon?* J. Hydrometeor., 117(5):849–868. doi:[10.1175/2011JHM1327.1](https://doi.org/10.1175/2011JHM1327.1).
- 5055 Mann, H. B. (1945). *Nonparametric Tests Against Trend.* Econometrica, 13(3):245–259.
- 5056 Maraun, D., F. Wetterhall, A. M. Ireson, R. E. Chandler, E. J. Kendon, M. Widmann,
5057 S. Brienen, H. W. Rust, T. Sauter, M. Themeßl, V. K. C. Venema, K. P. Chun, C. M.
5058 Goodess, R. G. Jones, C. Onof, M. Vrac and I. Thiele-Eich (2010). *Precipitation*
5059 *downscaling under climate change: Recent developments to bridge the gap between dy-*
5060 *namical models and the end user.* Rev. Geophys., 48(3). doi:[10.1029/2009RG000314](https://doi.org/10.1029/2009RG000314).
- 5061 Masood, M., P. J.-F. Yeh, N. Hanasaki and K. Takeuchi (2015). *Model study of the*
5062 *impacts of future climate change on the hydrology of Ganges-Brahmaputra-Meghna*
5063 *basin.* Hydrol. Earth Syst. Sci, 19:747–770. doi:[10.5194/hess-19-747-2015](https://doi.org/10.5194/hess-19-747-2015).
- 5064 Mathison, C., A. Wiltshire, A. P. Dimri, P. Falloon, D. Jacob, P. Kumar, E. Moors,
5065 J. Ridley, C. Siderius, M. Stoffel and T. Yasunari (2013). *Regional projections of*
5066 *North Indian climate for adaptation studies.* Sci. Total Environ., 468-469:S4–S17.
5067 doi:[10.1016/j.scitotenv.2012.04.066](https://doi.org/10.1016/j.scitotenv.2012.04.066).
- 5068 Matsuo, K., and K. Heki (2010). *Time-variable ice loss in Asian high mountains from*
5069 *satellite gravimetry.* Nat. Geosci., 290:30–36. doi:[10.1016/j.epsl.2009.11.053](https://doi.org/10.1016/j.epsl.2009.11.053).
- 5070 McKee, T.B., N. J. Doesken and J. Kliest (1993). *The relationship of drought frequency*
5071 *and duration to time scales.* In: *Proceedings of the 8th Conference of Applied Cli-*
5072 *matology, 17-22 January, Anaheim, CA,* 194–184. American Meteorological Society,
5073 Boston, MA.
- 5074 McSweeney, C. F., R. G. Jones and B. B. Booth (2012). *Selecting Ensemble Mem-*
5075 *bers to Provide Regional Climate Change Information.* J. Clim., 25(20):7100–7121.
5076 doi:[10.1175/JCLI-D-11-00526.1](https://doi.org/10.1175/JCLI-D-11-00526.1).
- 5077 McSweeney, C. F., R. G. Jones, R. W. Lee and D. P. Rowell (2015). *Selecting*
5078 *CMIP5 GCMs for downscaling over multiple regions.* Clim. Dyan., 44(11):3237–3260.
5079 doi:[10.1007/s00382-014-2418-8](https://doi.org/10.1007/s00382-014-2418-8).

- 5080 Meehl, A., C. Covey, K. E. Taylor, T. Delworth, R. J. Stouffer, M. Latif, B. McAvaney and J. F. B. Mitchell (2007). *THE WCRP CMIP3 Multimodel Dataset: A New Era in Climate Change Research*. Bull. Am. Meteorol. Soc., 88:1383–1394. doi:[10.1175/BAMS-88-9-1383](https://doi.org/10.1175/BAMS-88-9-1383).
- 5084 Meehl, G. A., H. Teng and G. Branstator (2006). *Future changes of El Niño in two global coupled climate models*. Clim. Dyn., 26(6):549–566. doi:[10.1007/s00382-005-0098-0](https://doi.org/10.1007/s00382-005-0098-0).
- 5086 Mehta, S. K., M. V. Ratnam and B. V. K. Murthy (2010). *Variability of the tropical tropopause over Indian monsoon region*. J. Geophys. Res., 115(D14). doi:[10.1029/2009JD012655](https://doi.org/10.1029/2009JD012655).
- 5089 Melbourne, W. G., E. S. Davis, C. B. Duncan, G. A. Hajj, K. R. Hardy, E. R. Kursinski, T. K. Meehan, L. E. Young and T. P. Yunck (1994). *The application of spaceborne GPS to atmospheric limb sounding and global change monitoring*. Technical Report, Jet Propulsion Laboratory, California Institute of Technology, Pasadena, CA, United States.
- 5094 Mendoza, P. A., M. P. Clark, N. Mizukami, A. J. Newman, M. Barlage, E. D. Gutmann, R. M. Rasmussen, B. Rajagopalan, L. D. Brekke and J. R. Arnold (2015). *Effects of Hydrologic Model Choice and Calibration on the Portrayal of Climate Change Impacts*. J. Hydrometeorol., 16:762–780. doi:[10.1175/JHM-D-14-0104.1](https://doi.org/10.1175/JHM-D-14-0104.1).
- 5098 Menon, A., A. Levermann, J. Schewe, J. Lehmann and K. Frieler (2013). *Consistent increase in Indian monsoon rainfall and its variability across CMIP5 models*. Earth Syst. Dynam., 4:287–300. doi:[10.5194/esd-4-287-2013](https://doi.org/10.5194/esd-4-287-2013).
- 5101 Mirza, M. M. Q., R.A. Warrick, N.J. Ericksen and G.J. Kenny (1998). *Trends and persistence in precipitation in the Ganges, Brahmaputra and Meghna river basins*. Hydrol. Sci. J., 43(6):845–858. doi:[10.1080/02626669809492182](https://doi.org/10.1080/02626669809492182).
- 5104 Mirza, M. M. Q., R. A. Warric and N. J. Ericksen (2003). *The implications of climate change on floods of the Ganges, Brahmaputra and Meghna rivers in Bangladesh*. Clim. Chang., 57:287–318. doi:[10.1023/A:1022825915791](https://doi.org/10.1023/A:1022825915791).
- 5107 Mishra, A., and S. C. Liu (2014). *Changes in precipitation pattern and risk of drought over India in the context of global warming*. J. Geophys. Res., 119(13):7833–7841. doi:[10.1002/2014JD021471](https://doi.org/10.1002/2014JD021471).
- 5110 Mishra, V., R. Shah and B. Thrasher (2014). *Soil Moisture Droughts under the Retrospective and Projected Climate in India*. J. Hydrometeorol., 15:2267–2292. doi:[10.1175/JHM-D-13-0177.1](https://doi.org/10.1175/JHM-D-13-0177.1).
- 5113 Misra, V., P. Pantina, S. C. Chan and S. DiNapoli (2012). *A comparative study of the Indian summer monsoon hydroclimate and its variations in three reanalyses*. Clim. Dyn., 39(5):1149–1168. doi:[10.1007/s00382-012-1319-y](https://doi.org/10.1007/s00382-012-1319-y).
- 5116 Mittal, N., A. Mishra, R. Singh and P. Kumar (2014). *Assessing future changes in seasonal climatic extremes in the Ganges river basin using an ensemble of regional climate models*. Clim. Chang., 123:273–286. doi:[10.1007/s10584-014-1056-9](https://doi.org/10.1007/s10584-014-1056-9).

- 5119 Moss, R. H., J. A. Edmonds, K. A. Hibbard, M. R. Manning, S. K. Rose, D. P. van
5120 Vuuren, T. R. Carter, S. Emori, M. Kainuma, T. Kram, G. A. Meehl, J. F. B. Mitchell,
5121 N. Nakicenovic, K. Riahi, S. J. Smith, R. J. Stouffer, A. M. Thomson, J. P. Weyant
5122 and T. J. Wilbanks (2010). *The next generation of scenarios for climate change*
5123 *research and assessment*. Nature, 463:747–756. doi:[10.1038/nature08823](https://doi.org/10.1038/nature08823).
- 5124 Mukherjee, A., D. Saha, C. F. Harvey, R. G. Taylor, K. M. Ahmed and S. N. Bhanja
5125 (2015). *Groundwater systems of the Indian Sub-Continent*. J. Hydrol., 4:1–14.
5126 doi:[10.1016/j.ejrh.2015.03.005](https://doi.org/10.1016/j.ejrh.2015.03.005).
- 5127 Müller Schmied, H., S. Eisner, D. Franz, M. Wattenbach, F.T. Portmann, M. Flörke
5128 and P. Döll (2014). *Sensitivity of simulated global-scale freshwater fluxes and storages*
5129 *to input data, hydrological model structure, human water use and calibration*. Hydrol.
5130 Earth. Syst. Sci., 18:3511–3538. doi:[10.5194/hess-18-3511-2014](https://doi.org/10.5194/hess-18-3511-2014).
- 5131 Murphy, J. M., B. B. Booth, M. Collins, G. R. Harris, D. M. H. Sexton and M. J.
5132 Webb (2007). *A Methodology for Probabilistic Predictions of Regional Climate Change*
5133 *from Perturbed Physics Ensembles*. Phil. Trans. R. Soc. A, 365(1857):1993–2028.
5134 doi:[10.1098/rsta.2007.2077](https://doi.org/10.1098/rsta.2007.2077).
- 5135 Nayak, S., M. Mandal and S. Maity (2015). *Customization of regional climate model*
5136 *(RegCM4) over Indian region*. Theor. Appl. Climatol., 1–6. doi:[10.1007/s00704-015-](https://doi.org/10.1007/s00704-015-1630-8)
5137 [1630-8](https://doi.org/10.1007/s00704-015-1630-8).
- 5138 NEC (2011). *Second National Communications to the UNFCCC*. Technical Report,
5139 National Environment Commission, Royal Government of Bhutan, Thimphu, Bhutan.
- 5140 Njoku, E.G., T. J. Jackson, V. Lakshmi, T. K. Chan and S. V. Nghiem (2003).
5141 *Soil moisture retrieval from AMSR-E*. IEEE Trans. Geosci. Remote Sens., 41(2).
5142 doi:[10.1109/TGRS.2002.808243](https://doi.org/10.1109/TGRS.2002.808243).
- 5143 Oleson, K. W., D.M. Lawrence, G.B. Bonan, B. Drewniak, M. Huang, C.D. Koven,
5144 S. Levis, F. Li, W.J. Riley, Z.M. Subin, S.C. Swenson, P.E. Thornton, A. Bozbiyik,
5145 R. Fisher, E. Kluzek, J.-F. Lamarque, P.J. Lawrence, L.R. Leung, W. Lipscomb,
5146 S. Muszala, D.M. Ricciuto, W. Sacks, J. Tang Y. Sun and Z.-L. Yang (2013). *Technical*
5147 *Description of version 4.5 of the Community Land Model (CLM)*. NCAR, National
5148 Center for Atmospheric Research, Boulder, CO, 422 pp, 2013.
- 5149 Onogi, K., H. Koide, M. Sakamoto, S. Kobayashi, J. Tsutsui, H. Hatsushika, T. Mat-
5150 sumoto, N. Yamazaki, H. Kamahori, K. Takahashi, K. Kato, T. Ose, S. Kadokura
5151 and K. Wada (2005). *JRA-2: Japanese 25-year Reanalysis*. Quart. J. R. Meteorol.
5152 Soc., 131(613):3259–3268. doi:[10.1256/qj.05.88](https://doi.org/10.1256/qj.05.88).
- 5153 Onogi, K., J. Tsutsui, H. Koide, M. Sakamoto, S. Kobayashi, H. Hatsushika, T. Mat-
5154 sumoto, N. Yamazaki, H. Kamahori, K. Takahashi, S. Kadokura, K. Wada, K. Kato,
5155 R. Oyama, T. Ose, N. Mannoji and R. Taira (2007). *The JRA-25 Reanalysis*. Quart.
5156 J. R. Meteorol. Soc., 85(3):369–432. doi:[10.2151/jmsj.85.369](https://doi.org/10.2151/jmsj.85.369).
- 5157 Pal, J. S. (2007). *Regional climate modeling for the developing world: The ICTP RegCM3*
5158 *and RegCNET*. Mon. Weather Rev., 88:1395–1409. doi:[10.1175/bams-88-9-1395](https://doi.org/10.1175/bams-88-9-1395).

- 5159 Pal, J. S., E. Small and E. Eltahir (2000). *Simulation of regional-scale water and energy*
5160 *budgets: representation of subgrid cloud and precipitation processes within RegCM.*
5161 *Geophys. Res. Lett.*, 105:29579–29594.
- 5162 Palmer, W. C. (1965). *Meteorological Drought.* NCAR Technical Report, Department
5163 of Commerce, Washington, D.C., USA.
- 5164 Pan, L. L., W. J. Randel, B. L. Gary, M. J. Mahoney and E. J. Hintsala (2004). *Definitions*
5165 *and sharpness of the extratropical tropopause: A trace gas perspective.* *Rev. Geophys.*,
5166 109(D23). doi:[10.1029/2004JD004982](https://doi.org/10.1029/2004JD004982).
- 5167 Papa, F., F. Frappart, Y. Malbeteau, M. Shamsudduha, V. Vuruputur, M. Sekhar,
5168 G. Ramillien, C. Prigent, F. Aires, R. K. Pandey, S. Bala and S. Calmant (2015).
5169 *Satellite-derived surface and sub-surface water storage in the Ganges–Brahmaputra*
5170 *River Basin.* *J. Hydrol.*, 4:15–35. doi:[10.1016/j.ejrh.2015.03.004](https://doi.org/10.1016/j.ejrh.2015.03.004).
- 5171 Peña-Arancibia, J. L., A. I. J. M. van Dijk, L. J. Renzullo and M. Mulligan (2013). *Eval-*
5172 *uation of Precipitation Estimation Accuracy in Reanalyses, Satellite Products, and an*
5173 *Ensemble Method for Regions in Australia and South and East Asia.* *J. Hydrometeor.*,
5174 4(14):1323–1333. doi:[10.1175/JHM-D-12-0132.1](https://doi.org/10.1175/JHM-D-12-0132.1).
- 5175 Pervez, M. S., and G. M. Henebry (2015). *Spatial and seasonal responses of precipitation*
5176 *in the Ganges and Brahmaputra river basins to ENSO and Indian Ocean dipole modes:*
5177 *Implications for flooding and drought.* *Nat. Hazards Earth Syst. Sci.*, 15:147–162.
5178 doi:[10.5194/nhess-15-147-2015](https://doi.org/10.5194/nhess-15-147-2015).
- 5179 Piani, C., J. O. Haerter and E. Coppola (2010). *Statistical bias correction for daily*
5180 *precipitation in regional climate models over Europe.* *Theor. Appl. Climatol.*, 99(1-2):
5181 187–192. doi:[10.1007/s00704-009-0134-9](https://doi.org/10.1007/s00704-009-0134-9).
- 5182 Poli, P., S. B. Healy, F. Rabier and J. Pailleux (2008). *Preliminary assessment of the*
5183 *scalability of GPS radio occultations impact in numerical weather prediction.* *Geophys.*
5184 *Res. Lett.*, 35(23). doi:[10.1029/2008GL035873](https://doi.org/10.1029/2008GL035873).
- 5185 Poli, P., S. B. Healy and D. P. Dee (2010). *Assimilation of Global Positioning System*
5186 *radio occultation data in the ECMWF ERA-Interim reanalysis.* *Q. J. R. Meteorolog.*
5187 *Soc.*, 136(653). doi:[10.1002/qj.722](https://doi.org/10.1002/qj.722).
- 5188 Prakash, S., V. Sathiyamoorthy, C. Mahesh and R. M. Gairola (2014). *An evaluation*
5189 *of high-resolution multisatellite rainfall products over the Indian monsoon region.* *Int.*
5190 *J. Remote Sens.*, 35(9):3018–3035. doi:[10.1080/01431161.2014.894661](https://doi.org/10.1080/01431161.2014.894661).
- 5191 Prakash, S., A. K. Mitra, I. M. Momin, E. N. Rajagopal, S. Basu, Mat Collins, A. G.
5192 Turner, K. A. Rao and K. Ashok (2015). *Seasonal intercomparison of observational*
5193 *rainfall datasets over India during the southwest monsoon season.* *Int. J. Remote*
5194 *Sens.*, 35(9):2326–2338. doi:[10.1002/joc.4129](https://doi.org/10.1002/joc.4129).
- 5195 Prasad, V. S., and T. Hayashi (2005). *Onset and withdrawal of Indian summer monsoon.*
5196 *Geophys. Res. Lett.*, 32(20). doi:[10.1029/2005GL023269](https://doi.org/10.1029/2005GL023269).

- 5197 Prasai, S., and M. D. Surie (2015). *Water and Climate Data in the Ganges Basin:*
5198 *Assessing Access to Information Regimes and Implications for Cooperation on Trans-*
5199 *boundary Rivers.* Water Alternatives, 8:20–35.
- 5200 Preisendorfer, R. W. (1988). *Principal component analysis in meteorology and oceanog-*
5201 *raphy.* Elsevier. ISBN 0444430148.
- 5202 PSAS (2004). *A Quick Derivation relating altitude to air pressure.* Portland State
5203 Aerospace Society, US, [http://psas.pdx.edu/RocketScience/PressureAltitude_](http://psas.pdx.edu/RocketScience/PressureAltitude_Derived.pdf)
5204 [Derived.pdf](http://psas.pdx.edu/RocketScience/PressureAltitude_Derived.pdf), 2004.
- 5205 Radić, V., and R. Hock (2010). *Regional and global volumes of glaciers derived*
5206 *from statistical upscaling of glacier inventory data.* J. Geophys. Res., 115(F1).
5207 doi:[10.1029/2009JF001373](https://doi.org/10.1029/2009JF001373).
- 5208 Rahman, M. M., M. N. Islam, A. U. Ahmed and F. Georgi (2012). *Rainfall and temper-*
5209 *ature scenarios for Bangladesh for the middle of 21st century using RegCM.* J. Earth
5210 Syst. Sci., 121:287–295. doi:[10.1007/s12040-012-0159-9](https://doi.org/10.1007/s12040-012-0159-9).
- 5211 Rajeevan, M., and J. Bhate (2009). *A high resolution daily gridded rainfall dataset*
5212 *(1971-2005) for mesoscale meteorological studies.* Curr. Sci., 96:558–562.
- 5213 Rajeevan, M., J. Bhate and A. K. Jaswal (2008). *Analysis of variability and trends*
5214 *of extreme rainfall events over India using 104 years of gridded daily rainfall data.*
5215 Geophys. Res. Lett., 35(18). doi:[10.1029/2008GL035143](https://doi.org/10.1029/2008GL035143).
- 5216 Rajendran, K., and A. Kitoh (2008). *Indian summer monsoon in future climate projec-*
5217 *tion by a super high-resolution global model.* Curr. Sci., 95:1560–1569.
- 5218 Raju, P. V. S., R. Bhatla, M. Almazroui and M. Assiri (2015). *Performance of convection*
5219 *schemes on the simulation of summer monsoon features over the South Asia CORDEX*
5220 *domain using RegCM-4.3.* Int. J. Climatol., 35(15):4695–4706. doi:[10.1002/joc.4317](https://doi.org/10.1002/joc.4317).
- 5221 Ramanathan, V., C. Chung, D. Kim, T. Bettge, L. Buja, J. T. Kiehl, W. M. Washington,
5222 Q. Fu, D. R. Sikka, and M. Wild (2005). *Atmospheric brown clouds: Impacts on*
5223 *South Asian climate and hydrological cycle.* Proc. Natl. Acad. Sci., 102(15):5326–
5224 5333. doi:[10.1073/pnas.0500656102](https://doi.org/10.1073/pnas.0500656102).
- 5225 Ramesh, K. V., and P. Goswami (2014). *Assessing reliability of regional climate projec-*
5226 *tions: the case of Indian monsoon.* Sci. Rep., 4(1071). doi:[10.1038/srep04071](https://doi.org/10.1038/srep04071).
- 5227 Randall, D. A., R.A. Wood, S. Bony, R. Colman, T. Fichefet, J. Fyfe, V. Kattsov,
5228 A. Pitman, J. Shukla, J. Srinivasan, R.J. Stouffer, A. Sumi and K.E. Taylor (2007).
5229 *Climate Models and Their Evaluation.* In: Solomon, S., D. Qin, M. Manning, Z. Chen,
5230 M. Marquis, K.B. Averyt, M. Tignor and H.L. Miller (Hrsg.), *Climate Change 2007:*
5231 *The Physical Science Basis. Contribution of Working Group I to the Fourth Assess-*
5232 *ment Report of the Intergovernmental Panel on Climate Change.* Cambridge Univer-
- 5233 sity Press, Cambridge, United Kingdom and New York, USA.

- 5234 Randel, W. J., F. Wu and D. J. Gaffen (2000). *Interannual variability of the tropical*
5235 *tropopause derived from radiosonde data and NCEP reanalyses*. J. Geophys. Res., 105
5236 (D12):15509–15523. doi:[10.1029/2000JD900155](https://doi.org/10.1029/2000JD900155).
- 5237 Rao, V. B., C. C. Ferreira, S. H. Franchito and S. S. V. S. Ramakrishna (2008). *In a*
5238 *changing climate weakening tropical easterly jet induces more violent tropical storms*
5239 *over the north Indian Ocean*. Geophys. Res. Lett., 35(15). doi:[10.1029/2008GL034729](https://doi.org/10.1029/2008GL034729).
- 5240 Rao, Y. P. (1976). *Onset and withdrawal of the monsoon*. In: *South west monsoon,*
5241 *Meteorological Monographs, Synoptic Meteorology, No. 1/1976*, chapter 3, 379. Indian
5242 Meteorological Department, Delhi, India.
- 5243 Rayner, N. A., D. E. Parker, E. B. Horton, C. K. Folland, L. V. Alexander, D. P. Rowell,
5244 E. C. Kent and A. Kaplan (2003). *Global reanalyses of sea surface temperature, sea*
5245 *ice, and night marine air temperature since the late nineteenth century*. J. Geophys.
5246 Res., 108(D14). doi:[10.1029/2002JD002670](https://doi.org/10.1029/2002JD002670).
- 5247 Reid, G. C., and K. S. Gage (1985). *Interannual variations in the height of the tropical*
5248 *tropopause*. J. Geophys. Res., 90:5629–5635. doi:[10.1029/JD090iD03p05629](https://doi.org/10.1029/JD090iD03p05629).
- 5249 Resmi, E.A., K. Mohanakumar and K.S. Appu (2013). *Effect of polar sudden*
5250 *stratospheric warming on the tropical stratosphere and troposphere and its sur-*
5251 *face signatures over the Indian region*. J. Atmos. Sol.-Terr. Phys., 105–106:15–29.
5252 doi:[10.1016/j.jastp.2013.07.003](https://doi.org/10.1016/j.jastp.2013.07.003).
- 5253 Richey, A.S., B.F. Thomas, M.H. Lo, J. T. Reager, J. S. Famiglietti, K. Voss, S. Swenson
5254 and M. Rodell (2015). *Quantifying renewable groundwater stress with GRACE*. Water
5255 Resour. Res., 51:1–20. doi:[10.1002/2015WR017349](https://doi.org/10.1002/2015WR017349).
- 5256 Rienecker, M. M., M. J. Suarez, R. Todling, J. Bacmeister, L. Takacs, H. C. Liu, W. Gu,
5257 M. Sienkiewicz, R. D. Koster, R. Gelaro, I. Stajner and J. E. Nielsen (2008). *The*
5258 *GEOS-5 Data Assimilation System-Documentation of versions 5.0.1, 5.1.0, and 5.2.0*.
5259 NASA Technical Report Series on Global Modeling and Data Assimilation, NASA
5260 Center for AeroSpace Information, Maryland, USA.
- 5261 Rienecker, M. M., M. J. Suarez, R. Gelaro, R. Todling, J. Bacmeister, E. Liu, M. G.
5262 Bosilovich, S. D. Schubert, L. Takacs, G. K. Kim, S. Bloom, J. Chen, D. Collins,
5263 A. Conaty, A. da Silva, W. Gu, J. Joiner, R. D. Koster, R. Lucchesi, A. Molod,
5264 T. Owens, S. Pawson, P. Pegion, C. R. Redder, R. Reichle, F. R. Robertson, A. G.
5265 Ruddick, M. Sienkiewicz and J. Woollen (2011). *MERRA: NASA's Modern-Era*
5266 *Retrospective Analysis for Research and Applications*. J. Clim., 24(14):3624–3648.
5267 doi:[10.1175/JCLI-D-11-00015.1](https://doi.org/10.1175/JCLI-D-11-00015.1).
- 5268 Robock, A., K. Y. Vinnikov, G. Srinivasan, J. K. Entin, S. E. Hollinger,
5269 N. A. Speranskaya, S. Liu and A. Namkhai (2000). *The Global Soil Mois-*
5270 *ture Data Bank*. Bull. Am. Meteorol. Soc., 81:1281–1299. doi:[10.1175/1520-0477\(2000\)081<1281:TGSMDB>2.3.CO;2](https://doi.org/10.1175/1520-0477(2000)081<1281:TGSMDB>2.3.CO;2).
- 5272 Rockel, B. (2015). *The Regional Downscaling Approach: a Brief History and Recent*
5273 *Advances*. Curr. Clim. Change. Rep., 1:22–29. doi:[10.1007/s40641-014-0001-3](https://doi.org/10.1007/s40641-014-0001-3).

- 5274 Rocken, C., R. Anthes, M. Exner, D. Hunt, S. Sokolovskiy, R. Ware, M. Gorbunov,
5275 W. Schreiner, D. Feng, B. Herman, Y.-H. Kuo and X. Zou (1997). *Analysis and*
5276 *validation of GPS/MET data in the neutral atmosphere*. J. Geophys. Res., 102(D25):
5277 29849–29866. doi:[10.1029/97JD02400](https://doi.org/10.1029/97JD02400).
- 5278 Rodell, M., and J. S. Famiglietti (2001). *An analysis of terrestrial water storage vari-*
5279 *ations in Illinois with implications for the Gravity Recovery and Climate Experiment*
5280 *(GRACE)*. Water Resour. Res., 37(5):1327–1339. doi:[10.1029/2000WR900306](https://doi.org/10.1029/2000WR900306).
- 5281 Rodell, M., P. R. Houser and U. Jambor, J. Gottschalck, K. Mitchell, C-J. Meng,
5282 K. Arsenault, B. Cosgrove, J. Radakovich, M. Bosilovich, J. K. Entin, J. P. Walker,
5283 D. Lohmann and D. Toll (2004). *The Global Land Data Assimilation System*. Bull.
5284 Am. Meteorol. Soc., 85:381–394. doi:[10.1175/BAMS-85-3-381](https://doi.org/10.1175/BAMS-85-3-381).
- 5285 Rodell, M., I. Velicogna and J. S. Famiglietti (2009). *Satellite-based estimates*
5286 *of groundwater depletion in India*. Hydrol. Earth Syst. Sci., 460:999–1002.
5287 doi:[10.1038/nature08238](https://doi.org/10.1038/nature08238).
- 5288 Roxy, M. K., K. Ritika, P. Terray and S. Masson (2014). *The Curious Case of Indian*
5289 *Ocean Warming*. J. Clim., 27:8501–8509. doi:[10.1175/JCLI-D-14-00471.1](https://doi.org/10.1175/JCLI-D-14-00471.1).
- 5290 Roy, S. S., and R. C. Balling (2004). *Trends in extreme daily precipitation indices in*
5291 *India*. Int. J. Climatol., 24(4):457–466. doi:[10.1002/joc.995](https://doi.org/10.1002/joc.995).
- 5292 Rummukainen, M. (2009). *State-of-the-art with regional climate models*. WIREs Clim.
5293 Change, 1:82–96. doi:[10.1002/wcc.8](https://doi.org/10.1002/wcc.8).
- 5294 Rummukainen, M., B. Rockel, L. Bärring, J. H. Christensen and M. Reckermann (2015).
5295 *Twenty-First-Century Challenges in Regional Climate Modeling*. Bull. Amer. Meteor.
5296 Soc., 96:ES135–ES138. doi:[10.1175/BAMS-D-14-00214.1](https://doi.org/10.1175/BAMS-D-14-00214.1).
- 5297 Saeed, F., S. Hagemann and D. Jacob (2009). *Impact of irrigation on the South Asian*
5298 *summer monsoon*. Geophys. Res. Lett., 36(20). doi:[10.1029/2009GL040625](https://doi.org/10.1029/2009GL040625).
- 5299 Saha, A., S. Ghosh, A. S. Sahana and E. P. Rao (2014). *Failure of CMIP5 climate*
5300 *models in simulating post-1950 decreasing trend of Indian monsoon*. Geophys. Res.
5301 Lett., 40(20):7323–7330. doi:[10.1002/2014GL061573](https://doi.org/10.1002/2014GL061573).
- 5302 Saha, S., S. Moorthi, H.-L. Pan, X. Wu, J. Wang, S. Nadiga, P. Tripp, R. Kistler,
5303 J. Woollen, D. Behringer, H. Liu, D. Stokes, R. Grumbine, G. Gayno, J. Wang, Y. T.
5304 Hou, H. Y. Chuang, H.-M. H. Juang, J. Sela, M. Iredell, R. Treadon, D. Kleist, P. V.
5305 Delst, D. Keyser, J. Derber, M. Ek, J. Meng, H. Wei, R. Yang, S. Lord, H. V. D.
5306 Dool, A. Kumar, W. Wang, C. Long, M. Chelliah, Y. Xue, B. Huang, J.-K. Schemm,
5307 W. Ebisuzaki, R. Lin, P. Xie, M. Chen, S. Zhou, W. Higgins, C.-Z. Zou, Q. Liu,
5308 Y. Chen, Y. Han, L. Cucurull, R. W. Reynolds, G. Rutledge and M. Goldberg (2010).
5309 *The NCEP Climate Forecast System Reanalysis*. Bull. Am. Meteorol. Soc., 91(8):
5310 1015–1057. doi:[10.1175/2010BAMS3001.1](https://doi.org/10.1175/2010BAMS3001.1).
- 5311 Saji, N. H., B. N. Goswami, P. N. Vinayachandran and T. Yamagata (1999). *A dipole*
5312 *mode in the tropical Indian Ocean*. Nature, 401:360–363.

- 5313 Salvi, K. Shashikanth K., S. Ghosh and K. Rajendran (2014). *Do CMIP5 simulations*
5314 *of Indian summer monsoon rainfall differ from those of CMIP3*. *Atmos. Sci. Lett.*,
5315 15(2):79–85. doi:[10.1002/asl2.466](https://doi.org/10.1002/asl2.466).
- 5316 Santer, B. D., M. F. Wehner, T. M. L. Wigley, R., G. A. Meehl, K. E. Taylor, C. Am-
5317 mann, J. Arblaster, W. M. Washington, J. S. Boyle and W. Brüggemann (2003a).
5318 *Contributions of Anthropogenic and Natural Forcing to Recent Tropopause Height*
5319 *Changes*. *Curr. Sci.*, 301(5632):479–483. doi:[10.1126/science.1084123](https://doi.org/10.1126/science.1084123).
- 5320 Santer, B. D., Sausen, T. M. L. Wigley, J. S. Boyle, K. AchutaRao and C. Doutriaux, J. E.
5321 Hansen, G. A. Meehl, E. Roeckner, R. Ruedy, G. Schmidt and K. E. Taylor (2003b).
5322 *Behavior of tropopause height and atmospheric temperature in models, reanalyses,*
5323 *and observations: Decadal changes*. *J. Geophys. Res.*, 108(D1):4ACL 1–1–ACL 1–22.
5324 doi:[10.1029/2002JD00225](https://doi.org/10.1029/2002JD00225).
- 5325 Santer, B. D., P. W. Thorne, L. Haimberger, K. E. Taylor, T. M. L. Wigley, J. R.
5326 Lanzante, S. Solomon, M. Free, P. J. Gleckler, P. D. Jones, T. R. Karl, S. A. Klein,
5327 C. Mears, D. Nychka, G. A. Schmidt, S. C. Sherwood and F. J. Wentz (2008). *Con-*
5328 *sistency of modelled and observed temperature trends in the tropical troposphere*. *Int.*
5329 *J. Climatol.*, 13:1703–1722. doi:[10.1002/joc.1756](https://doi.org/10.1002/joc.1756).
- 5330 Sarthi, P. P., P. Kumar and S. Ghosh (2015). *Possible future rainfall over Gangetic*
5331 *Plains (GP), India, in multi-model simulations of CMIP3 and CMIP5*. *Theor. Appl.*
5332 *Climatol.* doi:[10.1007/s00704-015-1447-5](https://doi.org/10.1007/s00704-015-1447-5).
- 5333 Sausen, R., and B. D. Santer (2003). *Use of changes in tropopause height to detect human*
5334 *influences on climate*. *Meteorologische Zeitschrift*, 3(12):131–136. doi:[10.1127/0941-](https://doi.org/10.1127/0941-2948/2003/0012-0131)
5335 [2948/2003/0012-0131](https://doi.org/10.1127/0941-2948/2003/0012-0131).
- 5336 Scherler, D., B. Bookhagen and M. R. Strecker (2011). *Spatially variable response of*
5337 *Himalayan glaciers to climate change affected by debris cover*. *Nat. Geosci.*, 4:156–159.
5338 doi:[10.1038/ngeo1068](https://doi.org/10.1038/ngeo1068).
- 5339 Schmidt, T., J. Wickert, G. Beyerle and S. Heise (2008). *Global tropopause height*
5340 *trends estimated from GPS radio occultation data*. *Geophys. Res. Lett.*, 35(11).
5341 doi:[10.1029/2008GL034012](https://doi.org/10.1029/2008GL034012).
- 5342 Schmidt, T., J. Wickert and A. Haser (2010). *Variability of the upper troposphere and*
5343 *lower stratosphere observed with GPS radio occultation bending angles and tempera-*
5344 *tures*. *Adv. Space Res.*, 46(2):150–161. doi:[10.1016/j.asr.2010.01.021](https://doi.org/10.1016/j.asr.2010.01.021).
- 5345 Schneider, T., P. A. O’Gorman and X. J. Levine (2010). *WATER VAPOR*
5346 *AND THE DYNAMICS OF CLIMATE CHANGES*. *Rev. Geophys.*, 48(3).
5347 doi:[10.1029/2009RG000302](https://doi.org/10.1029/2009RG000302).
- 5348 Schneider, U., A. Becker, P. Finger, A. M. Christoffer, M. Ziese and B. Rudolf (2014).
5349 *GPCC’s new land surface precipitation climatology based on quality-controlled in situ*
5350 *data and its role in quantifying the global water cycle*. *Theor. Appl. Climatol.*, 115
5351 (1–2):15–40. doi:[10.1007/s00704-013-0860-x](https://doi.org/10.1007/s00704-013-0860-x).

- 5352 Seidel, D. J., N. P. Gillett, J. R. Lanzante, K. P. Shine and P. W. Thorne (2011).
5353 *Stratospheric temperature trends: our evolving understanding*. WIREs Clim. Change,
5354 2:592–616. doi:10.1002/wcc.125.
- 5355 Sen, P. K. (1968). *Estimates of the Regression Coefficient Based on Kendall's Tau*. J.
5356 Am. Stat. Assoc., 63(324):1379–1389. doi:10.1080/01621459.1968.10480934.
- 5357 Seneviratne, S. I., T. Corti, E. L. Davin, M. Hirschi, E. B. Jaeger, I. Lehner, B. Orlowsky
5358 and A. J. Teuling (2010). *Investigating soil moisture-climate interactions in a chang-*
5359 *ing climate: A review*. Earth Sci. Rev., 99(3–4). doi:10.1016/j.earscirev.2010.02.004.
- 5360 Seneviratne, S. I., N. Nicholls, D. Easterling, C.M. Goodess, S. Kanae, J. Kossin, Y. Luo,
5361 J. Marengo, K. McInnes, M. Rahimi, M. Reichstein, A. Sorteberg, C. Vera and
5362 X. Zhang (2012). *Changes in Climate Extremes and their Impacts on the Natural*
5363 *Physical Environment*. In: Field, C.B., V. Barros, T.F. Stocker, D. Qin, D.J. Dokken,
5364 K.L. Ebi, M.D. Mastrandrea, K.J. Mach, G.-K. Plattner, S.K. Allen, M. Tignor and
5365 P.M. Midgley (Hrsg.), *Managing the Risks of Extreme Events and Disasters to Ad-*
5366 *vance Climate Change Adaptation*, 109–230. Cambridge University Press, Cambridge
5367 University Press, Cambridge, UK, and New York, NY, USA.
- 5368 Sengupta, A., and M. Rajeevan (2013). *Uncertainty quantification and reliability anal-*
5369 *ysis of CMIP5 projections for the Indian summer monsoon*. Curr. Sci., 105(12):
5370 1692–1703.
- 5371 Shah, R., and V. Mishra (2014). *Evaluation of the Reanalysis Products for the Monsoon*
5372 *Season Droughts in India*. J. Hydrometeor, 15(4):1575–1591. doi:10.1175/JHM-D-13-
5373 0103.1.
- 5374 Shahid, S. (2011). *Trends in extreme rainfall events of Bangladesh*. Theor. Appl. Cli-
5375 matol., 104(3–4):489–499. doi:10.1007/s00704-010-0363-y.
- 5376 Shahid, S., X.-J. Wang, M. M. Rahman, R. Hasan, S. B. Harun and S. Shamsudin (2015).
5377 *Spatial Assessment of Groundwater Over-Exploitation in Northwestern Districts of*
5378 *Bangladesh*. J. Geol. Soc. India, 85(4). Available at [http://www.geosocindia.org/](http://www.geosocindia.org/index.php/jgsi/article/view/62912)
5379 [index.php/jgsi/article/view/62912](http://www.geosocindia.org/index.php/jgsi/article/view/62912). Accessed 03 Dec 2015.
- 5380 Shamsudduha, M. (2013). *Groundwater resilience to human development and cli-*
5381 *mate change in South Asia*. Groundwater Forum. Available at: [http://www.](http://www.globalwaterforum.org/2013/08/19)
5382 [globalwaterforum.org/2013/08/19](http://www.globalwaterforum.org/2013/08/19). Accessed 19 December 2015.
- 5383 Shamsudduha, M., R. E. Chandler, R. G. Taylor and K. M. Ahmed (2009). *Re-*
5384 *cent trends in groundwater levels in a highly seasonal hydrological system: the*
5385 *Ganges-Brahmaputra-Meghna Delta*. Hydrol. Earth Syst. Sci., 13:2373–2385.
5386 doi:10.5194/hess-13-2373-2009.
- 5387 Shamsudduha, M., R. G. Taylor and R. E. Chandler (2009). *Monitoring groundwater*
5388 *storage changes in the highly seasonal humid tropics: Validation of GRACE measure-*
5389 *ments in the Bengal Basin*. Water Resour. Res., 48(2). doi:10.1029/2011WR010993.

- 5390 Sharmila, S., S. Joseph, A.K. Sahai, S. Abhilash and R. Chattopadhyay (2015). *Fu-*
5391 *ture projection of Indian summer monsoon variability under climate change sce-*
5392 *nario: An assessment from CMIP5 climate models.* Glob. Planet. Chang., 124:62–78.
5393 doi:[10.1016/j.gloplacha.2014.11.004](https://doi.org/10.1016/j.gloplacha.2014.11.004).
- 5394 Sherler, D., B. Bookhagen and M. R. Strecker (2011). *Spatially variable response of*
5395 *Himalayan glaciers to climate change affected by debris cover.* Nat. Geosci., 4:156–
5396 159. doi:[10.1038/ngeo1068](https://doi.org/10.1038/ngeo1068).
- 5397 Shrestha, D., P. Singh and K. Nakamura (2012). *Spatiotemporal variation of rainfall over*
5398 *the central Himalayan region revealed by TRMM Precipitation Radar.* J. Geophys.
5399 Res., 117(D22). doi:[10.1029/2012JD018140](https://doi.org/10.1029/2012JD018140).
- 5400 Shum, C. K., J. C. Ries and B. D. Tapley (1995). *The accuracy and applications of satel-*
5401 *lite altimetry.* Geophys. J. Int., 121:321–336. doi:[10.1111/j.1365-246X.1995.tb05714.x](https://doi.org/10.1111/j.1365-246X.1995.tb05714.x).
- 5402 Shum, C. K., J. Y. Guo, F. Hossain, J. Duan, D. E. Alsdorf, C. Y. Kuo X. J. Duan,
5403 H. Lee, M. Schmidt and L. Wang (2011). *Inter-annual Water Storage Changes in Asia*
5404 *from GRACE Data.* In: Lal, R., M. V. K. Sivakumar, S. M. A. Faiz, A. H. M. M.
5405 Rahman and K. R. Islam (Hrsg.), *Climate Change and Food Security in South Asia*,
5406 chapter 6, 69–83. Springer Netherlands. ISBN 978-90-481-9516-9.
- 5407 Siddique-E-Akbor, A. H. M., F. Hossain, S. Sikder, C. K. Shum, S. Tseng, Y. Yi, F. J.
5408 Turk and A. Limaye (2014). *Satellite Precipitation Data-Driven Hydrological Modeling*
5409 *for Water Resources Management in the Ganges, Brahmaputra, and Meghna Basins.*
5410 Earth Interact., 18:1–25. doi:[10.1175/EI-D-14-0017.1](https://doi.org/10.1175/EI-D-14-0017.1).
- 5411 Singh, Deepti, M. Tsiang, B. Rajaratnam and N. S. Diffenbaugh (2014). *Observed*
5412 *changes in extreme wet and dry spells during the South Asian summer monsoon sea-*
5413 *son.* Nat. Clim. Change, 4:456–461. doi:[10.1038/nclimate2208](https://doi.org/10.1038/nclimate2208).
- 5414 Singh, N., and A. Ranade (2010). *The Wet and Dry Spells across India during 1951–*
5415 *2007.* J. Hydrometeorol., 11(1):26–45. doi:[10.1175/2009JHM1161.1](https://doi.org/10.1175/2009JHM1161.1).
- 5416 Sinha, A., L. Stott, M. Berkelhammer, H. Cheng, R. L. Edwards, B. Buckley, M. Alden-
5417 derfer and M. Mudelsee (2011). *A global context for megadroughts in monsoon Asia*
5418 *during the past millennium.* Quat. Sci. Rev., 30:47–62. doi:[10.1175/JCLI3675.1](https://doi.org/10.1175/JCLI3675.1).
- 5419 Sinha, P., U. C. Mohanty, S. C. Kar, S. K. Dash and S. Kumari (2013). *Sensitivity of*
5420 *the GCM driven summer monsoon simulations to cumulus parameterization schemes*
5421 *in nested RegCM3.* Theor. Appl. Climatol., 112(1–2):285–306. doi:[10.1007/s00704-](https://doi.org/10.1007/s00704-012-0728-5)
5422 [012-0728-5](https://doi.org/10.1007/s00704-012-0728-5).
- 5423 Sinha, P., U. C. Mohanty, S. C. Kar and S. Kumari (2014). *Role of the Himalayan Oro-*
5424 *graphy in Simulation of the Indian Summer Monsoon using RegCM3.* Appl. Geophys.,
5425 171(7):1385–1407. doi:[10.1007/s00024-013-0675-9](https://doi.org/10.1007/s00024-013-0675-9).
- 5426 Skamarock, W. C., J. B. Klemp, J. Dudhia, D. O. Gill, D. M. Barker, W. Wang and
5427 J. G. Powers (2008). *A Description of the Advanced Research WRF Version 3.* NCAR
5428 Technical Note, Mesoscale and Microscale Meteorology Division, National Center for

- 5429 Atmospheric Research (NCAR), Boulder, Colorado, USA. Available at <http://www2.mmm.ucar.edu/wrf/users/docs/>. Accessed 02 Dec 2013.
- 5431 Smith, E. K., and S. Weintraub (1953). *The Constants in the Equation for Atmospheric*
5432 *Refractive Index at Radio Frequencies*. In: *Proceedings of the IRE*, Vol. 41, 1035–1037.
5433 IEEE. doi:[10.1109/JRPROC.1953.274297](https://doi.org/10.1109/JRPROC.1953.274297).
- 5434 Smith, R. N. B. (1990). *A scheme for predicting layer clouds and their water con-*
5435 *tent in a general circulation model*. Q. J. R. Meteorol. Soc., 116(492):435–460.
5436 doi:[10.1002/qj.49711649210](https://doi.org/10.1002/qj.49711649210).
- 5437 Sneed, M., J. Brandt and M. Solt (2013). *Land Subsidence along the Delta-Mendota*
5438 *Canal in the Northern Part of the San Joaquin Valley, California, 2003–10*. Ge-
5439 ological Survey Scientific Investigations Report, U.S. Department of the Interior,
5440 U.S. Geological Survey, U.S. Geological Survey, Reston, Virginia, USA. Available
5441 at <http://pubs.usgs.gov/sir/2013/5142/>. Accessed 13 June 2016.
- 5442 Snook, J. S., J. M. Cram and J. M. Schmidt (1995). *LAPS/RAMS. A nonhydrostatic*
5443 *mesoscale numerical modeling system configured for operational use*. Tellus A, 47(5):
5444 864–875. doi:[10.1034/j.1600-0870.1995.00125.x](https://doi.org/10.1034/j.1600-0870.1995.00125.x).
- 5445 Soja, R., and L. Starkel (2007). *Extreme rainfalls in Eastern Himalaya and southern*
5446 *slope of Meghalaya Plateau and their geomorphologic impacts*. Geomorphology, 84
5447 (3–4):170–180. doi:[10.1016/j.geomorph.2006.01.040](https://doi.org/10.1016/j.geomorph.2006.01.040).
- 5448 Sorooshian, S., K. Hsu, X. Gao, H.V. Gupta, B. Imam and Dan Braithwaitea (2000).
5449 *Evaluation of PERSIANN System Satellite-Based Estimates of Tropical Rainfall*. Bull.
5450 Am. Meteorol. Soc., 81(9):2035–2046.
- 5451 Sperber, K. R., H. Annamalai, I. S. Kang, A. Kitoh, A. Moise, A. Turner, B. Wang
5452 and T. Zhou (2013). *The Asian summer monsoon: an intercomparison of CMIP5*
5453 *vs. CMIP3 simulations of the late 20th century*. Clim. Dyn., 41(9–10):2711–2744.
5454 doi:[10.1007/s00382-012-1607-6](https://doi.org/10.1007/s00382-012-1607-6).
- 5455 Srinivas, C. V., D. Hariprasad, D. V. Bhaskar Rao, Y. Anjaneyulu, R. Baskaran and
5456 B. Venkatraman (2012). *Simulation of the Indian summer monsoon regional cli-*
5457 *mate using advanced research WRF model*. Theor. Appl. Climatol., 33(5):1195–1210.
5458 doi:[10.1002/joc.3505](https://doi.org/10.1002/joc.3505).
- 5459 Steckler, M. S., S. L. Nooner, S. H. Akhter, S. K. Chowdhury, S. Bettadpur, L. Seeber
5460 and M. G. Kogan (2010). *Modeling Earth deformation from monsoonal flooding in*
5461 *Bangladesh using hydrographic, GPS, and Gravity Recovery and Climate Experiment*
5462 *(GRACE) data*. J. Geophys. Res., 15(B8). doi:[10.1029/2009JB007018](https://doi.org/10.1029/2009JB007018).
- 5463 Steiner, A. K., G. Kirchengast, M. Borsche, U. Foelsche and T. Schoengassner
5464 (2007). *A multi-year comparison of lower stratospheric temperatures from CHAMP*
5465 *radio occultation data with MSU/AMSU records*. J. Geophys. Res., 112(D22).
5466 doi:[10.1029/2006JD008283](https://doi.org/10.1029/2006JD008283).

- 5467 Steiner, A. K., B. C. Lackner, F. Ladstädter, B. Scherllin-Pirscher, U. Foelsche and
5468 G. Kirchengast (2011). *GPS radio occultation for climate monitoring and change*
5469 *detection*. Radio Sci., 46(6). doi:[10.1029/2010RS004614](https://doi.org/10.1029/2010RS004614).
- 5470 Steiner, A. K., D. Hunt, S.-P. Ho, G. Kirchengast, A. J. Mannucci, B. Scherllin-
5471 Pirscher, H. Gleisner, A. von Engeln, T. Schmidt, C. Ao, S. S. Leroy, E. R. Kursin-
5472 ski, U. Foelsche, M. Gorbunov, S. Heise, Y.-H. Kuo, K. B. Lauritsen, C. Marquardt,
5473 C. Rocken, W. Schreiner, S. Sokolovskiy, S. Syndergaard and J. Wickert (2013). *Quan-*
5474 *tification of structural uncertainty in climate data records from GPS radio occultation*.
5475 Atmos. Chem. Phys., 13:1469–1484. doi:[10.5194/acp-13-1469-2013](https://doi.org/10.5194/acp-13-1469-2013).
- 5476 Su, F., X. Duan, D. Chen, Z. Hao and L. Cuo (2012). *Evaluation of the Global*
5477 *Climate Models in the CMIP5 over the Tibetan Plateau*. J. Clim., 26:3187–3208.
5478 doi:[10.1175/JCLI-D-12-00321.1](https://doi.org/10.1175/JCLI-D-12-00321.1).
- 5479 Su, F., X. Duan, D. Chen, Z. Hao and L. Cuo (2013). *Evaluation of the Global Cli-*
5480 *mate Models in the CMIP5 over the Tibetan Plateau*. Clim. Change, 26:3187–3208.
5481 doi:[10.1175/JCLI-D-12-00321.1](https://doi.org/10.1175/JCLI-D-12-00321.1).
- 5482 Sun, B., A. Reale, D. J. and D. C. Hunt (2010). *Comparing radiosonde and COSMIC*
5483 *atmospheric profile data to quantify differences among radiosonde types and the ef-*
5484 *fects of imperfect collocation on comparison statistics*. J. Geophys. Res., 115(D23).
5485 doi:[10.1029/2010JD014457](https://doi.org/10.1029/2010JD014457).
- 5486 Swenson, S., and J. Wahr (2006a). *Post-processing removal of correlated errors in*
5487 *GRACE data*. Geophys. Res. Lett., 33(8). doi:[10.1029/2005GL025285](https://doi.org/10.1029/2005GL025285).
- 5488 Swenson, S., D. P. Chambers and J. Wahr (2008). *Estimating geocenter variations*
5489 *from a combination of GRACE and ocean model output*. J. Geophys. Res., 113(B8).
5490 doi:[10.1029/2007JB005338](https://doi.org/10.1029/2007JB005338).
- 5491 Tapley, B. D., S. Bettadpur, M. Watkins and C. Reigber (2004). *The gravity recovery*
5492 *and climate experiment: Mission overview and early results*. Geophys. Res. Lett., 33.
5493 doi:[10.1029/2004GL019779](https://doi.org/10.1029/2004GL019779).
- 5494 Taylor, K. E., R. J. Stouffer and G. A. Meeh (2012). *An Overview of CMIP5 and the*
5495 *Experiment Design*. Bull. Am. Meteorol. Soc., 93:485–498. doi:[10.1175/BAMS-D-11-](https://doi.org/10.1175/BAMS-D-11-00094.1)
5496 [00094.1](https://doi.org/10.1175/BAMS-D-11-00094.1).
- 5497 Taylor, R. G., B. Scanlon, P. Dölland M. Rodell, R. van Beek, Y. Wada, L. Longuev-
5498 ergne, M. Leblanc, J. S. Famiglietti, M. Edmunds, L. Konikow, T. R. Green, J. Chen,
5499 M. Taniguchi, M. F. P. Bierkens, A. MacDonald, Y. Fan, R. M. Maxwell, Y. Yechieli,
5500 J. J. Gurdak, D. M. Allen, M. Shamsudduha, K. Hiscock, P. J. F. Yeh, I. Holman and
5501 H. Treidel (2013). *Ground water and climate change*. Nat. Clim. Change, 3:322–329.
5502 doi:[10.1038/nclimate1744](https://doi.org/10.1038/nclimate1744).
- 5503 Thompson, D. W. J., E. A. Barnes, C. Deser, W. E. Foust and A. S. Phillips (2015).
5504 *Quantifying the Role of Internal Climate Variability in Future Climate Trends*. J.
5505 Clim., 28:6443–6456. doi:[10.1175/JCLI-D-14-00830.1](https://doi.org/10.1175/JCLI-D-14-00830.1).

- 5506 Thorne, P. W., P. Brohan, H. A. Titchner, M. P. McCarthy, S. C. Sherwood, T. C.
5507 Peterson, L. Haimberger, D. E. Parker, S. F. B. Tett, B. D. Santer, D. R. Fereday,
5508 and J. J. Kennedy (2011). *A quantification of uncertainties in historical tropical*
5509 *tropospheric temperature trends from radiosondes*. *J. Geophys. Res.*, 116(D12116).
5510 doi:[10.1029/2010JD015487](https://doi.org/10.1029/2010JD015487).
- 5511 Tiwari, P. R., S. C. Kar, U. C. Mohanty, S. Dey, P. Sinha and P.V.S. Raju (2015). *The*
5512 *role of land surface schemes in the regional climate model (RegCM) for seasonal scale*
5513 *simulations over Western Himalaya*. *Atmósfera*, 28(2):129–142. doi:[10.1016/S0187-](https://doi.org/10.1016/S0187-6236(15)30005-9)
5514 [6236\(15\)30005-9](https://doi.org/10.1016/S0187-6236(15)30005-9).
- 5515 Tiwari, V. M., J. Wahr and S. Swenson (2009). *Dwindling groundwater resources in*
5516 *northern India, from satellite gravity observations*. *Geophys. Res. Lett.*, 36(L18401).
5517 doi:[10.1029/2009GL039401](https://doi.org/10.1029/2009GL039401).
- 5518 Treidel, H., J. L. Martin-Bordes and J. J. Gurdak (2012). In: Robins, N. S. (Hrsg.),
5519 *Climate Change Effects on Groundwater Resources, International Association of Hy-*
5520 *drogeologists*, 1–399. CRC Press/Balkema, AK Leiden, The Netherlands. ISBN 978-
5521 92-9115-032-8. Available at [http://unesdoc.unesco.org/images/0021/002155/](http://unesdoc.unesco.org/images/0021/002155/215556e.pdf)
5522 [215556e.pdf](http://unesdoc.unesco.org/images/0021/002155/215556e.pdf). Accessed on 02 April 2014.
- 5523 Trenberth, K. E. (1990). *Recent Observed Interdecadal Climate Changes in the North-*
5524 *ern Hemisphere*. *Bull. Amer. Meteor. Soc.*, 71(7):988–993. doi:[10.1175/1520-](https://doi.org/10.1175/1520-0477(1990)071<0988:ROICCI>2.0.CO;2)
5525 [0477\(1990\)071<0988:ROICCI>2.0.CO;2](https://doi.org/10.1175/1520-0477(1990)071<0988:ROICCI>2.0.CO;2).
- 5526 Trenberth, K. E. (1997). *The definition of El Niño*. *Bull. Am. Meteorol. Soc.*, 78:
5527 2771–2777.
- 5528 Trenberth, K. E., G. van der Schrier A. Dai, P. D. Jones, J. Barichivich, K. R. Briffa
5529 and J. Sheffield (2014). *Global warming and changes in drought*. *Nat. Clim. Change*,
5530 4:17–22. doi:[10.1038/nclimate2067](https://doi.org/10.1038/nclimate2067).
- 5531 Turk, F. J., and S. D Miller (2005). *Toward improved characterization of remotely*
5532 *sensed precipitation regimes with MODIS/AMSR-E blended data techniques*. *IEEE*
5533 *Trans. Geosci. Remote Sens.*, 43(5):1059–1069. doi:[10.1109/TGRS.2004.841627](https://doi.org/10.1109/TGRS.2004.841627).
- 5534 Turner, A. G., and H. Annamalai (2012). *Climate change and the South Asian summer*
5535 *monsoon*. *Nat. Clim. Chang.*, 2:587–595. doi:[10.1028/nclimate1495](https://doi.org/10.1028/nclimate1495).
- 5536 Turner, A. G., P. M. Inness and J. M. Slingo (2007). *The effect of doubled CO₂ and model*
5537 *basic state biases on the monsoon-ENSO system. I: Mean response and interannual*
5538 *variability*. *Q. J. R. Meteorol. Soc.*, 133(626):1143–1157. doi:[10.1002/qj.82](https://doi.org/10.1002/qj.82).
- 5539 Ueda, H., A. Iwai, K. Kuwako and M. E. Hori (2006). *Impact of anthropogenic forcing*
5540 *on the Asian summer monsoon as simulated by eight GCMs*. *Geophys. Res. Lett.*, 33
5541 (6). doi:[10.1029/2005GL025336](https://doi.org/10.1029/2005GL025336).
- 5542 Uppala, S. M., P. W. Källberg, A. J. Simmons, U. Andrae, V. Da Costa Bechtold,
5543 M. Fiorino, J. K. Gibson, J. Haseler, A. Hernandez, G. A. Kelly, X. Li, K. Onogi,
5544 S. Saarinen, N. Sokka, R. P. Allan, E. Andersson, K. Arpe, M. A. Balmaseda, A. C. M.

- 5545 Beljaars, L. Van De Berg, J. Bidlot, N. Bormann, S. Caires, F. Chevallier, A. Dethof,
5546 M. Dragosavac, M. Fisher, M. Fuentes, S. Hagemann, E. Hólm, B. J. Hoskins, L. Isak-
5547 sen, P. A. E. M. Janssen, R. Jenne, A. P. McNally, J.-F. Mahfouf, J.-J. Morcrette, N. A.
5548 Rayner, R. W. Saunders, P. Simon, A. Sterl, K. E. Trenberth, A. Untch, D. Vasiljevic,
5549 P. Viterbo and J. Woollen (2005). *The ERA-40 re-analysis*. Q. J. R. Meteorol. Soc.,
5550 131:2961–3012. doi:[10.1256/qj.04.176](https://doi.org/10.1256/qj.04.176).
- 5551 Ushio, T., K. Sasashige, T. Kubota, S. Shige, K. Okamoto, K. Aonashi, T. Inoue,
5552 N. Takahashi and T. Iguchi (2009). *A Kalman filter approach to the Global Satellite*
5553 *Mapping of Precipitation (GSMaP) from combined passive microwave and infrared ra-*
5554 *diometric data*. J. Meteor. Soc. Japan, 87A(9):3084–3097. doi:[10.2151/jmsj.87A.137](https://doi.org/10.2151/jmsj.87A.137).
- 5555 van den Dool, H., J. Huang and Y. Fan (2003). *Performance and Analysis of the con-*
5556 *structed analogue method applied to US soil moisture applied over 1981-2001*. Geo-
5557 phys. Res. Lett., 108(8617). doi:[10.1029/2002JD003114](https://doi.org/10.1029/2002JD003114).
- 5558 Vinnarasi, R., and C. T. Dhanya (2016). *Changing characteristics of extreme wet and*
5559 *dry spells of Indian monsoon rainfall*. J. Geophys. Res. Atmos., 121(5):2146–2160.
5560 doi:[10.1002/2015JD024310](https://doi.org/10.1002/2015JD024310).
- 5561 Wahr, J., M. Molenaar and F. Bryan (1998). *Time variability of the Earth's gravity*
5562 *field: Hydrological and oceanic effects and their possible detection using GRACE*. J.
5563 Geophys. Res., 103(B12):30205–30229. doi:[10.1029/98JB02844](https://doi.org/10.1029/98JB02844).
- 5564 Wahr, J., S. Swenson, V. Zlotnicki and I. Velicogna (2004). *Time-variable gravity from*
5565 *GRACE: First results*. Geophys. Res. Lett., 31(11). doi:[10.1029/2004GL019779](https://doi.org/10.1029/2004GL019779).
- 5566 Wang, B. R., X. Y. Liu and J. K. Wang (2013). *Assessment of COSMIC radio occultation*
5567 *retrieval product using global radiosonde data*. Atmos. Meas. Tech., 6:1073–1083.
5568 doi:[10.5194/amt-6-1073-2013](https://doi.org/10.5194/amt-6-1073-2013).
- 5569 Wang, Y. Q., L. R. Leung, J. L. McGregor, , D. K. Lee, W. C. Wang, Y. H. Ding, and
5570 F. Kimura (2004). *Regional climate modeling: progress, challenges, and prospects*.
5571 Meteor. Soc. Japan, 82:1599–1628. doi:[10.2151/jmsj.82.1599](https://doi.org/10.2151/jmsj.82.1599).
- 5572 Webster, P. J., A. M. Moore, J. P. Loschnigg and R. R. Leben (1999). *Coupled ocean-*
5573 *atmosphere dynamics in the Indian Ocean during 1997-98*. Nature, 401:356–360.
5574 doi:[10.1038/43848](https://doi.org/10.1038/43848).
- 5575 Whitehead, P. G., E. Barbour, M. N. Futter, S. Sarkar, H. Rodda, J. Caesar, D. Butter-
5576 field, L. Jin, R. Sinha, R. Nicholls and M. Salehin h (2015). *Impacts of climate change*
5577 *and socio-economic scenarios on flow and water quality of the Ganges, Brahmaputra*
5578 *and Meghna (GBM) river systems: low flow and flood statistics*. Environ. Sci.: Proc.
5579 Impacts, 17:1057–1069. doi:[10.1039/C4EM00619D](https://doi.org/10.1039/C4EM00619D).
- 5580 Wickert, J., C. Reigber, G. Beyerle, Rolf König, C. Marquardt, T. Schmidt, L. Grun-
5581 walddt, R. Galas, T. K. Meehan, W. G. Melbourne and K. Hocke (2001). *Atmosphere*
5582 *sounding by GPS radio occultation: First results from CHAMP*. Geophys. Res. Lett.,
5583 28(17):3263–3266. doi:[10.1029/2001GL013117](https://doi.org/10.1029/2001GL013117).

- 5584 Wickert, J., G. Michalak, T. Schmidt, G. Beyerle, C. Z. Cheng, S. B. Healy, S. Heise,
5585 C. Y. Huang, N. Jakowski, W. Kohler, C. Mayer, D. Offiler, E. Ozawa, A. G. Pavelyev,
5586 M. Rothacher, B. Tapley and C. Arras (2009). *GPS Radio Occultation: Results from*
5587 *CHAMP, GRACE and FORMOSAT-3/COSMIC*. Terr. Atmos. Ocean. Sci., 20(1):
5588 35–50. doi:[10.3319/TAO.2007.12.26.01\(F3C\)](https://doi.org/10.3319/TAO.2007.12.26.01(F3C)).
- 5589 Wilcox, L. J., B. J. Hoskins and K. P. Shine (2011). *A global blended tropopause based*
5590 *on ERA data. Part II: Trends and tropical broadening*. J. Geophys. Res., 138(664):
5591 576–584. doi:[10.1002/qj.910](https://doi.org/10.1002/qj.910).
- 5592 Wild, M., and B. Liepert (2010). *The Earth radiation balance as driver of the global*
5593 *hydrological cycle*. Earth Planet. Sci. Lett., 5(2). doi:[10.1088/1748-9326/5/2/025203](https://doi.org/10.1088/1748-9326/5/2/025203).
- 5594 Willmott, C. J., and S. M. Robeson (1995). *Climatologically aided interpo-*
5595 *lation (CAI) of terrestrial air temperature*. Int. J. Climatol., 15(2):221–229.
5596 doi:[10.1002/joc.3370150207](https://doi.org/10.1002/joc.3370150207).
- 5597 WMO (1957). *Meteorology - A three-dimensional science: Second session of the com-*
5598 *mission for aerology*. WMO Bull., IV(4):134–138.
- 5599 WMO (2012). *Standardized Precipitation Index User Guide*. World Meteorologi-
5600 cal Organization, Geneva, Switzerland, 2012. WMO-No. 1090, Available at http://library.wmo.int/pmb_ged/wmo_1090_en.pdf.
5601
- 5602 Wouters, B., J. A. Bonin, D. P. Chambers, R. E. M. Riva, I. Sasgen and J. Wahr (2014).
5603 *GRACE, time-varying gravity, Earth system dynamics and climate change*. Reports
5604 on Progress in Physics, 77(11):116801. doi:[10.1088/0034-4885/77/11/116801](https://doi.org/10.1088/0034-4885/77/11/116801).
- 5605 Xie, P., Y. Yarosh, T. Love, J. E. Janowiak and P. A. Arkin (2002). *A real-time daily*
5606 *precipitation analysis over South Asia*. In: *16th Conference of Hydrology*, Orlando,
5607 Florida. NOAA/Climate Prediction Center, American Meteorological Society. Avail-
5608 able at: http://www.cpc.ncep.noaa.gov/products/fews/sasia_rfe.pdf.
- 5609 Xie, P., M. Chen, S. Yang, A. Yatagai, T. Hayasaka, Y. Fukushima and C. Liu (2007).
5610 *A Gauge-Based Analysis of Daily Precipitation over East Asia*. J. Hydrometeorol., 8
5611 (3):607–626. doi:[10.1175/JHM583.1](https://doi.org/10.1175/JHM583.1).
- 5612 Xue, X., Y. Hong, A. S. Limaye, J. J. Gourley, G. J. Huffman, S. I. Khan, C. Dorji and
5613 S. Chen (2013). *Statistical and hydrological evaluation of TRMM-based Multi-satellite*
5614 *Precipitation Analysis over the Wangchu Basin of Bhutan: Are the latest satellite*
5615 *precipitation products 3B42V7 ready for use in ungauged basins?* J. Hydrol., 499:
5616 91–99. doi:[10.1016/j.jhydrol.2013.06.042](https://doi.org/10.1016/j.jhydrol.2013.06.042).
- 5617 Yadav, R.K., K. Rupa Kumar and M. Rajeevan (2008). *Climate change scenarios for*
5618 *Northwest India winter season*. Quat. Int., 213:12–19. doi:[10.1016/j.bbr.2011.03.031](https://doi.org/10.1016/j.bbr.2011.03.031).
- 5619 Yasutomi, N., A. Hamada and A. Yatagai (2011). *Development of a long-term daily*
5620 *gridded temperature dataset and its application to rain/snow discrimination of daily*
5621 *precipitation*. Global Environ. Res., V15N2:165–172.

- 5622 Yatagai, A., K. Kamiguchi, O. Arakawa, A. Hamada, N. Yasutomi and A. Kitoh (2012).
5623 *APHRODITE: Constructing a Long-term Daily Gridded Precipitation Dataset for*
5624 *Asia based on a Dense Network of Rain Gauges.* Bull. Am. Meteorol. Soc., 93:1401–
5625 1415. doi:[10.1175/BAMS-D-11-00122.1](https://doi.org/10.1175/BAMS-D-11-00122.1).
- 5626 Yin, Z Y., X. Zhang, X. Liu, M. Colella and X. Chen (2008). *An Assessment of the Biases*
5627 *of Satellite Rainfall Estimates over the Tibetan Plateau and Correction Methods Based*
5628 *on Topographic Analysis.* J. Hydrometeor, 9:301–326. doi:[10.1175/2007JHM903.1](https://doi.org/10.1175/2007JHM903.1).
- 5629 Yunus, F. Md., S. Khan, P. Chowdhury, A. H. Milton, S. Hussain and M. Rahman
5630 (2016). *A Review of Groundwater Arsenic Contamination in Bangladesh: The Mil-*
5631 *lennium Development Goal Era and Beyond.* Int. J. Environ. Res. Public Health, 13
5632 (2). doi:[10.3390/ijerph13020215](https://doi.org/10.3390/ijerph13020215).
- 5633 Zeng, X., and E. Lu (2003). *Globally unified monsoon onset and retreat indexes.* J.
5634 Clim., 17:2241–2248. doi:[10.1175/1520-0442\(2004\)017<2241:GUMOAR>2.0.CO;2](https://doi.org/10.1175/1520-0442(2004)017<2241:GUMOAR>2.0.CO;2).
- 5635 Zhang, K., E. Fu, D. Silcock, Y. Wang and Y. Kuleshov (2011). *An investigation of*
5636 *atmospheric temperature profiles in the Australian region using collocated GPS radio*
5637 *occultation and radiosonde data.* Atmos. Meas. Tech., 4:2087–2092. doi:[10.5194/amt-](https://doi.org/10.5194/amt-4-2087-2011)
5638 [4-2087-2011](https://doi.org/10.5194/amt-4-2087-2011).
- 5639 Zhang, M. L., L. Liu, W. Wan and . Ning B (2014). *An update global model of hmF2*
5640 *from values estimated from ionosonde and COSMIC/FORMOSAT-3 radio occultation.*
5641 Adv. Space Res., 53(3):395–402. doi:[10.1016/j.asr.2013.11.053](https://doi.org/10.1016/j.asr.2013.11.053).

List of Figures

| | | | |
|------|-----|---|----|
| 5646 | | | |
| 5647 | 1.1 | Outline of this thesis illustrating the studies conducted in each chapter. | 9 |
| 5648 | 2.1 | Overview of the Ganges–Brahmaputra–Meghna River Basin in South Asia. Brahmaputra and Meghna River Basins are merged together, which is represented by the thick black polygon, while the Ganges River Basin is shown in thick blue polygons. This representation will be used for the remainder of this thesis. Source: Khandu et al. (2016a). | 13 |
| 5649 | | | |
| 5650 | | | |
| 5651 | | | |
| 5652 | | | |
| 5653 | 2.2 | Spatial distribution of rain gauge stations across the GBM River Basin and its neighbouring regions that were used in (a) APHRODITE, (b) CRU_TS3.22, and (c) GPCCv6. Modified from Khandu et al. (2015). | 14 |
| 5654 | | | |
| 5655 | | | |
| 5656 | 2.3 | Monthly ENSO (Niño3.4 and IOD (-DMI) indices between 1980 and 2014. | 18 |
| 5657 | 2.4 | Spatial variations of mean annual amplitudes of monthly rainfall over the GBM River Basin based on (a) GPCCv6 (1980–2010), (b) TMPAv7 (1998–2013), (c) CHIRP (1998–2013), (d) ERA-Interim (1980–2010), (e) MERRA (1980–2010), (f) CFSR (1980–2010). | 23 |
| 5658 | | | |
| 5659 | | | |
| 5660 | | | |
| 5661 | 2.5 | Spatial distribution of monsoon (JJAS) rainfall over the GBM River Basin (a) GPCCv6 (1980–2010), (b) TMPAv7 (1998–2013), (c) CHIRP (1998–2013), (d) ERA-Interim (1980–2010), (e) MERRA (1980–2010), (f) CFSR (1980–2010). | 23 |
| 5662 | | | |
| 5663 | | | |
| 5664 | | | |
| 5665 | 2.6 | Spatial patterns of annual amplitudes of temperature over the GBM River Basin based on (a) CRU_TS3.22, (b) UDEL, (c) ERA-Interim, (d) MERRA, and (e) CFSR for the period 1980–2010. | 25 |
| 5666 | | | |
| 5667 | | | |
| 5668 | 2.7 | Precipitation changes over the GBM River Basin based on (a) GPCCv6 (1980–2010), (b) TMPAv7 (1998–2013), (c) CHIRP (1998–2013), (d) ERA-Interim (1980–2010), (e) MERRA (1980–2010), (f) CFSR (1980–2010). Trend values that are not significant at 95% confidence level are masked out. | 26 |
| 5669 | | | |
| 5670 | | | |
| 5671 | | | |
| 5672 | | | |
| 5673 | 2.8 | Spatial variation of temperature trends based on (a) CRU_TS3.22, (b) UDEL, (c) ERA-Interim, (d) MERRA, and (e) CFSR for the period 1980–2013 in the GBM River Basin. Trend values that are not significant at 95% confidence level are not shown. | 28 |
| 5674 | | | |
| 5675 | | | |
| 5676 | | | |
| 5677 | 2.9 | Spatial patterns or EOFs (a & b) and temporal components or PCs (c & d) based on first two leading modes of PCA analysis on monthly temperature anomaly of CRU_TS3.22 over the period 1980–2013. PCs of UDEL, ERA-Interim, MERRA, and CFSR indicated in (c & d) are derived by projecting their respective anomalies onto the EOFs of CRU_TS3.22. | 29 |
| 5678 | | | |
| 5679 | | | |
| 5680 | | | |
| 5681 | | | |

| | | | |
|------|------|---|----|
| 5682 | 2.10 | Correlation coefficients between monthly SST anomalies and surface temperature anomalies (represented by PC 1 and PC 2) derived from various observed and reanalysis temperature products for the period 1980–2013. Only those values that are significant at 95% confidence level are retained. | 31 |
| 5683 | | | |
| 5684 | | | |
| 5685 | | | |
| 5686 | 2.11 | Regression of Niño3.4 index and DMI on precipitation anomalies of APHRODITE (1980-2007) and TMPAv7 (1998-2013). Values that are not significant at 95% confidence level based on student's <i>t</i> -test are not shown. | 33 |
| 5687 | | | |
| 5688 | | | |
| 5689 | | | |
| 5690 | 2.12 | Regression Niño3.4 index and DMI on the precipitation anomalies of GPCCv6 and reanalysis products for the period 1980–2010. Precipitation contributions that are not significant at 95% confidence level based on student's <i>t</i> -test are not shown. | 33 |
| 5691 | | | |
| 5692 | | | |
| 5693 | | | |
| 5694 | 3.1 | The Ganges (thick black polygon) and Brahmaputra–Meghna (thick blue polygon) and its (a) area equipped for irrigation (%) from AQUASTAT data of the Food and Agricultural Organization (FAO) of the United Nations and (b) annual water use in irrigated agriculture (%) from Global Crop Water Model for the period 1998–2002. | 38 |
| 5695 | | | |
| 5696 | | | |
| 5697 | | | |
| 5698 | | | |
| 5699 | 3.2 | The concept of the GRACE satellite mission. The two satellites move in tandem to detect changes in Earth's gravity field. Separations as small as 10 microns are detected. Source: www.spaceflightnow.com/rockot/grace . | 42 |
| 5700 | | | |
| 5701 | | | |
| 5702 | 3.3 | (a) Gridded scale factor derived by fitting a least squares approach of Landerer and Swenson (2012), (b) correlation between filtered and unfiltered GLDAS soil moisture. | 44 |
| 5703 | | | |
| 5704 | | | |
| 5705 | 3.4 | A sample time-series of 3 datasets x_1 , x_2 , and x_3 that are used to demonstrate the generalized TCH approach. | 50 |
| 5706 | | | |
| 5707 | 3.5 | Relative uncertainties of (a) GPCCv7, (b) TMPAv7, and (c) CRU_TS3.22, and SNR values for (d) GPCCv7, (e) TMPAv7, and (f) CRU_TS3.22 estimated for the period 1998–2015. | 52 |
| 5708 | | | |
| 5709 | | | |
| 5710 | 3.6 | Spatial distribution of SNR values for (a) CPC, (b) MERRA, (c) ERA-Interim, and (d) Noah soil moisture datasets estimated for the period 2002–2015. | 53 |
| 5711 | | | |
| 5712 | | | |
| 5713 | 3.7 | Spatial distribution of SNR values of TWS changes derived from (a) CSR, (b) GFZ, and (c) JPL for the period 2002–2015. | 54 |
| 5714 | | | |
| 5715 | 3.8 | JJAS precipitation variations in the (a) Ganges and (b) Brahmaputra–Meghna River Basin between 1980 and 2013 based on GPCCv7 and CRU_TS3.22 datasets. | 55 |
| 5716 | | | |
| 5717 | | | |
| 5718 | 3.9 | Mean annual amplitudes and linear trends in soil moisture obtained from (a & d) CPC, (b & e) MERRA, and (c & f) ERA-Interim estimated for the period 1980–2015. Only values that are significant at 95% confidence level are shown. Updated from Khandu et al. (2016a). | 56 |
| 5719 | | | |
| 5720 | | | |
| 5721 | | | |

| | | |
|------|---|----|
| 5722 | 3.10 Linear trends in: (a) precipitation [TMPAv7], (b) soil moisture [reanalysis], (c) soil moisture [Noah], and (d) TWS [GRACE] estimated for the period 2002–2015. Values that are not significant at 95% confidence interval are not shown. Modified from Khandu et al. (2016a). | 57 |
| 5723 | | |
| 5724 | | |
| 5725 | | |
| 5726 | 3.11 (a–b) Precipitation anomalies derived from GPCCv7, CRU_TS3.22, and TMPAv7, (c–d) soil moisture anomalies plotted as a weighted average of four datasets, and (e–f) GRACE TWS anomalies plotted as a weighted average of data from three sources (CSR, GFZ, and JPL) for the Ganges and Brahmaputra–Meghna River Basins, respectively. The trend lines are indicated by red lines and their values are shown. | 58 |
| 5727 | | |
| 5728 | | |
| 5729 | | |
| 5730 | | |
| 5731 | | |
| 5732 | 3.12 Cumulative sums of precipitation, soil moisture, and GRACE-derived TWS changes in (a) Ganges, and (b) Brahmaputra River Basins. Updated from Khandu et al. (2016a). | 59 |
| 5733 | | |
| 5734 | | |
| 5735 | 3.13 SPI of precipitation (at 12 month time-scale) and soil moisture (at 6 month time-scale), and SI of TWS for the (a) Ganges and (b) Brahmaputra River Basins. These indices are derived for the respective data periods. Updated from Khandu et al. (2016a). | 60 |
| 5736 | | |
| 5737 | | |
| 5738 | | |
| 5739 | 3.14 Spatial distribution of correlation coefficients between (a) precipitation and reanalysis-based soil moisture, (b) precipitation and Noah-based soil moisture, (c) precipitation and GRACE-derived TWS, (d) soil moisture datasets of reanalysis and Noah, (e) reanalysis-based soil moisture and GRACE-derived TWS, and (f) Noah-based soil moisture and GRACE-derived TWS, estimated for the common data period of 2002 to 2015. | 61 |
| 5740 | | |
| 5741 | | |
| 5742 | | |
| 5743 | | |
| 5744 | | |
| 5745 | 3.15 Number of drought events calculated from (a) precipitation (12 month time-scale SPI) and (b) soil reanalysis-based soil moisture (6 month time-scale SPI) between 1980–2014. | 62 |
| 5746 | | |
| 5747 | | |
| 5748 | 3.16 Duration of the 2009/2010 drought event calculated from (a) precipitation, (b) reanalysis-based soil moisture, (c) Noah-based soil moisture, and (d) GRACE-derived TWS changes. The duration of drought is calculated by counting the number of months when SPI continuously remain below -0.9 between January 2009 and December 2010. | 63 |
| 5749 | | |
| 5750 | | |
| 5751 | | |
| 5752 | | |
| 5753 | 3.17 Maximum drought intensity of the 2009/2010 drought event calculated from (a) precipitation, (b) reanalysis-based soil moisture, (c) Noah-based soil moisture, and (d) GRACE-derived TWS changes. | 64 |
| 5754 | | |
| 5755 | | |
| 5756 | 3.18 RMS of difference between natural TWS (“NOUSE” and those under the influence of human water abstraction (IRR70_S) indicating the level of human water abstraction. Modified from Khandu et al. (2016a). | 65 |
| 5757 | | |
| 5758 | | |
| 5759 | 3.19 time-series of natural TWS (“NOUSE”, black dashed line), TWS under the influence of human water use (“IRR70_S”, gray line), and their difference (black line). Linear trends are shown for 1979–2009, 1979–2001 and 2002–2009. Adapted from Khandu et al. (2016a). | 66 |
| 5760 | | |
| 5761 | | |
| 5762 | | |

| | | | |
|------|-----|---|----|
| 5763 | 4.1 | Process involved in regional climate modelling using RCMs. Modified from Mathison et al. (2013) | 71 |
| 5764 | | | |
| 5765 | 4.2 | Elevation maps of the RegCM4.4 domain at various spatial resolutions: (a) GFDL-ESM, (b) MPI-ESM-MR, (c) ERA-Interim, and (d) RegCM4.4. Note that the nominal resolution of ERA-Interim is $0.79^\circ \times 0.79^\circ$. The Ganges and Brahmaputra–Meghna River Basins are shown in blue and black (thick) polygons. | 74 |
| 5766 | | | |
| 5767 | | | |
| 5768 | | | |
| 5769 | | | |
| 5770 | 4.3 | Cumulative sums of 5-day average precipitation (in %) based on APHRODITE (red) and TMPAv7 (blue) for (a) Ganges and (b) Brahmaputra–Meghna River Basins indicating their respective mean onset and retreat dates for the period 1998–2007. Gradients derived from (a & b) are shown in (c & d), respectively. The maxima and minima corresponds to the onset and withdrawal period of the Indian monsoon. A low-pass filter of approximately 30 days is applied to the pentad rainfall. | 79 |
| 5771 | | | |
| 5772 | | | |
| 5773 | | | |
| 5774 | | | |
| 5775 | | | |
| 5776 | | | |
| 5777 | 4.4 | (a–f) DJF and (g–l) JJAS precipitation and temperature climatology based on observed and reanalysis dataset. Mean precipitation is computed from TMPAv7, GPCCv7, and ERA-Interim between 1998 and 2012, and mean DJF temperature is computed from CRU_TS3.22, MERRA, and ERA-Interim for the period 1982–2012. | 80 |
| 5778 | | | |
| 5779 | | | |
| 5780 | | | |
| 5781 | | | |
| 5782 | 4.5 | (a–d) Mean precipitation (as well as 850 hPa circulation) bias during DJF between various RCM simulations and TMPAv7 (and ERA-Interim) for the period 1998–2012. The corresponding temperature biases with respect to CRU_TS3.22 for the period 1982–2012 are shown from (e–h). Note that the 850 hPa wind differences are plotted as vectors. | 82 |
| 5783 | | | |
| 5784 | | | |
| 5785 | | | |
| 5786 | | | |
| 5787 | 4.6 | (a–d) Mean precipitation (as well as 850 hPa circulation) bias during JJAS between various RCM simulations and TMPAv7 (and ERA-Interim) for the period 1998–2012. The corresponding temperature biases with respect to CRU_TS3.22 for the period 1982–2012 are shown from (e–h). Note that the 850 hPa wind differences are plotted as vectors. | 84 |
| 5788 | | | |
| 5789 | | | |
| 5790 | | | |
| 5791 | | | |
| 5792 | 4.7 | The annual cycle of precipitation and temperature based on observations, reanalysis products, and various RCM simulations spatially averaged over the Ganges and Brahmaputra–Meghna River Basins. Mean annual cycle of (a & b) precipitation over the period 1998–2012 and (c & d) temperature over the period 1982–2012. The annual cycle of low level (850 hPa level) and mid-level (200 hPa level) zonal winds shown in (e & f) are computed over land-only for the RegCM4.4 domain. | 86 |
| 5793 | | | |
| 5794 | | | |
| 5795 | | | |
| 5796 | | | |
| 5797 | | | |
| 5798 | | | |
| 5799 | 4.8 | Spatial patterns of pentad number representing the onset and withdrawal of the Indian monsoon. These pentads are derived from daily precipitation datasets from TMPAv7, ERA-Interim, and simulated RCM outputs for the period 1998–2012. The May–June mean 850 hPa level circulation patterns are plotted to indicate the monsoon flow during the onset period. | 88 |
| 5800 | | | |
| 5801 | | | |
| 5802 | | | |
| 5803 | | | |

| | | | |
|------|------|--|-----|
| 5804 | 4.9 | Monthly precipitation anomalies (1998–2012) for the GBM River Basin based on observed datasets, ERA-Interim, and RCM simulations. (a & c) | |
| 5805 | | DJF and JJAS precipitation anomalies for the Ganges River Basin, and | |
| 5806 | | (b & d) DJF and JJAS precipitation anomalies for the Brahmaputra– | |
| 5807 | | Meghna River Basin. | 90 |
| 5808 | | | |
| 5809 | 4.10 | Basin-averaged temperature anomalies (1982–2012) for the GBM River Basin based on observed datasets, MERRA, ERA-Interim, and RCM simulations. (a & c) | |
| 5810 | | DJF and JJAS temperature anomalies for the Ganges River Basin, and | |
| 5811 | | (b & d) DJF and JJAS temperature anomalies for the Brahmaputra– | |
| 5812 | | Meghna River Basin. | 92 |
| 5813 | | | |
| 5814 | 4.11 | PCA decomposition of the DJF and JJAS global (50°N–50°S) SST anomalies. Spatial patterns (or EOFs) of the first two leading modes of DJF (a & b) and JJAS (c & d) SST anomalies. The corresponding temporal patterns (or PCs) are shown in (e & f) for DJF and (g & h) for JJAS. | 93 |
| 5815 | | | |
| 5816 | | | |
| 5817 | | | |
| 5818 | | | |
| 5819 | 5.1 | Correlation between Niño3.4 index and gridded 12-month SPI derived from (a) GPCCv7, (b) CRU_TS3.22, (c) RegCM4.4 (driven by ERA-Interim and observed SST data), (d) RegCM4.4 (driven by GFDL-ESM), (e) RegCM4.4 (driven by MPI-ESM-MR), and (f) PRECIS ensemble mean (driven by six QUMP GCMs).. | 103 |
| 5820 | | | |
| 5821 | | | |
| 5822 | | | |
| 5823 | | | |
| 5824 | 5.2 | Correlation between DMI and gridded 12-month SPI derived from (a) GPCCv7, (b) CRU_TS3.22, (c) RegCM4.4 (driven by ERA-Interim and observed SST data), (d) RegCM4.4 (driven by GFDL-ESM), (e) RegCM4.4 (driven by MPI-ESM-MR), and (f) PRECIS ensemble mean (driven by six QUMP GCMs).. | 103 |
| 5825 | | | |
| 5826 | | | |
| 5827 | | | |
| 5828 | | | |
| 5829 | 5.3 | Number of drought events between April 1983 to March 2012 as shown by (a) GPCCv7, (b) CRU_TS3.22, (c) RegCM4.4 (driven by ERA-Interim and observed SST data), (d) RegCM4.4 (driven by GFDL-ESM), (e) RegCM4.4 (driven by MPI-ESM-MR), and (f) PRECIS ensemble mean (driven by six QUMP GCMs). These events were calculated from a 12 month time-scale SPI. | 105 |
| 5830 | | | |
| 5831 | | | |
| 5832 | | | |
| 5833 | | | |
| 5834 | | | |
| 5835 | 5.4 | Number of drought events between April 1950 to March 2012 as shown by (a) GPCCv7, (b) CRU_TS3.22, and (c) ensemble mean of 8 CMIP5 models. Number of wet events for the same period as shown by (d) GPCCv7, (e) CRU_TS3.22, and (f) CMIP5 ensemble mean of 8 CMIP5 models. These events are calculated from the 12 month time-scale SPI. | 106 |
| 5836 | | | |
| 5837 | | | |
| 5838 | | | |
| 5839 | | | |
| 5840 | 5.5 | Spatial distribution of JJAS precipitation changes (mm per decade) over the GBM River Basin based on (a) RegCM4.4 (driven by MPI-ESM-MR) and (b) PRECIS (driven by 6 QUMP GCMs) between 1982–2099 including the spatially-averaged temporal anomalies based on observations (GPCCv7 and CRU_TS3.22) and two RCMs (RegCM4.4 and PRECIS) for the (c) Ganges and (d) Brahmaputra-Meghna River Basins. | 107 |
| 5841 | | | |
| 5842 | | | |
| 5843 | | | |
| 5844 | | | |
| 5845 | | | |

| | | | |
|------|------|--|-----|
| 5846 | 5.6 | Spatial distribution of JJAS temperature changes ($^{\circ}\text{C}$ per decade) over the GBM River Basin based on (a) RegCM4.4 (driven by MPI-ESM-MR) and (b) PRECIS (driven by 6 QUMP GCMs) between 1982–2099 including the spatially-averaged temporal anomalies based on observed CRU_TS3.22 data and two RCMs (RegCM4.4 and PRECIS) for the (c) Ganges and (d) Brahmaputra-Meghna River Basins. | 108 |
| 5847 | | | |
| 5848 | | | |
| 5849 | | | |
| 5850 | | | |
| 5851 | | | |
| 5852 | 5.7 | Number of drought events for the periods 2001–2050 and 2050–2099 based on (a & d) RegCM4.4 (driven by MPI-ESM-MR), (b & e) PRECIS ensemble mean (driven by 6 QUMP GCMs), and (c & f) CMIP5 ensemble mean (based on 8 GCMs). | 110 |
| 5853 | | | |
| 5854 | | | |
| 5855 | | | |
| 5856 | 5.8 | Number of wet events for the periods 2001–2050 and 2050–2099 based on (a & d) RegCM4.4 (driven by MPI-ESM-MR), (b & e) PRECIS ensemble mean (driven by 6 QUMP GCMs), and (c & f) CMIP5 ensemble mean (based on 8 GCMs). | 111 |
| 5857 | | | |
| 5858 | | | |
| 5859 | | | |
| 5860 | 5.9 | Number of drought and wet events per decade based on observed (1983–2012) and RCM simulated (1983–2099) precipitation on a 12 month time-scale: (a & b) for drought events and (c & d) for wet events for the Ganges and Brahmaputra–Meghna River Basin, respectively. | 112 |
| 5861 | | | |
| 5862 | | | |
| 5863 | | | |
| 5864 | 5.10 | Number of drought and wet events per decade based on observed (1951–2012) and CMIP5 (1951–2099) precipitation on a 12 month time-scale: (a & b) for drought events and (c & d) for wet events for the Ganges and Brahmaputra-Meghna River Basin, respectively. | 112 |
| 5865 | | | |
| 5866 | | | |
| 5867 | | | |
| 5868 | 5.11 | Probability (in %) of drought year on a 12 month time-scale for (a & d) all drought, (b & e) severe drought, and (c & f) extreme drought based on PRECIS ensemble mean for the periods 2001–2050 and 2050–2099. g–i represents the same but for RegCM4.4 model. | 114 |
| 5869 | | | |
| 5870 | | | |
| 5871 | | | |
| 5872 | 5.12 | Probability (in %) of wet year on a 12 month time-scale for (a & d) all wet, (b & e) severe wet, and (c & f) extreme wet based on PRECIS ensemble mean for the periods 2001–2050 and 2050–2099. g–i represents the same but for RegCM4.4 model. | 115 |
| 5873 | | | |
| 5874 | | | |
| 5875 | | | |
| 5876 | 5.13 | Probability (in %) of drought-year on a 12 month time-scale for (a & d) all drought, (b & e) severe drought, and (c & f) extreme drought. The probability of wet-year is plotted in (g & j) for all wet, (h & k) severe wet, and (i & l) extreme wet, each representing for the periods 2001–2050 and 2050–2099. | 116 |
| 5877 | | | |
| 5878 | | | |
| 5879 | | | |
| 5880 | | | |
| 5881 | 5.14 | RCM projections drought and wet areas (as a fraction) in the Ganges and Brahmaputra–Meghna River Basin based on RegCM4.4 and PRECIS ensemble mean. The results from GPCCv7 and CRU_TS3.22 are also shown for the period 1983–2012. Area affected by drought (a & b) and wet events (c & d) in the Ganges and Brahmaputra-Meghna River Basin, respectively. The individual QUMP members outputs are plotted in grey colors. | 117 |
| 5882 | | | |
| 5883 | | | |
| 5884 | | | |
| 5885 | | | |
| 5886 | | | |
| 5887 | | | |

| | | | |
|------|------|---|-----|
| 5888 | 5.15 | Multimodel mean projections of drought and wet areas (as a fraction) in the Ganges and Brahmaputra–Meghna River Basin based on CMIP5 models. The results from GPCCv7 and CRU_TS3.22 are also shown for the period 1951–2012. Area affected by drought (a & b) and wet events (c & d) in the Ganges and Brahmaputra–Meghna River Basin, respectively. The individual CMIP5 outputs are plotted in grey colors. | 118 |
| 5894 | 6.1 | (a) Total number of monthly COSMIC RO profiles reported in and around the GBM River Basin between April 2006 and December 2013, and (b) the corresponding number of data points at each pressure levels 850–30 hPa (1.5–24.0 km). | 125 |
| 5898 | 6.2 | Spatial distribution of COSMIC data points in the lower troposphere for the year 2012: (a) 850 hPa (~ 1.5 km), (b) 700 hPa (~ 3.1 km), (c) 500 hPa (~ 5.8 km), and (d) 400 hPa (~ 7.5 km). | 126 |
| 5901 | 6.3 | The general topography and locations of the radiosonde stations in the GBM River Basin. The radiosondes are shown in different colors- green for IMD/MK4 (India), red for those over Bangladesh (unknown), and blue for ShangE/ShangM (China) | 127 |
| 5905 | 6.4 | Number of data pairs at each pressure level for temperature and humidity (water vapour pressure) for all the radiosonde types (see, Table 6.1) from August 2006 to December 2013. | 131 |
| 5908 | 6.5 | (a) Mean temperature bias and (b) standard deviations of various radiosondes (refer to Table 6.1) over the GBM River Basin with respect to COSMIC RO data between August 2006 and December 2013. | 132 |
| 5911 | 6.6 | (a) Mean temperature bias and (b) standard deviations of IMD/MK4 and IMD-GPS (refer to Table 6.1) with respect to COSMIC RO data over the GBM Basin. The temperature biases are plotted for two periods based on three radiosonde stations (New Delhi, Patna, and Dilbugarh), one between August 2006 and May 2009 (labelled as “IMD/MK4”) and the other between May 2009 and December 2013 (labelled as “IMD/GPS”). | 133 |
| 5917 | 6.7 | (a) Relative errors and (b) standard deviations of water vapour pressure (hPa) of various radiosondes over the GBM River Basin with respect to COSMIC RO data. | 135 |
| 5920 | 6.8 | (a) Relative errors and (b) standard deviations of refractivity (in %) of various radiosondes with respect to COSMIC RO data over the GBM River Basin between August 2006 and December 2013. | 135 |
| 5923 | 6.9 | Temporal evolution of temperature (°C) with the time mean removed at each pressure level (500–10 hPa) based on (a) COSMIC RO, (b) MERRA, and (c) ERA-Interim. Data span between August 2006 and December 2013 and contain area-average over the region (16–35°N, 71–100°E) covering the GBM River Basin. | 136 |

| | | |
|------|--|-----|
| 5928 | 6.10 Seasonal cycle of temperature ($^{\circ}\text{C}$) at (a) 200 hPa, (b) 100 hPa, (c) 70 | |
| 5929 | hPa, and (d) 50 hPa from August 2006 to December 2013 based on | |
| 5930 | COSMIC RO, MERRA, and ERA-Interim averaged over the GBM River | |
| 5931 | Basin. | 137 |
| 5932 | 6.11 Interannual variability of temperature ($^{\circ}\text{C}$) in the UTLS region based on | |
| 5933 | (a) COSMIC RO, (b) MERRA, and (c) ERA-Interim from August 2006 | |
| 5934 | to December 2013. | 138 |
| 5935 | 6.12 Interannual variability of temperature ($^{\circ}\text{C}$) at (a) 200 hPa, (b) 100 hPa, | |
| 5936 | (c) 70 hPa, and (d) 50 hPa from August 2006 to December 2013 based | |
| 5937 | on COSMIC RO, MERRA, and ERA-Interim. (e) Ocean–atmospheric | |
| 5938 | indices: Niño3.4, DMI, and QBO are also plotted for reference. | 139 |
| 5939 | 6.13 Spatial variation of mean and standard deviation of tropopause temper- | |
| 5940 | atures ($^{\circ}\text{C}$) derived from COSMIC RO and MERRA product based on | |
| 5941 | 89 months from August 2006 to December 2013. (a) Mean and (b) stan- | |
| 5942 | dard deviation of tropopause temperatures ($^{\circ}\text{C}$) from COSMIC RO, | |
| 5943 | (c) mean and (d) standard deviation of tropopause temperatures ($^{\circ}\text{C}$) | |
| 5944 | from MERRA product. | 141 |
| 5945 | 6.14 Spatial variation of mean and standard deviation of tropopause heights | |
| 5946 | (km) derived from COSMIC RO and MERRA datasets based on 89 | |
| 5947 | months from August 2006 to December 2013. (a) Mean and (b) standard | |
| 5948 | deviation of tropopause heights (km) from COSMIC RO, (c) mean and | |
| 5949 | (d) standard deviation of tropopause heights (km) estimated based on | |
| 5950 | MERRA temperature data. | 142 |
| 5951 | 6.15 Annual cycle of tropopause over the GBM River Basin computed from | |
| 5952 | MERRA and COSMIC RO data for the period between August 2006 and | |
| 5953 | December 2013: (a) tropopause temperatures and (b) tropopause heights. 143 | |
| 5954 | 6.16 The first three leading EOFs of tropopause temperature ($^{\circ}\text{C}$) based on | |
| 5955 | MERRA data and COSMIC RO data for the period August 2006 to | |
| 5956 | December 2013. | 144 |
| 5957 | 6.17 The corresponding PCs (temporal components) based on the three lead- | |
| 5958 | ing orthogonal modes shown in Fig. 6.16. | 145 |
| 5959 | 6.18 Seasonal mean tropopause temperature and height anomalies due to | |
| 5960 | ENSO mode together with the Niño3.4 index. The area-averaged time- | |
| 5961 | series were obtained by multiplying EOF 1 and PC 1, i.e., basically show- | |
| 5962 | ing the replication of ENSO mode. | 146 |

List of Tables

| | | | |
|------|-----|--|----|
| 5964 | 1.1 | Lists of papers published/submitted under respective chapters. The published version of the papers are provided in the Appendix. | 9 |
| 5965 | | | |
| 5966 | 2.1 | Details of rain gauge products and near-global high-resolution SRS-based precipitation products that have been regularly applied over various parts of the GBM River Basin. | 16 |
| 5967 | | | |
| 5968 | | | |
| 5969 | 2.2 | List of gridded temperature datasets used in this study. All datasets consist of land surface air temperatures derived from ground-based stations across the region. | 16 |
| 5970 | | | |
| 5971 | | | |
| 5972 | 2.3 | Details of the three reanalyses used in this study. All datasets consist of terrestrial surface air temperatures. | 17 |
| 5973 | | | |
| 5974 | 2.4 | Annual amplitudes of various precipitation and temperature products over the Ganges and Brahmaputra-Meghna-River Basins over the period 1980–2013. | 24 |
| 5975 | | | |
| 5976 | | | |
| 5977 | 2.5 | Precipitation trends (mm decade^{-1}) estimated from observed and reanalysis products for various periods between 1980 and 2013. Values that are significant at 95% confidence level are highlighted in bold. | 26 |
| 5978 | | | |
| 5979 | | | |
| 5980 | 2.6 | Linear trends in temperature ($^{\circ}\text{C decade}^{-1}$) derived from observations and reanalysis products for the period 1980–2010. The values that are significant at 95% confidence level are shown in bold. | 27 |
| 5981 | | | |
| 5982 | | | |
| 5983 | 2.7 | Correlation between CRU_TS3.22 and other temperature products over the GBM River Basin for the period 1980–2010. Correlations were computed between the PCs of first two leading modes of CRU_TS3.22 and other products. | 30 |
| 5984 | | | |
| 5985 | | | |
| 5986 | | | |
| 5987 | 2.8 | Correlation between SST anomalies and the first two PCs of various temperature products for the period 1980 to 2010. The correlation values that are significant at 95% confidence level are highlighted bold. | 31 |
| 5988 | | | |
| 5989 | | | |
| 5990 | 3.1 | Summary of the soil moisture products used in the study. | 41 |
| 5991 | 3.2 | Model variants of WaterGAP 2.2a. The model variants used in this study are indicated by an asterisk (*). Source: Döll et al. (2014) | 46 |
| 5992 | | | |
| 5993 | 3.3 | Various categories of extreme rainfall events and drought based on SPI and SIs of soil moisture and TWS (see e.g., McKee et al., 1993). | 47 |
| 5994 | | | |

| | | | |
|------|-----|---|-----|
| 5995 | 3.4 | Example of TCH algorithm. | 50 |
| 5996 | 3.5 | Uncertainties in precipitation (1998–2013), soil moisture (2002–2015), and GRACE TWS changes (2002–2015) in the two sub-basins of GBM River Basin estimated based on the generalized TCH method. | 52 |
| 5997 | | | |
| 5998 | | | |
| 5999 | 3.6 | Correlation coefficients and time lags between SPI (6-month) and SI of soil moisture and TWS in the GBM River Basin for the period 2002–2015. | 62 |
| 6000 | | | |
| 6001 | 4.1 | Summary of RegCM4.4. and PRECIS model settings. | 75 |
| 6002 | 4.2 | Lists of global reanalyses and GCMs that are used to drive the RegCM4.4. | 76 |
| 6003 | 4.3 | Mean biases in DJF and JJAS precipitation (1998–2012) and temperature (1982–2012) between various RCM simulations and TMPAv7 precipitation and CRU_TS3.22 temperature datasets for the Ganges and Brahmaputra–Meghna River Basins | 83 |
| 6004 | | | |
| 6005 | | | |
| 6006 | | | |
| 6007 | 4.4 | Pentad numbers representing the onset and withdrawal of the Indian monsoon based on observed datasets and various RCM simulations over the period 1998–2012. | 89 |
| 6008 | | | |
| 6009 | | | |
| 6010 | 4.5 | DJF and JJAS temperature trends (in °C/decade) estimated from observed, reanalyses, and RCM simulated temperature datasets for the Ganges and Brahmaputra–Meghna River Basins from 1982–2012. The trend values significant at 95% confidence level are highlighted in bold. | 92 |
| 6011 | | | |
| 6012 | | | |
| 6013 | | | |
| 6014 | 4.6 | Correlation between PC 2 (Fig. 4.11h) and basin-averaged temperature anomalies of the Ganges and Brahmaputra–Meghna River Basin for the period 1982–2012. The correlation coefficients presented here are found to be significant at 95% confidence level. | 93 |
| 6015 | | | |
| 6016 | | | |
| 6017 | | | |
| 6018 | 5.1 | Basic descriptions of 8 CMIP5 ESMs including their modelling group, name, and their horizontal (grid dimension) and vertical (number of atmospheric levels, L) resolution of atmospheric model. All models are based on the initial realistaion (r1i1p1) and forced by RCP4.5 scenario. | 100 |
| 6019 | | | |
| 6020 | | | |
| 6021 | | | |
| 6022 | 6.1 | Details of radiosondes shown in Fig. 6.3 and the total number of profiles recorded from 2006 to 2013 at each radiosonde stations. The upgraded IMD radiosondes are named as IMD GPS. The radiosondes within Bangladesh are catagorized as “unknown”. | 128 |
| 6023 | | | |
| 6024 | | | |
| 6025 | | | |
| 6026 | 6.2 | Mean biases and standard deviations in temperature, water vapour pressure, and refractivity of various existing radiosondes in the GBM River Basin with to COSMIC RO data (“wet profiles”). The statistics are computed separately for the upper troposphere (400–150 hPa) and the lower stratosphere (70–20 hPa) for the period 2006–2013. | 133 |
| 6027 | | | |
| 6028 | | | |
| 6029 | | | |
| 6030 | | | |

| | | | |
|------|-----|---|-----|
| 6031 | 6.3 | Mean biases and standard deviations in temperature, water vapour pressure, refractivity of three IMD/GPS-based radiosondes in reference to COSMIC RO data (“wet profiles”). Biases and standard deviations are estimated from Fig. 6.6. | 134 |
| 6032 | | | |
| 6033 | | | |
| 6034 | | | |
| 6035 | 6.4 | Correlation coefficients between various climate indices and temperature anomalies at 200 hPa, 100 hPa, 70 hPa, and 50 hPa for the period August 2006 to December 2013. The values that are significant at 95% confidence level based on the reduced degree of freedom are bolded. Positive time lag indicate ENSO/IOD/QBO fluctuating UTLS temperature and vice versa. | 140 |
| 6036 | | | |
| 6037 | | | |
| 6038 | | | |
| 6039 | | | |
| 6040 | | | |
| 6041 | 6.5 | Trends in temperature ($^{\circ}\text{C}/\text{yr}$) at 200 hPa, 100 hPa, 70 hPa, and 50 hPa for the period August 2006 to December 2013. Uncertainties in trend estimates are reported at 95% confidence interval. | 140 |
| 6042 | | | |
| 6043 | | | |
| 6044 | 6.6 | Trends in tropopause temperatures ($^{\circ}\text{C}/\text{yr}$) and heights (m/yr) based on the area-averaged time-series anomalies derived from COSMIC RO and MERRA. Data span between August 2006 and December 2013. Uncertainties in trend estimates are reported at 95% confidence interval. Note that the temperature trend estimates are not found to be significant at 95% confidence interval. | 143 |
| 6045 | | | |
| 6046 | | | |
| 6047 | | | |
| 6048 | | | |
| 6049 | | | |
| 6050 | 6.7 | Correlation coefficients between tropopause parameters (temperature and height) derived from COSMIC RO and MERRA and ocean-atmospheric indices for the period August 2006 to December 2013. The values that are significant at 95% confidence level based on the reduced degree of freedom are bolded. | 145 |
| 6051 | | | |
| 6052 | | | |
| 6053 | | | |
| 6054 | | | |

6055 Acronyms

| | | |
|-----------|---|--|
| APHRODITE | Asian Precipitation–Highly-Resolved Observational Data Integration Towards Evaluation | |
| CDAAC | COSMIC Data Analysis and Archive Center | |
| CHAMP | CHALLENGING Minisatellite Payload | |
| CMIP3 | Coupled Model Intercomparison Project Phase 3 | |
| CMIP5 | Coupled Model Intercomparison Project Phase 5 | |
| CFSR | Climate Forecast System Reanalysis | |
| CHIRP | Climate Hazards Group InfraRed Precipitation | |
| CMORPH | CPC (Climate Prediction Center) MORPHing technique | |
| COSMIC | Constellation Observing System for Meteorology, Ionosphere, and Climate | |
| CRU | Climate Research Unit, University of East Anglia, UK | |
| CSR | Center for Space Research, University of Texas at Austin | |
| DLR | Deutsches Zentrum für Luft- und Raumfahrt (German Aerospace Center) | |
| ECMWF | European Center for Medium-range Weather Forecast | |
| ENSO | El Niño Southern Oscillation | |
| EOF | Empirical Orthogonal Function | |
| ERA | ECMWF Retrospective Analysis | |
| 6056 | ESM | Earth System Model |
| | EWH | Equivalent Water Height |
| | GBM | Ganges–Brahmaputra–Meghna |
| | GCM | Global-Climate-Model |
| | GFDL | Geophysical Fluid Dynamics Laboratory |
| | GFZ | GeoForschungsZentrum Potsdam |
| | GIA | Glacial Isostatic Adjustment |
| | GLDAS | Global Land Data Assimilation System Hydrology Model |
| | GNSS | Global Navigation Satellite Systems |
| | GPCC | Global Precipitation Climatology Centre |
| | GPS | Global Positioning System |
| | GPS/MET | GPS/METEorology |
| | GRACE | Gravity Recovery And Climate Experiment |
| | GRACE-FO | Gravity Recovery And Climate Experiment-Follow On |
| | GRGS | Groupe de Recherches de Geodesie Spatiale |
| | GSFC | Goddard Space Flight Center |
| | GSMaP_MVK | Global Satellite Mapping of Precipitation Moving Vector with Kalman filter |
| | HadCM | Hadley Center Climate Model |

| | |
|------------------|--|
| IMD | I ndian M eteorological D epartment |
| IOD | I ndian O cean D ipole |
| ICESat | I ce C loud and L and E levation S atellite |
| IPCC | I ntergovernmental P anel on C limate C hange |
| ITG | I nstitute of T heoretical G eodesy, University of Bonn |
| JPL | J et P ropulsion L aboratory |
| KBR | K - B and R anging system |
| KS | K olmogorov- S mirnov T est |
| LEO | L ow E arth O rbiting |
| LSA | L east S quares A djustment |
| LSM | L and S urface M odel |
| MERRA | M odern- E ra R etrospective A nalysis for R esearch and A pplications |
| MPI | M ax- P lanck- I nstitute |
| NCEP/NCAR | N ational C enters for E nvironmental P rediction/ N ational C enter for A tmospheric R esearch |
| NASA | N ational A eronautics and S pace A dministration |
| PC | P rincipal C omponent |
| PCA | P rincipal C omponent A nalysis |
| PDF | P robability D istribution F unction |
| PERSIANN | P recipitation E stimation from R emote S ensing I nformation using A rtificial N eural N etwork |
| PRECIS | P roviding R egional C limate I nformation for I mpact S tudies |
| QUMP | Q uantifying U ncertainties in M odel P rojections |
| RCM | R egional C limate M odel |
| RCP | R epresentative C oncentration P athways |
| RegCM | R egional C limate M odel |
| RMS | R oot M ean S quare |
| RO | R adio O ccultation |
| SHC | S pherical H armonic C oefficient |
| SLR | S atellite L aser R anging |
| SOI | S outhern O scillation I ndex |
| SRES | S Special R eport on E mission S cenarios |
| SRS | S atellite R emote S ensing |
| SST | S ea S urface T emperature |
| SVD | S ingular V alue(V ector) D ecomposition |
| TRMM | T ropical R ainfall M easuring M ission |
| TMPA | T RMM M ultisatellite P recipitation A nalysis |
| TWS | T otal W ater S torage |
| USGS | U nited S tates G eological S urvey |
| UTLS | U pper T roposphere L ower S tratosphere |
| WGHM | W ater G AP G lobal H ydrology M odel |

6058 Appendix - Journal articles

6059 This appendix contains permission statements from the copyright owners of the four
6060 published journal articles (1–3, 6) as a result of this thesis. The list of the papers are
6061 given below:

6062 **Khandu**, J. L. Awange and E. Forootan (2015). An evaluation of high-resolution
6063 gridded precipitation products over Bhutan (1998–2012). *Int. J. Climatol.*, 36(3):1067–
6064 1087. doi:10.1002/joc.4402.

6065 **Khandu**, E. Forootan, M. Schumacher, J.L. Awange and H. Müller Schmied (2016a).
6066 Exploring the influence of precipitation extremes and human water use on total water
6067 storage (TWS) changes in Brahmaputra-Ganges-Meghna Basin. *Water Resour. Res.*,
6068 52(3):2240–2258. doi:10.1002/2015WR018113.

6069 **Khandu**, , J. L. Awange and E. Forootan (2016b). Interannual variability of tem-
6070 perature in the UTLS region over Ganges–Brahmaputra–Meghna river basin based on
6071 COSMIC GNSS RO data. *Atmos. Meas. Tech.*, 9:1685–1699. doi:10.5194/amt-9-1685-
6072 2016.

6073 **Khandu**, J. L. Awange, R. Anyah, M. Kuhn and E. Forootan (2016c). Changes and
6074 variability of precipitation and temperature in the Ganges–Brahmaputra–Meghna River
6075 Basin based on global high-resolution reanalyses. *Int. J. Climatol.*, doi:10.1002/joc.4842.

**JOHN WILEY AND SONS LICENSE
TERMS AND CONDITIONS**

Aug 07, 2016

This Agreement between Khandu Khandu ("You") and John Wiley and Sons ("John Wiley and Sons") consists of your license details and the terms and conditions provided by John Wiley and Sons and Copyright Clearance Center.

| | |
|-------------------------------------|--|
| License Number | 3923640893877 |
| License date | Aug 07, 2016 |
| Licensed Content Publisher | John Wiley and Sons |
| Licensed Content Publication | International Journal of Climatology |
| Licensed Content Title | An evaluation of high-resolution gridded precipitation products over Bhutan (1998–2012) |
| Licensed Content Author | Khandu,J. L. Awange,E. Forootan |
| Licensed Content Date | Jun 30, 2015 |
| Licensed Content Pages | 21 |
| Type of use | Dissertation/Thesis |
| Requestor type | Author of this Wiley article |
| Format | Electronic |
| Portion | Full article |
| Will you be translating? | No |
| Order reference number | 20161 |
| Title of your thesis / dissertation | Assessing impacts on water resources in GBM River Basin |
| Expected completion date | Sep 2016 |
| Expected size (number of pages) | 160 |
| Requestor Location | Khandu Khandu 19B Egerton Street Beckenham,WA, WA 6107 Australia Attn: Khandu Khandu |
| Publisher Tax ID | EU826007151 |
| Billing Type | Invoice |
| Billing Address | Khandu Khandu 19B Egerton Street Beckenham,WA, Australia 6107 Attn: Khandu Khandu |
| Total | 0.00 AUD |
| Terms and Conditions | |

TERMS AND CONDITIONS

This copyrighted material is owned by or exclusively licensed to John Wiley & Sons, Inc. or one of its group companies (each a "Wiley Company") or handled on behalf of a society with which a Wiley Company has exclusive publishing rights in relation to a particular work (collectively "WILEY"). By clicking "accept" in connection with completing this licensing transaction, you agree that the following terms and conditions apply to this transaction (along with the billing and payment terms and conditions established by the Copyright Clearance Center Inc., ("CCC's Billing and Payment terms and conditions"), at the time that you opened your RightsLink account (these are available at any time at <http://myaccount.copyright.com>).

Terms and Conditions

- The materials you have requested permission to reproduce or reuse (the "Wiley Materials") are protected by copyright.
- You are hereby granted a personal, non-exclusive, non-sub licensable (on a stand-alone basis), non-transferable, worldwide, limited license to reproduce the Wiley Materials for the purpose specified in the licensing process. This license, **and any CONTENT (PDF or image file) purchased as part of your order**, is for a one-time use only and limited to any maximum distribution number specified in the license. The first instance of republication or reuse granted by this license must be completed within two years of the date of the grant of this license (although copies prepared before the end date may be distributed thereafter). The Wiley Materials shall not be used in any other manner or for any other purpose, beyond what is granted in the license. Permission is granted subject to an appropriate acknowledgement given to the author, title of the material/book/journal and the publisher. You shall also duplicate the copyright notice that appears in the Wiley publication in your use of the Wiley Material. Permission is also granted on the understanding that nowhere in the text is a previously published source acknowledged for all or part of this Wiley Material. Any third party content is expressly excluded from this permission.
- With respect to the Wiley Materials, all rights are reserved. Except as expressly granted by the terms of the license, no part of the Wiley Materials may be copied, modified, adapted (except for minor reformatting required by the new Publication), translated, reproduced, transferred or distributed, in any form or by any means, and no derivative works may be made based on the Wiley Materials without the prior permission of the respective copyright owner. **For STM Signatory Publishers clearing permission under the terms of the [STM Permissions Guidelines](#) only, the**

terms of the license are extended to include subsequent editions and for editions in other languages, provided such editions are for the work as a whole in situ and does not involve the separate exploitation of the permitted figures or extracts, You may not alter, remove or suppress in any manner any copyright, trademark or other notices displayed by the Wiley Materials. You may not license, rent, sell, loan, lease, pledge, offer as security, transfer or assign the Wiley Materials on a stand-alone basis, or any of the rights granted to you hereunder to any other person.

- The Wiley Materials and all of the intellectual property rights therein shall at all times remain the exclusive property of John Wiley & Sons Inc, the Wiley Companies, or their respective licensors, and your interest therein is only that of having possession of and the right to reproduce the Wiley Materials pursuant to Section 2 herein during the continuance of this Agreement. You agree that you own no right, title or interest in or to the Wiley Materials or any of the intellectual property rights therein. You shall have no rights hereunder other than the license as provided for above in Section 2. No right, license or interest to any trademark, trade name, service mark or other branding ("Marks") of WILEY or its licensors is granted hereunder, and you agree that you shall not assert any such right, license or interest with respect thereto
- NEITHER WILEY NOR ITS LICENSORS MAKES ANY WARRANTY OR REPRESENTATION OF ANY KIND TO YOU OR ANY THIRD PARTY, EXPRESS, IMPLIED OR STATUTORY, WITH RESPECT TO THE MATERIALS OR THE ACCURACY OF ANY INFORMATION CONTAINED IN THE MATERIALS, INCLUDING, WITHOUT LIMITATION, ANY IMPLIED WARRANTY OF MERCHANTABILITY, ACCURACY, SATISFACTORY QUALITY, FITNESS FOR A PARTICULAR PURPOSE, USABILITY, INTEGRATION OR NON-INFRINGEMENT AND ALL SUCH WARRANTIES ARE HEREBY EXCLUDED BY WILEY AND ITS LICENSORS AND WAIVED BY YOU.
- WILEY shall have the right to terminate this Agreement immediately upon breach of this Agreement by you.
- You shall indemnify, defend and hold harmless WILEY, its Licensors and their respective directors, officers, agents and employees, from and against any actual or threatened claims, demands, causes of action or proceedings arising from any breach of this Agreement by you.

- IN NO EVENT SHALL WILEY OR ITS LICENSORS BE LIABLE TO YOU OR ANY OTHER PARTY OR ANY OTHER PERSON OR ENTITY FOR ANY SPECIAL, CONSEQUENTIAL, INCIDENTAL, INDIRECT, EXEMPLARY OR PUNITIVE DAMAGES, HOWEVER CAUSED, ARISING OUT OF OR IN CONNECTION WITH THE DOWNLOADING, PROVISIONING, VIEWING OR USE OF THE MATERIALS REGARDLESS OF THE FORM OF ACTION, WHETHER FOR BREACH OF CONTRACT, BREACH OF WARRANTY, TORT, NEGLIGENCE, INFRINGEMENT OR OTHERWISE (INCLUDING, WITHOUT LIMITATION, DAMAGES BASED ON LOSS OF PROFITS, DATA, FILES, USE, BUSINESS OPPORTUNITY OR CLAIMS OF THIRD PARTIES), AND WHETHER OR NOT THE PARTY HAS BEEN ADVISED OF THE POSSIBILITY OF SUCH DAMAGES. THIS LIMITATION SHALL APPLY NOTWITHSTANDING ANY FAILURE OF ESSENTIAL PURPOSE OF ANY LIMITED REMEDY PROVIDED HEREIN.
- Should any provision of this Agreement be held by a court of competent jurisdiction to be illegal, invalid, or unenforceable, that provision shall be deemed amended to achieve as nearly as possible the same economic effect as the original provision, and the legality, validity and enforceability of the remaining provisions of this Agreement shall not be affected or impaired thereby.
- The failure of either party to enforce any term or condition of this Agreement shall not constitute a waiver of either party's right to enforce each and every term and condition of this Agreement. No breach under this agreement shall be deemed waived or excused by either party unless such waiver or consent is in writing signed by the party granting such waiver or consent. The waiver by or consent of a party to a breach of any provision of this Agreement shall not operate or be construed as a waiver of or consent to any other or subsequent breach by such other party.
- This Agreement may not be assigned (including by operation of law or otherwise) by you without WILEY's prior written consent.
- Any fee required for this permission shall be non-refundable after thirty (30) days from receipt by the CCC.
- These terms and conditions together with CCC's Billing and Payment terms and conditions (which are incorporated herein) form the entire agreement between you and WILEY concerning this licensing transaction and (in the absence of fraud) supersedes all prior agreements and representations of the parties, oral or

written. This Agreement may not be amended except in writing signed by both parties. This Agreement shall be binding upon and inure to the benefit of the parties' successors, legal representatives, and authorized assigns.

- In the event of any conflict between your obligations established by these terms and conditions and those established by CCC's Billing and Payment terms and conditions, these terms and conditions shall prevail.
- WILEY expressly reserves all rights not specifically granted in the combination of (i) the license details provided by you and accepted in the course of this licensing transaction, (ii) these terms and conditions and (iii) CCC's Billing and Payment terms and conditions.
- This Agreement will be void if the Type of Use, Format, Circulation, or Requestor Type was misrepresented during the licensing process.
- This Agreement shall be governed by and construed in accordance with the laws of the State of New York, USA, without regards to such state's conflict of law rules. Any legal action, suit or proceeding arising out of or relating to these Terms and Conditions or the breach thereof shall be instituted in a court of competent jurisdiction in New York County in the State of New York in the United States of America and each party hereby consents and submits to the personal jurisdiction of such court, waives any objection to venue in such court and consents to service of process by registered or certified mail, return receipt requested, at the last known address of such party.

WILEY OPEN ACCESS TERMS AND CONDITIONS

Wiley Publishes Open Access Articles in fully Open Access Journals and in Subscription journals offering Online Open. Although most of the fully Open Access journals publish open access articles under the terms of the Creative Commons Attribution (CC BY) License only, the subscription journals and a few of the Open Access Journals offer a choice of Creative Commons Licenses. The license type is clearly identified on the article.

The Creative Commons Attribution License

The [Creative Commons Attribution License \(CC-BY\)](#) allows users to copy, distribute and transmit an article, adapt the article and make commercial use of the article. The CC-BY license permits commercial and non-

Creative Commons Attribution Non-Commercial License

The [Creative Commons Attribution Non-Commercial \(CC-BY-NC\) License](#) permits use, distribution and reproduction in any medium, provided the

original work is properly cited and is not used for commercial purposes.(see below)

Creative Commons Attribution-Non-Commercial-NoDerivs License

The [Creative Commons Attribution Non-Commercial-NoDerivs License](#) (CC-BY-NC-ND) permits use, distribution and reproduction in any medium, provided the original work is properly cited, is not used for commercial purposes and no modifications or adaptations are made. (see below)

Use by commercial "for-profit" organizations

Use of Wiley Open Access articles for commercial, promotional, or marketing purposes requires further explicit permission from Wiley and will be subject to a fee.

Further details can be found on Wiley Online Library

<http://olabout.wiley.com/WileyCDA/Section/id-410895.html>

Other Terms and Conditions:

v1.10 Last updated September 2015

Questions? customercare@copyright.com or +1-855-239-3415 (toll free in the US) or +1-978-646-2777.

JOHN WILEY AND SONS LICENSE TERMS AND CONDITIONS

Aug 07, 2016

This Agreement between Khandu Khandu ("You") and John Wiley and Sons ("John Wiley and Sons") consists of your license details and the terms and conditions provided by John Wiley and Sons and Copyright Clearance Center.

| | |
|--|---|
| License Number | 3923640826148 |
| License date | Aug 07, 2016 |
| Licensed Content Publisher | John Wiley and Sons |
| Licensed Content Publication | Water Resources Research |
| Licensed Content Title | Exploring the influence of precipitation extremes and human water use on total water storage (TWS) changes in the Ganges-Brahmaputra-Meghna River Basin |
| Licensed Content Author | Khandu,Ehsan Forootan,Maike Schumacher,Joseph L. Awange,Hannes Müller Schmied |
| Licensed Content Date | Mar 24, 2016 |
| Licensed Content Pages | 19 |
| Type of Use | Dissertation/Thesis |
| Requestor type | Author of this Wiley article |
| Format | Electronic |
| Portion | Full article |
| Will you be translating? | No |
| Order reference number | 20160 |
| Title of your thesis / dissertation | Assessing impacts on water resources in GBM River Basin |
| Expected completion date | Sep 2016 |
| Expected size (number of pages) | 160 |
| Requestor Location | Khandu Khandu 19B Egerton Street Beckenham,WA, WA 6107 Australia Attn: Khandu Khandu |
| Publisher Tax ID | EU826007151 |
| Billing Type | Invoice |
| Billing Address | Khandu Khandu 19B Egerton Street Beckenham,WA, Australia 6107 Attn: Khandu Khandu |
| Total | 0.00 AUD |
| Terms and Conditions | |

TERMS AND CONDITIONS

This copyrighted material is owned by or exclusively licensed to John Wiley & Sons, Inc. or one of its group companies (each a "Wiley Company") or handled on behalf of a society with which a Wiley Company has exclusive publishing rights in relation to a particular work (collectively "WILEY"). By clicking "accept" in connection with completing this licensing transaction, you agree that the following terms and conditions apply to this transaction (along with the billing and payment terms and conditions established by the Copyright Clearance Center Inc., ("CCC's Billing and Payment terms and conditions"), at the time that you opened your RightsLink account (these are available at any time at <http://myaccount.copyright.com>).

Terms and Conditions

- The materials you have requested permission to reproduce or reuse (the "Wiley Materials") are protected by copyright.
- You are hereby granted a personal, non-exclusive, non-sub licensable (on a stand-alone basis), non-transferable, worldwide, limited license to reproduce the Wiley Materials for the purpose specified in the licensing process. This license, **and any CONTENT (PDF or image file) purchased as part of your order,** is for a one-time use only and limited to any maximum distribution number specified in the license. The first instance of republication or reuse granted by this license must be completed within two years of the date of the grant of this license (although copies prepared before the end date may be distributed thereafter). The Wiley Materials shall not be used in any other manner or for any other purpose, beyond what is granted in the license. Permission is granted subject to an appropriate acknowledgement given to the author, title of the material/book/journal and the publisher. You shall also duplicate the copyright notice that appears in the Wiley publication in your use of the Wiley Material. Permission is also granted on the understanding that nowhere in the text is a previously published source acknowledged for all or part of this Wiley Material. Any third party content is expressly excluded from this permission.
- With respect to the Wiley Materials, all rights are reserved. Except as expressly granted by the terms of the license, no part of the Wiley Materials may be copied, modified, adapted (except for minor reformatting required by the new Publication), translated, reproduced, transferred or distributed, in any form or by any means, and no derivative works may be made based on the Wiley Materials without the prior permission of the respective copyright owner. **For STM Signatory Publishers clearing permission under the terms of the [STM Permissions Guidelines](#) only, the terms of the license are extended to include subsequent editions and for editions in other languages, provided such editions are for the work as a whole in situ and does not involve the separate exploitation of the permitted figures or extracts,** You may not alter, remove or suppress in any manner any copyright, trademark or other notices displayed by the Wiley Materials. You may not license, rent, sell, loan, lease, pledge, offer as security, transfer or assign the Wiley Materials on a stand-alone basis, or any of the rights granted to you hereunder to any other person.
- The Wiley Materials and all of the intellectual property rights therein shall at all times remain the exclusive property of John Wiley & Sons Inc, the Wiley Companies, or their respective licensors, and your interest therein is only that of having possession of and the right to reproduce the Wiley Materials pursuant to Section 2 herein during the continuance of this Agreement. You agree that you own no right, title or interest in or to the Wiley Materials or any of the intellectual property rights therein. You shall have no rights hereunder other than the license as provided for above in Section 2. No right, license or interest to any trademark, trade name, service mark or other branding ("Marks") of WILEY or its licensors is granted hereunder, and you agree that you shall not assert any such right, license or interest with respect thereto
- NEITHER WILEY NOR ITS LICENSORS MAKES ANY WARRANTY OR REPRESENTATION OF ANY KIND TO YOU OR ANY THIRD PARTY, EXPRESS, IMPLIED OR STATUTORY, WITH RESPECT TO THE MATERIALS OR THE ACCURACY OF ANY INFORMATION CONTAINED IN THE MATERIALS, INCLUDING, WITHOUT LIMITATION, ANY IMPLIED WARRANTY OF MERCHANTABILITY, ACCURACY, SATISFACTORY QUALITY, FITNESS FOR A PARTICULAR PURPOSE, USABILITY, INTEGRATION OR NON-INFRINGEMENT AND ALL SUCH WARRANTIES ARE HEREBY EXCLUDED BY WILEY AND ITS LICENSORS AND WAIVED BY YOU.
- WILEY shall have the right to terminate this Agreement immediately upon breach of this Agreement by you.

- You shall indemnify, defend and hold harmless WILEY, its Licensors and their respective directors, officers, agents and employees, from and against any actual or threatened claims, demands, causes of action or proceedings arising from any breach of this Agreement by you.
- IN NO EVENT SHALL WILEY OR ITS LICENSORS BE LIABLE TO YOU OR ANY OTHER PARTY OR ANY OTHER PERSON OR ENTITY FOR ANY SPECIAL, CONSEQUENTIAL, INCIDENTAL, INDIRECT, EXEMPLARY OR PUNITIVE DAMAGES, HOWEVER CAUSED, ARISING OUT OF OR IN CONNECTION WITH THE DOWNLOADING, PROVISIONING, VIEWING OR USE OF THE MATERIALS REGARDLESS OF THE FORM OF ACTION, WHETHER FOR BREACH OF CONTRACT, BREACH OF WARRANTY, TORT, NEGLIGENCE, INFRINGEMENT OR OTHERWISE (INCLUDING, WITHOUT LIMITATION, DAMAGES BASED ON LOSS OF PROFITS, DATA, FILES, USE, BUSINESS OPPORTUNITY OR CLAIMS OF THIRD PARTIES), AND WHETHER OR NOT THE PARTY HAS BEEN ADVISED OF THE POSSIBILITY OF SUCH DAMAGES. THIS LIMITATION SHALL APPLY NOTWITHSTANDING ANY FAILURE OF ESSENTIAL PURPOSE OF ANY LIMITED REMEDY PROVIDED HEREIN.
- Should any provision of this Agreement be held by a court of competent jurisdiction to be illegal, invalid, or unenforceable, that provision shall be deemed amended to achieve as nearly as possible the same economic effect as the original provision, and the legality, validity and enforceability of the remaining provisions of this Agreement shall not be affected or impaired thereby.
- The failure of either party to enforce any term or condition of this Agreement shall not constitute a waiver of either party's right to enforce each and every term and condition of this Agreement. No breach under this agreement shall be deemed waived or excused by either party unless such waiver or consent is in writing signed by the party granting such waiver or consent. The waiver by or consent of a party to a breach of any provision of this Agreement shall not operate or be construed as a waiver of or consent to any other or subsequent breach by such other party.
- This Agreement may not be assigned (including by operation of law or otherwise) by you without WILEY's prior written consent.
- Any fee required for this permission shall be non-refundable after thirty (30) days from receipt by the CCC.
- These terms and conditions together with CCC's Billing and Payment terms and conditions (which are incorporated herein) form the entire agreement between you and WILEY concerning this licensing transaction and (in the absence of fraud) supersedes all prior agreements and representations of the parties, oral or written. This Agreement may not be amended except in writing signed by both parties. This Agreement shall be binding upon and inure to the benefit of the parties' successors, legal representatives, and authorized assigns.
- In the event of any conflict between your obligations established by these terms and conditions and those established by CCC's Billing and Payment terms and conditions, these terms and conditions shall prevail.
- WILEY expressly reserves all rights not specifically granted in the combination of (i) the license details provided by you and accepted in the course of this licensing transaction, (ii) these terms and conditions and (iii) CCC's Billing and Payment terms and conditions.
- This Agreement will be void if the Type of Use, Format, Circulation, or Requestor Type was misrepresented during the licensing process.
- This Agreement shall be governed by and construed in accordance with the laws of the State of New York, USA, without regards to such state's conflict of law rules. Any legal action, suit or proceeding arising out of or relating to these Terms and Conditions or the breach thereof shall be instituted in a court of competent jurisdiction in New York County in the State of New York in the United States of America and each party hereby consents and submits to the personal jurisdiction of such court, waives any objection to venue in such court and consents to service of process by registered or certified mail, return receipt requested, at the last known address of such party.

WILEY OPEN ACCESS TERMS AND CONDITIONS

Wiley Publishes Open Access Articles in fully Open Access Journals and in Subscription journals offering Online Open. Although most of the fully Open Access journals publish open access articles under the terms of the Creative Commons Attribution (CC BY) License only, the subscription journals and a few of the Open Access Journals offer a choice of Creative Commons Licenses. The license type is clearly identified on the article.

The Creative Commons Attribution License

The [Creative Commons Attribution License \(CC-BY\)](#) allows users to copy, distribute and transmit an article, adapt the article and make commercial use of the article. The CC-BY license permits commercial and non-

Creative Commons Attribution Non-Commercial License

The [Creative Commons Attribution Non-Commercial \(CC-BY-NC\)License](#) permits use, distribution and reproduction in any medium, provided the original work is properly cited and is not used for commercial purposes.(see below)

Creative Commons Attribution-Non-Commercial-NoDerivs License

The [Creative Commons Attribution Non-Commercial-NoDerivs License](#) (CC-BY-NC-ND) permits use, distribution and reproduction in any medium, provided the original work is properly cited, is not used for commercial purposes and no modifications or adaptations are made. (see below)

Use by commercial "for-profit" organizations

Use of Wiley Open Access articles for commercial, promotional, or marketing purposes requires further explicit permission from Wiley and will be subject to a fee.

Further details can be found on Wiley Online Library <http://olabout.wiley.com/WileyCDA/Section/id-410895.html>

Other Terms and Conditions:

v1.10 Last updated September 2015

Questions? customercare@copyright.com or +1-855-239-3415 (toll free in the US) or +1-978-646-2777.

JOHN WILEY AND SONS LICENSE TERMS AND CONDITIONS

Aug 07, 2016

This Agreement between Khandu Khandu ("You") and John Wiley and Sons ("John Wiley and Sons") consists of your license details and the terms and conditions provided by John Wiley and Sons and Copyright Clearance Center.

| | |
|--|--|
| License Number | 3923640693469 |
| License date | Aug 07, 2016 |
| Licensed Content Publisher | John Wiley and Sons |
| Licensed Content Publication | International Journal of Climatology |
| Licensed Content Title | Changes and variability of precipitation and temperature in the Ganges–Brahmaputra– Meghna River Basin based on global high-resolution reanalyses |
| Licensed Content Author | Khandu,Joseph L. Awange,Michael Kuhn,Richard Anyah,Ehsan Frootan |
| Licensed Content Date | Aug 4, 2016 |
| Licensed Content Pages | 1 |
| Type of Use | Dissertation/Thesis |
| Requestor type | Author of this Wiley article |
| Format | Print and electronic |
| Portion | Full article |
| Will you be translating? | No |
| Order reference number | 2016 |
| Title of your thesis / dissertation | Assessing impacts on water resources in GBM River Basin |
| Expected completion date | Sep 2016 |
| Expected size (number of pages) | 160 |
| Requestor Location | Khandu Khandu 19B Egerton Street Beckenham,WA, WA 6107 Australia Attn: Khandu Khandu |
| Publisher Tax ID | EU826007151 |
| Billing Type | Invoice |
| Billing Address | Khandu Khandu 19B Egerton Street Beckenham,WA, Australia 6107 Attn: Khandu Khandu |
| Total | 0.00 AUD |
| Terms and Conditions | |

TERMS AND CONDITIONS

This copyrighted material is owned by or exclusively licensed to John Wiley & Sons, Inc. or one of its group companies (each a "Wiley Company") or handled on behalf of a society with which a Wiley Company has exclusive publishing rights in relation to a particular work (collectively "WILEY"). By clicking "accept" in connection with completing this licensing transaction, you agree that the following terms and conditions apply to this transaction (along with the billing and payment terms and conditions established by the Copyright Clearance Center Inc., ("CCC's Billing and Payment terms and conditions"), at the time that you opened your RightsLink account (these are available at any time at <http://myaccount.copyright.com>).

Terms and Conditions

- The materials you have requested permission to reproduce or reuse (the "Wiley Materials") are protected by copyright.
- You are hereby granted a personal, non-exclusive, non-sub licensable (on a stand-alone basis), non-transferable, worldwide, limited license to reproduce the Wiley Materials for the purpose specified in the licensing process. This license, **and any CONTENT (PDF or image file) purchased as part of your order,** is for a one-time use only and limited to any maximum distribution number specified in the license. The first instance of republication or reuse granted by this license must be completed within two years of the date of the grant of this license (although copies prepared before the end date may be distributed thereafter). The Wiley Materials shall not be used in any other manner or for any other purpose, beyond what is granted in the license. Permission is granted subject to an appropriate acknowledgement given to the author, title of the material/book/journal and the publisher. You shall also duplicate the copyright notice that appears in the Wiley publication in your use of the Wiley Material. Permission is also granted on the understanding that nowhere in the text is a previously published source acknowledged for all or part of this Wiley Material. Any third party content is expressly excluded from this permission.
- With respect to the Wiley Materials, all rights are reserved. Except as expressly granted by the terms of the license, no part of the Wiley Materials may be copied, modified, adapted (except for minor reformatting required by the new Publication), translated, reproduced, transferred or distributed, in any form or by any means, and no derivative works may be made based on the Wiley Materials without the prior permission of the respective copyright owner. **For STM Signatory Publishers clearing permission under the terms of the [STM Permissions Guidelines](#) only, the terms of the license are extended to include subsequent editions and for editions in other languages, provided such editions are for the work as a whole in situ and does not involve the separate exploitation of the permitted figures or extracts,** You may not alter, remove or suppress in any manner any copyright, trademark or other notices displayed by the Wiley Materials. You may not license, rent, sell, loan, lease, pledge, offer as security, transfer or assign the Wiley Materials on a stand-alone basis, or any of the rights granted to you hereunder to any other person.
- The Wiley Materials and all of the intellectual property rights therein shall at all times remain the exclusive property of John Wiley & Sons Inc, the Wiley Companies, or their respective licensors, and your interest therein is only that of having possession of and the right to reproduce the Wiley Materials pursuant to Section 2 herein during the continuance of this Agreement. You agree that you own no right, title or interest in or to the Wiley Materials or any of the intellectual property rights therein. You shall have no rights hereunder other than the license as provided for above in Section 2. No right, license or interest to any trademark, trade name, service mark or other branding ("Marks") of WILEY or its licensors is granted hereunder, and you agree that you shall not assert any such right, license or interest with respect thereto
- NEITHER WILEY NOR ITS LICENSORS MAKES ANY WARRANTY OR REPRESENTATION OF ANY KIND TO YOU OR ANY THIRD PARTY, EXPRESS, IMPLIED OR STATUTORY, WITH RESPECT TO THE MATERIALS OR THE ACCURACY OF ANY INFORMATION CONTAINED IN THE MATERIALS, INCLUDING, WITHOUT LIMITATION, ANY IMPLIED WARRANTY OF MERCHANTABILITY, ACCURACY, SATISFACTORY QUALITY, FITNESS FOR A PARTICULAR PURPOSE, USABILITY, INTEGRATION OR NON-INFRINGEMENT AND ALL SUCH WARRANTIES ARE HEREBY EXCLUDED BY WILEY AND ITS LICENSORS AND WAIVED BY YOU.
- WILEY shall have the right to terminate this Agreement immediately upon breach of this Agreement by you.

- You shall indemnify, defend and hold harmless WILEY, its Licensors and their respective directors, officers, agents and employees, from and against any actual or threatened claims, demands, causes of action or proceedings arising from any breach of this Agreement by you.
- IN NO EVENT SHALL WILEY OR ITS LICENSORS BE LIABLE TO YOU OR ANY OTHER PARTY OR ANY OTHER PERSON OR ENTITY FOR ANY SPECIAL, CONSEQUENTIAL, INCIDENTAL, INDIRECT, EXEMPLARY OR PUNITIVE DAMAGES, HOWEVER CAUSED, ARISING OUT OF OR IN CONNECTION WITH THE DOWNLOADING, PROVISIONING, VIEWING OR USE OF THE MATERIALS REGARDLESS OF THE FORM OF ACTION, WHETHER FOR BREACH OF CONTRACT, BREACH OF WARRANTY, TORT, NEGLIGENCE, INFRINGEMENT OR OTHERWISE (INCLUDING, WITHOUT LIMITATION, DAMAGES BASED ON LOSS OF PROFITS, DATA, FILES, USE, BUSINESS OPPORTUNITY OR CLAIMS OF THIRD PARTIES), AND WHETHER OR NOT THE PARTY HAS BEEN ADVISED OF THE POSSIBILITY OF SUCH DAMAGES. THIS LIMITATION SHALL APPLY NOTWITHSTANDING ANY FAILURE OF ESSENTIAL PURPOSE OF ANY LIMITED REMEDY PROVIDED HEREIN.
- Should any provision of this Agreement be held by a court of competent jurisdiction to be illegal, invalid, or unenforceable, that provision shall be deemed amended to achieve as nearly as possible the same economic effect as the original provision, and the legality, validity and enforceability of the remaining provisions of this Agreement shall not be affected or impaired thereby.
- The failure of either party to enforce any term or condition of this Agreement shall not constitute a waiver of either party's right to enforce each and every term and condition of this Agreement. No breach under this agreement shall be deemed waived or excused by either party unless such waiver or consent is in writing signed by the party granting such waiver or consent. The waiver by or consent of a party to a breach of any provision of this Agreement shall not operate or be construed as a waiver of or consent to any other or subsequent breach by such other party.
- This Agreement may not be assigned (including by operation of law or otherwise) by you without WILEY's prior written consent.
- Any fee required for this permission shall be non-refundable after thirty (30) days from receipt by the CCC.
- These terms and conditions together with CCC's Billing and Payment terms and conditions (which are incorporated herein) form the entire agreement between you and WILEY concerning this licensing transaction and (in the absence of fraud) supersedes all prior agreements and representations of the parties, oral or written. This Agreement may not be amended except in writing signed by both parties. This Agreement shall be binding upon and inure to the benefit of the parties' successors, legal representatives, and authorized assigns.
- In the event of any conflict between your obligations established by these terms and conditions and those established by CCC's Billing and Payment terms and conditions, these terms and conditions shall prevail.
- WILEY expressly reserves all rights not specifically granted in the combination of (i) the license details provided by you and accepted in the course of this licensing transaction, (ii) these terms and conditions and (iii) CCC's Billing and Payment terms and conditions.
- This Agreement will be void if the Type of Use, Format, Circulation, or Requestor Type was misrepresented during the licensing process.
- This Agreement shall be governed by and construed in accordance with the laws of the State of New York, USA, without regards to such state's conflict of law rules. Any legal action, suit or proceeding arising out of or relating to these Terms and Conditions or the breach thereof shall be instituted in a court of competent jurisdiction in New York County in the State of New York in the United States of America and each party hereby consents and submits to the personal jurisdiction of such court, waives any objection to venue in such court and consents to service of process by registered or certified mail, return receipt requested, at the last known address of such party.

WILEY OPEN ACCESS TERMS AND CONDITIONS

Wiley Publishes Open Access Articles in fully Open Access Journals and in Subscription journals offering Online Open. Although most of the fully Open Access journals publish open access articles under the terms of the Creative Commons Attribution (CC BY) License only, the subscription journals and a few of the Open Access Journals offer a choice of Creative Commons Licenses. The license type is clearly identified on the article.

The Creative Commons Attribution License

The [Creative Commons Attribution License \(CC-BY\)](#) allows users to copy, distribute and transmit an article, adapt the article and make commercial use of the article. The CC-BY license permits commercial and non-

Creative Commons Attribution Non-Commercial License

The [Creative Commons Attribution Non-Commercial \(CC-BY-NC\)License](#) permits use, distribution and reproduction in any medium, provided the original work is properly cited and is not used for commercial purposes.(see below)

Creative Commons Attribution-Non-Commercial-NoDerivs License

The [Creative Commons Attribution Non-Commercial-NoDerivs License](#) (CC-BY-NC-ND) permits use, distribution and reproduction in any medium, provided the original work is properly cited, is not used for commercial purposes and no modifications or adaptations are made. (see below)

Use by commercial "for-profit" organizations

Use of Wiley Open Access articles for commercial, promotional, or marketing purposes requires further explicit permission from Wiley and will be subject to a fee.

Further details can be found on Wiley Online Library <http://olabout.wiley.com/WileyCDA/Section/id-410895.html>

Other Terms and Conditions:

v1.10 Last updated September 2015

Questions? customercare@copyright.com or +1-855-239-3415 (toll free in the US) or +1-978-646-2777.

License and copyright agreement



The following license and copyright agreement is valid for any article published by Copernicus Publications whose original manuscript was received from **10 December 2007** on.

Author's certification

In submitting the manuscript, the authors certify that:

They are authorized by their co-authors to enter into these arrangements.

The work described has not been published before (except in the form of an abstract or as part of a published lecture, review or thesis), that it is not under consideration for publication elsewhere, that its publication has been approved by all the author(s) and by the responsible authorities – tacitly or explicitly – of the institutes where the work has been carried out.

They secure the right to reproduce any material that has already been published or copyrighted elsewhere.

They agree to the following license and copyright agreement:

Copyright

Copyright on any article is retained by the author(s). Regarding copyright transfers please see below.

Authors grant Copernicus Publications a license to publish the article and identify itself as the original publisher.

Authors grant Copernicus Publications commercial rights to produce hardcopy volumes of the journal for sale to libraries and individuals.

Authors grant any third party the right to use the article freely as long as its original authors and citation details are identified.

The article is distributed under the [Creative Commons Attribution 3.0](#) License. Unless otherwise stated, associated published material is distributed under the same licence:

Creative Commons Attribution 3.0 License

Anyone is free:



to Share — to copy, distribute and transmit the work



to Remix — to adapt the work

Under the following conditions:



Attribution — The original authors must be given credit.

For any reuse or distribution, it must be made clear to others what the license terms of this work are.

Any of these conditions can be waived if the copyright holders give permission.

Nothing in this license impairs or restricts the author's moral rights.

The full [legal code](#) of this license.

Copyright transfers

Many authors have strict regulations in their contract of employment regarding their works. A transfer of copyright to the institution or company, as well as the reservation of specific usage rights, is typical. Please note that in the case of open-access publications in combination with a Creative Commons License, a transfer of the **copyright** to the institution is possible, as it belongs to the author anyway and is not subject to the publisher.

Any **usage rights** are regulated through the Creative Commons License. As Copernicus Publications uses the Creative Commons Attribution 3.0 License, anyone (the author, his/her institution/company, the publisher, as well as the public) is free to copy, distribute, transmit, and adapt the work as long as the original author is given credit (see above). Therefore, specific usage rights cannot be reserved by the author or his/her institution/company, and the publisher cannot include a statement "all rights reserved" in any published paper.

A copyright transfer from the author to his/her institution/company will be expressed in a special "Copyright Statement" at the end of the publication rather than on the first page in the article citation header. Authors are asked to include the following sentence: "The author's copyright for this publication is transferred to *institution/company*".

Crown copyright

The license and copyright agreement of Copernicus Publications respects the Crown copyright. For works written by authors affiliated with the British Government and its institutions, a copyright statement will be included at the end of the publication. Authors are asked to use the following statement, which has been approved by the Information Policy department of The National Archives:

The works published in this journal are distributed under the Creative Commons Attribution 3.0 License. This license does not affect the Crown copyright work, which is re-usable under the Open Government Licence (OGL). The Creative Commons Attribution 3.0 License and the OGL are interoperable and do not conflict with, reduce or limit each other.

© Crown copyright YEAR

Reproduction request

All articles published by Copernicus Publications are licensed under the Creative Commons Attribution 3.0 License (see details above) together with an author copyright. Therefore, there is no need from the publisher's side to allow/confirm a reproduction. We would suggest contacting the author to inform him/her about the further usage of the material. But as the author decided to publish the scientific results under the "CC-BY" license, he/she decided to share the work under the condition that the original authors must be given credit.